

Confronting FU Orionis outbursts and
Pre/transitional disks: protostellar/protoplanetary
disk structure and evolution

by

Zhaohuan Zhu

A dissertation submitted in partial fulfillment
of the requirements for the degree of
Doctor of Philosophy
(Astronomy and Astrophysics)
in The University of Michigan
2011

Doctoral Committee:

Professor Lee W. Hartmann, Chair

Professor Fred C. Adams

Professor Nuria P. Calvet

Associate Professor John D. Monnier

Professor Charles F. Gammie, University of Illinois at

Urbana-Champaign

Copyright © $\frac{\text{Zhaohuan Zhu}}{\text{All Rights Reserved}}$ 2011

To my parents Shi Zhu and Jinli Chen

ACKNOWLEDGMENTS

This thesis would not have been possible without support from a lot of people.

I owe my deepest gratitude to my thesis advisor Prof. Lee W. Hartmann for his guidance, encouragement, patience, understanding, enthusiasm, and vast knowledge. He always stands in my shoes and thinks hard what is the best for me. He had a clear vision how the project would progress, gave me abundant suggestions, but also left plenty of room for me to think in my own way. Although with his deep insight and vast experience, he treats a fresh PhD student as a colleague. Every discussion was pleasant, productive, and full of passion. Besides science, Lee also helped me, a non native english speaker, to improve my scientific writing with an extraordinary patience, e.g. our latest paper is undergoing 24th revision. It is difficult to overstate my appreciation for being under guidance with Lee.

Prof. Nuria P. Calvet, with whom I finished my first year project, has been giving me continuous advices throughout the past six years. Besides science, I am also grateful to her for her care for my daily graduate life.

I am deeply grateful to Prof. Charles F. Gammie who helped me to establish my thesis project. His great physical insight lead me all the way to the end of my thesis work. As the only committee member knowing details of the numerical simulations, his suggestions has always being to the point and shaped the project.

I would like to thank Prof. Fred C. Adams and Prof. John D. Monnier for their advices and hard questions, which are very valuable for me.

I am indebted to my colleagues and fellow graduate students, without whom, the graduate student life in a foreign country would not be as easy as it seems.

And to my wife Mo Weng and son Leo who make everyday full of love and joy.

Finally and most importantly, I want to thank my parents, Shi Zhu and Jinli

Chen, for continuous support and understanding. Leaving a kid studying abroad for six years was not easy for them. This thesis is dedicated to my parents.

CONTENTS

DEDICATION	ii
ACKNOWLEDGMENTS	iii
LIST OF FIGURES	x
LIST OF TABLES	xvi
ABSTRACT	xvii

CHAPTER

1 Introduction	1
1.1 Protostellar & Protoplanetary Disks	1
1.2 The “luminosity problem” and outbursting accretion disks	3
1.3 Planet formation	5
2 The Hot Inner Disk of FU ORI	14
2.1 Abstract	14
2.2 Introduction	15
2.3 Optical and infrared data	16
2.4 Model	18
2.5 Comparison with observations	22
2.6 Discussion	27
2.6.1 The steady accretion disk model and the inner boundary condition	27
2.6.2 R_{out} and α	28
2.6.3 Thermal and other instabilities	30
2.7 Conclusions	33

3	Long-wavelength Excesses of FU Orionis Objects: Flared outer disks or Infalling envelopes?	46
3.1	Abstract	46
3.2	Introduction	47
3.3	Optical and infrared data	48
3.3.1	Photometry and Spectra	48
3.3.2	Interferometry	49
3.4	Model calculations	49
3.4.1	Temperature structure of the irradiated surface	49
3.4.2	Emergent spectra and disk images	53
3.5	Results	53
3.5.1	FU Ori	53
3.5.2	BBW 76	56
3.5.3	V1515 Cyg	56
3.6	Discussion	57
3.6.1	Flared Disks	57
3.6.2	Envelopes	58
3.6.3	Do FU Ori and BBW 76 have envelopes?	60
3.6.4	Dust properties	61
3.6.5	Evolutionary states and FU Ori classification	61
3.7	Conclusions	64
3.8	Appendix	64
3.8.1	Flared surface geometry	64
3.8.2	Emergent flux and image	66
4	The Differential Rotation of FU Ori	76
4.1	Abstract	76
4.2	Introduction	77
4.3	Observations	78
4.4	Results	79
4.5	Discussion	81

5	Non-steady Accretion in Protostars	89
5.1	Abstract	89
5.2	Introduction	89
5.3	Overview	91
5.4	Methods	94
5.5	Results	97
5.6	Discussion	100
5.6.1	Outbursts?	101
5.6.2	Local vs. non-local GI transport	102
5.6.3	What is α_M ?	103
5.6.4	Protostellar accretion	104
5.6.5	FU Ori outbursts	105
5.7	Conclusions	106
5.8	Appendix: Rosseland mean opacity	106
6	2-D simulations of FU Orionis disk outbursts	116
6.1	Abstract	116
6.2	Introduction	116
6.3	Methods	118
6.3.1	Viscous heating	119
6.3.2	Radiative cooling	120
6.3.3	Angular Momentum Transport	125
6.4	2D results	126
6.4.1	Initial and Boundary Conditions	127
6.4.2	Outbursts	128
6.4.3	Resolution Study	130
6.4.4	Boundary effects	131
6.5	Vertical Structure and Convection	132
6.6	Discussion	136
6.7	Conclusions	140
6.8	Appendix A: Radiative cooling scheme tests	141

6.9	Appendix B: Thermal instability	142
6.9.1	'S' curve of 2D models	142
6.9.2	'S' curve of 1D models	143
7	Long-term Evolution of Protostellar and Protoplanetary Disks.	
	I. Outbursts	159
7.1	Abstract	159
7.2	Introduction	160
7.3	One-dimensional two-zone models	161
7.4	Outburst behavior	166
7.5	Parameter study	168
7.5.1	Dependence on \dot{M}_{in}	169
7.5.2	Dependence on α_M and T_M	170
7.5.3	Dependence on M_* and Σ_A	171
7.6	Discussion	172
7.6.1	Unsteady accretion region	172
7.6.2	Steady vs Non-steady accretion	174
7.6.3	Constraints from observations of FU Orionis objects . . .	174
7.7	Conclusions	176
7.8	appendix	177
8	Long-term Evolution of Protostellar and Protoplanetary Disks.	
	II. Layered Accretion with Infall	188
8.1	Abstract	188
8.2	Introduction	189
8.3	1D2Z models with infall	191
8.4	Layered accretion with infall	196
8.4.1	Fiducial model	196
8.4.2	Varying core rotation	199
8.4.3	Different disk configurations	201
8.5	Discussion	203
8.5.1	Dead zones and star formation by disk accretion	203

8.5.2	Relation to previous work	204
8.5.3	Outbursts and luminosity problem	206
8.5.4	Rotation and Fragmentation	208
8.5.5	Dead zones: do they exist?	208
8.5.6	R_D and planet migration	211
8.5.7	MMSN and planet formation in the layered disk	211
8.6	Conclusions	212
8.7	Appendix A. Layered accretion	213
8.7.1	A.1 Dead zone	214
8.7.2	A.2 Outer pure MRI active disk beyond R_D	216
8.7.3	A.3 Residual dead zone viscosity	220
8.8	Appendix B. GI disk fragmentation radius	221
9	Transitional and Pre-Transitional disks: Gap Opening by Multiple Planets ?	239
9.1	Abstract	239
9.2	Introduction	240
9.3	Inferred properties of pre/transitional disks	242
9.4	Methods: Disk–planet simulations	244
9.5	Results	250
9.5.1	Viscous disks with one planet	251
9.5.2	Viscous disks with two planets	253
9.5.3	Viscous disks with three and four planets	254
9.6	Discussion	255
9.6.1	Gap structure and dust depletion	257
9.6.2	Limitations	260
9.7	Summary	261
10	Conclusions	269
10.1	Thesis Work	269
10.2	Future work	270
	BIBLIOGRAPHY	273

LIST OF FIGURES

Figure

1.1	Angular momentum transfer in a shearing disk.	8
1.2	Layered accretion for protostellar and protoplanetary disks.	9
1.3	Protostar mass accretion rate with time.	10
1.4	Optical images for FU Orionis objects.	11
1.5	Light curves of FU Orionis objects.	12
1.6	Disk fragmentation by GI.	12
1.7	GM Aur SED and image.	13
2.1	The spectral energy distribution of FU Ori.	36
2.2	Our calculated Rosseland mean opacity as a function of temperature for solar composition.	37
2.3	The spectrum predicted by the annulus with $T_{eff}=5300$ K (solid line) and the spectrum of SAO 21446 which is a G1 I star (Jacoby et al., 1984) (dotted line).	38
2.4	Emergent intensities from selected annuli of the disk model calculated for a 55 degree emergent angle.	39
2.5	Observed UBV _R photometry and optical spectra with different A_V : 2.2,1.9,1.5,1.3 (dotted lines, from top to bottom) and model spectra with T_{max} : 7240, 6770, 6420, 5840 (solid lines, from top to bottom).	40
2.6	Comparison between observed data and disk models for different values of the outer radii.	41
2.7	Two truncated models fitting the observations corrected by $A_V=2.2$ and $A_V=1.5$	42

2.8	CO first overtone of FU Ori.	43
2.9	The mid-infrared part of the observed spectra in Figure 2.1 compared with the model spectra.	44
2.10	The equilibrium curves for thermal-instability.	45
3.1	The geometry used to calculate the irradiation and the emergent flux.	66
3.2	SED of FU Ori and the adopted model.	67
3.3	The absorption height of the surface of the outer disk for FU Ori (dotted line), BBW 76 (dashed line) and V1515 Cyg (long dashed line) as de- scribed in Eq. (3.10).	68
3.4	The effective temperature of V1515 Cyg (solid line) and FU Ori (dot- ted line) with respect to the radius.	69
3.5	The H band image of the FU Ori model with -30° position angle.	70
3.6	Visibility square-baseline at H and K band.	71
3.7	Visibility-wavelength at three baselines (44.56 m, 56.74 m, 86.25 m).	72
3.8	SED of BBW 76 and adopted model.	73
3.9	SED of V1515 Cyg and adopted model.	74
4.1	Observed $4.9 \mu\text{m}$ Phoenix spectrum of FU Ori (solid curve) compared with our synthetic disk model spectrum (upper dotted curve).	86
4.2	Comparison of the observed MIKE spectrum of FU Ori near 7080 \AA (solid curve) with the synthetic disk spectrum (dotted curve).	87
4.3	Dependence of the model line half-width at half-depth (HWHD) on excitation potential (EP) (left) and the wavelength (right), taken from Table 4.5.	88
5.1	Steady-state disk calculations for four accretion rates - 10^{-4} , 10^{-5} , 10^{-6} , and $10^{-7} M_\odot \text{ yr}^{-1}$, assuming a central star of mass $1 M_\odot$	108
5.2	Unstable regions in the $r - \dot{M}$ plane for a $1 M_\odot$ central star.	109
5.3	Same as in Figure 5.1 but for a central star mass of $0.3 M_\odot$	110
5.4	Same as in Figure 5.1 but for a central star mass of $0.05 M_\odot$	111

5.5	Same as figure 5.2 for $0.3M_{\odot}$ central star.	112
5.6	Same as Figure 5.2 for the $0.05M_{\odot}$ central star.	112
5.7	The mass of the disk integrated between radius R and the outer radius of 20 AU for steady-state $Q=2$ disks, at four accretion rates - 10^{-4} , 10^{-5} , 10^{-6} , and $10^{-7}M_{\odot} \text{ yr}^{-1}$	113
5.8	Same as Figure 5.2 for the parameters of Armitage et al. (2001) (see text)	114
5.9	Rosseland mean opacities.	115
6.1	The disk's temperature color contours at four stages during the out- burst in R-Z coordinate.	144
6.2	The disk's temperature color contours at four stages during the out- burst, the same as Fig. 6.1.	145
6.3	Similar to Figure 6.2 but shows the density contours.	146
6.4	The distribution of the vertically integrated surface density at four corresponding stages as shown Figure 6.2.	147
6.5	Similar to Figure 6.4 but shows the effective temperature distribution at the four stages.	148
6.6	The disk's mass accretion rate through the innermost boundary with time for models with four different resolutions.	149
6.7	The disk's mass accretion rate for different disk configurations.	150
6.8	The temperature contours at the stage when their mass accretion rates reach maximum for the four models shown in Figure 6.7.	151
6.9	The disk's vertical structure at 0.1 AU in the TI active stage.	152
6.10	The contours for the temperature, temperature gradient, velocity and Mach number at the TI active stage.	153
6.11	The velocity vectors of the computational grid are plotted on top of the temperature contours at the TI active region.	154
6.12	the 'S' curve calculated by the LVMZ (solid curve) and the midplane approximation (dotted curve) at 0.1 AU.	155

6.13	The solid curve shows the $1\mu\text{m}$ magnitude derived from the 2D disk at the beginning of the outburst.	156
6.14	Grey atmosphere test.	157
7.1	The mass accretion rate with time for both 1-D (dotted curve) and 2-D (solid curve) simulations.	179
7.2	The mass accretion rate with time for different α_M and T_M for the mass infall rate of $10^{-4}M_\odot \text{yr}^{-1}$	180
7.3	The mass accretion rate with time for different α_M and T_M for the mass infall rate of $10^{-5}M_\odot \text{yr}^{-1}$	181
7.4	The mass accretion rate with time for different α_M and T_M for the mass infall rate of $10^{-6}M_\odot \text{yr}^{-1}$	182
7.5	The disk's radial structure at the stage just before the MRI is triggered in cases where $T_M=1800$ K (dotted curve) and $T_M=1400$ K (solid curve).	183
7.6	The disk mass accretion rate with time for different active layer surface density (50 g cm^{-2} for the dotted curve and 10 g cm^{-2} for the solid curve).	184
7.7	The mass accretion rate with time for different central star masses: $1 M_\odot$ (solid curve), $0.3 M_\odot$ (dotted curve), $0.1 M_\odot$ (dashed curve).	185
7.8	Unstable regions in the $R - \dot{M}$ plane for a $1M_\odot$ central star.	186
8.1	The disk mass accretion rate (upper panel) and the mass of the central star and disk (lower panel) with time for our fiducial model ($\Omega_c = 10^{-14} \text{rad s}^{-1}$).	223
8.2	The disk surface density, temperature structure, mass accretion rate and α and Q-parameter at the end of the infall phase (0.2 Myr) for various models.	224
8.3	The same as figure 8.2 but at $t=1$ Myr. The triangle labels the maximum centrifugal radius.	225
8.4	The disk mass accretion rates and the mass of the central star and disk with time for different core rotations.	226

8.5	Unstable regions in the $R - \dot{M}$ plane for an accretion disk around $1M_{\odot}$ central star.	227
8.6	The disk surface density with radii for different rotation cores as shown in figure 8.4 at 0.3 million years (solid curves) and 1 million years (dashed curves).	228
8.7	The disk surface density distributions at 1 million years for various models.	229
8.8	Disk evolution of the model without the active layer, in which case only GI has been considered to transport mass from the outer disk to the inner disk.	230
8.9	Disk evolution of the model similar to our fiducial layered model but with a residual dead zone viscosity ($\alpha_{rd} = 10^{-3}$).	231
8.10	Constant- α disks.	232
8.11	In the layered disk model, the dead zone outer radius R_D with time for $\Omega_c = 2 \times 10^{-14} \text{rad s}^{-1}$ (upper two curves) and $\Omega_c = 3 \times 10^{-15} \text{rad s}^{-1}$ (lower two curves).	233
8.12	Our simulated disk surface density compared with different MMSN models.	234
8.13	The disk surface density distribution of various models.	235
8.14	The disk surface brightness temperature for the models in Figure 8.13.	236
8.15	The viscous disk surface density with radii.	237
9.1	Disk surface densities at 0.5 Myr for viscous disks ($\alpha=0.01$) with one planet accreting at different rates.	264
9.2	The planet's semi-major axis, eccentricity, and mass as a function of time for the P1A1 case (left) and P1A10 case (right).	264
9.3	Left: disk surface densities at 0.5 Myr for two planets with no planet accretion (solid curve), $f=100$ (dotted curve), $f=10$ (short-dashed curve), and $f=1$ (long-dashed curve). Right: the disk accretion rates onto the central star for these four cases.	265

9.4	The planets' semi-major axis, eccentricities, and masses as a function of time for the two accreting planets in the P2A1 case (left) and P2A10 case (right).	265
9.5	Left: disk surface densities at 0.4 Myrs for three planets with no planet accretion (solid curve), $f=100$ (dotted curve), $f = 10$ (short-dashed curve), and $f = 1$ (long-dashed curve). Right: the corresponding disk accretion rates.	266
9.6	The planets' semi-major axis, eccentricities, and masses as a function of time for three accreting planets in P3A1 case (left) and P3A10 case (right).	266
9.7	Left: disk surface densities at 0.4 Myrs for four planets with no planet accretion (solid curve), $f=100$ (dotted curve), $f = 10$ (short-dashed curve), and $f = 1$ (long-dashed curve). Right: the corresponding disk accretion rates.	267
9.8	The planets' semi-major axis, eccentricities, resonant angles (2:1), masses with time for four planets in P4AN case (left) and P4A10 case (right).	267
9.9	The pre-transitional disk structure taken from Espaillat et al. (2010) compared with the azimuthal-averaged dust surface density of the P4A10 case.	268

LIST OF TABLES

Table

2.1	Best fit model	34
2.2	Optical lines used to determine the spectral type	35
3.1	Adopted dust composition	75
3.2	Parameters for best fit models	75
4.1	HWHD of lines of FU Ori	85
5.1	Fit to Zhu et al. (2007, 2008) opacity	107
6.1	2D models	158
7.1	1D2Z models	187
8.1	1D2Z models at 0.3 and 1 Myr	238
9.1	Stellar and Model Properties	262
9.2	Models	263

ABSTRACT

The mechanisms and efficiencies of mass transport in accretion disks can be best constrained by studying their time-dependent behavior. For the first part of my thesis work, I studied outbursts of rapid accretion in protostellar disks. This was motivated by observations of the FU Orionis objects, which are young stellar objects with a sudden increase of their brightness. I first constructed disk radiative transfer models to compare with *Spitzer* observations, and found that the outburst disk region extends to scales of an AU or more, with the inferred limits on the viscosity parameter $\alpha \sim 0.02-0.2$. I further analyzed the multi-wavelength high resolution spectra to show the outbursting disk follows Keplerian rotation. I next studied the thermal structure of the disk which leads us to propose that the outburst is due to the thermal activation of the magnetorotational instability (MRI) at \sim AU scales by the gravitational instability (GI). We carried out both analytic studies and 2-Dimensional radiationhydrodynamic simulations to study the outbursts and constrain the activation of the MRI. Then I extended this work by constructing simplified 1-dimensional time-dependent simulations with infall from the protostellar envelope to study protostellar disk formation and long term evolution. I found that the outbursting behavior of the protostellar disks during the infall phase alleviates the so called “luminosity problem”, and the layered accretion at the later phase leads to a massive dead zone where planet formation is favored.

In the second part of my thesis work, I studied protoplanetary disks with gaps and holes-so called “pretransitional and transitional disks”,- to study planet formation in young disks. I have studied gap opening by dynamically-interacting multiple giant planets with two-dimensional hydrodynamic simulations. I found that even with as many as four giant planets, additional substantial dust depletion (e.g. growth)

is required to explain these gaps and holes, which sheds light on the early planet formation environment.

CHAPTER 1

Introduction

1.1 Protostellar & Protoplanetary Disks

Stars form through the collapse of the molecular cloud cores which are embedded in the large chaotic and dynamical molecular clouds. Due to the six orders of magnitude difference in size between a molecular cloud core and a star, any small initial perturbation of the core will lead to a disk configuration around the forming protostar to conserve angular momentum. Since the disk continuously accretes to the central protostar and builds up the mass of the star, such a disk is called the protostellar disk. At a later stage, planets start forming in this disk, and then the disk is called the protoplanetary disk.

This modern view of star and planet formation is not different from what Swedenborg, Kant and Laplace have proposed 300 years ago, known as “the nebular hypothesis”. Noting that all the known planets orbit the Sun in a plane and in the same direction, they proposed that the sun was originally a giant cloud of gas or nebulae rotating evenly. During the cloud’s contraction from gravity and cooling, it flattened and gave birth to stars and planets. This solar nebular model was later improved by Von Weizsacker (1943) and Kuiper (1951). A mathematical evolutionary model for purely viscous protostellar and protoplanetary disks was developed 30 years ago (Lynden-Bell & Pringle 1974). However, because the disks emit most of their light at infrared wavelengths, their presence was not really made clear until after the Infrared Astronomical Satellite (*IRAS*) was launched, when the first statistical studies of protostellar and protoplanetary disks have been made (Strom et al. 1989). The emission from dust grains in these disks have been detected shortly afterwards

with the millimeter telescopes (Weintraub, Sandell & Duncan 1989). The flattened and slightly flared disk morphology was inferred from the spectral energy distribution (SED) from young stellar objects (Shu et al. 1987, Kenyon & Hartmann 1987), and later is indisputably revealed in optical wavelengths by the Hubble Space Telescope (*Hubble*), showing the disk shadow against a bright nebular background (O'dell & Wen 1994). A great detail about protostellar and protoplanetary disks has been revealed during the last decade thanks to both ground based and space telescopes (such as the Infrared Space Observatory *ISO*, and the Spitzer Space Telescope *Spitzer*) operating at multiple wavelengths.

Although the generic viscous disk evolutionary model by Lynden-Bell & Pringle (1974) has its beauty of simplicity and seems to be quite successful by comparing with observations (Hartmann et al. 1998), the nature of disk viscosity remains a mystery. Through dimensional analysis, Shakura & Sunyaev (1973) attempted to use a dimensionless number α to parameterize the disk viscosity as $\nu = \alpha c_s^2 / \Omega$, where c_s and Ω are the disk sound speed and orbital angular frequency at the disk radius R respectively. With the protostellar and protoplanetary disk life time $\sim 10^6$ years, α is quantified to be around 0.01-0.1. However, except the gravitational instability (GI) which may not be applicable to protostellar disks after the envelope infall phase, the underlying disk accretion mechanism is hardly understood until the magnetorotational instability (MRI, Balbus & Hawley 1998) is rediscovered (Chandrasekhar 1961). The schematic demonstration of how MRI and GI transfer angular momentum is shown in Figure 1.1. Both GI and MRI lead to turbulence which has an averaging effect on the disk angular momentum transfer and can be roughly approximated as kinematic viscosities.

At early evolutionary stages GI may transfer mass in the disk since the disk is likely to be quite massive with respect to the central protostar. At later stages, the disk becomes gravitationally stable as mass is accreted and/or blown away. Because these disks are so cold, thermal ionization cannot sustain the MRI, which requires coupling of the magnetic field to the mostly-neutral gas through collisions (e.g., Reyes-Ruiz & Stepinski 1995). On the other hand, external ionizing sources (cosmic and/or X

rays) can provide the necessary ionization for MRI activation up to a limiting surface density, ionizing the outer surfaces of the disk and leading to accretion in an “active layer”, leaving a “dead zone” in the midplane (Gammie 1996, Figure 1.2).

Studying accretion phenomenon from both observations and theories is essential to understand both star and planet formation, since the accretion process not only builds up the star but also determines the initial disk condition for planet formation. With high-resolution instruments on the horizon (the mm and submm wave interferometers *EVLA* and *ALMA* will be completed within 3 years) and planet demographics becoming more complete (500 extrasolar planets have been found and more from *Kepler*), there comes a great need to study accretion mechanisms and their implications. In my thesis, I took two approaches to understand the accretion and its implications: 1) constrain disk accretion structure using outbursting disks: FU Orionis objects, and 2) explore planet formation by the gravitational instability and constrain planet formation environment in protoplanetary disks whose inner regions are cleared.

1.2 The “luminosity problem” and outbursting accretion disks

The outburst phenomenon of protostellar disks was revealed by both discovery of the high accretion young stellar objects (FU Orionis objects, Herbig 1977) and statistical studies of embedded young stellar objects.

The FU Orionis systems are a small but remarkable class of variable young objects which undergo outbursts in optical light of 5 magnitudes or more (Herbig 1977, Figure 1.4 and 1.5), with a F-G supergiant optical spectra and K-M supergiant near-infrared spectra dominated by deep CO overtone absorption. While the rise times for outbursts are usually very short ($\sim 1-10$ yr), the decay timescales range from decades to centuries. The FU Ori objects also show distinctive reflection nebulae, large infrared excesses of radiation, wavelength dependent spectral types, and “double-peaked” absorption line profiles (Hartmann & Kenyon 1985, 1996 and references therein). The frequency of these outbursts is uncertain; in recent years an increasing number of heavily extinct potential FU Ori objects have been identified on

the basis of their spectroscopic characteristics at near-infrared wavelengths (Kenyon et al. 1993; Reipurth & Aspin 1997; Sandell & Aspin 1998; Aspin & Reipurth 2003).

The accretion disk model for FU Ori objects proposed by Hartmann & Kenyon (1985, 1987a, 1987b) and Kenyon et al. 1988 can explain the peculiarities enumerated above in a straightforward manner. The high luminosities ($\sim 100 L_{\odot}$) of these objects suggest the disk accretion rates are extremely high ($10^{-4} M_{\odot} \text{ yr}^{-1}$) during the outbursts and the emission from the disk outshines the central star. The high temperature of the inner disk produces the observed F-G supergiant optical spectrum, while the cooler outer disk produces an infrared spectrum having the spectral type of a K-M supergiant. The Keplerian rotation of the disk can produce double-peaked line profiles as often observed, with peak separation decreasing with increasing wavelength of observations, since the inner hotter disk which produces the optical spectrum rotates faster than the outer cooler disk which produces the infrared spectrum (Hartmann & Kenyon 1996).

The indirect evidence for the outbursting young stellar objects comes from the statistical studies. A complete sample of embedded young stellar objects with luminosities $L \geq 0.5 L_{\odot}$ was made available by *IRAS* towards the Taurus-Auriga region (Kenyon et al. 1990). By comparing the total number of these embedded sources to the T Tauri stars, the embedded phase is estimated to last $\sim 10^5$ yr (if the T Tauri phase is $\sim 10^6$ yr), which agrees with core collapse models (e.g., Shu, Adams, & Lizano 1987). However, most of these embedded young stars have luminosities $0.4-4 L_{\odot}$, which is significantly smaller than the luminosity derived by assuming steady disk accretion with accretion rate $10^{-5} M_{\odot} \text{ yr}^{-1}$ and considering half of the gravitational energy is radiated away:

$$L = \frac{GM_* \dot{M}}{2R_*} \quad (1.1)$$

which is $10-50 L_{\odot}$ with substellar central star mass and $R_* = 3 R_{\odot}$. This discrepancy is called the ‘‘Luminosity Problem’’. To get the idea how much gravitational energy

has to be radiated, let's calculate the gravitational potential for one proton at $3 R_{\odot}$.

$$\frac{GM_p M_{\odot}}{3R_{\odot}} \sim 2000\text{ev} \quad (1.2)$$

which is equivalent to Sun's viral temperature $2 \times 10^7 \text{K}$. Since half of this energy has to be gotten rid off in order for accretion, and this energy is much higher than the thermal energy of the accretion disk (even considering the dissociation and ionization potential of hydrogen), most of this energy needs to be radiated away. One solution to this "luminosity problem" is that most infalling matter first falls to the circumstellar disk and then is accreted to the star during short-lived outbursts (Figure 1.3); in this model protostars are usually observed in quiescence, which is the reason why they appear fainter.

Due to the high disk accretion luminosity, FU Orionis objects can be a good test ground for various disk accretion models. With new observations available (e.g. *Spitzer*), we can further study FU Ori accretion disks and provide insight into the disk accretion and outburst mechanisms. In §2, I will constrain FU Ori's inner disk structure by multi-wavelength studies. In §3, I will study the outer structure of FU Ori. In §4, I will study FU Ori's differential rotation. In §5, I will explore FU Ori's outburst mechanism. In §6 2-Dimensional simulations have been carried out. In §7 and 8, simplified 1-Dimensional models are constructed and used to reveal the protoplanetary disk structure throughout the disk evolution over millions of years.

The material in these chapters has been published in ApJ as Zhu et al. 2007, 2008, 2009abc, 2010ab.

1.3 Planet formation

The protostellar and protoplanetary disk structure revealed from both observational and theoretical studies provides the initial condition to study planet formation. Terrestrial planets form through the growth of dust grains in the protoplanetary disk, while the giant planets have to form before the gas in the protoplanetary disks disperses at $\sim 10^6$ yr.

The terrestrial planet formation theory was quantitatively developed in the pioneering work by V. Safronov (1969) who suggested terrestrial planets are assembled by km-sized objects (called “planetesimals”) which originate from dust grains in protoplanetary disks. To begin with, micron sized grains in the disk settle to the disk midplane due to both the gas drag force and the gravitational force from the central star. For a $1\ \mu\text{m}$ sized grain, the velocity relaxation time due to the drag force is only $\sim 10\text{s}$ at 1 AU. During the settling process, the dust grain gains its mass by accumulating all other grains on its way (both vertical settling and radially drift), which eventually leads to 0.1-1 m particles within the settling time $10^3\ \text{yr}$ (Weidenschilling 1980).

The next stage when dust particles grow from cm/m size to km size planetesimals is not well understood. Since the drift timescale for 1 m particle is only $\sim 100\ \text{yr}$ at 1 AU, the dust needs to grow from meter size to km size super fast or the fast dust drift is hindered by some other mechanisms (e.g. vortices). Various mechanisms have been proposed to explain the fast planetesimal formation, such as the gravitational instability for settled dust grains (Safronov 1969, Goldreich and Ward 1973) and streaming instability (Goodman & Pindor 2000). However, the main issue is whether the turbulence (e.g. dust collective effect) can inhibit the dust concentration. On the other hand, the slower dust drift due to some features in the disk (e.g. spiral arms, vortices) suffered the longevity of these features.

Once planetesimals of 10 km have formed, they can continue growing by sticking with each other and the growth is accelerated by gravitational focusing (Safronov 1969). Due to the fast accretion nature from gravitational focusing, a slightly larger planetesimal can quickly grow and run away from the remaining planetesimals. Then these run away planetesimals can collisionally scatter the planetesimal swarm. Although the scattered planetesimals can be damped by the gas-drag and tidal torque with the gaseous disk, the effect of gravitational focusing is limited and these big planetesimals grow together with separation around 10 Hill radius, turning into the oligarchs stage. After the gas disperses, the accretion further slows down and it can assemble earth mass planet at 1 AU within $2 \times 10^8\ \text{yr}$.

On the other hand, giant planets have to form before the gaseous disk disperses, which constrains the formation mechanism. Mainly, two mechanisms have been proposed: 1) the core accretion model; 2) the gravitational instability model.

The core accretion model: Core accretion model can be considered as an extension to the terrestrial planet formation model. After runaway planetesimal accretion, the protoplanet has accreted all the small planetesimals within several Hill radius. A significant atmosphere has been developed at this stage which has a positive feedback to further planetesimal accretion: planetesimal accretion adds energy to the envelope which expands and intercepts more planetesimals. This is also the longest stage for giant planet formation until the envelope mass is close to the solid core mass (cross over mass) and runaway gas accretion occurs. The long timescale at this stage ($\sim 10^6$ yr) is one big problem for this model. However, this timescale can be significantly reduced if the dust in the protoplanetary disk is settled and agglomerated, since dust depletion allows for a more rapid giant planet formation due to less radiation trapping (Hubickyj et al. 2005).

The gravitational instability model: Toomre (1964) has shown that a differentially rotating disk becomes unstable due to its self-gravity when the Toomre Q parameter is smaller than some value. For a gaseous disk the criterion is

$$\frac{c_s \Omega}{\pi G \Sigma} < 1. \quad (1.3)$$

Gammie (2001) has shown that a gravitationally unstable disk can fragment if the disk can cool faster than its orbital timescale (Figure 1.6). The fragmentation process also takes place on about an orbital timescale, which is much shorter than the disk lifetime. However, Rafikov (2005) has shown that the fragmentation condition can be satisfied for a protoplanetary disk beyond 50 AU. Such model can potentially explain extrasolar planets found beyond 50 AU (e.g. Fomalhaut, Kalas et al. 2008; HR 8799, Marois et al. 2008).

Recently discovered pretransitional and transitional disks for the first time allow us to study the environment of the forming planets. Transitional disks are protoplan-

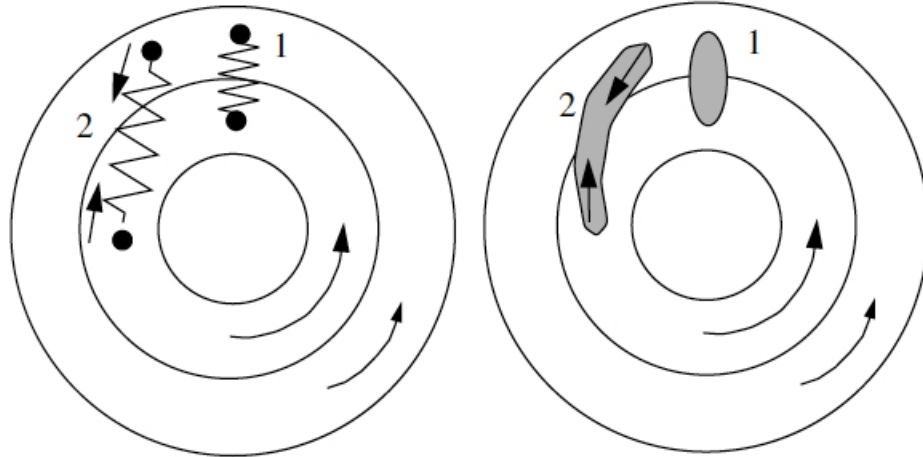


Figure 1.1 Angular momentum transfer in a shearing disk. The left panel demonstrates angular momentum transfer by MRI while the right one demonstrates GI. Magnetic fields act like an elastic spring connecting different annuli in the disk. Due to the disk differential rotation, the inner annuli rotates faster than the outer annuli so that the string is stretched and the angular momentum is transferred outwards. Eventually this instability becomes non-linear and leads to disk turbulence. The spiral arms of the GI disk works in a similar way as the “spring” in the MRI disk. The self-gravity of these spiral arms connect the inner disk and outer disk. Excerpted from Hartmann 2009. Courtesy of L. Hartmann.

etary disks having optically thin holes inside tens of AU. They were first discovered by noticing the significantly reduced near to mid-IR fluxes relative to typical T Tauri disks (e.g., Calvet et al. 2002, 2005). Later these optically thin holes have been confirmed by submm interferometric studies (e.g. Hughs et al. 2009, Figure 1.7). In the pre-transitional disks, there is evidence for emission from warm, optically-thick dust near the star (Espaillat et al. 2007, 2008, 2010) but with optically thin gaps outwards. The population, disk accretion rates, and gap structure have put stringent constraints on planet formation process, the details about which will be presented in Chapter 10 together with planet-disk interaction theoretical studies, which is published in Zhu et al. 2010c.

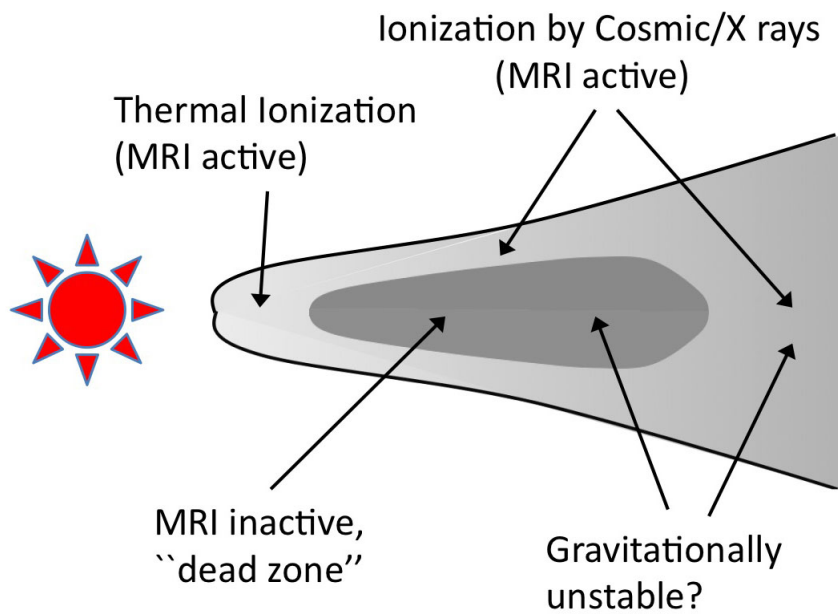


Figure 1.2 Layered accretion for protostellar and protoplanetary disks. The inner disk within tens of AU is MRI active since enough thermal ionization is sustained by the central star irradiation. At larger radii, the disk is MRI active only at the disk surface where cosmic and X rays can ionize the disk.

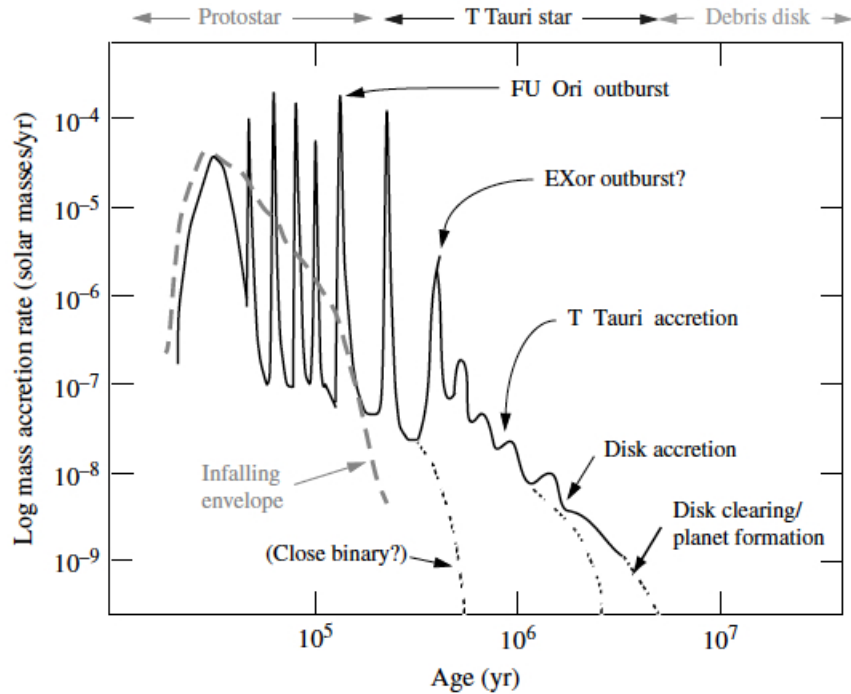


Figure 1.3 Protostar mass accretion rate with time. The collapse of the parent molecular core of a solar mass star lasts ~ 0.1 Myr. A protostar and a circumstellar disk form during the collapse. Most of the time the disk's accretion rate is lower than the infall rate, while occasionally the disk accretes rapidly through outbursts. Each outburst can dump $\sim 0.01 M_{\odot}$ mass to the central star. Considering the outbursting FU Orionis systems are found embedded in the molecular envelope, they should occur relatively early when there is significant infall onto the disk to replenish the disk after the outburst. When the infall stops, the disk enters the T Tauri stage with accretion rate $\sim 10^{-8} M_{\odot} \text{ yr}^{-1}$. Giant planets need to form during this stage before the gas in the disk evacuates. Excerpted from Hartmann 2009. Courtesy of L. Hartmann.

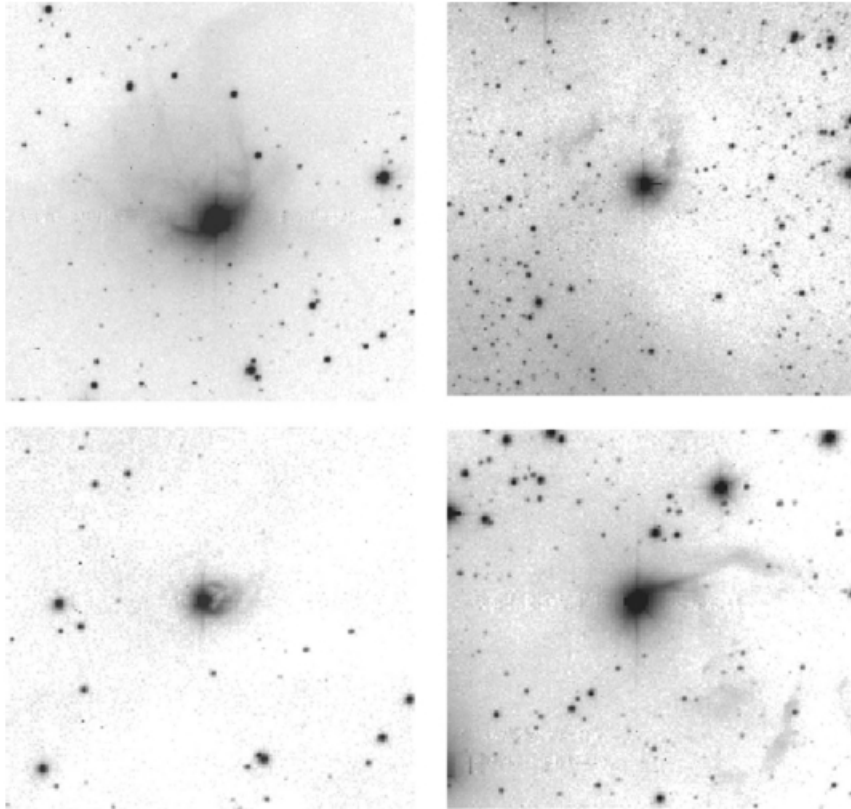


Figure 1.4 Optical images for FU Orionis objects. FU Ori (upper left), V 1057 Cyg (upper right), V 1515 Cyg (lower left) and Z CMa (lower right) are shown. Excerpted from Hartmann 2009.

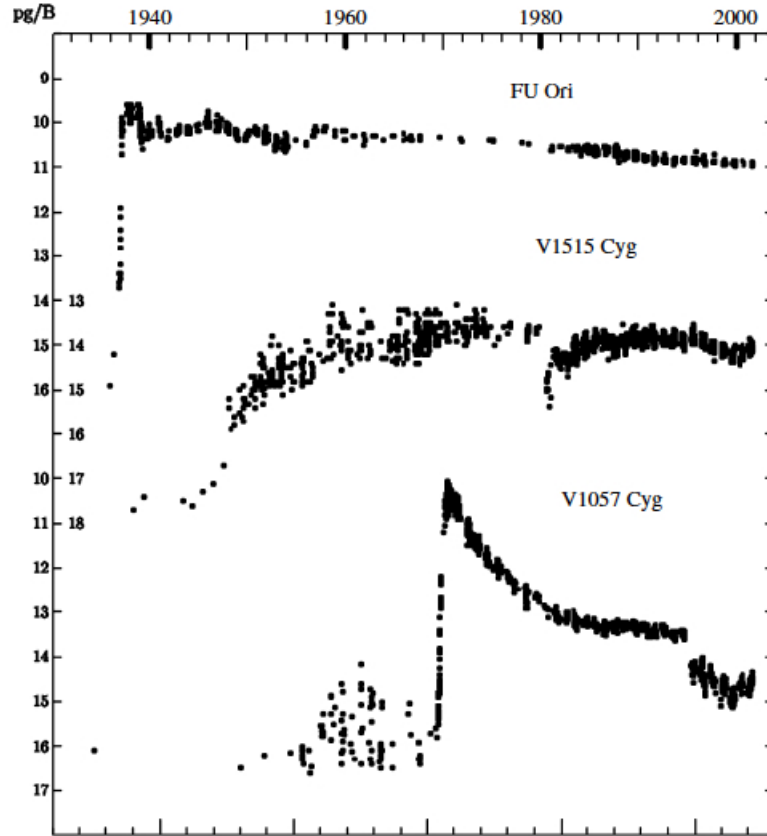


Figure 1.5 Light curves of FU Orionis objects. Excerpted from Hartmann 2009.

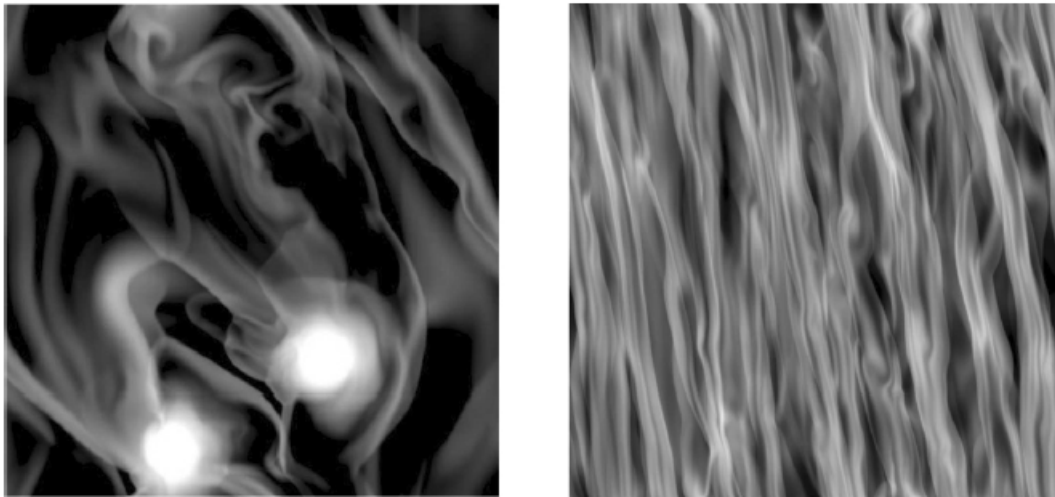


Figure 1.6 Disk fragmentation by GI. Surface density maps for a gravitationally unstable disk. Fragmentation results from a fast cooling ($t_c=2 \Omega^{-1}$, left panel), while a quasi-steady structure can be present if the disk cools slowly ($t_c=10 \Omega^{-1}$, right pane. Taken from Gammie 2001. Courtesy of C. Gammie.).

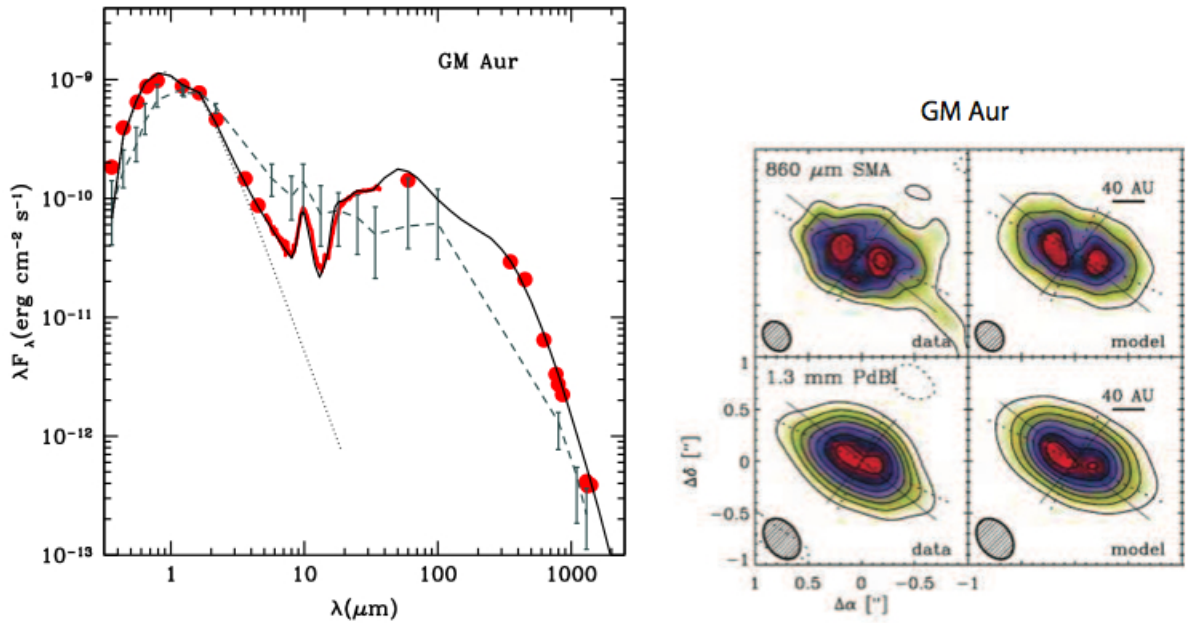


Figure 1.7 GM Aur SED and image. The left panel shows the SED of GM Aur. The red dots are the photometric data, while the red curve is the IRS spectra from 5-30 μm . The solid black curve is from the SED modeling. Compared with the median SED of T Tauri stars (dashed curve), there is a strong deficit of emission at 5-20 μm , suggesting a cleared inner disk (Calvet et al. 2002). The dotted curve is the expected photospheric emission from the central star. The right panel shows the disk hole with outer radii ~ 20 AU predicted by SED modeling is confirmed by the SMA observations (Hughes et al. 2009).

CHAPTER 2

The Hot Inner Disk of FU ORI

2.1 Abstract

We have constructed a detailed radiative transfer disk model which reproduces the main features of the spectrum of the outbursting young stellar object FU Orionis from $\sim 4000 \text{ \AA}$ to $\sim 8\mu\text{m}$. Using an estimated visual extinction $A_V \sim 1.5$, a steady disk model with a central star mass $\sim 0.3M_\odot$ and a mass accretion rate $\sim 2 \times 10^{-4} M_\odot \text{yr}^{-1}$, we can reproduce the spectral energy distribution of FU Ori quite well. Higher values of extinction used in previous analysis ($A_V \sim 2.1$) result in spectral energy distributions which are less well-fitted by a steady disk model, but might be explained by extra energy dissipation of the boundary layer in the inner disk. With the mid-infrared spectrum obtained by the Infrared Spectrograph (IRS) on board the *Spitzer Space Telescope*, we estimate that the outer radius of the hot, rapidly accreting inner disk is $\sim 1 \text{ AU}$ using disk models truncated at this outer radius. Inclusion of radiation from a cooler irradiated outer disk might reduce the outer limit of the hot inner disk to $\sim 0.5 \text{ AU}$. In either case, the radius is inconsistent with a pure thermal instability model for the outburst. Our radiative transfer model implies that the central disk temperature $T_c \geq 1000 \text{ K}$ out to $\sim 0.5 - 1 \text{ AU}$, suggesting that the magnetorotational instability can be supported out to that distance. Assuming that the $\sim 100 \text{ yr}$ decay timescale in brightness of FU Ori represents the viscous timescale of the hot inner disk, we estimate the viscosity parameter to be $\alpha \sim 0.2 - 0.02$ in the outburst state, consistent with numerical simulations of the magnetorotational instability in disks. The radial extent of the high \dot{M} region is inconsistent with the model of Bell & Lin, but may be consistent with theories incorporating both gravitational and

magnetorotational instabilities. This chapter has been published in the paper: “The Hot Inner Disk of FU Orionis”, 2007, *ApJ*, 669, 483 with Lee Hartmann, Nuria Calvet, Jesus Hernandez, James Muzerolle, and Ajay-Kumar Tannirkulam.

2.2 Introduction

The FU Orionis systems are a small but remarkable class of variable young objects which undergo outbursts in optical light of 5 magnitudes or more (Herbig, 1977), with a F-G supergiant optical spectra and K-M supergiant near-infrared spectra dominated by deep CO overtone absorption. While the rise times for outbursts are usually very short (~ 1 -10 yr), the decay timescales range from decades to centuries. The FU Ori objects also show distinctive reflection nebulae, large infrared excesses of radiation, wavelength dependent spectral types, and “double-peaked” absorption line profiles (?). The frequency of these outbursts is uncertain; in recent years an increasing number of heavily extincted potential FU Ori objects have been identified on the basis of their spectroscopic characteristics at near-infrared wavelengths (Kenyon et al., 1993; Reipurth & Aspin, 1997; Sandell & Aspin, 1998; Aspin & Reipurth, 2003).

The accretion disk model for FU Ori objects proposed by Hartmann & Kenyon (1985, 1987a, 1987b) and Kenyon et al. (1988) can explain the peculiarities enumerated above in a straightforward manner. Outbursts are known in other accreting disk systems and may be the result of a common mechanism (e.g., Bell & Lin 1994). The high temperature of the inner disk produces the observed F-G supergiant optical spectrum, while the cooler outer disk produces an infrared spectrum having the spectral type of a K-M supergiant. The Keplerian rotation of the disk can produce double-peaked line profiles as often observed, with peak separation decreasing with increasing wavelength of observations, since the inner hotter disk which produces the optical spectrum rotates faster than the outer cooler disk which produces the infrared spectrum (Hartmann & Kenyon 1996).

While the accretion disk model has been successful so far, it is important to continue to test it and to derive further insights into the origins of the accretion outbursts as new observations become available. In particular, the mid-infrared spectrum ob-

tained with the Infrared Spectrograph (IRS) on the *Spitzer Space Telescope* provides important constraints on the outer edge of the hot inner disk (Green et al., 2006), which in turn can test theories of outbursts. For example, the thermal instability model of Bell & Lin (1994) predicts an outer radius for the outburst region of only $\sim 20R_{\odot}$, which is smaller than that estimated by Green et al. (2006) on the basis of simple blackbody disk models. Armitage et al. (2001) suggested that a combination of gravitational instability (GI) with triggering of the magnetorotational instability (MRI) might also explain FU Ori outbursts; in this model the high accretion rate region in outburst would be much larger, of order 0.5 AU. Vorobyov & Basu (2005,2006) suggested that FU Ori outbursts could also be produced by the accretion of clumps formed in a gravitationally unstable disk. This model predicts high accretion rates at its inner radius of 10 AU. These differing predictions for the size of the outburst region should be testable with detailed models of the spectral energy distribution (SED). Furthermore, if we can constrain the size of the outburst region, the timescales of decay may provide quantitative estimates of the viscosity, vital for understanding the evolution of young protoplanetary disks.

In this chapter we present new steady, optically-thick accretion disk spectrum calculations, and compare the results with observations from the ultraviolet to the mid-infrared of FU Ori—the prototype of these systems. In chapter 2.3 we describe the observational material used to constrain the models, while in chapter 2.4 we describe the methods used to calculate the disk models. We show in chapter 2.5 that the steady disk model reproduces the variation of the observed spectral features over this very large wavelength range quite well. In chapter 2.6 we consider some implications of our results for disk viscosities, outburst mechanisms, and disk masses, and summarize our conclusions in chapter 2.7.

2.3 Optical and infrared data

An essential part of the spectral energy distribution (SED) of FU Ori for our model is the IRS spectrum from *Spitzer* observed on March 4, 2004 (see Green et al. 2006 for details). As FU Ori has been fading slowly over the last 60 years, we need to obtain

data at other wavelengths near the same time as the IRS spectrum to construct a complete spectral energy distribution (SED).

Optical photometry (UBVR) was obtained in 2004 at the Maidanak Observatory (Ibrahimov, 1999; Green et al., 2006). As FU Ori exhibits small, irregular variability on timescales much less than a year, we averaged the Maidanak data to form the mean values (with RMS uncertainty in each band ~ 0.02 magnitude) used in this chapter. In addition, we include an optical spectrum of FU Ori obtained on March 27th, 2004, near the time of the IRS observations, using the 1.5m telescope of the Whipple Observatory with the FAST Spectrograph (Fabricant et al., 1998), equipped with the Loral 512×2688 CCD. This instrument provides 3400 \AA of spectral coverage centered at 5500 \AA , with a resolution of 6 \AA . The spectrum was wavelength calibrated and combined using standard IRAF routines ¹. The spectrum was corrected for the relative system response using the IRAF *sensfunc* task. The optical spectrum was placed on an absolute flux scale using the averaged 2004 UBVR photometry.

Near-infrared fluxes were determined from several sources. 2MASS JHK photometry is available from October 7th, 1999, five years before IRS observations. We also include data from Reipurth & Aspin (2004) on December 15, 2003, using the NAOJ 8 m Subaru Telescope on Mauna Kea and the Infrared Camera and Spectrograph (IRCS). Finally, we obtained JHK magnitudes on December 17th 2005, using the Near-IR Imager/Spectrometer TIFKAM on the 2.4 m MDM telescope at Kitt Peak. Although the 2.4m telescope had to be defocused to avoid saturation because FU Ori is so bright, our JHK magnitudes of 6.57, 5.91 and 5.33, respectively, are in reasonable agreement with the JHK_s 2MASS magnitudes of 6.519, 5.699, 5.159, respectively, indicating that the FU Ori fluxes have not changed dramatically over that six year period. The Reipurth & Aspin (2004) observations are on a different system, but when converted to fluxes yield reasonably similar results. We therefore adopted the 2MASS magnitudes as our standard in this wavelength region.

¹IRAF is distributed by the National Optical Astronomy Observatories, which are operated by the Association of Universities for Research in Astronomy, Inc., under cooperative agreement with the National Science Foundation.

We then incorporated the KSPEC spectrum (resolution $R \sim 500$, $1.15\text{-}2.42\mu\text{m}$) observed on Dec 15th, 1994 by Greene & Lada (1996) and the observation with SpeX ($2.1\text{-}4.8\mu\text{m}$) on the Infrared Telescope Facility (IRTF; Rayner et al. 1998) obtained during the nights of January 5-6th, 2001 (see Muzerolle et al. 2003 for details). We placed these spectra on an absolute scale by convolving the spectra with the relative spectral response curve (RSRs) of the 2MASS system (Cohen et al., 2003) and tying the overall result to the 2MASS K_s magnitude.

The collected observations are shown in Figure 2.1, where we assume an A_V of 1.5 instead of the usually assumed value of ~ 2.2 (Kenyon et al. 1988; KHH88). The previously discussed variation of spectral type with wavelength is immediately apparent in Figure 2.1; the optical spectrum corresponds to a G type spectrum as estimated from the atomic metal lines while the near-IR and IRS wavelength ranges are dominated by molecular bands indicative of a much later spectral type. While the optical and infrared spectra are dominated by absorption features, dust emission dominates longward of $8\mu\text{m}$, as shown by the silicate emission features at 10 and $20\mu\text{m}$.

2.4 Model

In this chapter we only model the absorption spectrum ($\lambda < 8\mu\text{m}$) which is produced by the centrally-heated accretion disk. The silicate emission features are produced by externally-heated regions of the outer disk or possibly a circumstellar dusty envelope (Kenyon & Hartmann 1991; Green et al. 2006); we defer modeling of this region to a subsequent chapter.

We follow the method of Calvet et al. (1991a,b) to calculate the disk spectrum. In summary, we calculate the emission from the atmosphere of a viscous, geometrically thin, optically thick accretion disk with constant mass accretion rate \dot{M} around a star with mass M and radius R . The disk height H is assumed to vary with the distance from the rotational axis of the star R as $H = H_0(R/R_i)^{9/8}$, where we take $H_0 = 0.1R_i$ and R_i is the radius of the central star. This approximation is not very accurate but it only affects the local surface gravity of the disk atmosphere, which has only a small

effect on the emergent spectrum. Viscous dissipation in the atmosphere is neglected, which is a good approximation for cases of interest (?). Thus, radiative equilibrium holds in the disk atmosphere, and the surface flux is determined by the viscous energy generation in the deeper disk layers. This constant radiative flux through the disk atmosphere can be characterized by the effective temperature distribution of the steady optically-thick disk,

$$T_{eff}^4 = \frac{3GM\dot{M}}{8\pi\sigma R^3} \left[1 - \left(\frac{R_i}{R} \right)^{1/2} \right]. \quad (2.1)$$

This equation predicts that the maximum disk temperature T_{max} occurs at $1.36R_i$ and then decreases to zero at $R = R_i$. The latter is unphysical, and so we modify equation (2.1) so that when the radius is smaller than $1.36 R_i$, we assume that the temperature is constant and equal to $T = T_{max}$. (e.g., KHH88) The vertical temperature structure at each radius is calculated using the gray-atmosphere approximation in the Eddington limit, adopting the Rosseland mean optical depth τ .

The opacity of atomic and molecular lines has been calculated using the Opacity Distribution Function (ODF) method (Castelli & Kurucz, 2004; Sbordone et al., 2004; Castelli, 2005). Briefly, the ODF method is a statistical approach to handling line blanketing when millions of lines are present in a short wavelength range (Kurucz et al., 1974). For a given temperature and pressure, the absorption coefficient for each line is exactly computed, then the profiles of all the lines in each small interval $\Delta\nu$ are rearranged monotonically as a function of ν . The opacity increases as the frequency increases in this $\Delta\nu$. A step function with 12 subintervals in frequency is used to represent this monotonic function. The height of every step is the averaged opacity of the monotonic function in this subinterval. The width of the 12 subintervals are $\Delta\nu/10$ for 9 intervals and $\Delta\nu/20$, $\Delta\nu/30$, $\Delta\nu/60$ for the last 3 intervals where the monotonic function increases steeply and reaches the maximum. Thus, in every interval $\Delta\nu$ we obtain 12 representative averaged opacities at a given temperature and pressure. We then construct an opacity table as a function of λ for each temperature and pressure. The wavelength grid is the same as used in the code DFSYNTH

(Castelli, 2005) from 8.976 nm to 10000 nm with 328 BIG intervals (resolution 30-100) and 1212 LITTLE intervals (resolution 60-500). However, we extend the temperature grid and pressure grid to lower temperatures and pressures ($\log T$ ranging from 1.5 to 5.3, $\log P$ from -24 to 8 in cgs units) than DFSYNTH, so that it can be used in our disk models for which the temperatures and pressures reach lower values than in typical stellar atmosphere models. Because the line opacity usually varies by several orders of magnitude within a line width, the ODF method is substantially more accurate than either straight or harmonic means.

The line list is taken from Kurucz's CD-ROMs Nos. 1, 15, 24, and 26 (Kurucz, 2005). Not only atomic lines but also many molecular lines (C_2 , CN, CO, H_2 , CH, NH, OH, MgH, SiH, SiO, TiO, H_2O) are included. The opacities of TiO and H_2O , the most important molecules in the infrared, are from Partridge & Schwenke (1997) and Schwenke (1998). We do not include a detailed calculation of the dust condensation process; instead, we add the dust opacity when $T < 1500$ K (the condensation temperature of silicates at typical disk densities). We use the ISM dust model of Draine & Lee (1984, 1987) to represent the dust in the disk. This assumption is unlikely to be correct but mostly affects the continuum at the very longest wavelengths and in particular the silicate emission features, which we do not model in this chapter.

At low temperatures complex chemical processes occur which are not included in the Kurucz data. We have not calculated the low temperature molecular opacity in detail; instead, we have assumed that the abundance ratio between different types of molecules below 700 K is the same as the ratio at 700 K. This is unimportant for our purposes because dust opacity dominates at such low temperatures.

In Figure 2.2 we show the Rosseland mean opacity calculated for solar abundances and a turbulent velocity $v = 2 \text{ km s}^{-1}$ for different values of ρ/T_6^3 to be compared with Alexander & Ferguson (1994), where ρ is the density in g cm^{-3} and T_6 is the temperature in millions of degrees. The results closely match the more detailed calculations by Alexander & Ferguson (1994) and Ferguson et al. (2005) except near 1500 K, where our dust opacity rises more rapidly due to our neglect of dust condensation processes.

Calvet et al. (1991b) showed that the near-infrared spectrum of FU Ori could be well-modeled with the then-current water vapor opacities and a similar calculational method to the one we are using here. We now have a much better set of opacities, and can treat the optical spectrum. To test the code at optical wavelengths, we compare the model spectrum from the annulus with $T_{eff}=5300$ K with the observed spectrum of SAO 21446 which is a G1 supergiant (Jacoby et al., 1984). The spectrum of SAO 21446 has been obtained using the Intensified Reticon Scanner (IRS) on the No.1 90 cm telescope at Kitt Peak by Jacoby et al. (1984). Here we have convolved this spectrum to a resolution of 300 to agree with our model spectrum. As shown in Figure 2.3, our model reproduces the continuum spectrum fairly well except for a few strong features. These discrepancies are probably due to the limitation of the grey atmospheric assumption.

Figure 2.4 shows the emergent intensities with 55° emergent angle from different annuli of our final disk model (parameters can be found in chapter 2.5), which has 45 annuli. The 55° inclination angle is estimated from the near-infrared interferometric observations by Malbet et al. (2005) and mid-infrared interferometric observations by Quanz et al. (2006). The radii of these annuli are chosen to increase exponentially from $r = R_i$ to $1000R_i$. At the first annulus ($r = 1R_i$), we can see a significant Balmer jump at $0.36 \mu\text{m}$, similar to the spectra of early type stars. As the radius increases, the temperatures of the annuli become lower and lower. Infrared molecular features appear at larger annuli with effective temperatures less than 5000K ($r > 3R_i$). For the outermost annuli with effective temperature less than 1500 K ($r > 15R_i$), the molecular features have almost disappeared because dust opacity dominates. The final spectrum is the result of the addition of the fluxes from each of these annuli weighted by the appropriate annular surface area.

In addition to these calculations aimed at comparing with low-resolution spectra, we also calculated high-resolution spectra in restricted wavelength regions. For these calculations, the vertical structure of every annulus is calculated as above, and then this structure is imported into the program SYNTHE (Kurucz & Avrett, 1981; Kurucz, 1993). SYNTHE is a suite of programs which solve the radiative transfer

equations in LTE with a very high spectrum resolution ($\sim 500,000$). Each annular spectrum is broadened with the rotational profile appropriate to a Keplerian disk and then the summed spectrum is calculated (e.g., KHH88). These calculations are very time-consuming, and were used only to produce a high resolution spectrum of a small wavelength range around 6170 \AA for the purpose of estimating the central mass, and for examining the CO first-overtone lines.

2.5 Comparison with observations

The SED of a steady, optically-thick disk model is determined by two parameters: the product of the mass accretion rate and the mass of the central star, $M\dot{M}$, and the inner radius R_i . One observational constraint comes from the observed spectral lines and/or the peak of the SED (after reddening correction), which determines the maximum temperature of the steady disk model,

$$T_{max} = 0.488 \left(\frac{3GM\dot{M}}{8\pi R_i^3 \sigma} \right)^{1/4}. \quad (2.2)$$

The other observational constraint is given by the true luminosity of a flat disk L_d ,

$$L_d = 2\pi d^2 \frac{F}{\cos i} = \frac{GM\dot{M}}{2R_i}, \quad (2.3)$$

where d is the distance of FU Ori, i is the inclination angle of the disk to the line of sight, and F is the observed total flux corrected for extinction. If the distance and inclination are known, we can solve for the inner disk radius and thus for the product $M\dot{M}$. If we then further use the observed rotational velocities, it is then possible to derive independent values of the central mass M and the accretion rate \dot{M} , in the manner outlined by KHH88.

The best constraints on T_{max} come from the optical spectrum, as the uncertain extinction makes it difficult to constrain by overall SED fitting. From the lines of our optical FAST spectrum we derive a spectral type of $\sim G2$ for FU Ori using the methods of Hernández et al. (2004), which agrees with previous results (Herbig, 1977).

However, it is not straightforward to derive a value of extinction and thus T_{max} from this spectral type determination; the disk spectrum is not that of a single (standard) star with a well-defined effective temperature, but instead it is a combination of hotter and cooler regions, with an overall spectrum that clearly varies with the wavelength of observation in a complicated way. To address this problem, we constructed several disk models with a modest range of T_{max} and compared them with the observed optical spectrum dereddened by differing amounts of visual extinction A_V , as shown in Figure 2.5.

The uppermost model in Figure 2.5 has $T_{max} = 7240$ K, comparable to that of the FU Ori disk model of KHH88. The model optical spectrum is too flat longward of ~ 3900 Å in comparison with the observations dereddened by the $A_V = 2.2$, suggested by KHH88, or for $A_V = 1.9$. At the other extreme, we find that the bottom model, with $T_{max} = 5840$ K, matches the observed spectrum dereddened by only $A_V = 1.3$ quite well. However, we suspect that our gray-atmosphere approximation somewhat underestimates the amount of line blanketing in the blue optical region, especially shortward of the Ca II resonance lines at 3933 and 3968 Å leading us to suspect that this agreement is somewhat misleading. We therefore provide our best estimate of the extinction as $A_V = 1.5 \pm 0.2$, and adopt the model which best matches the mean extinction with $T_{max} = 6420$ K as our standard model.

In this connection it is worth noting that KHH88 did not actually find a good fit for the optical spectrum of FU Ori using a GOI standard star and extinctions $A_V > 2$. They speculated that the discrepancy might be alleviated by an improved treatment of limb darkening in the disk. However, Hartmann & Kenyon (1985) had found that a G2I standard star and $A_V = 1.55$ provided a good match to the optical spectrum between 3900 Å and 7400 Å, consistent with our results here.

The accretion disk luminosity L depends upon the distance, inclination, and dereddened flux. We adopt a distance of ~ 500 pc, consistent with membership in the general Orion region (Herbig 1977). The inclination 55° is adopted (Malbet et al. 2005, Quanz et al. 2006). Using these parameters, observed total flux and $A_V = 1.5$, we obtain the true luminosity $L_d = 8.66 \times 10^{35} \text{ ergs s}^{-1} \sim 226 L_\odot$ according to equation 2.3.

As mentioned before, fitting the observed spectrum yields $T_{max} = 6420$ K. We derive $\dot{M} = 7.2 \times 10^{-5} M_{\odot} \text{yr}^{-1}$ and $R_i = 5R_{\odot}$ by solving equation 2.2 and equation 2.3 simultaneously.

Figure 2.6 shows the predicted spectrum for the adopted parameters and several values of the outer radius. Our computed spectrum matches the observations at wavelengths shortward of about $4\mu\text{m}$, indicating that the innermost region of the inner disk is reasonably well reproduced by the adopted \dot{M} and R_i parameters.

Because the optical and near-infrared SED is well-matched by the model, we may then proceed to estimate the central stellar mass and thus the accretion rate. We used the observed optical rotation from KHH88 to constrain the central star mass. We computed the line profiles around 6170 \AA using SYNTHE, cross correlated it with a non-rotating disk spectrum, and compared it with the observed cross-correlation line profile given in KHH88. The uncertainty in fitting the line profile widths is about $\pm 20\%$. However, systematic errors in the inclination angle are probably more important for the mass estimate, and for that reason we give an uncertainty $0.3M_{\odot} \pm 0.1M_{\odot}$ (consistent with the earlier estimate of KHH88 assuming $i = 50^{\circ}$). For a mass of $0.3 M_{\odot}$, $\dot{M} \sim 2.4 \times 10^{-4} M_{\odot} \text{yr}^{-1}$. Parameters of the model are given in Table 2.2.

As shown in Figure 2.6, we find that regardless of extinction and disk parameters, steady accretion models which fit the optical to near-infrared region predict too much emission in the IRS range for very large outer radii. This can only be remedied by truncating the hot inner disk. The estimate of the outburst models of Bell & Lin (1994) suggested an outer radius of the high state of $\sim 20R_{\odot}$ (with somewhat different parameters for the accretion rate and inner disk radius); as shown in Figure 2.6 this truncation radius fails to explain the SED. A truncation radius of $R_{out} \sim 210R_{\odot} \sim 1 \text{ AU}$ provides a better fit to the flux at $\sim 5 - 8\mu\text{m}$, although is somewhat low in the $3\mu\text{m}$ band. Our results are reasonably consistent with Green et al. (2006), considering the limitations of their blackbody modeling only out to 5 microns.

As discussed above, models with outer radii larger than $\sim 200R_{\odot}$ overpredict the flux at $\sim 5 - 8\mu\text{m}$. At even longer wavelengths, absorption features are no longer present; instead, silicate dust emission features are seen in IRS spectra at ~ 10 and

$20\mu\text{m}$. As discussed by Green et al. (2006), these silicate features are signatures of heating from above, rather than from internal viscous dissipation, and may be produced in upper atmosphere of the outer disk which absorb light from the central disk. An outer disk is expected to be present, since a disk radius of $\sim 0.5 - 1$ AU is extremely small by standards of typical T Tauri disks, for which $R_{out} \sim 100$ AU or more are common (e.g., Simon, Dutrey, & Guilloteau 2000). Moreover, such a small radius would imply a low-mass optically-thick disk, making it difficult to explain the observed submm flux from FU Ori (Sandell & Weintraub 2001). So, it is very likely that an outer disk is present with a lower accretion rate, which could contribute some flux in the $5 - 8\mu\text{m}$ wavelength range and thus reduce the radius of the hot, high-accretion rate region. An outer disk accretion rate of about $10^{-5}M_{\odot}\text{yr}^{-1}$ is comparable to some of the highest infall rates estimated for (not heavily embedded) protostars (e.g., Kenyon, Calvet & Hartmann 1993); higher accretion rates would imply implausibly short evolutionary timescales $M/\dot{M} \sim 3 \times 10^4$ yr. In any event, if the outer disk accretion rate is not significantly smaller than the inner disk accretion rate, the problem of a large outer radius yielding too much flux remains. More likely, the emission from the outer disk is dominated by irradiation from the inner disk independent of the (lower) accretion rate there (Turner et al., 1997), as indicated by the presence of emission rather than absorption features.

In the Bell & Lin (1994) thermal instability models for FU Ori outbursts, the outer disk accretion rate is of order 10^{-1} of the inner disk accretion rate in outburst. We have therefore investigated the effect of an outer disk accretion rate of $2.4 \times 10^{-5}M_{\odot}\text{yr}^{-1}$ on the SED. The dotted curves in Figure 2.6 show the results of adding in such outer disk emission from disk internal viscous dissipation. The effect is relatively small so that our estimate of the outer radius of the hot disk with the high accretion rate is relatively robust. Of course we cannot rule out other kinds of temperature distributions, such as a smooth decline of accretion rate from, say, 100 to 200 R_{\odot} and the irradiation effect from the inner disk to the outer disk. We are presently carrying out more detailed calculations of the outer disk, including irradiation by the inner disk. Preliminary results indicate that the addition of the irradiated outer disk

emission will decrease our hot disk outer radius estimate by no more than a factor of two (Zhu et al. 2008).

We explored the effects of a larger visual extinction by scaling the observations to $A_V=2.2$. As shown in Figure 2.7, this makes only a very slight difference to the long-wavelength spectrum and does not change our estimate of the outer radius.

To examine our consistency with previous results, we calculated the CO first overtone high resolution spectrum with $R_{out} = 210R_{\odot}$ using SYNTHE program and compared it with the high resolution spectrum from Hartmann et al. (2004). The comparison is shown in Figure 2.8. We found that we needed to adopt a turbulent velocity of 4 km s^{-1} to obtain lines that are deep enough in comparison with the observations. This is the sound speed of gas with temperature around 4000 K, slightly supersonic for the annulus with radius larger than 4 stellar radius; Hartmann, Hinkle, & Calvet (2004) similarly found that slightly supersonic turbulence was needed to explain the first-overtone CO lines, and pointed out that this would not be surprising in the context of turbulence driven by the magnetorotational instability.

In Figure 2.9 we show an expanded view of the wavelength region between ~ 3 and $8\mu\text{m}$. The model accounts for the overall shape of the SED reasonably well, and yields a reasonable strength for the $6.8\mu\text{m}$ water vapor absorption feature. However, the $5.8\mu\text{m}$ water vapor feature of the model is not as strong as it is in the observations ((Green et al., 2006)). In this wavelength region the contributions from the dust-dominated regions of the disk are significant, and the contribution of this dust (relatively featureless) continuum emission could reduce the strength of the absorption feature. To investigate this possibility, we reduced the dust opacity to only 1% that of Draine & Lee (1984, 1987) and recalculated the model (with a slightly larger outer radius). As can be seen in Figure 2.9, this reduction in dust opacity strengthens the absorption features, although the predicted $5.8\mu\text{m}$ feature is still not strong enough, perhaps suggesting some difficulty with the opacities. It is not clear whether we require dust depletion, because we have not considered the temperature dependence of dust condensation in our model. We also cannot rule out uncertainties due to our simple treatment of the vertical temperature structure of the disk.

2.6 Discussion

2.6.1 The steady accretion disk model and the inner boundary condition

We have shown that the steady accretion disk model can quantitatively account for the observed SED of FU Ori over a factor of nearly 20 in wavelength, from 4000 Å to about 8 μm. This is accomplished with only three adjustable parameters: R_i , $\dot{M}M$, and R_{out} . No alternative model proposed for FU Ori has explained the SED over such a large wavelength range. The accretion disk explanation is bolstered by this work.

Within the context of the steady disk model, however, there remains the question of the appropriate inner boundary condition. The steady disk model considered here only accounts for half of the accretion luminosity ($L = G\dot{M}M/(2R_i)$) potentially available from accretion onto a slowly rotating star. As Kenyon et al. (1989) showed from ultraviolet spectra, there is no evidence in FU Ori for boundary layer emission which would account for this missing luminosity, up to ~ 10 -20% of the total luminosity; and if our lower estimate of extinction is correct, the potential boundary layer emission would be much less. This leaves as possibilities that the missing accretion energy is going into spinning up the central star, expanding the central star, being radiated over a larger radial distance of the disk, or some combination of all three effects.

Hartmann & Kenyon (1985; also Kenyon et al. 1989) pointed out that the $5 R_\odot$ inner radius implied by steady disk models is considerably larger than that of the typical T Tauri star ($R \sim 2R_\odot$), and suggested that this might be due to the disk dumping large amounts of thermal energy into the star, expanding its outer layers.

Popham et al. (1993, 1996) suggested that the the missing boundary layer energy could be distributed over a significant range of radii in the disk at high accretion rates. They found that as \dot{M} increases to $\sim 10^{-4} M_\odot \text{yr}^{-1}$ the dynamical boundary layer (the radial extent of the region where Ω drops from Keplerian angular velocity to 0) grows to 10-20 % of a stellar radius and the thermal boundary layer (the radial width over which the boundary layer luminosity is radiated) grows to the point that it becomes impossible to distinguish the boundary layer from the inner parts of the disk. Popham

et al. (1996) showed that this model would imply somewhat slower than Keplerian rotation in the innermost disk. In this chapter we find no evidence for extra radiation if $A_V=1.5$. We cannot rule out a slightly larger A_V , which would allow some extra dissipation of kinetic energy in the inner disk. However, the shape of the spectrum in the blue-optical region (Figure 2.5) suggests that the higher extinction value is not preferred, limiting the amount of excess radiation to a modest fraction of the total luminosity. We speculate that the missing energy is mostly going into expanding the outer stellar layers, with perhaps a small amount of excess radiation that is difficult to discern given the uncertainties in the extinction.

2.6.2 R_{out} and α

Our estimate of the outer radius of the high state of FU Ori is around $200 R_\odot$, although the irradiation effect from the hot inner disk to the outer disk may decrease this value to no less than $100 R_\odot$. Bell & Lin (1994) assume low viscosity parameters ($\alpha \sim 10^{-3}$) and derive a small outer radius ($R_{out} \sim 20 R_\odot$) for the high \dot{M} , hot inner disk during outbursts. Our model of FU Ori is inconsistent with such a small hot region; instead, we require the high \dot{M} region to be an order of magnitude larger in radius.

FU Ori has been fading slowly in brightness over the last ~ 70 years (Ibrahimov, 1999). If we attribute this fading to the emptying out of mass from the inner hot disk onto the central star, this timescale gives us a way to constrain the viscosity in this region. We make the simple assumption that the decay timescale is the viscous timescale

$$t_v \sim R^2/\nu, \quad (2.4)$$

where the viscosity is $\nu = \alpha c_s^2/\Omega$, α is the viscosity parameter (Shakura & Sunyaev 1973), c_s is the sound speed in the disk midplane, and Ω is the Keplerian angular frequency at R . We use the isothermal sound speed with a mean molecular weight of 2.3, appropriate for molecular hydrogen. We then need an estimate of the central temperature to evaluate t_v . Our radiative transfer model shows that the effective temperature is $T_{eff} \sim 800$ K at the outer radius of $R \sim 200 R_\odot$. This is a lower limit

for the central temperature as the absorption features in the spectrum show that the central temperature is higher than the surface temperature. The disk is likely to be very optically thick in this region, such that the central temperature is considerably larger than the effective temperature due to radiative trapping. We choose 1500 K as the central temperature above which MRI is active and thus high α can sustain high mass accretion rate. We therefore find

$$t_v \sim 141 \text{ yrs} \times \left(\frac{M}{0.3M_\odot} \right)^{1/2} \left(\frac{R}{210R_\odot} \right)^{1/2} \left(\frac{T}{1500K} \right)^{-1} \left(\frac{\alpha}{10^{-1}} \right)^{-1}. \quad (2.5)$$

where M is the mass of the central star, R is the outer radius of the high mass accretion disk, T is the central disk temperature of the high mass accretion disk, and α is the viscosity parameter. If we estimate a typical decay timescale of FU Ori as ~ 100 yr, then we find $\alpha \sim 0.14$. For the smaller hot disk radius with an irradiated outer disk, our preliminary results yield (Zhu et al. 2008) $R \geq 0.5$ AU and thus $\alpha \sim 0.1$.

It is important to recognize that equation (2.5) is only an order of magnitude estimate. The decay timescale of accretion can be affected by whatever mechanism makes the transition from high to low state; for example, in the thermal instability model, the decay time may not be the timescale for emptying out half the material in the affected region of the disk, but only that (smaller) amount necessary to shut off the thermal instability. Nevertheless, it is suggestive that we find a larger value of α in the high state than the 10^{-3} of Bell & Lin (1994).

A value of $\alpha \sim 0.2 - 0.02$ is roughly consistent with estimates from compact systems with accretion disks (King et al., 2007) as well as with numerical simulations of the magnetorotational instability (MRI) in ionized disks (Balbus & Hawley 1988). In this connection, we note that the requirement for enough thermal ionization to initiate a robust MRI is a central temperature $T \gtrsim 1000$ K (Gammie 1996), comparable to our observationally-based estimates ($T_{eff} \sim 800$ K at $R \sim 200 R_\odot$).

2.6.3 Thermal and other instabilities

The thermal instability model was originally suggested to account for outbursts in dwarf nova systems (Faulkner, Lin, & Papaloizou 1983) and has attractive properties for explaining FU Ori outbursts (Bell & Lin, 1994). However, the observed large outer radius, 0.5 – 1 AU, of the high accretion rate portion of the FU Ori disk poses difficulties for the pure thermal instability model. Even in the situation explored by Lodato & Clarke (2004), in which the thermal instability is triggered by a massive planet in the inner disk, the outer radius of the high state is still the same as in Bell & Lin (1994), $\sim 20 R_{\odot}$. The relatively high temperatures ($2 - 4 \times 10^3$ K) required to trigger the thermal instability (due to the ionization of hydrogen) are difficult to achieve at large radii; they require large surface densities which in turn produce large optical depths, trapping the radiation internally and making the central temperature much higher than the surface (effective) temperature.

To illustrate the problem, we calculated thermal equilibrium “S” curves (e.g., Faulkner et al. 1983) for our disk parameters at $R = 210R_{\odot}$ but various values of α . The equilibrium curve represents energy balance between viscous energy generation and radiative losses,

$$F_{vis} = F_{rad} \quad (2.6)$$

Thus,

$$\frac{9}{4}\alpha\Omega\Sigma c_s^2 = 2\sigma T_{eff}^4, \quad (2.7)$$

where Σ is the surface density and c_s is the sound speed at the local central disk. For an optically-thick disk, we have $T_c^4 = \frac{3}{8}\tau_R T_{eff}^4$, where $\tau_R = \kappa_R \Sigma$ and κ is the Rosseland mean opacity (Hubeny, 1990). Then,

$$T_c^3 = \frac{27}{64\mu\sigma}\alpha\Omega\Sigma^2\mathcal{R}_c\kappa, \quad (2.8)$$

where \mathcal{R}_c is the gas constant, and μ is the mean molecular weight. As long as we know T_c , we can derive T_{eff} and the corresponding \dot{M} at this radius. Because the Rosseland mean opacity is also dependent on temperature and pressure, iteration of

the disk structure calculation is needed to derive the equilibrium curve.

We show in Figure 2.10 the equilibrium curve at $R=210 R_\odot$ for five values of α : 10^{-1} , 10^{-2} , 10^{-3} , 10^{-4} , 10^{-5} . In discussing our results, we define Σ_A to be the highest stable low state for a given α . If at any radius the surface density increases above Σ_A , the disk can no longer stay stable on the lower branch and strong local heating begins. If the α of the low state is the same as the α of the high state, then $\alpha \geq 10^{-2}$; in this case, to trigger the thermal instability at Σ_A , the mass accretion rate in the low state would need to be $\sim 10^{-3}$ (see Figure 2.10), which is higher than the \dot{M} of the high state that we have determined. To have a mass accretion in the low state at least one order of magnitude lower than that of the high state, we would need $\alpha \leq 10^{-4}$ for the low state (see Figure 2.10). This is comparable to the low state α used by Bell & Lin (1994), but very much lower than our high state estimate. Changing the outer radius to $R \sim 100 R_\odot$ does not change these results by more than a factor of 10.

With $\alpha=10^{-4}$, the critical surface density at $210 R_\odot$ is $\Sigma_A \sim 10^6 \text{ g cm}^{-2}$. Then we can estimate the Toomre Q parameter,

$$Q = \frac{c_s \Omega}{\pi G \Sigma_A} \sim 0.1, \quad (2.9)$$

where $Q < 1$ implies gravitational instability. Thus, a thermal instability model for FU Ori implies a massive, probably gravitationally-unstable disk, which raises the question: could the outburst be driven by gravity instead?

Armitage et al. (2001) proposed an alternative model of disk outbursts in which material piles up at radii of order 1-2 AU, consistent with layered disk models (Gammie, 1996), achieving repeated outbursts with high accretion on size scales much closer to our inferred R_{out} . In this model, gravitational torques lead to increased accretion, which in turn heats up the inner disk until temperatures are high enough (800 K in their model) to trigger the MRI, which results in very much higher viscosities and rapid accretion. The Armitage et al. (2001) model does not give exactly FU Ori-type outbursts; instead, the accretion events last for $\sim 10^4$ yr and achieve peak accretion rates of only $\sim 10^{-5} M_\odot \text{ yr}^{-1}$. However, Armitage et al. (2001) suggested that ther-

mal instabilities might be triggered by their gravitationally-driven outbursts. Simple models with somewhat different parameters demonstrate that it is indeed possible to trigger thermal instabilities in the context of this general model (Gammie, Book, & Hartmann 2007, in preparation), resulting in outbursts more similar to that of FU Ori.

Vorobyov & Basu (2005,2006) suggest FU Ori outburst could be explained by the accretion of clumps formed in a gravitationally unstable disk. The disk becomes gravitationally unstable because of the infall of the matter from the envelope. The spiral arms and clumps form and grow in the unstable disk. The redistribution of mass and angular momentum leads to centrifugal disbalance in the disk and further triggers the outburst when the dense clumps are driven into the central star. The authors derive a mass accretion rate at 10 AU of $\sim 10^{-4}M_{\odot}/\text{yr}$, which could result in too much emission from the outer disk; this issue requires further exploration.

The rapid rise time of the outburst of FU Ori in the B band, ~ 1 year, provides the best evidence for a thermal instability. We can test this idea very crudely by using our steady disk model to estimate the range of radii in the disk which can contribute to the B band magnitude in the light curve, finding that only the inner $R \lesssim 20R_{\odot}$ disk are involved. If we then assumed that the rise in B light is due to the inward propagation of a thermal instability front across this region at a (maximum) speed $\sim \alpha c_s$ (Lin et al., 1985; Bell et al., 1995), and assume a sound speed characteristic of $2 - 4 \times 10^3$ K (the minimum temperature for instability), then we derive $\alpha \sim 0.1$. While this calculation is very crude, it does suggest consistency with the idea of a thermal instability with a viscosity parameter comparable to that which we inferred from the decaying light curve (chapter 2.6.2).

Finally, we estimate the amount of mass in the inner disk. An upper mass limit for the inner disk can be estimated by assuming $Q \sim 1$ (the approximate limit for strong gravitational instability) at $R \sim 200 R_{\odot}$. Adopting a central temperature $T \sim 1000$ K, the gravitational instability limit leads to an approximate surface density limit $\Sigma \lesssim 10^5 gcm^{-2}$ and thus a maximum inner disk mass $\sim \pi \Sigma R^2 \sim 0.05M_{\odot}$. This leads us to an inner disk mass estimate $0.05M_{\odot} \gtrsim M_{\text{in}} \gtrsim 0.01M_{\odot}$, where the lower

limit comes from requiring the outburst mass accretion rate of $\sim 10^{-4}M_{\odot}\text{yr}^{-1}$ to be sustained for the observed decay timescale of ~ 100 yr.

2.7 Conclusions

Using the latest opacities and the ODF method, we have constructed a new detailed radiative transfer disk model which reproduces the main features of the FU Ori spectrum from $\sim 4000\text{\AA}$ to about $8\ \mu\text{m}$. The SED of FU Ori can be fitted with a steady disk model and no boundary layer emission if $A_V \sim 1.5$, a somewhat lower valued extinction than previously estimated. A larger A_V would imply extra heating at small radii which would result from dissipation of kinetic energy as material accretes onto the central star. With $A_V=1.5$, the inclination estimated from near-IR interferometry and the observed rotation of the inner disk, we estimate that the central star has a mass $\sim 0.3M_{\odot}$ (typical of low-mass TTS) and a disk mass accretion rate of $\sim 2.4 \times 10^{-4}M_{\odot}\text{yr}^{-1}$.

Relying on the Infrared Spectrograph Spectrum of FU Ori from the Spitzer Space Telescope presented by Green et al. (2006), we estimate that the outer radius of the hot, rapidly accreting region of the inner disk is ~ 1 AU, although the irradiation effect may decrease this value by no more than a factor of two (Zhu et al. 2008). Either way, this is inconsistent with the pure thermal instability models of Bell & Lin (1994) who adopted a low α viscosity parameter $\sim 10^{-3}$ - 10^{-4} . If we assume that the observed decay timescale of FU Ori (~ 100 years) is the viscous transport time from the outer edge of the hot region, then we derive $\alpha \sim 0.2 - 0.02$, comparable to the predictions of simulations of the magnetohydrodynamic (MHD) turbulence. The effective temperature at the outer edge of the hot region in our model is ~ 800 K; the presence of absorption features shows that the central disk temperature must be higher. Thus, our model suggests that the central disk temperature is greater than the $T_c \sim 1000$ K required to maintain full MHD turbulence by thermal ionization out to ~ 1 AU.

We show that pure thermal instability models have difficulty in explaining the outburst of FU Ori, and suggest that models including gravitational torques and

Table 2.1 Best fit model

M_{star}/M_{\odot}	\dot{M}	R_i/R_{\odot}	R_{out}/R_{\odot}	$\theta(\text{a})$	Distance/pc
0.3	$2.4 \times 10^{-4} M_{\odot}/\text{yr}$	5	210	55°	500

MRI activation, such as those of Armitage et al. (2001), are more promising.

Table 2.2 Optical lines used to determine the spectral type

Lines (a)	Metals	Spectral type
4047.00	Fe I+Sc I	F8
4226.00	Ca I	G1
4271.00	Fe I	G4
4305.00	CH(Gband)	G1
4458.00	Mn I+Fe I	G1
5329.00	Fe I	G2
5404.00	Fe I	G3
6162.00	Ca I+TiO	F9

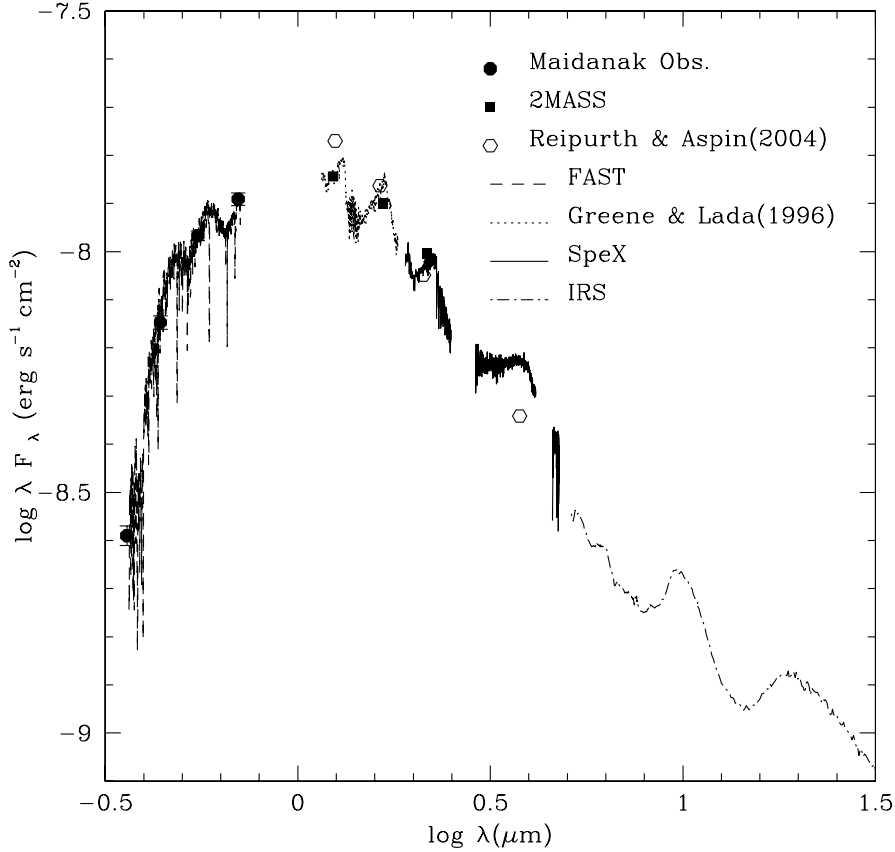


Figure 2.1 The spectral energy distribution of FU Ori. Collected photometric and spectroscopic data of FU Ori with $A_v=1.5$ (see chapter 2.5). The solid circles with error bars are the UBV R photometry from the Maidanak Observatory, the squares are 2MASS JHK photometry, and the open circles are JHK'L' photometry from Reipurth & Aspin (2004). The dashed curve is the FAST spectrum from 3650 Å to 7500 Å, the dotted curve is the KSPEC spectrum from 1.15 μm to 2.42 μm (Greene & Lada, 1996), and the solid curve is the SpeX spectrum from 2.1 μm to 4.8 μm (Muzerolle et al., 2003), both scaled to the 2MASS photometry. Finally, the dot-dash curve is the IRS spectrum from 5 μm to 35 μm from Green et al. (2006). The spectra were put on an absolute flux scale as discussed in chapter 2.3.

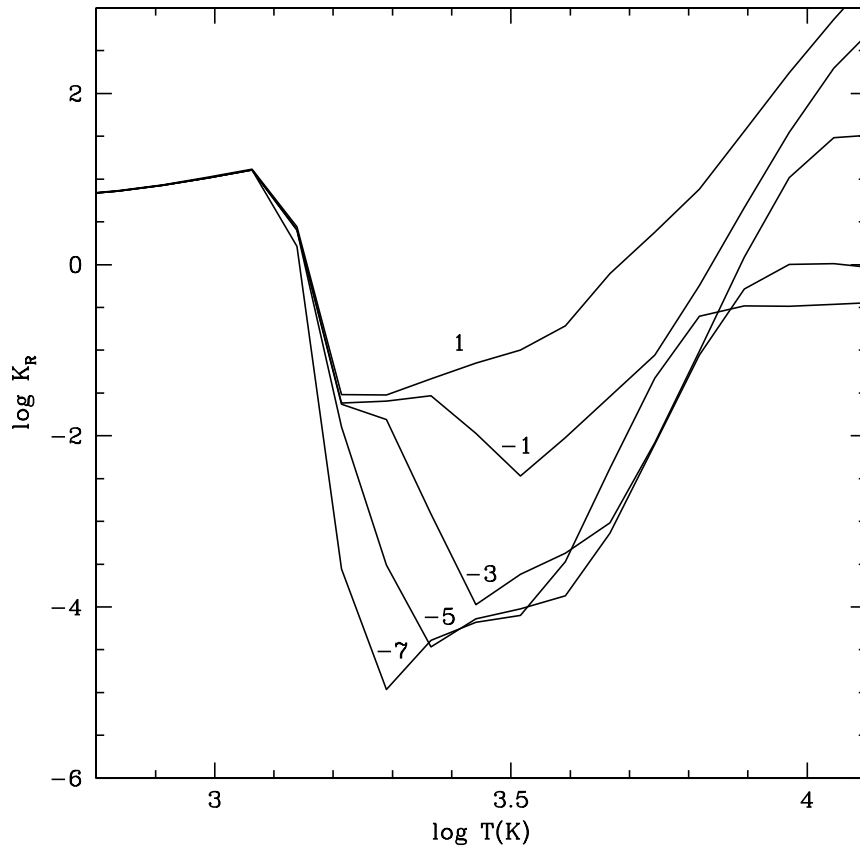


Figure 2.2 Our calculated Rosseland mean opacity as a function of temperature for solar composition. Each curve is labeled with the value of $\log(\rho/T_6^3)$ to be compared with Alexander & Ferguson (1994), where T_6 is the temperature in millions of degrees.

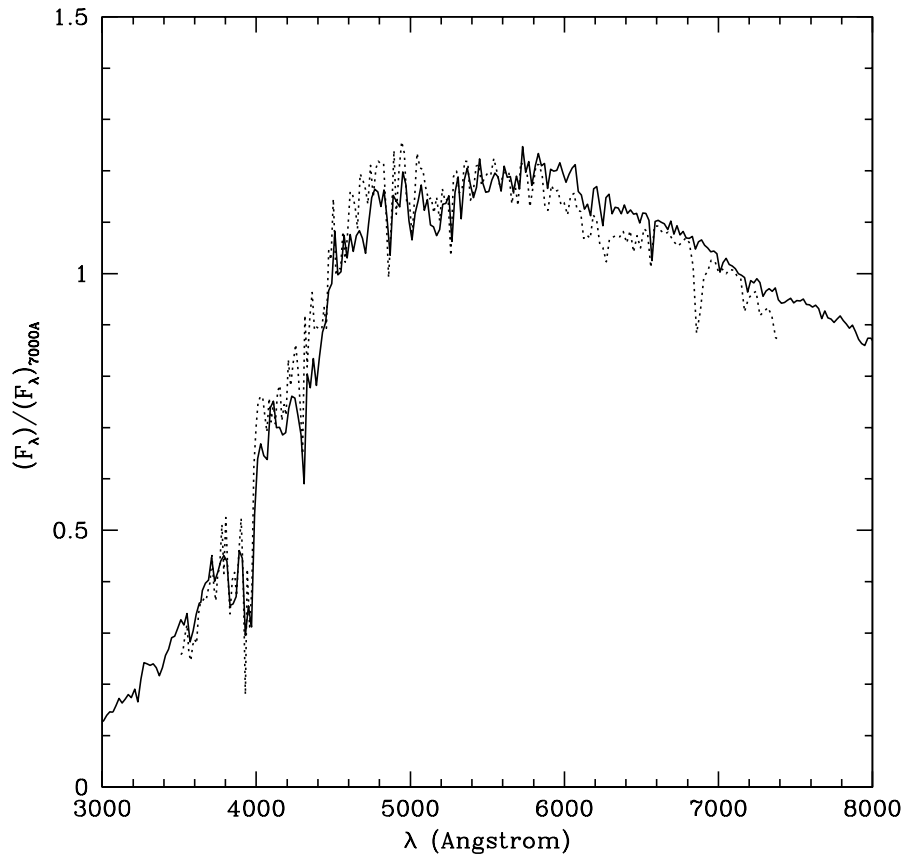


Figure 2.3 The spectrum predicted by the annulus with $T_{eff}=5300$ K (solid line) and the spectrum of SAO 21446 which is a G1 I star (Jacoby et al., 1984) (dotted line). The spectra are scaled to the same flux at 7000\AA .

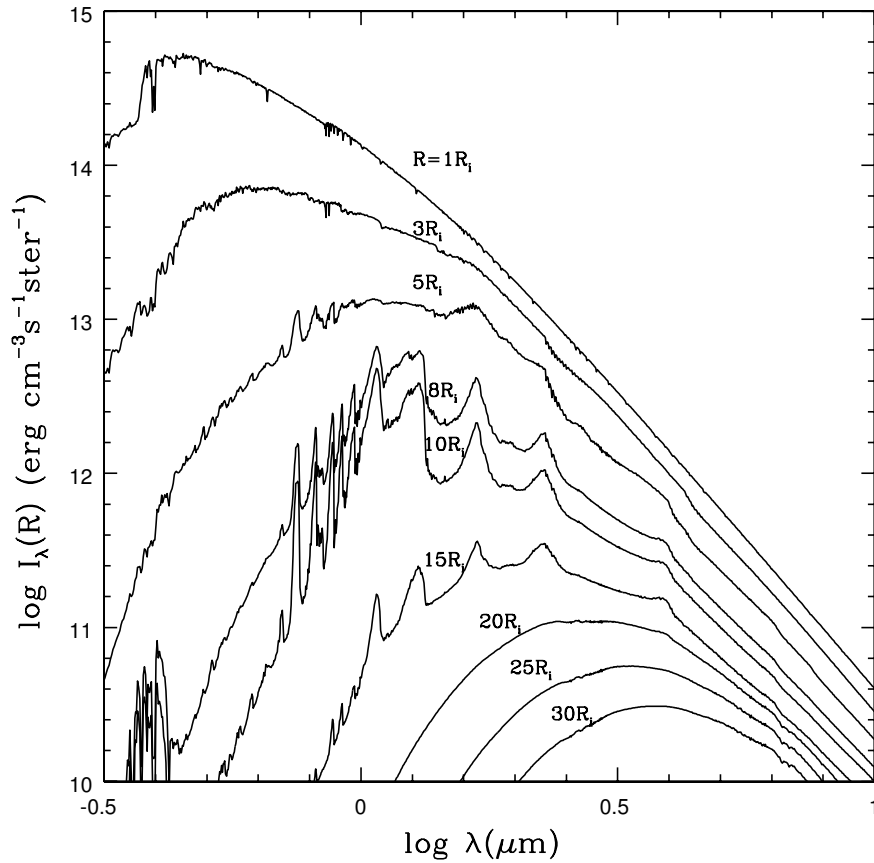


Figure 2.4 Emergent intensities from selected annuli of the disk model calculated for a 55 degree emergent angle. Effective temperatures of the annuli at 1, 3, 5, 6, 8, 10, 15, 20, 25, and 30 R_i are 6420, 4660, 3400, 2480, 2130, 1630, 1310, 1110, and 977 K, respectively. Molecular absorption features in the near-IR arise from cool regions of the disk, which do not contribute to the optical spectrum.

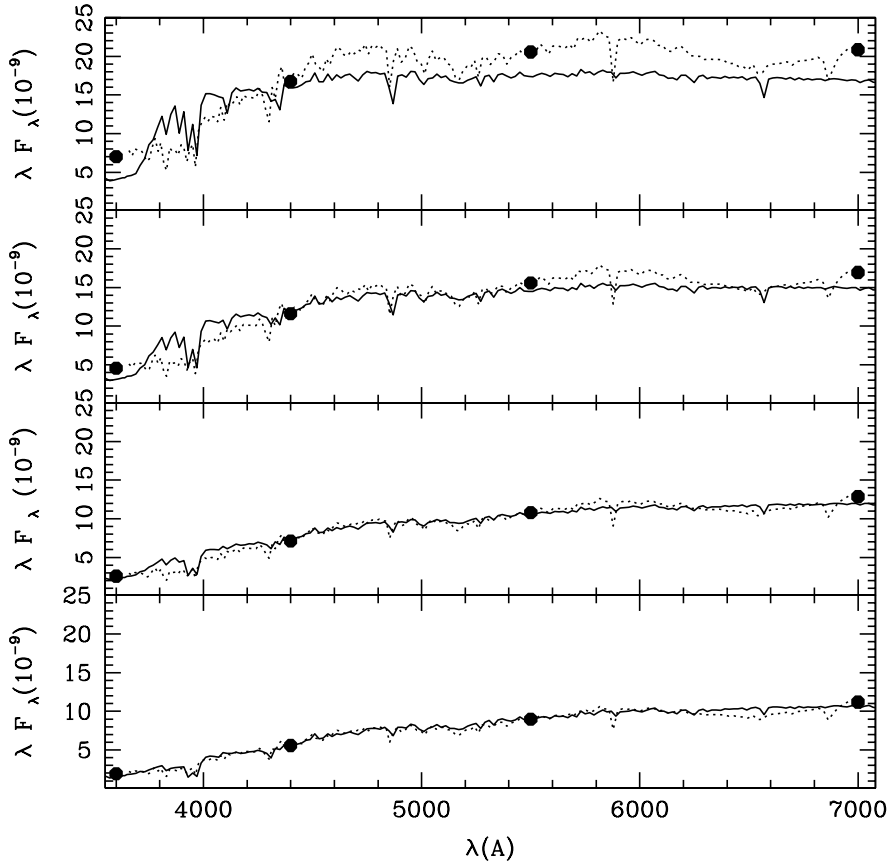


Figure 2.5 Observed UBVR photometry and optical spectra with different A_V : 2.2, 1.9, 1.5, 1.3 (dotted lines, from top to bottom) and model spectra with T_{max} : 7240, 6770, 6420, 5840 (solid lines, from top to bottom). The total flux spectra are produced by weighting the intensities (Figure 4) by the appropriate annular surface areas.

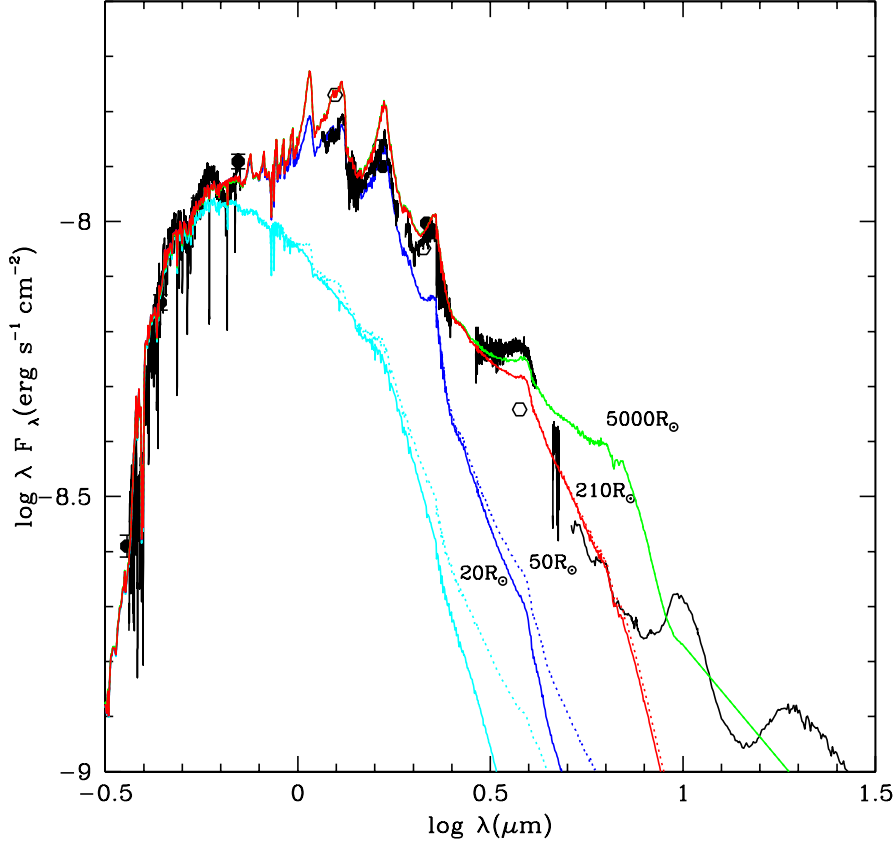


Figure 2.6 Comparison between observed data and disk models for different values of the outer radii. All the black lines and dots are observed spectra and photometry data as shown in figure 2.1. All the color lines are model spectra. The parameters of the disk models are inner disk radius $5 R_{\odot}$, and $\dot{M} \sim 7.2 \times 10^{-5} M_{\odot}/\text{yr}$. The corresponding T_{max} is 6420 K. The four model spectra from top to bottom are for the disk models truncated at $5000 R_{\odot}$, $210 R_{\odot}$, $50 R_{\odot}$ and $20 R_{\odot}$. The solid lines are model spectra for a high mass accretion rate region with outer radii as shown. The dotted lines are spectra for models where an outer region with mass accretion one order of magnitude smaller has been added. For the disk model truncated at $5000 R_{\odot}$, the dotted line is coincident with the solid line. The extinction parameter is $A_V = 1.5$.

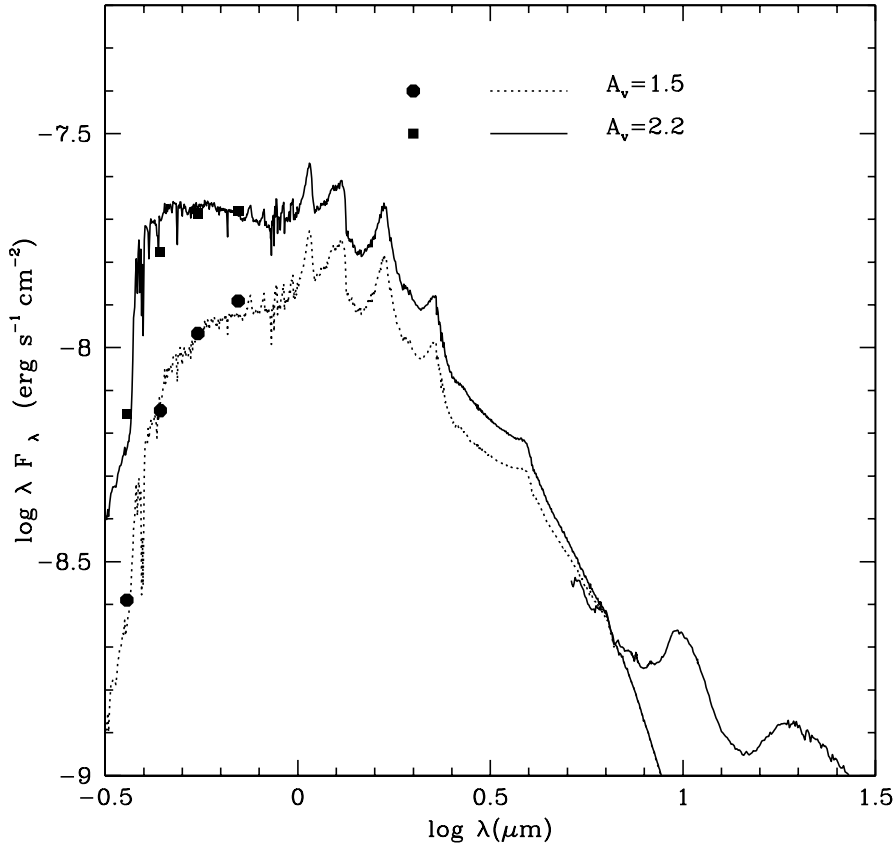


Figure 2.7 Two truncated models fitting the observations corrected by $A_V=2.2$ and $A_V=1.5$. Only optical photometries and IRS spectra (5-30 microns) are shown. The square points are the photometries corrected by $A_V=2.2$, while the round points are the photometries corrected by $A_V=1.5$. The IRS spectra corrected by these two A_V are coincident. The solid line is the model fitting to observations with $A_V=2.2$, while the dotted line is the model fitting to observations with $A_V=1.5$. Both of the two models have the same outer radius of the high state $R_{out}=210 R_{\odot}$.

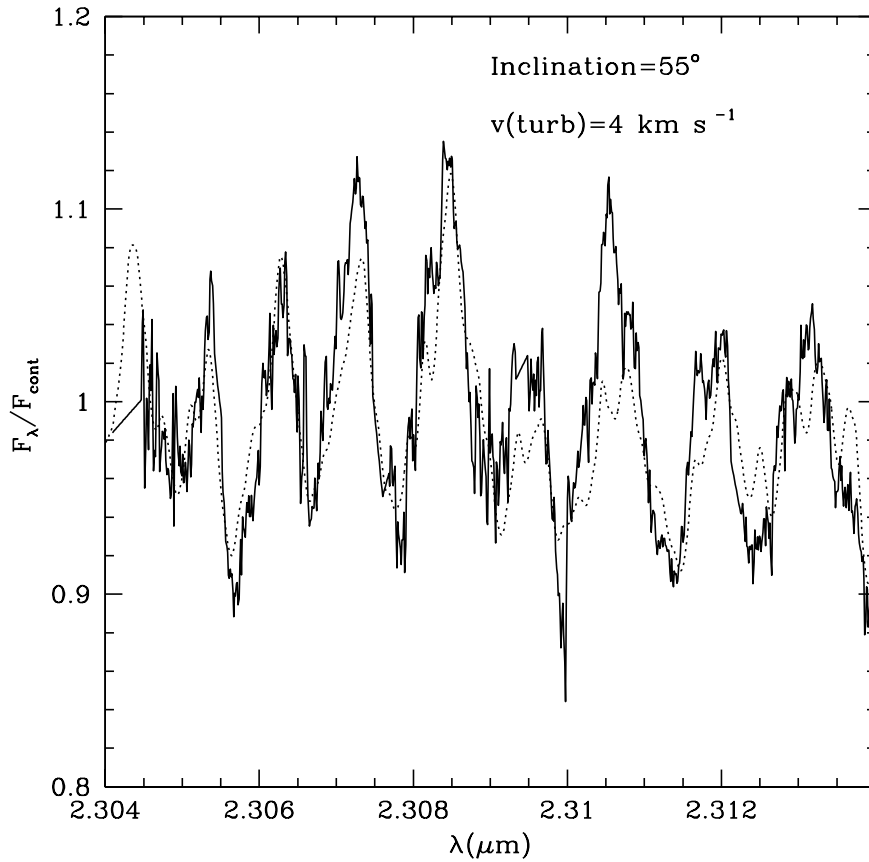


Figure 2.8 CO first overtone absorption band around 2.3 μm . The solid line is the observed CO first overtone absorption feature from Hartmann et al. (2004) and the dotted line is the model spectrum after being convolved to the same spectrum resolution. The turbulent velocity is 4 km s^{-1} and the inclination angle is 55 degrees.

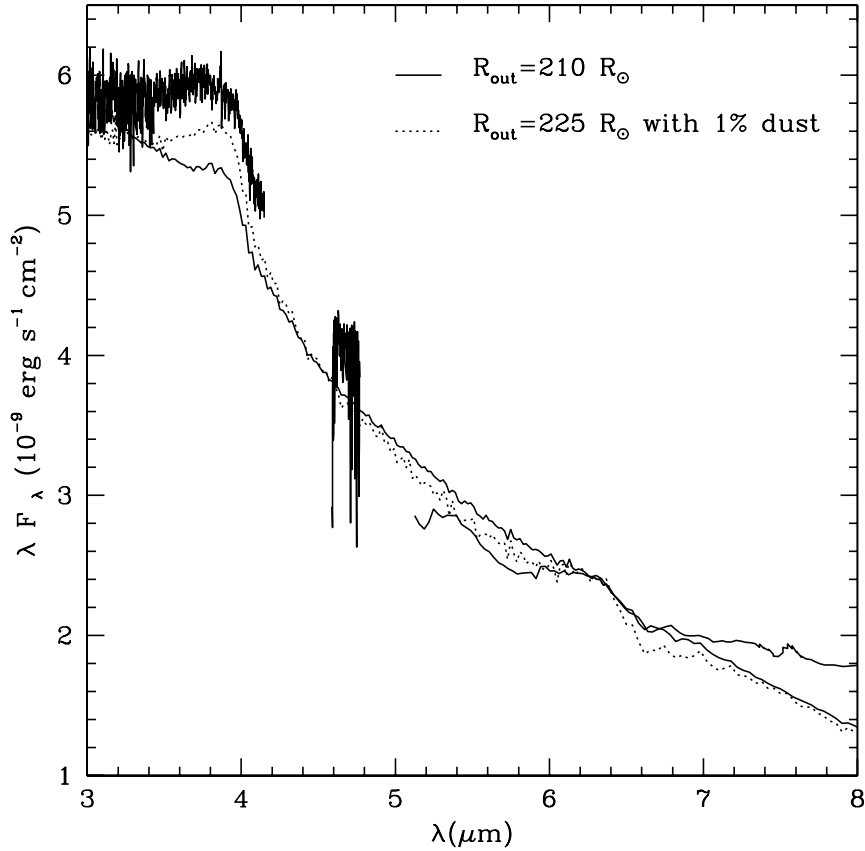


Figure 2.9 The mid-infrared part of the observed spectra in Figure 2.1 compared with the model spectra. The solid line is the model with $R_{out}=210 R_{\odot}$ and the dotted line is the model with 1 % dust opacity (dust opacity reduced by a factor of 100) and $R_{out}=225 R_{\odot}$. We do not have the CO fundamental opacities in our model and thus cannot reproduce these strong spectral features at $4.6 \mu\text{m}$.

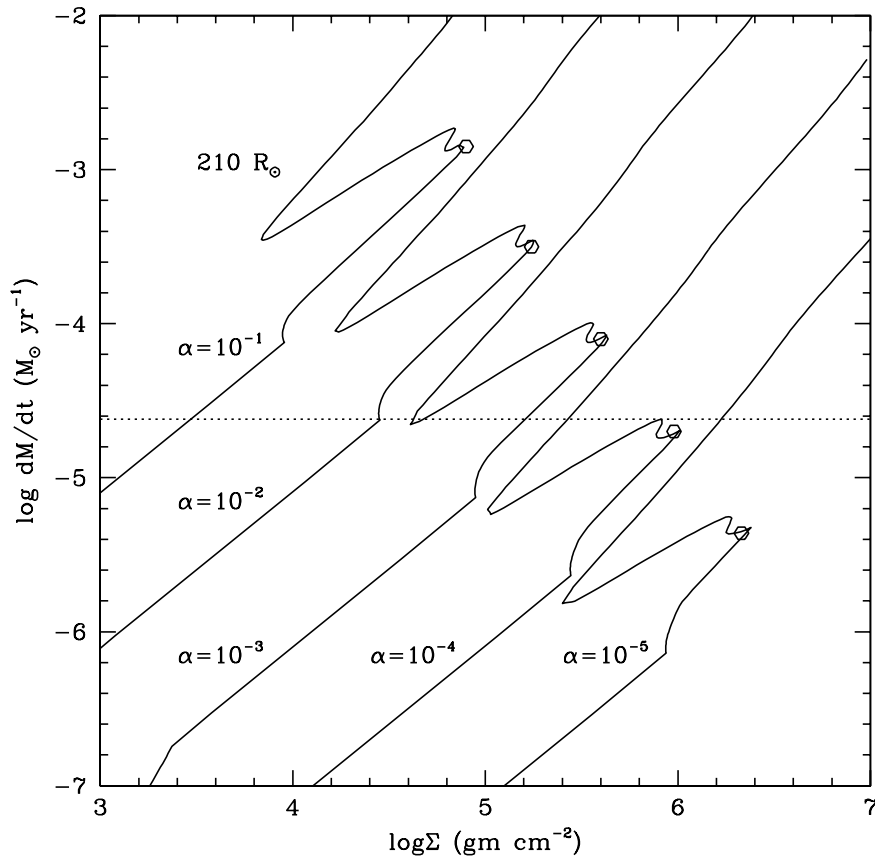


Figure 2.10 The equilibrium curves for thermal-instability. $R=210 R_{\odot}$ with five values of α : $10^{-1}, 10^{-2}, 10^{-3}, 10^{-4}, 10^{-5}$ (from top to bottom). The dotted line is $\dot{M} = 2.4 \times 10^{-5} M_{\odot}/\text{yr}$, set to be one order of magnitude lower accretion rate than the accretion rate of the inner disk. If the outer disk \dot{M} were one order of magnitude higher than this (so that the outer disk and inner disk accretion rates are the same) the mid-infrared flux would be much larger than observed (see discussion in chapter 2.5). The open circles denote the critical surface densities Σ_A for triggering the thermal instability at each value of α (see chapter 2.6.3)

CHAPTER 3

Long-wavelength Excesses of FU Orionis Objects: Flared outer disks or Infalling envelopes?

3.1 Abstract

The mid- to far-infrared emission of the outbursting FU Orionis objects has been attributed either to a flared outer disk or to an infalling envelope. We revisit this issue using detailed radiative transfer calculations to model the recent, high signal-to-noise data from the IRS instrument on the *Spitzer Space Telescope*. In the case of FU Ori, we find that a physically-plausible flared disk irradiated by the central accretion disk matches the observations. Building on our previous work, our accretion disk model with outer disk irradiation by the inner disk reproduces the spectral energy distribution between $\sim 4000 \text{ \AA}$ to $\sim 40 \mu\text{m}$. Our model is consistent with near-infrared interferometry but there are some inconsistencies with mid-infrared interferometric results. Including the outer disk allows us to refine our estimate of the outer radius of the outbursting, high mass accretion rate disk in FU Ori as $\sim 0.5 \text{ AU}$, which is a crucial parameter in assessing theories of the FU Orionis phenomenon. We are able to place an upper limit on the mass infall rate of any remnant envelope infall rate to $\sim 7 \times 10^{-7} \text{ M}_{\odot} \text{ yr}^{-1}$ assuming a centrifugal radius of 200 AU. The FUor BBW 76 is also well modelled by a 0.6 AU inner disk and a flared outer disk. However, V1515 Cyg requires an envelope with an outflow cavity to adequately reproduce the IRS spectrum. In contrast with the suggestion by Green et al., we do not require a flattened envelope to match the observations; the inferred cavity shape is qualitatively consistent with typical protostellar envelopes. This variety of dusty structures suggests that the FU Orionis phase can be present at either early or late stages of protostellar evolution.

This chapter has been published in the paper: “ Long-Wavelength Excesses of FU Orionis Objects: Flared Outer Disks or Infalling Envelopes?”, 2008, ApJ, 684, 1281 with Lee Hartmann, Nuria Calvet, Jesus Hernandez, Ajay-Kumar Tannirkulam, and Paola D’Alessio.

3.2 Introduction

The FU Orionis systems are a small but remarkable class of variable young stellar objects (YSOs) which undergo outbursts in optical light of 5 magnitudes or more (Herbig, 1977), with a F-G supergiant optical spectra and K-M supergiant near-infrared (near-IR) spectra dominated by deep CO overtone absorption. FU Orionis objects (FUors) have been modelled as a high mass accretion disk around pre-main-sequence stars (Hartmann & Kenyon 1985, 1987a, 1987b) to explain the infrared color excesses and the variations of both the spectral type and rotational line width with wavelength (Hartmann & Kenyon 1996; chapter 2).

Herbig (1977) argued that at least some FU Orionis outbursts must be repetitive, and ? suggested that this could be explained by infall from an envelope to the disk, replenishing the disk mass for further outbursts. The infall picture is also suggested by the presence of scattered light envelopes around FUors, suggesting that they are objects in early stages of star formation (Herbig, 1977; Goodrich, 1987). In the evolution sequence, FUors may play significant role in transferring a large amount of mass ($\geq 10\%$) to the central star, which is even higher than the mass accumulated in the T Tauri phase (Hartmann, 1998).

However, not all FUors show the large mid-infrared (mid-IR) excesses that clearly demand dense infalling envelopes. In particular, Adams et al. (1987) suggested that FU Ori itself had only a depleted or low-density envelope. Kenyon & Hartmann (1991) suggested that a pure flared disk model could explain FU Ori while an infalling envelope was needed for V1057 Cyg, but Turner et al. (1997) proposed that both FU Ori and V1057 Cyg required flattened envelopes. Finally, taking advantage of IRS spectra obtained with the Spitzer Space Telescope, Green et al. (2006) concluded that the SEDs of V1057 and V1515 Cyg required envelopes and derived crude models for

these objects, while FU Ori and BBW 76 might be explained with flared disks only. Some recent studies about the silicate features also show FUors can be classified as two categories and some objects are evolved (FU Ori and BBW 76) with only disks left (Quanz et al., 2007).

The IRS spectra provide us with the opportunity to perform a much more detailed SED analysis for FUors. In chapter 2, we developed detailed accretion disk models to study the inner disk of FU Ori and we derived an inner disk size ~ 1 AU. In this paper, we re-examine the interpretation of mid-IR excesses, taking advantage of the IRS spectra, with more detailed radiative transfer models, to resolve the disk/envelope problem. We will describe the observational data in chapter 3.3. In chapter 3.4, the method to calculate the temperature structure of the irradiated surface and the resulting spectrum is described. Model results for three FU Orionis objects (FU Ori, BBW 76, and V1515 Cyg) are presented in chapter 3.5. Finally, in chapter 3.6 we discuss some implications of our results.

3.3 Optical and infrared data

3.3.1 Photometry and Spectra

Because FU Orionis objects are significantly variable, it is crucial to minimize differences in the times of observations at differing wavelengths. We build on the database assembled in chapter 2 for FU Ori. For other FU Orionis objects, we also collected optical photometry from Green et al. (2006). These data were obtained in 2004 at the Maidanak Observatory and all the data collected in this year for the same band were averaged considering FUors are variable objects. Near-IR fluxes are from 2MASS point-source catalog (PSC). V1057 Cyg was observed in June, 2000; V1515 Cyg was observed in November, 1998; BBW 76 was observed in February 1999. As mentioned in Green et al. (2006), because FU Orionis objects are fading slowly, the extrapolation from the 2MASS epoch (~ 1998) to the IRS epoch (~ 2004) is not important; thus, we adopted the 2MASS JHK photometry without any correction. Mid-infrared fluxes are derived from the *Spitzer* IRS spectra observed in 2004 (Green et al., 2006).

The spectral energy distributions (SEDs) need to be corrected for extinction to assess the brightness of the mid-IR excess relative to the central hot disk, which will determine whether or not a flared disk can explain the observations. To get the right extinction correction, we de-reddened the optical and near-IR photometry by a variety of extinction parameters (A_V). Then we compared these de-reddened observations with the steady disk spectra calculated with our disk model (chapter 2), in which disk temperatures peak around 6000 K. Through this comparison, the extinction parameter which gave the best fit to the model spectrum was chosen for that object. Because the disk radial temperature distribution may deviate from the steady disk and boundary layer emission may be present, we estimate the uncertainty of our extinction values as $\Delta A_V \sim 0.5$.

3.3.2 Interferometry

We use both the near-IR and mid-IR interferometry to test our modelling of FU Ori. The near-IR interferometric data are from Malbet et al. (2005), who obtained 287 long-baseline interferometric observations in the H and K bands from 1998 to 2003, with resolution of AU scales at the distance of FU Ori. The (u, v) -plane coverage is shown in Fig. 1 in their paper and the averaged square visibilities are provided in Table 3 of their paper. The mid-IR interferometric data are from Quanz et al. (2006), who carried measurements from 8 μm to 13 μm at three baselines (44.56m, 86.25m, and 56.74m) between October 31 and November 4 2004 with the Mid-Infrared Interferometric Instrument (MIDI) at ESO's Very Large Telescope Interferometer (VLTI) on Paranal, Chile. The visibilities are provided in Table 5 of their paper.

3.4 Model calculations

3.4.1 Temperature structure of the irradiated surface

We follow the method of Calvet et al. (1991a) to calculate the temperature structure of the outer flaring surface irradiated by the inner hot high \dot{M} disk. In this treatment we have not considered the outer disk self-heating, which is not important for a moderate flaring disk, but has a non-negligible effect on a highly flared envelope, as discussed

further in chapter 3.6.2. We have assumed the flaring surface is very optically thick whether it is the disk surface or the outflow cavity driven into an opaque envelope. Milne's reflection effect is included and LTE is assumed. Milne's reflection effect tells us that, without additional heating sources, the incident radiation alters the temperature structure of the low-optical depth layers such that all the energy incident on those layers is radiated back or, in other words, the net fluxes of those layers are zero. In the case of LTE, when the source function is determined by local conditions, the transfer equation is a linear equation and solutions can be superposed.

Specifically, if $T_1(\tau)$ is the temperature structure of the standard viscous heating disk with zero incident radiation but net viscous flux

$$F_V = \frac{3GM\dot{M}}{8\pi R^3} \left[1 - \left(\frac{R_*}{R} \right)^{1/2} \right] \quad (3.1)$$

and $T_2(\tau)$ is a temperature structure with a given incident radiation but zero net flux, then the temperature structure of the disk with both of a net flux F_V and a given incident radiation is $T^4 = T_1^4 + T_2^4$. We can solve T_2 by assuming the incident radiation from the central star/high \dot{M} disk covers a well separated frequency range from the disk emergent radiation; details can be found in Calvet et al. (1991a). If the incident radiation consists of a parallel beam carrying energy $E_0(\text{ergs cm}^{-2})$, incident at an angle $\cos^{-1}\mu_0$ to the normal of the disk surface, a fraction σ of the energy in the beam will be scattered and a fraction α of the incident beam will be truly absorbed and remitted. The temperature structure corresponding to an atmosphere that has F_V net flux and incident radiation of flux $E_0\mu_0$ is

$$T^4(\tau_d) = \frac{3}{4}T_V^4\left(\tau_d + \frac{2}{3}\right) + \frac{\alpha E_0\mu_0}{4\sigma R} \times [C'_1 + C'_2 e^{-q\tau_d/\mu_0} + C'_3 e^{-\beta q\tau_d}] \quad (3.2)$$

where

$$C'_1 = (1 + C_1)\left(2 + \frac{3\mu_0}{q}\right) + C_2\left(2 + \frac{3}{\beta q}\right) \quad (3.3)$$

$$C'_2 = \frac{1 + C_1}{\mu_0}\left(q - \frac{3\mu_0^2}{q}\right) \quad (3.4)$$

$$C'_3 = C_2\beta\left(q - \frac{3}{q\beta^2}\right) \quad (3.5)$$

and

$$C_1 = -\frac{3\sigma\mu_0^2}{1 - \beta^2\mu_0^2} \quad (3.6)$$

$$C_2 = \frac{\sigma(2 + 3\mu_0)}{\beta[1 + (2\beta/3)](1 - \beta^2\mu_0^2)} \quad (3.7)$$

where $\alpha = 1 - \sigma$, $\beta = (3\alpha)^{1/2}$ and $q = \tau_s/\tau_d$. τ_s and τ_d are the optical depths at the stellar and disk frequency. For a viscous heating disk,

$$\sigma_R T_V^4 = \frac{3GM\dot{M}}{8\pi R^3} \left[1 - \left(\frac{R_*}{R}\right)^{1/2}\right], \quad (3.8)$$

while for an envelope without viscous heating, $T_V = 0$.

We assume a two part model: an inner steady accretion disk of high mass accretion rate \dot{M} with outer radius R_{in} , which is optically thick but geometrically thin and flat with height H_0 ; and an outer optically thick region, $R \geq R_{in}$, which is heated by absorption of the light from the inner disk. The geometrical details are described in the Appendix 3.8.1 and Fig. 3.1. The values of the quantities μ_0 and E_0 characterizing the incoming radiation to every outer annulus are calculated by integrating the mean intensity arriving from every part of the inner disk. These quantities depend on both of the inner disk physical condition (eg. the peak temperature, disk size) and the geometry of the outer disk surface (Appendix 3.8.1).

We used the same parametrization to describe the flared surface geometry of the disk outside R_{in} as Calvet et al. (1991a). The scale height of a vertically isothermal disk is

$$H = \frac{c_s}{\Omega} \quad (3.9)$$

where c_s is the sound speed at the disk midplane and Ω is the angular velocity. For typical disk temperature distributions, $T \propto R^{-n}$, where $3/4 \lesssim n \lesssim 1/2$. Thus, for a Keplerian disk, $H \propto R^\gamma$, where $9/8 \lesssim \gamma \lesssim 5/4$.

For a very optically thick disk, the absorption height H_s , where most of the inner disk radiation is absorbed is a nearly constant multiple of H (D'Alessio et al., 2001);

thus we parameterize H_s as

$$H_s = H_0 \left(\frac{R}{R_{in}} \right)^\gamma \quad (3.10)$$

where H_0 is the disk height of the inner high \dot{M} disk and R_{in} is the outer radius of the inner high \dot{M} disk, which is also the inner boundary of the flared outer surface (Fig. 3.1). Thus, for FU Ori, $R_{in} \sim 0.5-1$ AU. We adopt this form to model all objects. When it turns out that $H_s \gg H$, or $\gamma > 5/4$, we conclude that the absorbing surface we are describing is not that of a flared disk but rather represents the edge of a cavity in a dusty opaque envelope. Our outer disk (or envelope) structure joins abruptly to the inner flat thin disk. In reality we expect a smoother joining between inner and outer regions, but this depends upon the precise geometry of the inner disk (height, flaring) which in turn depends upon the detailed viscosity, etc. Thus, the details of our model near R_{in} (and the precise values of R_{in} and H_0) are uncertain, while the structure at $R > R_{in}$ is more robustly modeled.

The gas opacity used in this model is the same as we used in chapter 2. We improve our dust opacity by using the prescription in D'Alessio et al. (2001). For each dust component, the grain size distribution is given by a power law of the grain radius, $n(a) = n_0 a^{-p}$, between a minimum and maximum radius. We choose $a_{min} = 0.005 \mu\text{m}$, $a_{max} = 1 \mu\text{m}$, and $p = 3.5$. The detailed ingredients of the dust are shown in Table 3.1. With this monochromatic dust opacity and gas opacity from chapter 2, we calculate the α and q parameters of Eq. (3.2). For α , we weight the monochromatic α_ν by the Planck function at the stellar temperature. For q , we calculate the Rosseland mean opacity weighted by the planck function at the stellar temperature and the disk temperature separately, and then divide them. We also use the same opacity to calculate the emergent spectra and disk images. Although the dust ingredients may vary for different objects, we use the ingredients in Table 9.2 for all, considering that larger uncertainties caused by the invalidity of the plane parallel assumption, as discussed below.

3.4.2 Emergent spectra and disk images

Given α , q , μ_0 and E_0 , we can calculate the temperature structure of every outer irradiated annulus using Eq. (3.2). The emergent intensity of any annulus at any outgoing direction then can be derived by solving the radiative transfer equation. Our calculation of the emergent spectrum does not include scattering. Scattering is unlikely to be important in the mid-infrared but may have an effect in the near-infrared; we will consider a detailed scattering treatment in a future paper.

When the intensity of every annulus, every outgoing direction and every wavelength is derived, the total flux and the image of the flared surface for any inclination angle can be derived, for given flared surface geometry. The total flux can be compared with the IRS spectra while the image can be used to do interferometric tests. The details are shown in Appendix 3.8.2.

3.5 Results

3.5.1 FU Ori

Fig. 3.2 shows the final model spectra for FU Ori compared with the observed SED. The parameters are in Table 3.2. The inner disk model is that of chapter 2, which shows absorption features because it is internally heated by viscous dissipation. The outer flared disk exhibits 10 and 18 μm silicate emission features due to the strong irradiation by the inner high \dot{M} disk, which produces a temperature inversion at its surface. The model does not fit the 18 μm feature very well, suggesting that either the size distribution we are using for the dust may vary with radius or the temperature structure of the outer region is not accurate.

The adopted surface has the parameters $H_s = 0.19(R/R_{in})^{1.125}$ AU, where $R_{in}=0.58$ AU (see Fig. 3.3). To investigate whether this surface is plausibly that of a flared disk, we computed the approximate local vertical scale height $H = c_s/\Omega$, assuming that the central mass is $0.3 M_\odot$ (chapter 2) and the temperature at the mid-plane is equal to the temperature at $\tau_d=10$ (i.e., the disk interior temperature distribution is roughly isothermal.). The results indicate that our adopted surface lies roughly

3 scale heights above the midplane (Fig. 3.3), comparable to the dusty disk scale heights estimated for typical T Tauri stars (Kenyon & Hartmann, 1987; D’Alessio et al., 1998, 2001). Thus, a physically-plausible flared disk can reproduce the mid-IR flux of FU Ori. The temperature at $\tau_d = 2/3$ is shown in Fig. 3.4. Because the disk is isothermal when $\tau_d > \sim 1$, the midplane temperature is almost the same as Fig. 3.4.

In chapter 2, without considering the flux from the flared outer surface, we derived an inner high \dot{M} disk size of ~ 1 AU, constrained by the mid-IR IRS spectrum. The flared outer disk contributes some emission shortward of $10 \mu\text{m}$, necessitating a reduction of the outer radius of the inner outbursting disk from 1 AU to ~ 0.58 AU. This reduction of the outer radius does not significantly affect the conclusions of chapter 2; in particular, the model of Bell & Lin (1994) still cannot reproduce the observations.

We next compare model results with near-IR and mid-IR interferometry. The images at the H and K bands are calculated by assuming the above flared surface geometry and all the parameters flow strictly from the SED fitting. To compensate for the lack of scattering in our models, we add an extra component of emission corresponding to an “effective albedo” of about 30% in H and K; compared with the case without scattering, the scattering model decreases the square visibilities by only 5%. We adopt the 55 degree inclination angle estimated by Malbet et al. (2005). We further adopt a -30 degree position angle for the disk, which is roughly perpendicular to the axis of large-scale reflection nebulosity seen in optical imaging (?), although due to the large error bars in the observed visibilities, the choice of the position angle has little effect.

With the image as shown in Fig. 3.5, the resulting model visibilities are compared with the observations in Fig. 3.6. Within the relatively large observational errors, our FU Ori model is consistent with the near-IR interferometry. Considering 90% of the flux at H and K bands is from the inner disk, the near-IR interferometry only tests the inner disk modeling and longer wavelength data are needed to test the outer disk modeling. We compute the mid-infrared visibilities, and compare with the VLTI-MIDI data from Quanz et al. (2006); The comparison is shown in Fig. 3.7. While the

model predictions are in reasonable agreement with the observations at the shortest wavelengths, the predicted visibilities are considerably lower than the observations at long wavelengths. Although self-heating is not important in SED fitting because only 17% of the inner disk radiation intercepted by the outer disk within 10 AU by Eq. 7 in Green et al. (2006), self-heating may change the visibility a little bit. However, it is not apparent to tell whether the visibility will increase or decrease, because the inclusion of the self-heating will decrease the flaring slightly, and thus decrease the amount of light intercepted from the inner disk, to keep the same SED.

The comparison with the mid-infrared observation might be improved if the disk has a higher inclination angle than estimated by Malbet et al. With a bigger inclination angle, the disk would be less resolved (higher visibility) for the 44.56 m baseline which lies on the short axes of the disk image. The visibilities for other two baselines would also increase, though not as much as for the 44.56 m baseline. However, a bigger inclination angle may also increase the visibilities at shorter wavelengths which may contradict with the observed visibilities around $8 \mu\text{m}$. Unfortunately we can not test this by our model because the light from the inner disk has to travel through the outer disk to reach us at higher inclination angle and this needs a more complicated radiative transfer treatment than adopted in this chapter.

Another possibility is that there might be an abrupt change in the disk absorption height at the radius around R_{in} where dust condenses, due to the much larger opacity of dust than gas; this might produce a radially-sharp mid-infrared emission feature in the disk where the dust begins to form at $T \sim 1500 \text{ K}$, by intercepting more irradiated flux from the inner disk. Finally, there might simply be narrower structures than we can model, such as non-axisymmetric spiral arms due to gravitational instability in the outer disk (chapter 2).

Overall, the spectrum fitting and the near-infrared interferometry support our flared disk model. Better uv plane coverage in mid-infrared interferometry would help to improve our understanding of the outer disk structure.

3.5.2 BBW 76

We fit the SED of BBW 76 following the same procedure as used for FU Ori (Fig. 3.8). Given the similarity of the large scale nebulosity to that of FU Ori, we adopt a similar inclination angle of 50 degrees. Because BBW 76 has the same rotational velocity broadening as FU Ori (Reipurth et al. 2002), we choose the same central star mass $0.3 M_{\odot}$. The parameters of the best fit model are displayed in Table 3.2. The flared surface (solid curve in Fig. 3.3) also lies close to 3 scale heights, and is therefore consistent with a flared disk structure. With the same relative strength of the IRS spectrum with respect to the optical flux and the same IRS spectrum shape as FU Ori, we derived a similar outer radius of the inner high \dot{M} disk ~ 0.6 AU. However, the outer disk extends further than in FU Ori, to ~ 200 AU, due to the slightly higher $18 \mu\text{m}$ excess of BBW 76.

3.5.3 V1515 Cyg

The nebulosity seen on large scales suggests that we view V1515 Cyg nearly pole-on, looking right down an outflow cavity (Goodrich 1987). For simplicity we assume an inclination angle of 0; small departures from this will have little effect on our modelling. Because of the low inclination, it is difficult to constrain the central star mass very well (Kenyon, Hartmann, & Hewett 1988). We therefore assume the central star is like FU Ori with a mass of $0.3 M_{\odot}$. In contrast to FU Ori and BBW 76, the absorption height of the surface required to fit the SED of V1515 Cyg is highly flared (Fig. 3.9). This surface lies at about 6 scale heights (Fig. 3.3) with the assumption that the central star mass is $0.3 M_{\odot}$; this value is higher than a physically plausible height for a disk. Instead, the large dust surface height and relatively small opening angle ($H/R > \sim 1$) strongly suggest that this surface defines an outflow-driven cavity in an infalling envelope, as suggested by Kenyon & Hartmann (1991) and Green et al. (2006).

Though this surface may extend to a very large radius, most of the IRS mid-IR flux comes from small radii, eg. 80 % of $10 \mu\text{m}$ flux and 50 % of $20 \mu\text{m}$ flux come within 10 AU. This can be roughly estimated from Fig. 3.4. By Wien's law, 100 K

blackbody has its peak flux at $20 \mu\text{m}$ and from Fig. 3.4 100 K corresponds to 10 AU.

Our assumed dust properties fit the silicate emission features of FU Ori very well, but in V1515 Cyg the model continuum is a bit too steeply declining longward of $30 \mu\text{m}$; in addition, the model predicts slightly stronger silicate features than observed (Fig. 3.9). These discrepancies might be reduced if we had adopted larger dust grain sizes which can make the silicate features wider and shallower. However, it could also be that our assumption of plane-parallel geometry is not correct for the outer envelope. As Fig. 3.4 shows, although the fluxes at $\lambda < 10 \mu\text{m}$ (characteristic of a black body temperature $< 300 \text{ K}$) are mainly from the surface within 10 AU, the long wavelength fluxes may come from a much larger radius from 10 AU to 100 AU. Because infalling envelopes are much less optically thick than disks at these radii, long wavelength photons may travel further into the envelope, invalidating the plane-parallel assumption.

3.6 Discussion

3.6.1 Flared Disks

The inner disks of the FUors are internally-heated accretion disks, which produce absorption features. However, the silicate emission features must arise in a dusty region that is externally heated to produce a temperature inversion in the surface of optically-thick dusty disks and envelopes. In the cases of FU Ori and BBW 76, we find that the IRS SED can be explained with physically plausible flared disks.

For the flared disks of FU Ori and BBW 76 we derived $H_s/R \sim 0.5$ which is larger than the value of 0.2 crudely estimated by Green et al. (2006) for FU Ori. The main reason for the discrepancy is that we adopt a smaller A_V than Green et al. (2006), which makes the inner disk fainter and thus requires a more flared outer disk to absorb and reemit the same luminosity (the long-wavelength spectrum is relatively unaffected at these low values of extinctions). If anything our extinction estimate is likely to be low, which means that we may have overestimated the required flaring, and thus makes it even more plausible that the long-wavelength emission comes from

the outer disks.

We note that, in estimating the number of scale heights for the disk, we have assumed that the disk has been able to relax to vertical hydrostatic equilibrium after the outburst. Before the outburst, we expect the outer disk to be cooler and thus thinner. After the outburst, the outer disk is heated by the inner hot disk and gets puffed up. The time scale for the disk to adjust its vertical hydrostatic equilibrium to the extra irradiation is H/c_s , where H is the disk scale height and c_s is the sound speed. Since $H = c_s/\Omega$, $H/c_s = 1/\Omega$ or $P/2\pi$, where P is the orbital period. Thus,

$$\frac{H}{C_s} = \frac{1}{2\pi} \frac{(R/1AU)^{3/2}}{(M/M_\odot)^{1/2}} yr \quad (3.11)$$

As the outburst of FU Ori has been proceeding for over 70 years now, our assumption of hydrostatic equilibrium is good for the inner parts of the flared disk, but may be less appropriate for the outer disk; beyond 50 AU for an assumed $0.3 M_\odot$ central star (chapter 2), the hydrostatic equilibrium time starts to become longer (100 yrs) than the length of the current outburst.

While it is not necessary to include disk accretion energy in the outer disk to fit the spectrum reasonably well, this does not mean that the disk is not accreting; the local viscous energy release is simply much less than the irradiation heating. We find that outer disk accretion rates greater than $\sim 1/4$ of the inner disk accretion rate yield silicate features shallower than observed in the IRS spectra. Thus, the data suggest that the outer disk accretion rates in BBW 76 and FU Ori are significantly smaller than the inner disk accretion rates. This is consistent with models in which material piles up and then accretes in bursts (e.g., Kenyon & Hartmann 1991; Armitage et al. 2001).

3.6.2 Envelopes

The IRS SED of V1515 Cyg cannot be explained with a reasonably flared disk. A much more plausible explanation is that we are observing emission from the surface of a cavity in a dusty, infalling envelope. Green et al. (2006) also inferred an envelope

around V1515 Cyg, and estimated a maximum solid angle of the outer envelope of $H_s/R \sim 0.37$ based on 14% of the inner disk radiation being intercepted and reradiated by the envelope. However, their estimate was a lower limit because they did not include emission at longer wavelengths than observed by the IRS.

In our radiative transfer model, 80% of the 10 μm flux and 50% of the 20 μm flux arises from within 10 AU. At this radius the height of the envelope surface is about 10 AU (Fig. 3.3), so that the fraction of solid angle covered at this point is about 70%. This is roughly twice the solid angle estimated by $H_s/R \sim 0.37$ from Green et al. , but the assumed geometries are different. Our cavity structure (Fig. 3.2) is much more consistent with typical outflow cavity structures (Dougados et al., 2000) and our radiative transfer methods are more robust. We estimate that self-heating of the outer flared disks, which we ignore, is a relatively small effect because the outer disk only intercepts a small fraction of the inner disk flux. This is not true of the envelope for V1515 Cyg, and so our results for this object can only be suggestive rather than conclusive. Our main point is that a flared disk model cannot reproduce the observations of V1515 Cyg and V1057 Cyg.

We have also begun to investigate V1057 Cyg. Our preliminary model is very similar to that of V1515 Cyg, with a highly flared envelope. However, when the object is not pole-on or a flat disk our method is questionable (i.e., maybe we are looking along the edge of the envelope, or even through some of the envelope), thus we will revisit V1057 Cyg using a more detailed radiative transfer method in future.

The near-IR Keck interferometer (Millan-Gabet et al., 2006) also found a difference between the near-IR sizes for V1515 Cyg and V1057 Cyg compared with FU Ori. The low near-IR visibilities suggest V1515 Cyg and V1057 Cyg are more resolved than FU Ori, which suggests dense envelopes may be present for these objects. This is an additional support for the envelope model, but in future the detailed modeling is needed to fit these interferometry data.

3.6.3 Do FU Ori and BBW 76 have envelopes?

As both FU Ori and BBW 76 have large-scale reflection nebulosities, it suggests that they have remnant infalling envelopes, if sufficiently optically thin. We can estimate an upper limit to the amount of possible envelope material in FU Ori and BBW 76 from a limit on the visual extinction. We use the rotating collapse model of Terebey, Shu, & Cassen (1984). When $r \gg r_c$, where r_c is the centrifugal radius,

$$\rho \sim \frac{\dot{M}}{4\pi(2GM)^{1/2}}r^{-3/2}; \quad (3.12)$$

when $r \ll r_c$,

$$\rho \sim \frac{\dot{M}}{8\pi r_c(GM)^{1/2}}(1 + \cos\theta)^{-1/2}r^{-1/2} \quad (3.13)$$

Integrating the above equations from 0 to ∞ and then multiplying by the visual dust opacity κ_V at the V band,

$$\tau_V = \int_0^\infty \kappa_V \rho dr = \frac{\dot{M}\kappa_V}{4\pi(GMr_c)^{1/2}}((1 + \cos(\theta))^{-1/2} + 2^{1/2}) \quad (3.14)$$

With $\theta = 60^\circ$, $M = 0.3M_\odot$, $\kappa_V = 100 \text{ cm}^2/\text{gr}$, and $\tau_V < 2$ constrained by $A_V \sim 2$, we find

$$\frac{\dot{M}}{r_c^{1/2}} < \frac{7 \times 10^{-7} M_\odot \text{yr}^{-1}}{(200 \text{AU})^{1/2}} \quad (3.15)$$

If $r_c = 200 \text{ AU}$, we thus estimate an upper limit of $\dot{M} \lesssim 7 \times 10^{-7} M_\odot \text{yr}^{-1}$, which is considerably smaller than typical Class I infall rates of $2 - 10 \times 10^{-6} M_\odot \text{yr}^{-1}$.

Adams et al. (1987) also suggested that FU Ori has a highly depleted dusty envelope, with a density depletion factor 0.01 with respect to the density derived by their standard infall envelope model. Though they didn't give the mass infall rate for the depleted envelope models, we can estimate their mass infall rate is $\sim 10^{-7} M_\odot/\text{yr}$ by multiplying the depletion factor 0.01 by their standard mass infall rate $10^{-5} M_\odot/\text{yr}$. Because they didn't consider the flared outer disk which is the main contributor at IRS range, this infall rate is an upper limit. Submillimeter observations barely resolve FU Ori and BBW 76 (Sandell & Weintraub, 2001), which also implies highly evolved

or absent envelopes.

3.6.4 Dust properties

The 18 μm features in the SEDs are not well fit, indicating that we may need to use a different grain opacity or a more detailed radiative transfer method. However, we can still study the dust properties from the 10 μm silicate emission features. The dust, with a power-law distribution of the grain radius and a maximum radius 1 μm , is larger than the typical interstellar medium dust with a maximum grain radius 0.25 μm (D'Alessio et al., 2001). Although this dust composition differs from the one used by Quanz et al. (2007), where they use a mixture of grains with three different sizes (0.1, 1.5 and 6 μm), it also suggests that grain growth has taken place in the disk. Our results confirm Quanz et al. (2007) that a significantly higher fraction of $\sim 1\mu\text{m}$ grains is required. BBW 76 is similar to FU Ori while V1515 Cyg seems to require grains growing to even larger sizes.

In chapter 2, we suggested that dust might be depleted in the inner disk, based on the observed water vapor absorption features at 8 μm . However, if we deplete the dust in the outer disk of FU Ori and BBW 76, we predict a strong water vapor emission at 8 μm , which is not observed. Thus, there may not be significant depletion in the outer disk, which may be reasonable given the youth of the system and the likelihood that grain growth/settling timescales are longer at larger radii (Weidenschilling et al., 1997). However, this is not a firm conclusion, as the abundance of water vapor is poorly understood and the region of the disk where most of the 8 μm flux comes from is at the region where we join the inner and outer disk solutions, and thus is uncertain.

3.6.5 Evolutionary states and FU Ori classification

The (meager) event statistics suggest that there must be repeated FU Orionis outbursts in at least some young stars (Herbig 1977; Hartmann & Kenyon 1996). Kenyon & Hartmann (1991) proposed that continued infall was needed to replenish the material accreted onto the central star during an outburst. While we are unable to

determine the infall rate for V1515 Cyg from our particular modelling, previous estimates suggest that sufficient matter may be falling in to make repeat outbursts possible in V1515 Cyg and in V1057 Cyg (Kenyon & Hartmann 1991; Green et al. 2006).

In contrast, we have shown that FU Ori and BBW 76 have little or no infall from remnant envelopes. The low upper limits of infall in these objects suggest that continuing infall may not be important in continuing outbursts; any subsequent outbursts may have to rely on material already present in these disks. Thus, we suggest that FU Ori and BBW 76 are nearing the end of their outburst lives, while V1515 Cyg and V1057 Cyg have a much higher probability of continuing their activity.

The significant difference between FU Ori and BBW 76 on the one hand, and V1515 Cyg and V1057 Cyg on the other, is also supported by submillimeter observations. FU Ori and BBW 76 are very faint and hardly resolved at submillimeter wavelengths (Sandell & Weintraub, 2001), suggesting that they have more depleted envelopes than other FU Orionis objects.

Overall, the variety of the FU Orionis envelopes suggests that FU Orionis phenomenon is observed at different stages of the protostars and every YSO may experience several FU Orionis outbursts from the early to the late stages of protostellar infall.

In this regard, young stellar objects (YSO) have been classified as two categories based on their spectral index $n \equiv d \log(\nu F_\nu) / d \log \nu$ in the near-infrared and mid-infrared (Adams et al., 1987). $n \leq 0$ represents the protostars embedded in infalling envelopes (Class I) and $n > 0$ represents the T Tauri stars without envelopes (Class II). This classification helps us to understand the evolutionary sequence of YSO, from protostars to pre-main-sequence stars. As we discussed above, FU Orions objects are in a stage between Class I and Class II. Thus, it is also helpful to classify FU Orions objects in two categories (Quanz et al., 2007). However because of the strong near-IR flux produced by the high \dot{M} disk, n is always positive in the near-IR and mid-IR (1-10 μm) range. Thus, based on the spectra and envelope structures of FU Ori, BBW 76 and V1057 Cyg, we suggest a criterion to classify FU Orionis objects by

using mid-IR spectral index $n \equiv d \log(\nu F_\nu) / d \log \nu$ from 14 to 40 μm , where most of the flux is contributed by the outer region beyond the inner disk. If n is negative or close to zero, this FU Orionis object has a circumstellar envelope which produces a flat mid-IR spectrum (eg: V1057 Cyg and V1515 Cyg). If n is positive it may have a remnant envelope far away and the mid-IR flux is contributed by a flared outer disk (eg: FU Ori and BBW 76).

This classification method is different from the method used by Quanz et al. (2007) where they used the 10 μm silicate feature to classify FU Orionis objects. They suggest that the objects with absorption features are in Category I, embedded in circumstellar envelopes, while the objects with emission features are in Category II, which are more evolved and show properties of Class II sources. However, as discussed above, some FU Orionis objects embedded in envelopes have cavities (eg. V1057 Cyg and V1515 Cyg) with moderate opening angles. Thus, if we view these objects pole on, we will still detect the emission features and would classify them as Category I by the emission silicate feature method.

Another benefit of using a mid-IR index is that the strength of 10 μm silicate features are dependent on the inclination angle. In contrast, for continuum emission at 14-40 μm is not affected significantly by the inclination and envelope extinction, since the opacity at 14 μm is close to the opacity at 30 μm , and 5 times smaller than the opacity at 9 μm for $a_{max}=1 \mu\text{m}$ olivine grains. Even for a highly embedded FU Orionis objects, $A_V=10$ ($A_{silicate}=0.7$), $A_{14\mu\text{m}}$ is only ~ 0.15 , in which case an extinction correction is not necessary. With the mid-IR index method, we get the same classification for the objects listed in Quanz et al. (2007) except that V1057 Cyg, V1515 Cyg, and V 1647 Ori are identified in Category I. In this chapter, we suggest that V1057 Cyg, V1515 Cyg have normal envelopes, thus they are indeed in Category I. V1647 Ori object is a special FUor with both large extinctions, $A_V \simeq 11$ and silicate emission features. Quanz et al. (2007) suggests there maybe a foreground cloud between this object and us, which makes it hard to classify and it needs detailed modelling.

3.7 Conclusions

With the latest IRS spectra and a detailed radiative transfer model including irradiation, we revisited the envelope/flared disk problem of FUors. We confirmed the results of Green et al. (2006) that FU Ori and BBW 76 have flared outer disks while V1515 Cyg has a circumstellar envelope. However, instead of a flattened envelope and a large opening angle (Green et al., 2006), we derived a more reasonable cavity structure.

For FU Ori, near-infrared interferometry also supports our model, while mid-infrared interferometry does not fit perfectly and needs further modelling. Including the contribution from the outer flared disk, we gave a tighter constraint on the outer radius of the inner disk ~ 0.5 AU, which is essential to test outburst theories (chapter 2).

We also suggest using a spectral index n from $14 \mu\text{m}$ to $40 \mu\text{m}$ to classify FUors into early (Category I) and late (Category II), which is less sensitive to the viewing angle. The variety of FU Orionis envelopes suggests that FU Orionis phenomenon is observed at different stages of the protostars, and every YSO may experience several FU Orionis outbursts from very early to late stages of the infalling envelope.

3.8 Appendix

3.8.1 Flared surface geometry

The inner disk and outer flared surface are shown in Figure 1. For point A, located at distance R_A from the center, the quantities μ_0 and E_0 are derived as follows. We define several vectors as shown in the Figure 1; the normal vector to the flaring surface at A is:

$$\hat{n} = -\sin\alpha \hat{y} + \cos\alpha \hat{z} \quad (3.16)$$

The vector from the shaded area at R_i in the inner disk to point A at the flaring outer disk is:

$$\vec{r} = R_i \sin\phi \hat{x} + (R_A - R_i \cos\phi) \hat{y} + (H_A - H_0) \hat{z} \quad (3.17)$$

where

$$\hat{r} = \frac{\vec{r}}{|\vec{r}|} \quad (3.18)$$

The solid angle $d\omega$ extended by S with respect to point A is (S is the area of the tiny shaded region at R_i in figure 1.)

$$d\omega = \frac{\vec{S} \cdot \hat{r}}{|\vec{r}|^2} \quad (3.19)$$

where

$$\vec{S} = S\hat{z} \quad (3.20)$$

Thus E_{in}^i , the amount of energy irradiated from the inner disk annulus R_i to unit area normal to \vec{r} at point A , is $I_i\Delta\omega$ integrated over all the area of annulus i. Thus,

$$E_{in}^i = \int_{annulus R_i} I_i d\omega = \int_0^{2\pi} I_i \frac{\hat{z} \cdot \hat{r}}{|\vec{r}|^2} R_i \Delta R d\phi = I_i \frac{2\pi R_i \sin\gamma \Delta R}{R_A^2 + (H_A - H_0)^2} \quad (3.21)$$

Because of limb darkening, I_i from the inner disk annulus i equals to $I_i^0 \times \frac{3}{5}(\frac{2}{3} + \mu)$, where I_i^0 is the intensity at radius R_i towards z direction (direction perpendicular to the inner disk surface) and μ is the cosine of the angle between \vec{r} and z direction; thus we use $\sin\gamma$ to approximate μ .

Then, $E_{in}^i \mu_i$, the amount of energy irradiated from the inner disk annulus R_i to unit area at the flaring surface point A (notice it is different from the above unit area normal to \vec{r} at point A), is

$$E_{in}^i \mu_i = \int_{annulus R_i} I_i \hat{n} \cdot \hat{r} d\omega = \int_0^{2\pi} I_i \frac{\hat{z} \cdot \hat{r}}{|\vec{r}|^2} \hat{n} \cdot \hat{r} R_i \Delta R d\phi \quad (3.22)$$

Finally, we add the contributions of all the inner annuli together to get the flux E_0 ,

$$E_0 = \sum_i E_{in}^i \quad (3.23)$$

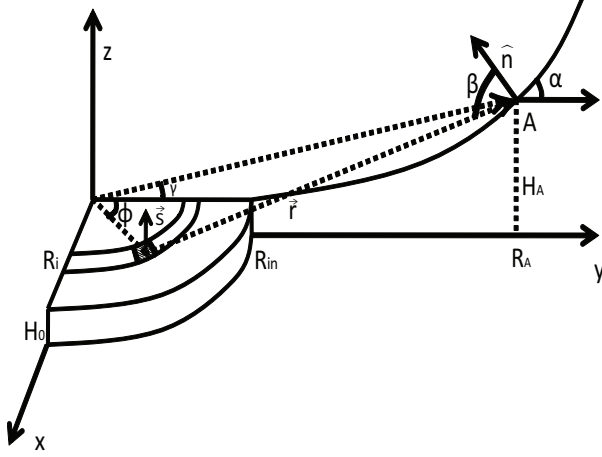


Figure 3.1 The geometry used to calculate the irradiation and the emergent flux. The inner disk has the radius R_{in} and a height H_0 . The absorption height of the outer disk at R_A is H_A , and the normal to the flared surface is \hat{n} .

and the equivalent μ_0 (cosine of the equivalent incident angle $\bar{\beta}$) :

$$\mu_0 = \cos \bar{\beta} = \frac{\sum_i (E_{in}^i \mu_i)}{\sum_i E_{in}^i} \quad (3.24)$$

3.8.2 Emergent flux and image

To derive the total flux and the image detected by the observer on earth, the flared surface needs to be projected onto the plane of sky . For a tiny patch of the flared surface dS_A , with area vector $d\vec{S}_A$ normal to the surface, the projection area to the plane which is normal to our line of sight is $dS_A^\perp = d\vec{S}_A \cdot \hat{l}$, where \hat{l} is the unit vector pointing to the observer along our line of sight. The angle between \hat{l} and $d\vec{S}_A$ is $\varphi = \cos^{-1}(\hat{l} \cdot d\vec{S}_A / |d\vec{S}_A|)$. The flux we observed from dS_A can be derived by multiplying the intensity at direction φ , I_φ , and the solid angle extended by dS_A towards us, $F_A = I_\varphi dS_A^\perp / d^2$, d is the distance between the object and the observer. The addition over all the surface, $\int I_\varphi dS_A^\perp / d^2$, is the total flux. The image of the flared surface could also be derived in this way.

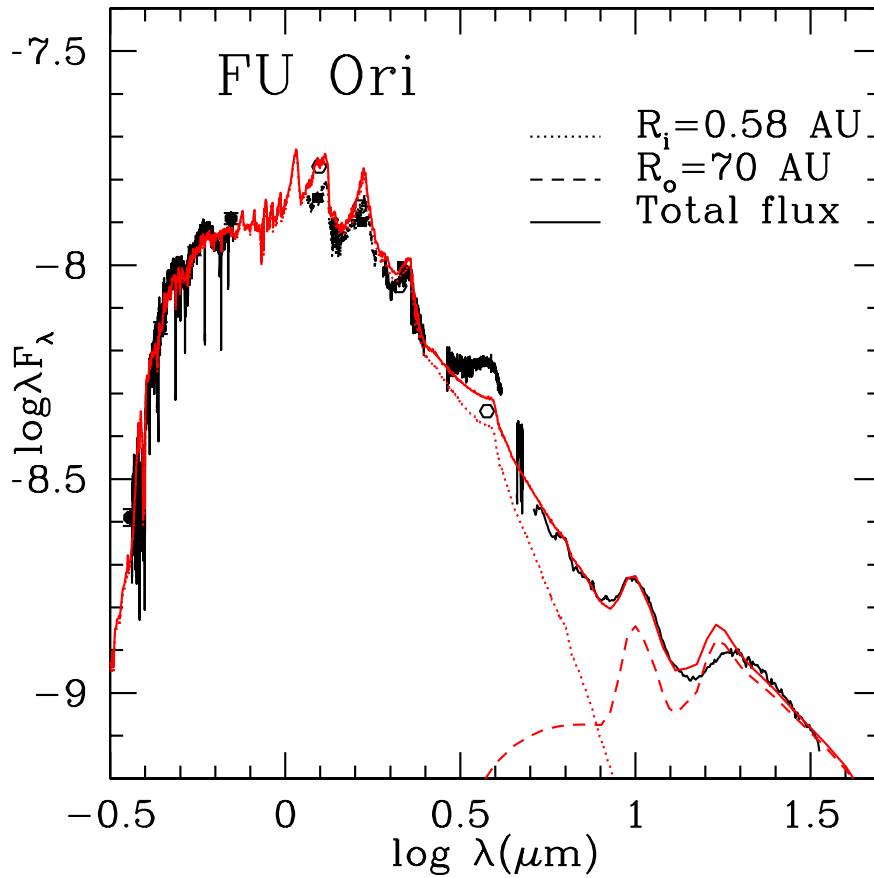


Figure 3.2 SED of FU Ori and the adopted model. Dark curves and dots are observed spectra and photometry. The light dotted curve is the SED of the inner hot disk with outer radius $R_i=0.58$ AU, while the light dashed curve is the SED of the flared outer disk with outer radius $R_o=70$ AU. The light solid curve is the total SED with both of the inner and outer disk.

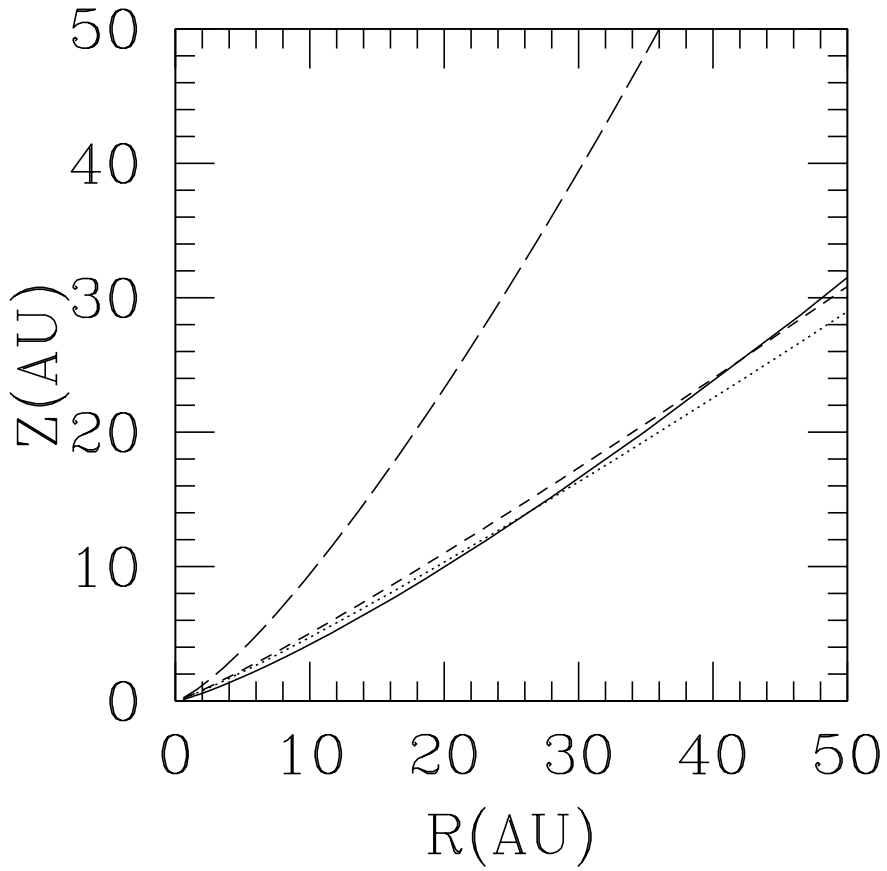


Figure 3.3 The absorption height of the surface of the outer disk for FU Ori(dotted line), BBW 76 (dashed line) and V1515 Cyg (long dashed line) as described in Eq. (3.10). The solid line corresponds to three scale height of the FU Ori disk (see text).

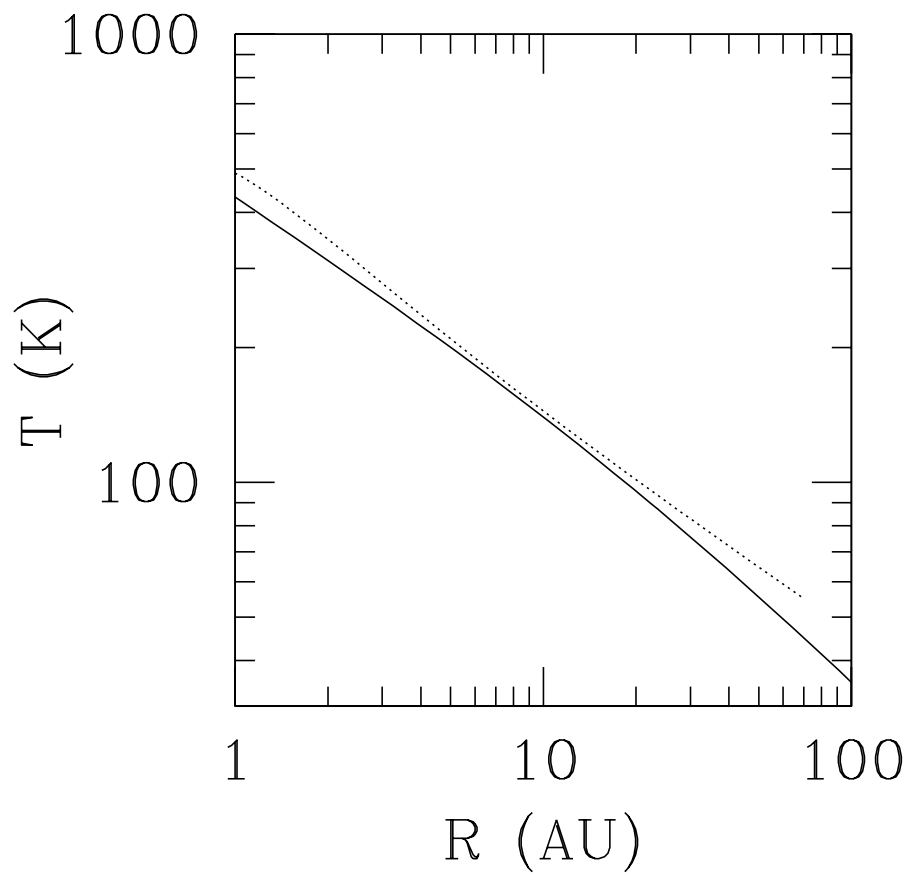


Figure 3.4 The effective temperature of V1515 Cyg (solid line) and FU Ori (dotted line) with respect to the radius.

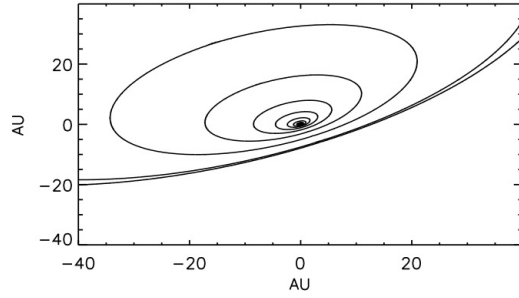


Figure 3.5 The H band image of the FU Ori model with -30° position angle. Each contour corresponds to a decrease a factor of 4 in intensity, starting at the innermost contour.

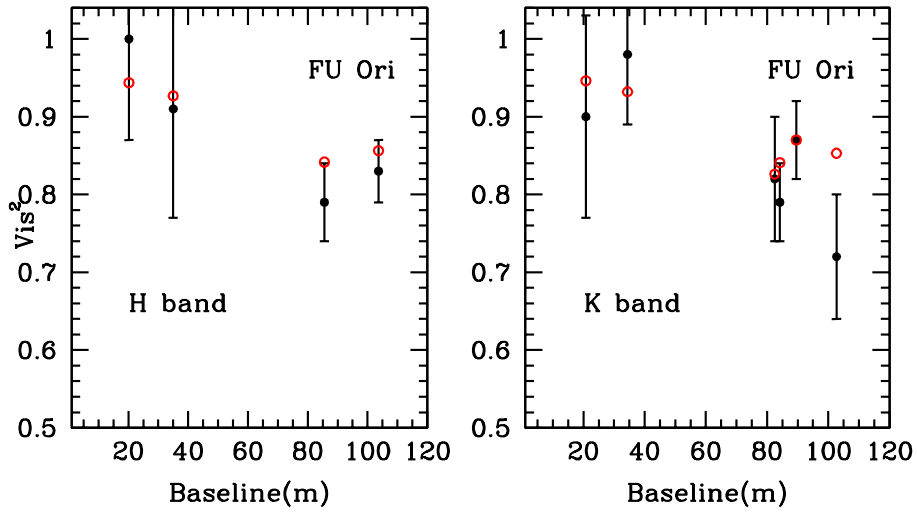


Figure 3.6 Visibility square-baseline at H and K band. Solid dots with error bars are the visibilities from Malbet et al. (2005) and the dots are the synthetic visibilities predicted by our model.

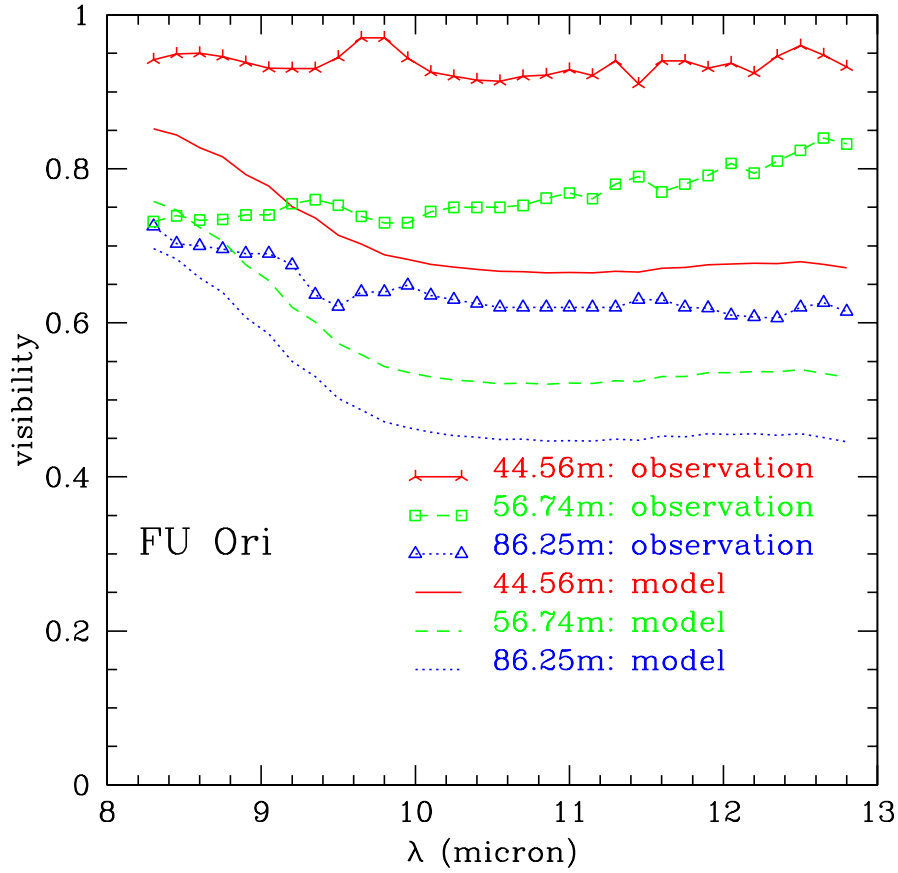


Figure 3.7 Visibility-wavelength at three baselines (44.56 m, 56.74 m, 86.25 m). Observations are from Quanz et al. (2006). The synthetic visibilities are calculated by assuming -30° position angle.

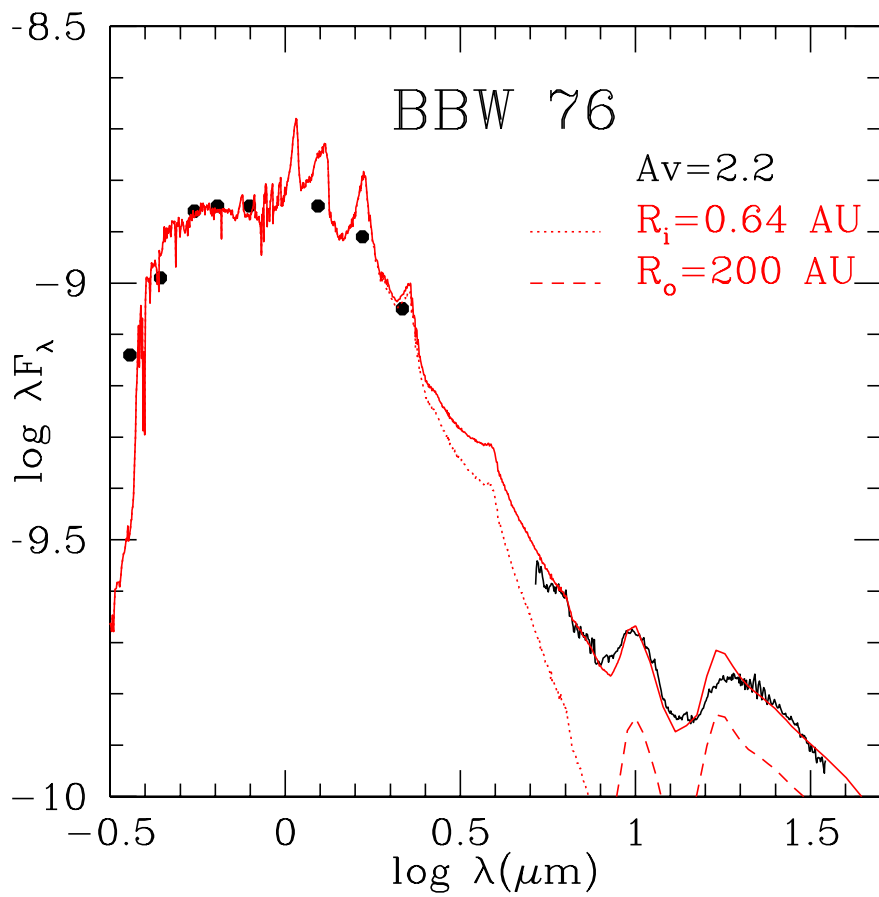


Figure 3.8 SED of BBW 76 and adopted model. Symbols are as in Fig. 3.2.

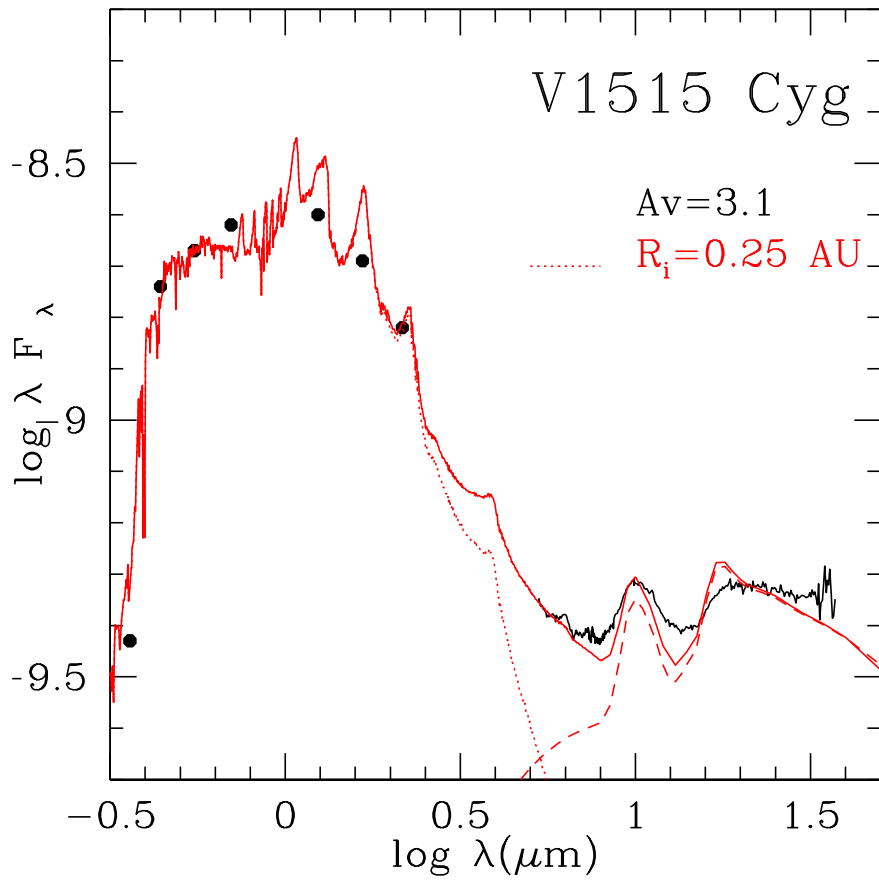


Figure 3.9 SED of V1515 Cyg and adopted model. Symbols are as in Fig. 3.2.

Table 3.1 Adopted dust composition

Ingredient	ζ^a	T_{sub} (K) ^b
Mg _{0.8} Fe _{1.2} SiO ₄ (Olivine)	0.0017	1460
Mg _{0.8} Fe _{0.2} SiO ₃ (Pyroxene)	0.0017	1460
Graphite	0.0041	734
Water ice	0.0056	146

^aDust-to-gas mass ratio of the particular ingredient

^bSublimation temperature at the gas density $\rho=10^{-10}$ g/cm³

Table 3.2 Parameters for best fit models

Object	A_V	Inclination angle	$\dot{M}\dot{M}$ $10^{-5}M_{\odot}^2\text{yr}^{-1}$	R_* R_{\odot}	L_d L_{\odot}	R_{in} ^a AU	H_0 R_{\odot}	γ	R_o ^b AU
FU Ori	1.5	55	7.4	5	232	0.58	41.5	1.125	70 :
BBW 76	2.2	50	8.1	4.6	277	0.64	49.22	1.125	200 :
V1515 Cyg	3.2	0	1.3	2.8	73	0.25	16.8	1.3	10^4 :

^a R_{in} and H_0 are described in Eq. 3.10

^bThe outer radii are poorly constrained by the data.

CHAPTER 4

The Differential Rotation of FU Ori

4.1 Abstract

The emission of FU Orionis objects in outburst has been identified as arising in rapidly accreting protoplanetary disks, based on a number of observational properties. A fundamental test of the accretion disk scenario is that the differentially rotating disk spectrum should produce a variation of rotational velocity with the wavelength of observation, as spectra taken at longer wavelengths probe outer, more slowly rotating disk regions. Previous observations of FU Ori have shown smaller rotation at near-infrared ($\sim 2.2\mu\text{m}$) wavelengths than observed at optical ($\sim 0.6\mu\text{m}$) wavelengths consistent with the assumption of Keplerian rotation. Here we report a spectrum from the Phoenix instrument on Gemini South which shows that differential (slower) rotation continues to be observed out to $\sim 5\mu\text{m}$. The observed spectrum is well matched by the prediction of our accretion disk model previously constructed to match the observed spectral energy distribution and the differential rotation at wavelengths $\lesssim 2.2\mu\text{m}$. This kinematic result allows us to confirm our previous inference of a large outer radius (~ 1 AU) for the rapidly accreting region of the FU Ori disk, which presents difficulties for outburst models relying purely on thermal instability. While some optical spectra have been interpreted to pose problems for the disk interpretation of FU Ori, we show that the adjustment of the maximum effective temperature of the disk model, proposed in a previous chapter, greatly reduces these difficulties. This chapter has been published in the paper: “The Differential Rotation of FU Ori”, 2009, *ApJ*, 694, 64 with Catherine Espaillat, Kenneth Hinkle, Jesus Hernandez, Lee Hartmann, and Nuria Calvet.

4.2 Introduction

FU Orionis systems are a class of exceptionally luminous young stellar objects found in star-forming regions (Hartmann & Kenyon 1996). Originally identified from their very large increases in optical brightness over timescales of years or less (Herbig 1977), a larger group of heavily extincted probable members of the class have been identified by their characteristic infrared spectra, which strongly differ from those of typical T Tauri stars (Reipurth & Aspin 1997; Aspin & Reipurth 2003; Reipurth et al. 2007). Additional support for the identification of these heavily embedded objects comes from recent high-resolution infrared spectroscopy, which indicates that many of these sources are rapidly rotating and exhibit double-peaked absorption line profiles as observed in FU Ori (Greene, Aspin, & Reipurth 2008).

The accretion disk model for FU Ori objects (Hartmann & Kenyon 1996, and references therein) rests fundamentally on the need to explain the peculiar spectral energy distributions (SEDs) of these objects, which are much broader than that of a single temperature blackbody or star, and which exhibit a continuously varying spectral type as a function of wavelength. The disk model naturally accounts for these properties, as observations at longer wavelengths probe increasingly cooler disk regions with later spectral types; our detailed model for FU Ori matches the SED from optical wavelengths to the mid-infrared region (Zhu et al. 2007, 2008). In addition, the disk model predicts that differential rotation should be observed, with slower rotation seen at longer wavelengths, which arise from outer disk radii, and this has been confirmed by comparing optical ($\sim 0.6\mu\text{m}$) and near-infrared ($\sim 2.2\mu\text{m}$) spectral line profiles (Hartmann & Kenyon 1987a,b; Kenyon, Hartmann, & Hewett 1988).

A desirable feature in a model or theory is an ability to make predictions that can be tested observationally. The disk model predicts that the observed rotational spectral line broadening should be even smaller at $\lambda \sim 5\mu\text{m}$ (using the fundamental CO vibrational transitions) than at $2.2\mu\text{m}$ (using the first overtone CO vibrational lines). In this chapter we present a high-resolution spectrum of FU Ori in the $5\mu\text{m}$

region which matches the predictions of the disk model. We also show that some discrepancies seen in optical spectra of FU Ori in comparison with simple disk models are alleviated by a decrease in the maximum disk temperature which we proposed in Zhu et al. (2007).

4.3 Observations

A high-resolution spectrum of FU Ori at $4.9\mu\text{m}$ was obtained at UT 01:00:29 on 2007 February 4 using the Phoenix spectrometer (Hinkle et al. 1998, 2000, 2003) on the 8-m Gemini South telescope. Observations were taken with a two-pixel slit ($0.17''$) for a resolution of $\lambda/\delta\lambda = 75,000$ over the wavelength range $4.808 - 5.050\mu\text{m}$. We observed FU Ori at two positions along the slit for eight 2 minute exposures. We also observed the B2 III star HR1790 for telluric line correction and took 10 flat-field and dark images.

We reduced the data using IRAF.¹ We averaged the flat-field and dark images and subtracted the average dark image from the average flat-field image. This averaged, dark-subtracted flat-field image was then divided into the target spectra. Images at different positions of the slit were differenced to remove the sky and dark backgrounds. We then extracted the spectra using the IRAF *apall* routine and later combined and flattened the spectra using *splot* in IRAF. The spectrum of the hot star HR1790 was used to divide out the telluric lines from the FU Ori spectrum. Wavelength calibration was computed using telluric lines from the Arcturus atlas of Hinkle et al. (1995).

We also obtained a high-resolution spectrum of FU Ori at UT 17:59:15 on 2008 November 14 using the Magellan Inamori Kyocera Echelle (MIKE) spectrograph on the 6.5 m Magellan Clay telescope at Las Campanas observatory (Bernstein et al. 2003). MIKE is a double echelle spectrograph which delivers full wavelength coverage from about $3350 - 5000 \text{ \AA}$ (blue side) and $4900 - 9500 \text{ \AA}$ (red side). The data were

¹IRAF is distributed by the National Optical Astronomy Observatories, which are operated by the Association of Universities for Research in Astronomy, Inc., under cooperative agreement with the National Science Foundation.

obtained in subarcsecond seeing with a $0.7''$ slit, binning 2×2 and an exposure time of 120s. The resolutions were $\sim 40,000$ and $\sim 30,000$ for the blue and red sides respectively. The MIKE data were reduced using the MIKE Redux IDL pipeline.²

4.4 Results

Figure 4.5 shows the reduced Phoenix spectrum of FU Ori. Strong telluric features mean that regions around wavenumber 2009.3 cm^{-1} are not usable, and small residuals from the telluric correction can be seen at wavenumbers 2010.4, 2010.9, 2011.9, and 2013.5 cm^{-1} . The spike around wavenumber 2012.5 cm^{-1} is due to a bad pixel. Outside of these regions, an absorption spectrum is clearly present, with relatively broad features and substantial blending. Most of the lines are due to the P-branch of the fundamental rotational-vibrational transitions of CO.

To interpret the results, we calculated a synthetic disk spectrum using the methods described by Zhu et al. (2007). The model parameters were those used by Zhu et al. (2007) to fit the SED of FU Ori and to match the observed rotational broadening observed at optical and near-infrared wavelengths: central star mass $\sim 0.3 M_{\odot}$, mass accretion rate of the inner high \dot{M} disk $\sim 2.4 \times 10^{-4} M_{\odot} \text{ yr}^{-1}$, disk inner radius $\sim 5 R_{\odot}$, outer radius of the inner high \dot{M} disk $\sim 1 \text{ AU}$, and the disk inclination angle $\sim 55^{\circ}$. (See Figure 8 of Zhu et al. for the fit to the $2.2 \mu\text{m}$ CO lines). We emphasize that we have *not* changed or adjusted any parameters from the Zhu et al. (2007) FU Ori model; these are predicted spectra.

The lower dotted curve in Figure 4.5 shows the synthetic disk spectrum observed pole-on, so that individual spectral lines can be seen without the blending that occurs due to the large rotational broadening. Comparison of the nonrotating spectrum with the observations shows that FU Ori has significantly larger line widths, consistent with rapid rotation, and unlike profiles of M giants and supergiants. The upper dotted curve shows the synthesized spectrum using the inclination and central mass used to obtain a match to the $2.2 \mu\text{m}$ CO line widths. The agreement between synthetic and

²<http://web.mit.edu/~burles/www/MIKE/>

real spectra is quite good, except near 2010.7cm^{-1} where we are missing the CO 5-4 P7 line in the model. This could be due to adopting too small an oscillator strength³. The half-width at half-depth (HWHD) of the lines in this spectral region ($5\ \mu\text{m}$) is $\sim 22\ \text{km s}^{-1}$, considerably smaller than the line widths measured at $2.2\ \mu\text{m}$ (HWHD $\sim 36\ \text{km s}^{-1}$) (Hartmann & Kenyon 1987a; Hartmann, Hinkle, & Calvet 2004; Zhu et al. 2007). This HWHD at $5\ \mu\text{m}$ is close to the Keplerian velocity at 0.5 AU around $0.3\ M_{\odot}$ central star. All the strong lines have been identified in the pole-on model spectrum. Though some water lines are present in this spectrum, they are washed out or blended in the broadened spectrum (upper dotted curve). Only the strong CO fundamental lines can be identified with certainty.

It is also worth noting that some of the unblended line profiles exhibit evidence for double-peaked shapes predicted by simple disk models (e.g., Hartmann & Kenyon 1987a,b). In addition, some of the blends show sharp features (eg. $2011.2\ \text{cm}^{-1}$ line) which are the result of overlapping double-peaked lines. These features naturally arise in a disk model but would not be seen in rotating star models (unless large polar spots are invoked; see below).

In Figure 4.5 we display a segment of the MIKE spectrum of FU Ori in the wavelength range $7030 - 7100\ \text{\AA}$ for comparison with the synthetic Keplerian disk spectrum. We again find good agreement between model and observation, demonstrating that there has been no change in the estimated optical rotational velocity of the object between the observations in chapter 2, which we used to set the disk parameters, and this chapter. The HWHD of the optical lines in this wavelength range is $\sim 65 \pm 5\ \text{km s}^{-1}$, consistent with HWHD $\sim 62 \pm 5\ \text{km s}^{-1}$ measured by Petrov & Herbig (2008; PH08).

Thus, compared with HWHD of 2 micron CO first-overtone lines $\sim 36 \pm 3\ \text{km s}^{-1}$ and HWHD of 5 micron CO fundamental lines $\sim 22 \pm 2\ \text{km s}^{-1}$, the differential rotation in FU Ori observed over nearly an order of magnitude in wavelength is consistent with Keplerian rotation. The slow rotation observed at $5\ \mu\text{m}$ implies spectral formation at radii out to $\sim 0.5\ \text{AU}$, in agreement with our SED modeling; this supports

³This work employed the line lists from Kurucz CD ROM-15

our conclusion in Zhu et al. (2007, 2008) that the extent of the high-accretion rate disk is larger than can be explained by pure thermal instability models for outbursts (Bell & Lin, 1994).

4.5 Discussion

The consistency of the variation of rotational velocities as observed over to $\lambda \sim 0.7\text{--}5\mu\text{m}$ with Keplerian rotation seemingly provides strong evidence for the accretion disk interpretation of FU Ori. However, PH08 recently argued that while the infrared spectrum is that of an accretion disk, the optical spectrum is produced by a rapidly-rotating star with a dark polar spot. The PH08 argument against a pure disk model for a central star rests on three main points: there is no evidence for a variation of absorption line width as a function of excitation potential over the wavelength range $\lambda \sim 0.52\text{--}0.86\mu\text{m}$; there is no evidence for a variation of rotational velocity with wavelength over that wavelength range; and the observed line profiles are more “boxy” or flat-bottomed than the double-peaked profiles of the disk model.

It is important to recognize that the above-listed effects expected for a disk spectrum require not only differential rotation but a temperature gradient as well. A Keplerian disk exhibiting a constant effective temperature would not show any effect of rotational velocity with either excitation or wavelength; and the double-peaked behavior of line profiles only occurs because the outer, slowly rotating regions do not fill in the profile at line center, as these regions are too cool to emit significantly at the wavelength of observation. While the standard steady disk temperature distribution $T_{eff}^4 \propto [1 - (R_i/R)^{1/2}]R^{-3}$ is a power law at large radii, it is relatively flat at distances within about twice the inner radius R_i . Therefore, observations at long wavelengths which probe the outer disk where the temperature falls rapidly with radius will exhibit stronger rotational velocity variations and more double-peaked line profiles than observations at short wavelengths probing the inner, more nearly isothermal disk.

In Zhu et al. (2007) we were forced to use a maximum disk temperature $T_{max} = 6420\text{ K}$ to match the SED of FU Ori, which is lower than the 7200 K maximum temperature adopted in the model used by PH08 (which was based on the earlier model

by Kenyon, Hartmann, & Hewett 1988). Lowering the maximum temperature has the effect of making the flatter part of the accretion disk temperature distribution more dominant at optical wavelengths. As shown in Table 4.5 and Figure 4.5, this model predicts essentially no variation of line width with lower level excitation potential and a very slight dependence on wavelength in the optical region. (Note that PH08 predict a much larger effect of line width on excitation potential than Welty et al. (1992) for what should be essentially the same disk model; the reason for the large discrepancy is unclear.) In any case, measurement of rotation is best done through cross-correlation using suitable templates, as many of the lines used by PH08 are blends and introduce very large scatter into the model predictions (see Table 4.1 and Figure 4.5).

PH08 also noted that their disk model predicts very strong TiO absorption bands at ~ 7054 and 7087 \AA which are not observed. However, as shown in Figure 4.5, our lower-temperature disk model does not predict strong TiO absorption bands in this region. In addition there is evidence for 7087 \AA bandhead absorption in our MIKE spectra, at the level predicted by our disk model. Once again this difference in the predicted disk model spectra arises simply by reducing the maximum disk temperature, which increases the importance of hot inner disk relative to the outer cool disk at the wavelength of observation.

It has long been known that many optical line profiles in FU Ori are less double-peaked than predicted by simple quiescent disk models (Hartmann & Kenyon 1985). There are, however, alternative possibilities to explain the profiles which do not demand abandonment of the accretion disk hypothesis. If, as currently thought, ionized disks accrete through the action of the magnetorotational instability (MRI; Balbus & Hawley 1998), such disks must be turbulent. The disk models with resolved vertical structure computed by Miller & Stone (2000) predict that turbulence driven by the MRI in the central layers of the disk produces waves which propagate outward and shock in the upper layers. It would be surprising if the MRI did not produce significant turbulent motions in the upper atmospheric layers of the disk, which would tend to wash out the double profile structure. Hartmann, Hinkle, & Calvet (2004)

found that that some mildly supersonic turbulence was needed to explain the ^{12}CO first-overtone lines of FU Ori.

It should be noted that the standard steady disk structure may not be completely applicable in the innermost disk. Standard thin-disk models predict that accretion onto a slowly rotating star should give rise to boundary-layer emission with roughly half the system luminosity; this is not observed in FU Ori (Kenyon et al. 1989). Popham et al. (1996) considered disk models which suppress boundary layer radiation; such models exhibit less doubled line profiles in inner disk regions, largely because the angular velocity of the disk departs from Keplerian values near the inner disk boundary.

To explain the optical spectrum of FU Ori with a central star, the star would be required to have essentially the same total system luminosity $L \sim 230L_{\odot}$, and would need to have a radius roughly twice the inner radius of the disk model, $R \sim 10R_{\odot}$ (Zhu et al. 2007). Assuming Keplerian rotation for the infrared disk, Zhu et al. estimated a central mass $M \sim 0.3M_{\odot}$. Such a star cannot be an isolated product of stellar evolution, as it has an implausibly short Kelvin-Helmholtz contraction time $\sim GM^2R^{-1}L^{-1} \sim 1200$ yr. The energy to power the star would have to come from disk accretion, which would also potentially explain the outburst (Larson 1983). However, as the ratio of optical-to-infrared rotational velocities is consistent with a Keplerian profile, this implies that any central star would have to be rotating nearly at breakup; this means that the assumption of solid-body rotation in the PH08 model is unlikely to be correct. It is also unclear whether the accretion of a large amount of hot disk material would add enough angular momentum to spin up the outer layers of the star to breakup velocity as it expanded the outer atmosphere.

In summary, the accretion disk model for FU Ori provides a coherent explanation of the observed spectral energy distribution and differential rotation over more than a decade in wavelength. The slow rotation observed at $5\mu\text{m}$ supports our previous result that the high mass accretion rate disk could extend to $0.5 - 1$ AU, which is significantly larger than that predicted by the pure thermal instability theory (Bell & Lin, 1994). On the other hand, the theory incorporating both gravitational and

magnetorotational (Gammie, 1999; Book & Hartmann, 2005; ?) successfully predicts AU scale high mass accretion rate inner disk during outbursts (?). With the advent of more powerful computers and sophisticated magnetohydrodynamic codes, and the assumption of MRI-driven accretion, it should be possible to explore the possibility that atmospheric turbulence and/or nonstandard inner thin disk structure can explain details of the optical line profiles.

Table 4.1 HWHD of lines selected by PH08 as measured from Our synthetic disk spectrum

λ (Å)	Ion	EP (eV)	HWHD (km s ⁻¹)	Grade ^a	λ (Å)	Ion	EP (eV)	HWHD (km s ⁻¹)	Grade
5383.37	Fe I	4.31	-	0	6726.66	Fe I	4.61	66.2	3
5717.83	Fe I	4.28	-	1	6767.79	Ni I	1.83	65.4	3
5772.15	Si I	5.08	-	0	6810.26	Fe I	4.61	-	1
5775.08	Fe I	4.22	-	1	6814.94	Co I	1.96	-	0
5862.35	Fe I	4.55	-	0	6828.59	Fe I	4.64	78	3
5899.29	Ti I	1.05	61.3	2	7090.38	Fe I	4.23	66.8	4
5922.11	Ti I	1.05	61.8	3	7122.19	Ni I	3.54	66.1	4
5934.66	Fe I	3.93	78.4	3	7344.70	Ti I	1.46	76.8	2
5965.83	Ti I	1.88	65.9	3	7393.60	Ni I	3.61	68	3
5987.07	Fe I	4.80	71.7	3	7445.75	Fe I	4.26	-	0
6016.66	Fe I	3.55	-	1	7511.02	Fe I	4.18	61.7	4
6024.06	Fe I	4.55	-	1	7525.11	Ni I	3.63	-	1
6027.05	Fe I	4.09	-	0	7555.60	Ni I	3.85	68.3	3
6056.01	Fe I	4.73	-	1	7568.89	Fe I	4.28	69.4	4
6108.11	Ni I	1.68	-	1	7574.04	Ni I	3.83	-	1
6180.20	Fe I	2.73	70	2	7586.01	Fe I	4.31	65.8	5
6270.23	Fe I	2.86	72.2	3	7727.61	Ni I	3.68	65.4	4
6355.03	Fe I	2.85	64.4	3	7780.55	Fe I	4.47	65.4	4
6358.70	Fe I	0.86	66.05	4	7788.94	Ni I	1.95	64.13	4
6380.74	Fe I	4.19	72.2	3	7855.44	Fe I	5.06	62.1	4
6411.65	Fe I	3.65	67.8	2	7912.87	Fe I	0.86	-	0
6439.08	Ca I	2.53	74.5	3	7937.13	Fe I	4.33	63.5	4
6471.66	Ca I	2.53	72.8	3	8075.15	Fe I	0.92	-	0
6475.62	Fe I	2.56	66.3	5	8080.55	Fe I	3.30	-	0
6569.22	Fe I	4.73	67.8	5	8085.18	Fe I	4.45	64.7	3
6581.21	Fe I	1.49	64.7	4	8426.51	Ti I	0.83	-	0
6586.31	Ni I	1.95	-	1	8611.80	Fe I	2.85	65.0	4
6707.89	Li I	0.00	-	0	8621.60	Fe I	2.95	63.5	3
6717.68	Ca I	2.71	69.0	4	8648.47	Si I	6.21	73.9	3
6721.85	Si I	5.86	65.2	2					

^aHWHD means "half-width at half-depth" as illustrated and defined in Figure 3 of PH08. Grade indicates the amount of line blending due to rapid rotation: grades 0 and 1 signify badly blended lines, grade 2 identifies less-blended lines that are difficult to use, and grade 3 means that the line is moderately blended so that the true HWHD may be slightly smaller than our measured value to within 10 km s⁻¹. Grade 4 means the line is slightly blended with an errorbar of only 3 km s⁻¹, while grade 5 means that the line is blend-free.

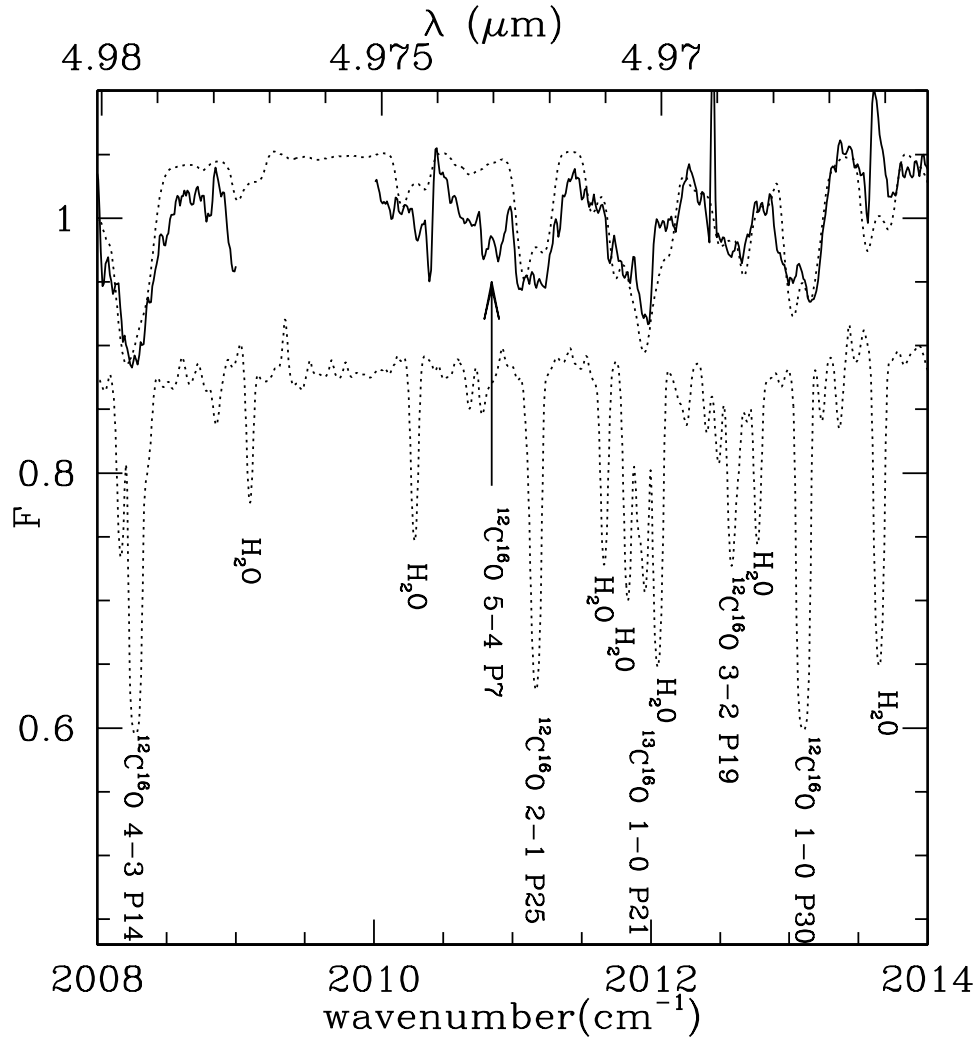


Figure 4.1 Observed 4.9 μm Phoenix spectrum of FU Ori (solid curve) compared with our synthetic disk model spectrum (upper dotted curve). While the wavenumber is shown at the bottom, the wavelength in microns is shown at the top of the figure. The lower dotted curve shows the model spectrum observed pole-on, which removes the rotational broadening, illustrating the need for rapid rotation to match the observations (see the text). The strong lines are identified in the lower model spectrum. The arrow points to the strong CO line which is missing in our model.

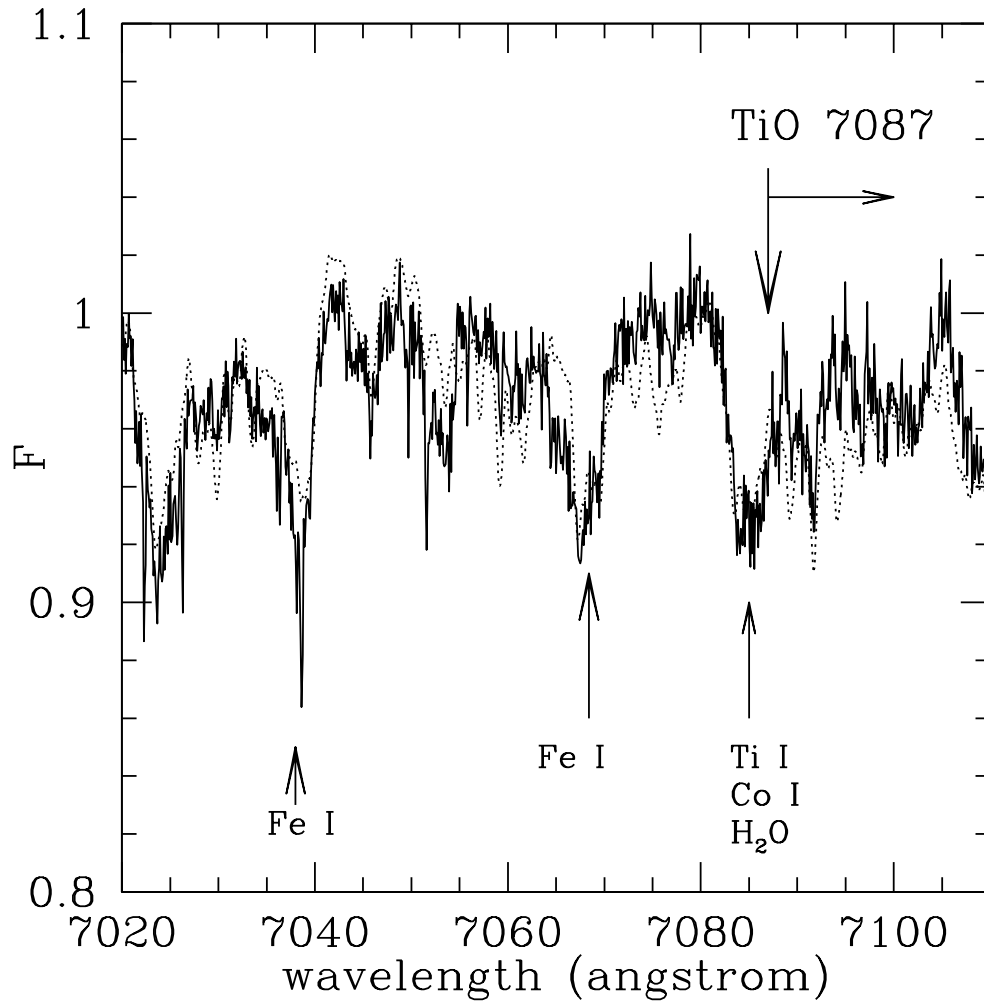


Figure 4.2 Comparison of the observed MIKE spectrum of FU Ori near 7080 Å (solid curve) with the synthetic disk spectrum (dotted curve). Compared with the continuum flux ~ 7080 Å, there is some evidence for weak TiO 7087 Å band absorption in both the observed and the model spectrum (see text).

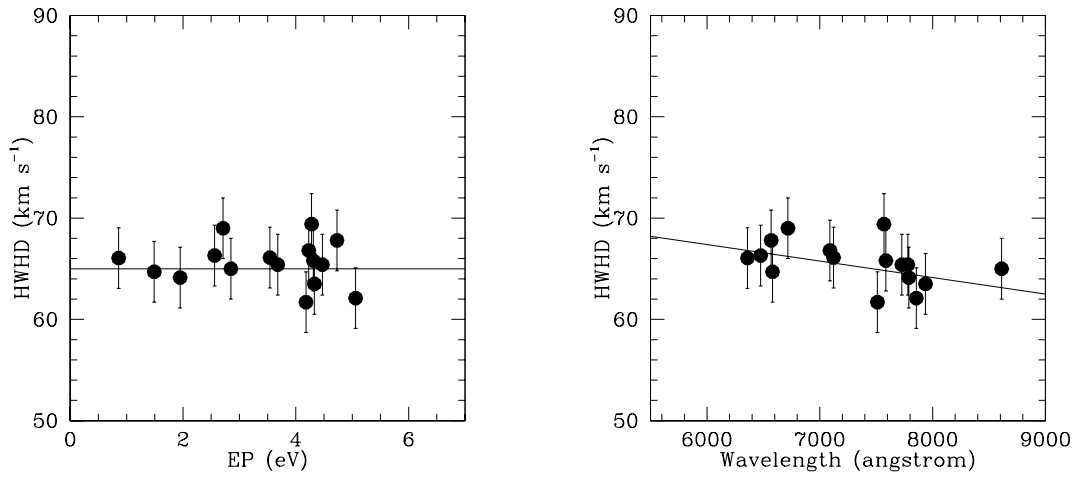


Figure 4.3 Dependence of the model line half-width at half-depth (HWHH) on excitation potential (EP) (left) and the wavelength (right), taken from Table 4.5. We show only the grade 4 and 5 line widths for clarity (see Table 4.5 for their definitions).

CHAPTER 5

Non-steady Accretion in Protostars

5.1 Abstract

Observations indicate that mass accretion rates onto low-mass protostars are generally lower than the rates of infall to their disks; this suggests that much of the protostellar mass must be accreted during rare, short outbursts of rapid accretion. We explore when protostellar disk accretion is likely to be highly variable. While constant α disks can in principle adjust their accretion rates to match infall rates, protostellar disks are unlikely to have constant α . In particular we show that neither models with angular momentum transport due solely to the magnetorotational instability (MRI) nor gravitational instability (GI) are likely to transport disk mass at protostellar infall rates over the large range of radii needed to move infalling envelope material down to the central protostar. We show that the MRI and GI are likely to combine to produce outbursts of rapid accretion starting at a few AU. Our analysis is consistent with the time-dependent models of Armitage, Livio, & Pringle (2001) and agrees with our observational study of the outbursting object FU Ori. This chapter has been published in the paper: “Nonsteady Accretion in Protostars”, 2009, ApJ, 694, 1045 with Charles Gammie, and Lee Hartmann.

5.2 Introduction

The standard model of low-mass star formation posits the free-fall collapse of a protostellar molecular cloud core to a protostar plus disk during times of a few times 10^5 yr (e.g., Shu, Adams, & Lizano 1987), consistent with the statistics of protostellar objects in Taurus (Kenyon et al. 1990, 1994). To build up a star over these timescales

requires a time-averaged infall rate of order $2 \times 10^{-6} - 10^{-5} M_{\odot} \text{ yr}^{-1}$, rates typically used in calculations of protostellar properties at the end of accretion (Stahler 1988; Hartmann, Cassen, & Kenyon 1997). The numerical simulations of dynamic star cluster formation by Bate et al. (2003) found that stars and brown dwarfs formed in burst lasting $\sim 2 \times 10^4$ years, implying infall rates of $\sim 10^{-4}$ to $10^{-5} M_{\odot} \text{ yr}^{-1}$. However, the accretion luminosity implied by such infall rates is considerably higher than typical observed protostellar luminosities (Kenyon et al. 1990, 1994). This “luminosity problem” can be solved temporarily by piling up infalling matter in the circumstellar disk. Most of the mass must eventually be accreted onto the star, however. This requires major accretion events that are sufficiently short-lived that protostars are usually observed in quiescence.

This picture of highly time-dependent accretion is supported by observations. Individual knots in jets and Herbig-Haro objects, thought to be the result of outflows driven by accretion energy, argue for substantial disk variability (e.g., Bally, Reipurth, & Davis 2007). The FU Ori objects provide direct evidence for short episodes of rapid accretion in early stages of stellar evolution, with accretion rates of $10^{-4} M_{\odot} \text{ yr}^{-1}$ or more (Herbig 1977; Hartmann & Kenyon 1996), vastly larger than typical infall rates of $\lesssim 10^{-5} M_{\odot} \text{ yr}^{-1}$ for low-mass objects (e.g., Kenyon, Calvet, & Hartmann 1993; Furlan et al. 2008).

The mechanism driving FU Ori outbursts is not yet clear. A variety of models have been proposed: thermal instability (TI; Lin & Papaloizou 1985; Bell & Lin 1994); gravitational instability (GI; Vorobyov & Basu 2005, 2005); gravitational instability and activation of the magnetorotational instability (MRI; Armitage, Livio, & Pringle 2001; also Gammie 1999 and Book & Hartmann 2005); and even models in which planets act as a dam limiting downstream accretion onto the star (Clarke & Syer 1996; Lodato & Clarke 2004). Our recent analysis based on Spitzer IRS data (Zhu et al. 2007) led us to conclude that a pure TI model cannot work for FU Ori.

In view of the complexity of the problem and the physical uncertainties we adopt a schematic approach. We start with the (optimistic) assumption that protostellar accretion can be steady. We then show that the GI is likely to dominate in the outer

disk, while the MRI is likely to be important in the inner disk, and that mismatches between the GI and MRI result in non-steady accretion for expected protostellar infall rates.¹ Our analysis agrees with the results found in the time-dependent outburst model of Armitage et al. (2001), and is consistent with our empirical analysis of the outbursting system FU Ori (Zhu et al. 2007). Although our results depend on simplified treatments of the GI and MRI, the overall picture is insensitive to parameter choices. We predict that above a critical infall rate protostellar disk accretion can be (relatively) steady; observational confirmation would help constrain mass transport rates by the GI and the MRI.

5.3 Overview

A disk with viscosity² ν will evolve at cylindrical radius r on a timescale

$$t_\nu \sim r^2/\nu \tag{5.1}$$

If this is comparable to the timescales over which mass is being added to the disk, then in principle the disk can adjust to an approximate steady state with infall balanced by accretion. To fix ideas, we assume that the disk beyond 1 AU is mostly heated by irradiation from the central protostar of mass M_* , so that the temperature $T \propto r^{-1/2}$. For a fully viscous disk, we adopt the usual parametrization of the viscosity $\nu = \alpha c_s^2/\Omega$, where c_s is the sound speed (for a molecular gas) and Ω is the (roughly Keplerian) angular velocity. Then

$$t_\nu \sim \frac{r^2\Omega}{\alpha c_s^2} \sim 1.3 \times 10^3 \alpha_{-1}^{-1} M_1 T_{300}^{-1} R_{AU} yr, \tag{5.2}$$

where $\alpha_{-1} \equiv \alpha/0.1$ is the viscosity parameter $M_1 \equiv M_*/M_\odot$, $R_{AU} \equiv r/\text{AU}$, and T_{300} is the temperature at 1 AU in units of 300K. From this relation we see that a fully viscous

¹GI and MRI here means turbulent states initiated by gravitational or magnetic instabilities, respectively.

²We use “viscosity” as shorthand for internal, localized transport of angular momentum by turbulence. We will also make the nontrivial assumption that external torques (e.g. MHD winds) can be neglected.

disk might be able to keep up with mass infall over typical protostellar lifetimes of $\sim 10^5$ yr if the radius at which matter is being added satisfies $R_{AU} \lesssim 10^2 \alpha_{-1}$. In a layered disk picture, the viscosity may need to be modified such that $\nu = \alpha c_s h$, where h should be the thickness of the active layer instead of the midplane scale height. However, this difference is significant only if the temperatures differ at the active layer and the midplane, which they do not unless there is some midplane viscosity. In any case, Eq. (2) provides an upper limit to R_{AU} . Since typical observational estimates of infall radii are ~ 10 -100 AU (Kenyon et al. 1993), protostellar infall to a constant α disk is likely to pile up unless α is relatively large.

A more serious problem is that protostellar disks are unlikely to have constant α . The best studied mechanism for angular momentum transport in disks, turbulence driven by the MRI (e.g., Balbus & Hawley 1998), requires a minimum ionization fraction to couple the magnetic fields to the mostly neutral disk. As substantial regions of protostellar disks will generally be too cold for thermal (collisional) ionization, ionization by nonthermal processes becomes important. This led Gammie (1996) to suggest a layered model in which non-thermally ionized surface layers are magnetically coupled while the disk midplane remain inert. We modify Gammie's analysis by assuming that the heating of the outer disk is not determined by local viscous dissipation but by irradiation from the central protostar, as above.

The mass accretion rate in a layered disk is

$$\dot{M} = 6\pi r^{1/2} \frac{\partial}{\partial r} \left(2\Sigma_a \nu r^{1/2} \right), \quad (5.3)$$

where Σ_a is the (one-sided) surface density of the active layers. Taking $\Sigma_a = \text{constant}$, and assuming that the disk temperature $T \propto r^{-1/2}$,

$$\dot{M} = 5 \times 10^{-7} \Sigma_{100} T_{300} \alpha_{-1} R_{AU}, \quad (5.4)$$

where $\Sigma_{100} \equiv \Sigma_a / 100 \text{g cm}^{-2}$.

Our nominal value of $\alpha = 0.1$ may be reasonable for well-ionized regions, but it

may be an overestimate for the outer regions of T Tauri disks (see chapter 5.6.3). Also, the fiducial value for Σ_a is based upon Gammie's (1996) assumption of cosmic ray ionization, which may be an overestimate due to exclusion of cosmic rays by scattering and advection in the magnetized protostellar wind. X-rays provide a higher ionization rate near the surface of the disk but are attenuated more rapidly than cosmic rays (Glassgold & Igea 1999), yielding similar or smaller Σ_a . Both calculations assume that absorption of ions and electrons by grains is unimportant, which is only true if small dust is highly depleted in the active layer (e.g., Sano et al. 2000, also Ilgner & Nelson 2006a,b,c). In summary, it is likely that the estimate in equation (5.4) is an upper limit, and thus it appears unlikely that the MRI can transport mass at $r \sim$ a few AU at protostellar infall rates $2 \times 10^{-6} - 10^{-5} M_\odot \text{yr}^{-1}$. MRI transport resulting from non-thermal ionization might however move material adequately in response to infall at $r \gtrsim 10 - 100$ AU.

On the other hand, if some nonmagnetic angular momentum transport mechanism can get matter in to $r \lesssim 1$ AU, *thermal* ionization can occur and activate the MRI. A *minimum* disk temperature is given by the effective temperature generated solely by local energy dissipation

$$T > T_{eff} \sim 1600(M_1 \dot{M}_{-5})^{1/4} (R/0.2\text{AU})^{-3/4} \text{K}, \quad (5.5)$$

where $\dot{M}_{-5} \equiv \dot{M}/10^{-5} M_\odot \text{yr}^{-1}$. Radiative trapping in an optically thick disk will make internal temperatures even higher. If $T \gtrsim 1400$ K most of the silicate particles will evaporate, thus eliminating a major sink for current-carrying electrons. Therefore, high accretion rates can potentially activate the MRI on distance scales of order 1 AU or less.

If magnetic angular momentum transport is weak then mass will accumulate in the disk until the disk becomes gravitationally unstable, at which point gravitational torques can transfer mass inward. GI alone may result cause accretion outbursts (Vorobyov & Basu 2006, 2008), although the details of disk cooling are crucial in determining if such bursts actually occur due to pure GI. Moreover the GI may be

unable to drive accretion in the inner disk. GI sets in when the Toomre parameter

$$Q = \frac{c_s \kappa}{\pi G \Sigma} \simeq \frac{c_s \Omega}{\pi G \Sigma} \sim 1, \quad (5.6)$$

where we have set the epicyclic frequency $\kappa \simeq \Omega$, appropriate for a near-Keplerian disk. At small radius Ω and c_s will be large and therefore Σ must also be large if we are to have GI. Since rapid accretion causes significant internal heating (compared to heating by protostellar irradiation), large surface densities imply significant radiative trapping, raising internal disk temperatures above the effective temperature estimate above. Thus, when considering rapid mass transfer by GI, either in a quasi-steady state or in bursts, it is necessary to consider thermal MRI activation in the inner disk.

The above considerations suggest that the only way low-mass protostellar disks can accrete steadily during infall is if a smooth transition can be made from the GI operating on scales of $\sim 1 - 10$ AU to the thermally-activated MRI at smaller radii. To test this idea, we have constructed a series of steady-state disk models with realistic opacities. We compute both MRI and GI steady models and then investigate whether a smooth, steady, or quasi-steady transition is likely. Our results indicate that making the optimistic assumptions of steady GI and MRI accretion results in a contradiction for infall rates thought to be typical of low-mass protostars.

5.4 Methods

We compute steady disk models employing cylindrical coordinates (r, z) , treating radiative energy transport only in the vertical (z) direction. Energy conservation requires that

$$\sigma T_{eff}^4 = \frac{3GM_*\dot{M}}{8\pi\sigma r^3} \left(1 - \left(\frac{r_{in}}{r}\right)^{1/2}\right), \quad (5.7)$$

where M_* is the central star's mass and we have assumed that the disk is not so massive as to make its rotation significantly non-Keplerian. Balance between heating

by dissipation of turbulence and radiative cooling requires that

$$\frac{9}{4}\nu\rho_z\Omega^2 = \frac{d}{dz} \left(\frac{4\sigma}{3} \frac{dT^4}{d\tau} \right), \quad (5.8)$$

where

$$\nu = \alpha c_s^2 / \Omega \quad (5.9)$$

and

$$d\tau = \rho\kappa dz, \quad (5.10)$$

and κ is the Rosseland mean opacity. We have updated the fitting formulae provided by Bell & Lin (1994) for the Rosseland mean opacity to include more recent molecular opacities and an improved treatment of the pressure-dependence of dust sublimation (Zhu et al. 2007). The new fit and a comparison with the Bell & Lin (1994) opacity treatment is given in the Appendix 5.8.

Convection has not been included in our treatment. Lin & Papaloizou (1980) show that for a power law opacity ($\kappa = \kappa_0 T^\beta$), convection will occur when $\beta \gtrsim 1$. Our opacity calculations show that $\beta \gtrsim 1$ only occurs for $T \gtrsim 2000K$. As our steady-state analysis depends upon disk properties for $T \lesssim 1400 K$, the neglect of convection will not affect our results (see also Cassen 1993).

We ignore irradiation of the disk by the central star, as we are assuming high accretion rates and a low central protostellar luminosity. The diffusion approximation (equation 8.36) is adequate since the disk is optically thick at the high mass accretion rates ($\dot{M} > 10^{-7} M_\odot / yr$) we are interested in.

We also require hydrostatic equilibrium perpendicular to the disk plane,

$$\frac{dP_z}{dz} = \frac{GM_*\rho z}{r^3}, \quad (5.11)$$

and use the ideal gas equation of state

$$P = \frac{k}{\mu} \rho T. \quad (5.12)$$

Given a viscosity prescription, equations (5.6) - (6.34) can be solved iteratively for the vertical structure of the disk at each radius, resulting in self-consistent values of the surface density Σ , and the temperature at the disk midplane T_c .

In detail, we use a shooting method based on a Runge-Kutta integrator rather than a relaxation method (e.g., D'Alessio et al. 1998) to solve the two-point boundary value problem. Given α and \dot{M} at r , we fix $z = z_i$ and set $T = T_{eff}$ and $\tau = 2/3$ (this is adequate in the absence of significant protostellar irradiation), then integrate toward the midplane. We stop when the total radiative flux $= \sigma T_{eff}^4$ at $z = z_f$. In general $z_f \neq 0$; we alter the initial conditions and iterate until $z_f = 0$.

For an MRI active disk we fix $\alpha = \alpha_M$, assuming the disk is active through the entire column. We then check to see if thermal ionization is sufficient or if the surface density is low enough that non-thermal ionization is plausible. The exact temperatures above which MRI activity can be sustained are somewhat uncertain; here we assume the transition occurs for a central temperature of 1400 K, when the dust grains that can absorb ions and electrons and thus inactivate the MRI (e.g., Sano et al. 2000) are evaporated. We set $\alpha_M = 10^{-2}$ to 10^{-1} to span a reasonable range given current estimates (see chapter 5.6.3).

For simplicity we neglect the possible presence of an actively accreting, non-thermally-ionized layer. This omission will not affect our results at high accretion rates, for which the layered contribution is unimportant (equation 5.4); our approximation then breaks down for $\dot{M} \leq 10^{-6} M_\odot \text{yr}^{-1}$ for large values of Σ_a and α_M .

For the steady GI disk models α is not fixed. Instead we start with a large value of $\alpha = \alpha_Q$ and then vary α_Q until $Q = 2$. The adoption of the local treatment of GI energy dissipation requires some comment. Since gravity is a long-range force a local viscous description is not generally applicable (Balbus & Papaloizou 1999). However, as Gammie (2001) and Gammie & Johnson (2003) argue, a local treatment is adequate if $\lambda_c \equiv 2c_s^2/(G\Sigma) = 2\pi H Q \lesssim r$; here λ_c is the characteristic wavelength of the GI. More broadly, our main result involves order-of-magnitude arguments; that is, as long as inner disks must be quite massive to sustain GI transport, and as long as there is *some* local dissipation of energy as this transport and accretion occurs,

steady accretion will not occur for a significant range of infall rates. To change our conclusions dramatically, one would need to show that the GI causes rapid accretion through the inner disk without substantial local heating. We return to this issue in chapter 5.6.1.

5.5 Results

Figures 5.1 show steady disk results for a central star mass of $1M_{\odot}$ and accretion rates of 10^{-4} , 10^{-5} , 10^{-6} , and $10^{-7}M_{\odot}\text{yr}^{-1}$. Proceeding counterclockwise from upper left, the panels show the central disk temperature, α_Q , the one-sided surface density $\Sigma \equiv \int_0^{\infty} dz\rho$, and the viscous timescale r^2/ν as a function of radius. The solid curves show results for pure-GI models, while the dotted and dashed curves show results for $\alpha_M = 0.1$ and 0.01 , respectively.

The upper left panels show that the central temperatures rise more dramatically toward small radius in the GI models than in the MRI models. The GI models have higher temperatures because their higher surface densities lead to stronger radiative trapping. The GI solutions in these high-temperature regimes are unrealistic because they assume the MRI is absent, when it seems likely the MRI will in fact be active. These high temperature states do, however, suggest the possibility of thermal instability in the inner disk at high accretion rates, especially as the solutions near ~ 3000 K represent unstable equilibria (e.g., Bell & Lin 1994; chapter 5.6). We consider the MRI models to be inconsistent at $T \lesssim 1400$ K (collisional ionization would be absent) and when $\Sigma > \Sigma_a < 100\text{g cm}^{-2}$.

Can a smooth or steady transition between MRI and GI transport occur? The transition region would be the “plateau” in the temperature structure which occurs near $T \sim 1400$ K (see Figure 5.1). This plateau is a consequence of the thermostatic effects of dust opacity, which vanishes rapidly at slightly higher temperatures. A small increase in temperature past this critical temperature causes a large decrease in the disk opacity and thus the optical depth; this in turn reduces the radiative trapping and decreases the central temperature. Thus disk models tend to hover around the dust destruction temperature over roughly an order of magnitude in radius, with the

plateau occurring farther out in the disk for larger accretion rates. Since the plateau is connected with the evaporation of dust, it corresponds to a region where we might expect MRI activity.³

First consider the case $\dot{M} = 10^{-4}M_{\odot}\text{yr}^{-1}$ (upper left corner of Figure 5.1). The plateau region is very similar in extent for all models. More importantly, $\alpha_Q \sim 10^{-2}$ in this region, and so the surface densities of the GI and $\alpha_M = 10^{-2}$ models are nearly the same. This suggests that a steady disk solution is plausible with a transition from GI to MRI at a few AU for these parameters. Depending on the precise thermal activation temperature for the MRI, a smooth transition at around 10 AU might also occur for $\alpha_M = 0.1$.

Next consider the case $\dot{M} = 10^{-5}M_{\odot}\text{yr}^{-1}$ (upper right corner of Figure 5.1). Here $\alpha_Q \sim 10^{-3}$ in the plateau region, with resulting surface densities much higher than for either of the MRI cases. This discrepancy in α and Σ between the two solutions makes a steady disk unlikely. A small increase in surface density in a GI model near the transition region, resulting in increased heating and thus thermal activation of the MRI, would suddenly raise the effective transport rates by one or two orders of magnitude, depending upon α_M . The result would be an accretion outburst. This is qualitatively the same situation as proposed for outbursts in dwarf novae, where thermal instability is coupled to an increase in α from the initial low state to the high state (similar to what Bell & Lin 1994 adopted to obtain FU Ori outbursts). Our inference of non-steady accretion also agrees with the time-dependent one-dimensional models of Armitage et al. (2001) and of Gammie (1999) and Book & Hartmann (2005), as discussed further in chapter 5.6.

A similar situation holds at $10^{-6}M_{\odot}\text{yr}^{-1}$, although the evolutionary (viscous) timescales of the GI model are of order 10^5 yr, comparable to protostellar infall timescales. At this infall rate, the disk would only amass $\sim 0.1M_{\odot} = 0.1M_{*}$,

³There will be hysteresis because the dust size spectrum in a parcel of gas will depend on the parcel's thermal history. Heating the parcel destroys the dust and the accumulated effects of grain growth. Cooling it again would presumably condense dust with small mean size (and therefore a strong damping effects on MHD turbulence). The opacity would then vary strongly with time as the grains grow again. These effects are not considered here.

and so the disk might not need to transfer this mass into the star to avoid GI. At $10^{-7}M_{\odot}\text{yr}^{-1}$, evolutionary timescales become much longer than protostellar lifetimes, and become comparable to T Tauri lifetimes; disk material can pile up without generating GI transport and consequent thermal activation of the MRI. In addition, an $\alpha_M = 0.1$ value could result in a steady disk with surface densities low enough to be activated entirely by cosmic ray or X-ray ionization. This does not mean, however, that T Tauri disks do not have layered accretion, as the surface density distribution depends upon the history of mass transport.

The results of our calculations are summarized in the $\dot{M} - r$ plane in Figure 5.2. The solid curves farthest to the lower right, labeled R_Q , are the radii at which the pure GI-driven disk would have a central temperature of 1400 K (at which temperature the dust starts to sublimate), and thus activate the MRI. Moving up and left, the solid curve labeled R_M denotes the radii at which a pure MRI disk of the given α_M would have a central temperature of 1400 K. When these two curves are close together, or cross, α_Q and α_M are similar, making possible a smooth transition between GI and MRI and thus steady accretion. In the (shaded) regions between these two curves the viscosity parameters diverge, making non-steady accretion likely.

The radial regions at which we predict material will pile up, trigger the MRI, and result in rapid accretion lie in the shaded regions. The dotted curve shows R_Q and R_M where the disk has a central temperature of 1800 K (at which temperature all dust has sublimated). R_Q and R_M at 1800 K are smaller than they are at 1400 K because of the plateau region discussed above. Thus if the MRI trigger temperature is higher the outbursts are expected to be shorter because the outburst drains the smaller inner disk ($r < R_Q$) on the viscous timescale.

Figure 5.2 indicates that non-steady accretion, with potential outbursts, is predicted to occur for infall rates $\lesssim 10^{-5}M_{\odot}\text{yr}^{-1}$ for $\alpha_M = 0.01$ and $\lesssim 10^{-4}M_{\odot}\text{yr}^{-1}$ for $\alpha_M = 0.1$. As described above, for $\dot{M} < 10^{-6}M_{\odot}\text{yr}^{-1}$ outbursts are unlikely, simply because the transport timescales are too long. Outbursts are expected to be triggered at $r \sim 1 - 10$ AU for protostellar infall rates $\sim 10^{-5} - 10^{-6}M_{\odot}\text{yr}^{-1}$. These predictions are relatively insensitive to the precise temperature of MRI activation;

the dotted curves in Figure 5.2 show the results for a critical MRI temperature of 1400 K, which simply shift the regions of instability to slightly smaller radii without changing the qualitative results.

The other shaded band in Figure 5.2 denotes the region where thermal instability might occur. The two limits correspond to the two limiting values of the ‘‘S curve’’ (e.g., Faulkner, Lin, & Papaloizou 1983) at which transitions up to the high (rapid accretion) state and the low (slow accretion) state occur.

Figures 5.3-5.6 show results for central star masses of 0.3 and 0.05 M_{\odot} , respectively. The predictions are qualitatively similar to the case of the 1 M_{\odot} protostar, with the exception that thermal instability is less likely for the brown dwarf. This also implies generally unstable protostellar accretion for more massive protostars during the time that they are increasing substantially in mass.

Much of the overall behavior of our results derive from the general property that disk temperatures rise strongly toward smaller radii. For optically-thick viscous disks, the central temperatures are proportional to

$$T_c \sim T_{eff}\tau^{1/4} \propto \dot{M}^{1/4}\Gamma^{-3/4}(\kappa_R\Sigma)^{1/4}, \quad (5.13)$$

where τ is the vertical optical depth. Thus, even changes in surface density for differing values of α result in modest changes in radii where a specific temperature is achieved. Changing the mass accretion rate has a bigger effect, because $\Sigma \propto \dot{M}$.

5.6 Discussion

Our prediction of unsteady accretion during protostellar disk evolution is the result of the inefficiency of angular momentum transport of the two mechanisms considered here: the MRI, because of low ionization in the disk; and the GI, because it tends to be inefficient at small radii, where Ω and c_s will be large, forcing Σ to be large. To provide a feeling of just how large the surface density must be for $Q = 2$ in the inner disk, at accretion rates of 10^{-4} and $10^{-5}M_{\odot}\text{yr}^{-1}$ for the 1 M_{\odot} star the disk mass interior to 1 AU would have to be $\sim 0.6M_{\odot}$ and $\sim 0.5M_{\odot}$, respectively (Fig.

??), which are implausibly large. At some point the disk must accrete most of its mass into the star, forcing the inner disk temperatures to be very large and thermally activating the MRI, resulting in outburst of accretion. Here we consider whether the assumptions leading to this picture are reasonable, then discuss applications to outbursting systems.

5.6.1 Outbursts?

Our inference of cycles of outbursts of accretion - piling up of mass by GI transport, followed by thermal triggering of the MRI - was found in the models of Armitage et al. (2001), as well as in the calculations of Gammie (1999) and Book & Hartmann (2005). We have also found outbursting behavior in time-dependent two-dimensional disk models, to be reported in a subsequent chapter (chapter 6). Here we compare our results with those of Armitage et al. .

Figure ?? shows the results of our stability calculations for parameters and opacities adopted by Armitage et al. : a central star mass of $1M_{\odot}$, $\alpha_M = 0.01$, and an assumed triggering temperature for the MRI of 800 K. Armitage et al. found steady accretion at an infall rate of $\dot{M} = 3 \times 10^{-6}M_{\odot} \text{ yr}^{-1}$ but outbursting behavior at $1.5 \times 10^{-6}M_{\odot} \text{ yr}^{-1}$. This is reasonably consistent with our calculations; R_M and R_Q are close together at $\dot{M} = 3 \times 10^{-6}M_{\odot} \text{ yr}^{-1}$ and cross near $\dot{M} = 1 \times 10^{-5}M_{\odot} \text{ yr}^{-1}$, suggesting stable accretion somewhere in this range. Armitage et al. find that the MRI is triggered at about 2 AU, whereas our analysis (for $\dot{M} \sim 10^{-6}M_{\odot} \text{ yr}^{-1}$) would suggest a triggering radius of about 3 AU. Our ability to reproduce the results of Armitage et al. is adequate, considering that steady models do not precisely reproduce the behavior of time-dependent models, and that the form of α_Q used by Armitage et al. is somewhat different from ours, though it still retains the feature of non-negligible GI only for small Q .

Our finding of non-steady accretion is the result of assuming no other significant level of angular momentum transport that is not due to GI or thermal MRI. Terquem (2008) has shown that steady accretion is possible for a layered disk accreting at $\dot{M} = 10^{-8}M_{\odot}/\text{yr}$ if there is a non-zero (non-gravitational) viscosity in disk regions

below the surface active layers. Simulations have indicated that active layers can have an effect on non-magnetically active regions below, producing a Reynolds stress promoting accretion in the lower regions (Fleming & Stone, 2003; Turner & Sano, 2008; Ilgner & Nelson, 2008). We argue that this effect is unlikely to be important for the much higher accretion rates considered here, simply because the amount of mass transfer that needs to occur is much higher than what is sustainable by a non-thermally ionized surface layer. It seems implausible that a small amount of surface energy and turbulence generation can activate a very large amount of turbulence and energy dissipation in a much more massive region.

5.6.2 Local vs. non-local GI transport

We have adopted a local formalism for GI whereas it has non-local properties. Furthermore, we have adopted azimuthal symmetry in calculating the dissipation of energy whereas energy will be deposited in nonaxisymmetric spiral shocks. Neither of these assumptions is strictly correct.

Boley et al. (2006) performed a careful analysis of the torques in a three-dimensional model of a self-gravitating disk, including radiative transfer. They found that the mass transfer was dominated by global modes, but could be consistent with a locally-defined $\alpha(r, t)$. This result did not hold near the inner and outer edge of their disk, although this is not surprising as these regions were characterized by $Q > 2$ and thus one would not expect the GI to be operating. Boley et al. were unable to address whether energy dissipation was localized. Nevertheless it is difficult to imagine that gravitational instability could avoid some heating in regions with $Q \sim 1$, and only relatively small amounts of heating are required to activate the MRI at small radii.

The details of the disk temperature structure near 1 AU must be found by three dimensional simulations of the GI with realistic cooling. The analysis presented here suggests that pure GI in the absence of MRI tends to lead to very long transport times in the inner disk, as required by our low values of α_Q . This presents two potential technical problems for a numerical investigation: first, numerical viscosity must be smaller than α_Q to follow the evolution; and second, the disk must be followed over

long, evolutionary timescales. It will be challenging to follow the GI near 1 AU numerically.

5.6.3 What is α_M ?

The magnetic transport rate α_M is constrained by both observations and theory. A recent review of the observational evidence by King, Pringle, & Livio (2007) argues that α_M must be large, of the order 0.1-0.4, based in part on observations of dwarf novae and X-ray binaries where there is no question of gravitational instability. Our own analysis required $\alpha \sim 0.1$ in FU Ori (Zhu et al. 2007).

On the theoretical side the situation is murky. Early calculations (Hawley et al., 1996) suggested that for “shearing box” models with zero mean azimuthal and vertical field $\alpha_M \simeq 0.01$. Recent work (Fromang & Papaloizou, 2007), however, shows that α_M does not converge in the sense that $\alpha_M \rightarrow 0$ as the numerical resolution increases.

But are the zero mean field models relevant to astrophysical disks? Global disk simulations (Hirose et al., 2004; McKinney & Narayan, 2007; Beckwith et al., 2008), local disk simulations in which the mean field is allowed to evolve because of the boundary conditions (Brandenburg et al., 1995), and observations of the galactic disk (Vallee, 2004) all exhibit a “mean” azimuthal field when an average is taken over areas of $\gtrsim H^2$ in the plane of the disk. This suggests that the zero mean field local models are a singular case, and that mean azimuthal field models are most relevant to real disks (strong vertical fields would appear to be easily removed from disks according to the plausible phenomenological argument originally advanced by van Ballegoijen (1989)).

So what do numerical simulations tell us about disks with mean azimuthal field? Recent work shows that in this case the outcome depends on the magnetic Prandtl number $Pr_M \equiv \nu/\eta$ (Fromang et al., 2007; Lesur & Longaretti, 2007) ($\nu \equiv$ viscosity and $\eta \equiv$ resistivity) and that α_M is a monotonically increasing function of Pr_M . This intriguing result, and the fact that YSO disks have $Pr_M \ll 1$ throughout (although more dimensionless parameters are required to characterize YSO disks, where the Hall effect and ambipolar diffusion can also be important), might suggest that α_M

should be small. But the numerical evidence also shows that α_M depends on ν in the sense that the dependence on Pr_M weakens as ν decreases. In sum, the outcome is not known as ν drops toward astrophysically plausible values. Mean azimuthal field models with effective $Pr_M \sim 1$ Guan et al. (2009) are also not fully converged; they show that α_M *increases*, albeit slightly, as the resolution is increased. For a mean field with plasma $\beta = 400$ Guan et al. (2009) find $\alpha_M = 0.03$ at their highest resolution. In disks with an initial strong azimuthal magnetic field in equipartition with thermal pressure, Johansen & Levin (2008) find $\alpha = 0.1$ resulting from a combination of the Parker instability and an MRI-driven dynamo.

Very small α_M would pose a problem for T Tauri accretion. In the layered disk model, Gammie estimated the accretion rate to be

$$\dot{M} \sim 2 \times 10^{-8} \left(\frac{\alpha_M}{0.01} \right)^2 \left(\frac{\Sigma_a}{100 \text{g cm}^{-2}} \right)^3 M_\odot \text{yr}^{-1}, \quad (5.14)$$

where Σ_a is the surface density of the layer which is non-thermally ionized. Thus with $\alpha_M \lesssim 10^{-3}$ it would be difficult to explain typical T Tauri accretion rates.

On the other hand $\alpha_M \sim 0.1$ could cause the outer disks of T Tauri stars to expand to radii of 1000 AU or more in 1 Myr (Hartmann et al. 1998). There is no particular reason why the $\alpha_M \sim 0.1$ that we estimated for the thermally-ionized inner disk region in FU Ori should be the same as the effective α in the outer disks of T Tauri stars, which cannot be thermally ionized.

5.6.4 Protostellar accretion

Our models predict that most low-mass protostars will be accreting more slowly than matter is falling onto their disks. This is consistent with observational results, as outlined in the Introduction. The results of Armitage et al. (2001) suggested that steady accretion might be possible at $\sim 3 \times 10^{-6} M_\odot \text{yr}^{-1}$ and above (for $1 M_\odot$). We find a different result because we adopt a significantly higher temperature for thermal MRI activation, closer to that required for dust evaporation. This means that our MRI triggering occurs at smaller radii, where the GI is less effective. It does seem

likely that higher activation temperatures than the 800 K adopted by Armitage et al. are more plausible. Even if thermal ionization in the absence of dust is sufficient at around 1000 K in statistical equilibrium, ionization rates are so low that equilibrium is unlikely (e.g. Desch 1998). We also note that Armitage et al. were unable to obtain the high accretion rates and short outburst durations characteristic of FU Ori objects, but Book & Hartmann (2005) were able to reproduce the FU Ori characteristics better with a higher MRI activation temperature.

At infall rates $\gtrsim 10^{-4}M_{\odot}\text{yr}^{-1}$, our models predict (quasi-) steady accretion (also Armitage et al. 2001); but such high rates are not expected to last long, perhaps only during an initial rapid phase of infall (Foster & Chevalier 1993; Hartmann et al. 1994; Henriksen, Andre, & Bontemps 1997). Testing this prediction may be difficult as relatively few objects will be caught in this phase and they will likely be heavily embedded.

At lower infall rates, GI-driven accretion timescales are longer than evolutionary times and/or layered MRI turbulence may produce sufficient mass transport. Thus, we would not expect outbursts for Class II (T Tauri) stars.

5.6.5 FU Ori outbursts

In our radiative transfer modeling of the outbursting disk system FU Ori (Zhu et al. 2007), we found that to fit the *Spitzer Space Telescope* IRS spectrum the rapidly-accreting, hot inner disk must extend out to ~ 1 AU, inconsistent with a pure thermal instability model. In contrast, the results of this chapter suggest thermal MRI triggering can occur at a few AU, in much better agreement with observation.

Our recent analysis of the silicate emission features of FU Ori (Zhu et al. 2008) also suggests that the disk becomes dominated by irradiation rather than internal heating at distances of $\gtrsim 1$ AU, but this is consistent with the results of this chapter, as irradiation from the central disk can dominate local viscous dissipation if the disk is sufficiently flared.

We also found that the decay timescales of FU Ori suggest $\alpha_M \sim 10^{-1}$; large values of α_M are more likely to lead to outbursting behavior. High inner disk accretion rates

also make thermal instability more likely very close to the central star; the presence or absence of this instability may account for the difference in rise times seen in some FU Ori objects (Hartmann & Kenyon 1996).

5.7 Conclusions

Our study predicts that the disk accretion of low-mass protostars will generally be unsteady for typical infall rates. During the protostellar phase, GI is likely to dominate at radii beyond 1 AU but not at smaller radii; in contrast, rapid accretion should drive thermal activation of the MRI in the inner disk. Because of the differing transport rates comparable to typical infall values results in high inner disk temperatures sufficient to trigger the MRI. This is a general conclusion, though if the external disk accretion is driven by GI, the radius at which the MRI can be triggered thermally is much larger, because of the high surface density needed to produce a low value of Q . Furthermore, GI-driving in the inner disk results in a low value of α_Q , much lower than the expected α_M , for a wide range of \dot{M} . The feature of mass accumulation at low external α followed by a change to a high inner viscosity is similar to thermal instability models (and also Armitage et al. 2001). Thermal instabilities may also occur in the inner disk at very high accretion rates, enhancing the potential for non-steady protostellar accretion.

5.8 Appendix: Rosseland mean opacity

The Bell & Lin (1994) Rosseland mean opacity fit has been widely used to study high temperature accretion disks (CV objects, FU Ori, et al.) for more than a decade, with opacities generated almost two decades ago. Our understanding of opacity sources (especially dust and molecular line spectra) has improved both observationally and theoretically since then (Alexander & Ferguson, 1994; Ferguson et al., 2005; D’Alessio et al., 1998, 2001; Zhu et al., 2007).

We have generated Rosseland mean opacity assuming LTE for a wide range of temperature and pressure during our study of FU Orionis objects (Zhu et al., 2007; ?). The molecular, atomic, and ionized gas opacities have been calculated using the

Table 5.1 Fit to Zhu et al. (2007, 2008) opacity

$\log_{10} T$	$\log_{10} \kappa$	comments
$< 0.03 \log_{10} P + 3.12$	$0.738 \log_{10} T - 1.277$	grain opacity
$< 0.0281 \log_{10} P + 3.19$	$-42.98 \log_{10} T + 1.312 \log_{10} P + 135.1$	grain evaporation
$< 0.03 \log_{10} P + 3.28$	$4.063 \log_{10} T - 15.013$	water vapor
$< 0.00832 \log_{10} P + 3.41$	$-18.48 \log_{10} T + 0.676 \log_{10} P + 58.93$	
$< 0.015 \log_{10} P + 3.7$	$2.905 \log_{10} T + 0.498 \log_{10} P - 13.995$	molecular opacities
$< 0.04 \log_{10} P + 3.91$	$10.19 \log_{10} T + 0.382 \log_{10} P - 40.936$	H scattering
$< 0.28 \log_{10} P + 3.69$	$-3.36 \log_{10} T + 0.928 \log_{10} P + 12.026$	bound-free, free-free
else ^a	-0.48	electron scattering

^awith two additional condition to set the boundary: if $\log_{10} \kappa < 3.586 \log_{10} T - 16.85$ and $\log_{10} T < 4$, $\log_{10} \kappa = 3.586 \log_{10} T - 16.85$; if $\log_{10} T < 2.9$, $\log_{10} \kappa = 0.738 \log_{10} T - 1.277$

Opacity Distribution Function (ODF) method (Castelli & Kurucz, 2004; Sbordone et al., 2004; Castelli, 2005; Zhu et al., 2007) which is a statistical approach to handling line blanketing when millions of lines are present in a small wavelength range (Kurucz et al., 1974). The dust opacity was derived by the prescription in D’Alessio et al. (2001) (?). Our opacity has been used not only to study FU Orionis objects but also to fit the gas opacity for Herbig Ae star disks constrained by interferometric observations (Tannirkulam et al., 2008). The opacities are shown in Figure 5.9). Compared with Alexander & Ferguson (1994) or Zhu et al. (2007,2008), the Bell & Lin opacity lacks water vapor and TiO opacity around 2000 K and has a lower dust sublimation temperature.

We have made a piecewise power-law fit to the Zhu et al. (2007, 2008) opacity (analogous to the Bell & Lin fit) to enhance computational efficiency (Table 5.1; see also Figure 5.9). This speedup has been useful in performing the calculations of this chapter, and is essential for our forthcoming two-dimensional hydrodynamic simulations of FU Ori outbursts (Zhu, Hartmann, & Gammie 2009).

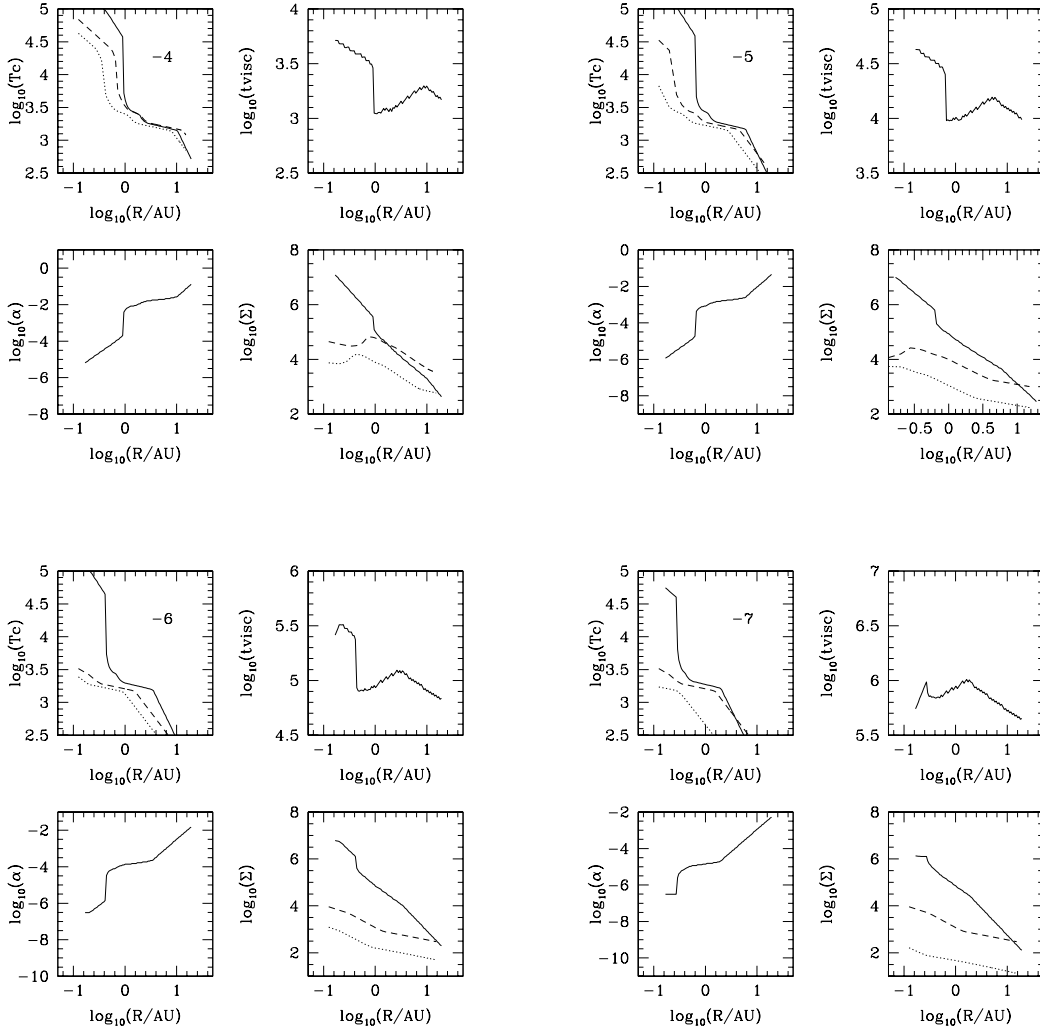


Figure 5.1 Steady-state disk calculations for four accretion rates - 10^{-4} , 10^{-5} , 10^{-6} , and $10^{-7} M_{\odot} \text{yr}^{-1}$, assuming a central star of mass $1 M_{\odot}$. The solid curves show solutions for GI-driven accretion, as described in the text. The dashed and dotted curves yield results for steady disk models with a constant $\alpha = 10^{-2}$ and 10^{-1} , respectively (see text)

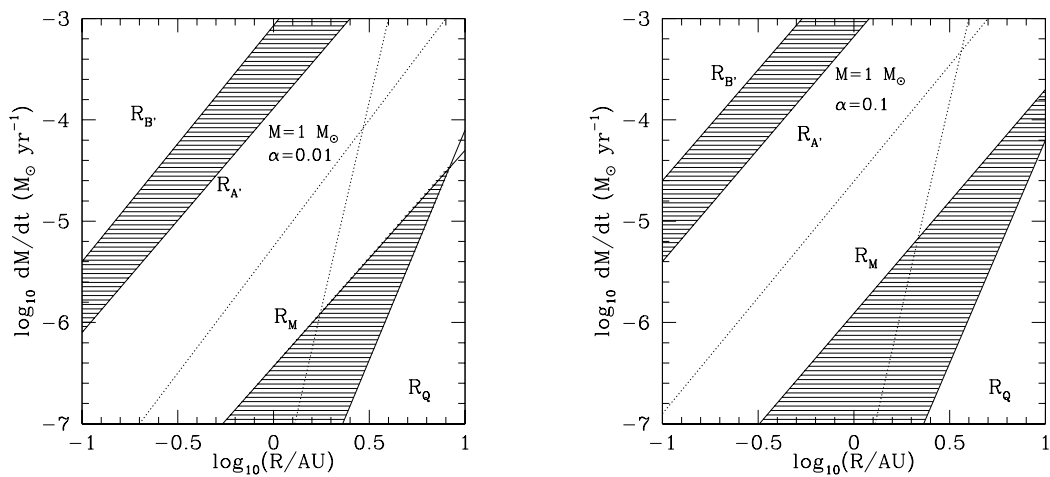


Figure 5.2 Unstable regions in the $r - \dot{M}$ plane for a $1M_{\odot}$ central star. The shaded region in the lower right shows where the central temperature of steady GI models exceeds an assumed MRI trigger temperature of 1400 K. The dotted curves show R_M and R_Q (the boundaries of the shaded region; see text for definition) for an MRI trigger temperature of 1800 K. The shaded region in the upper left shows the region subject to classical thermal instability.

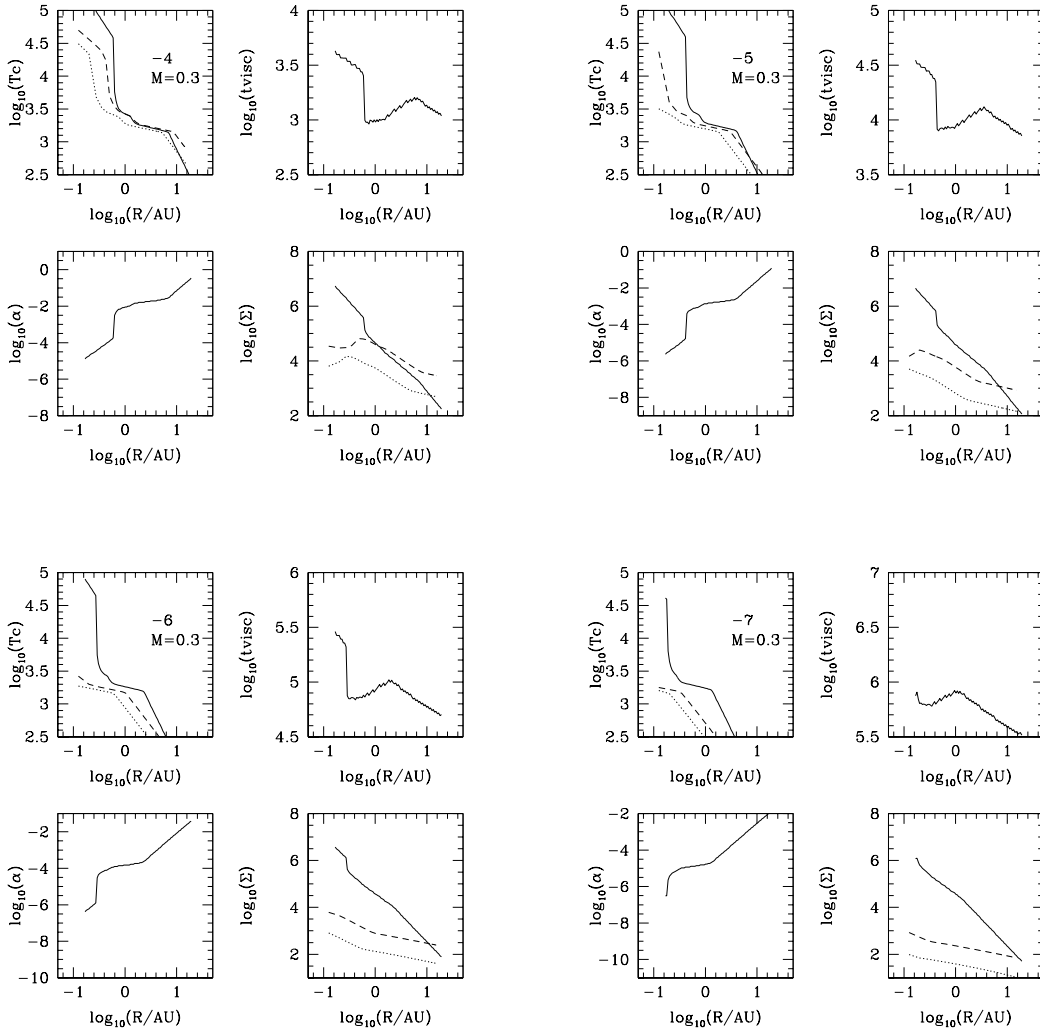


Figure 5.3 Same as in Figure 5.1 but for a central star mass of $0.3M_{\odot}$.

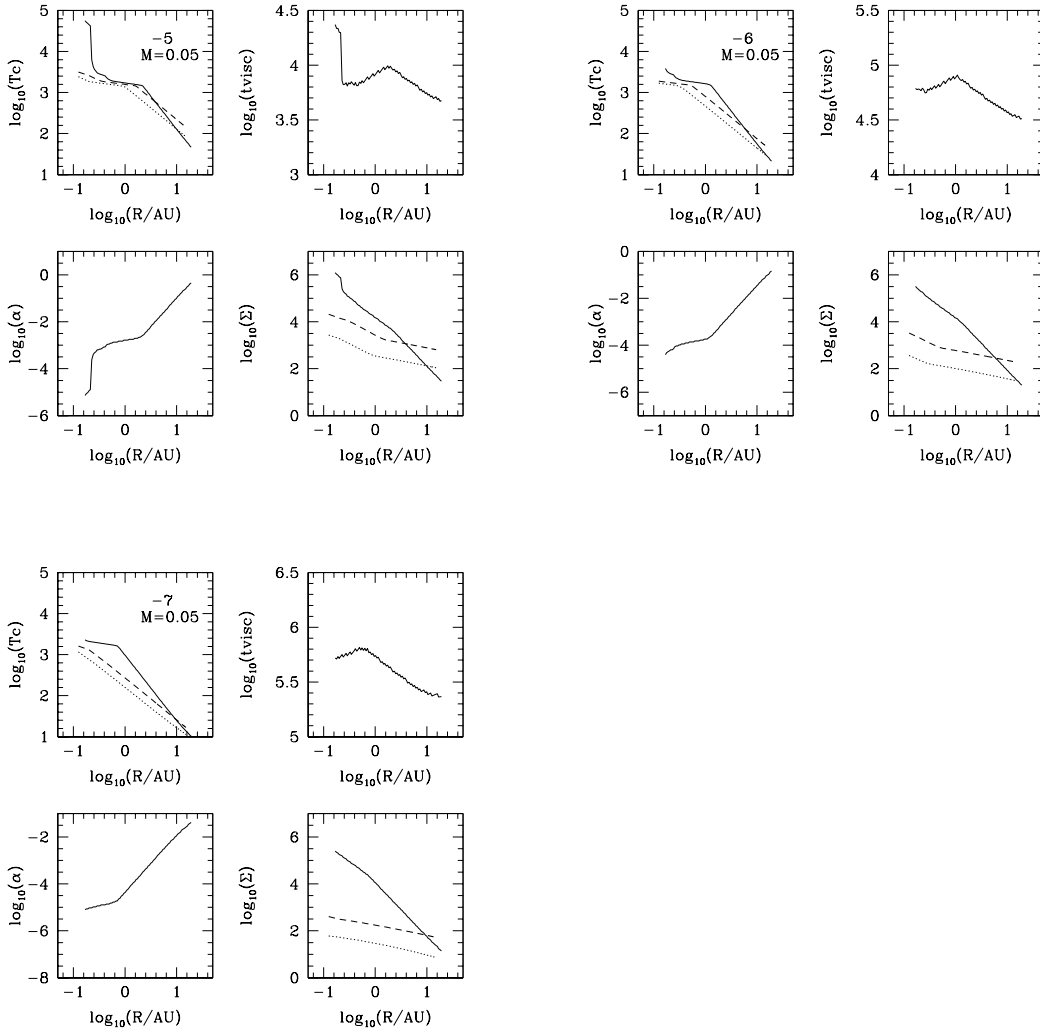


Figure 5.4 Same as in Figure 5.1 but for a central star mass of $0.05M_{\odot}$.

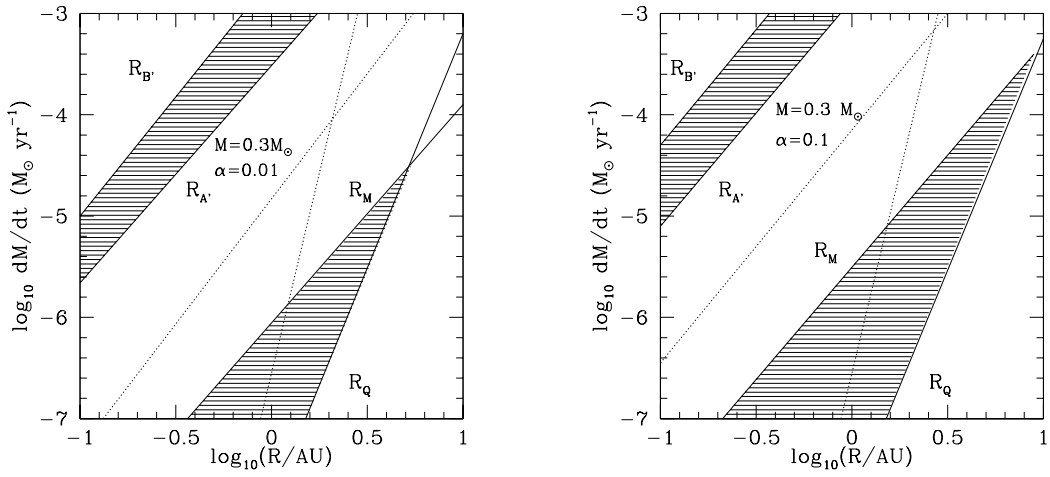


Figure 5.5 Same as figure 5.2 for $0.3M_{\odot}$ central star.

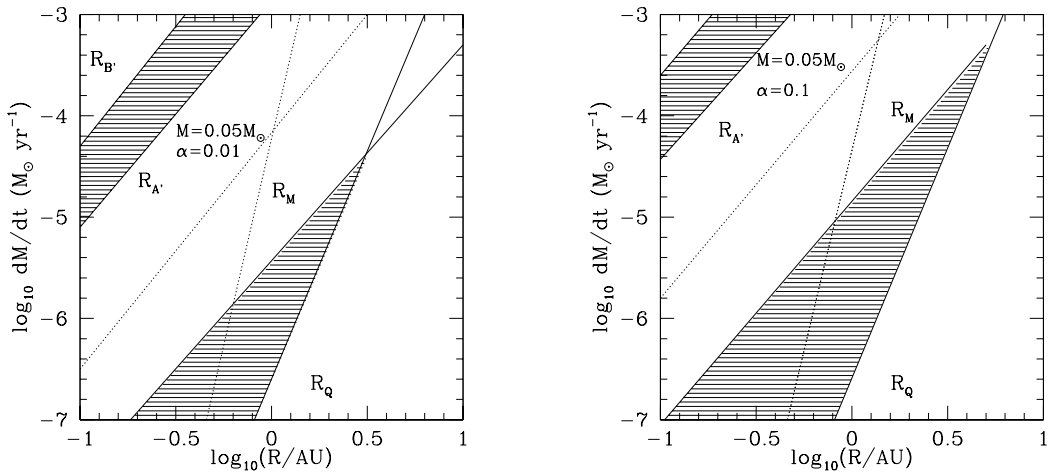


Figure 5.6 Same as Figure 5.2 for the $0.05M_{\odot}$ central star.

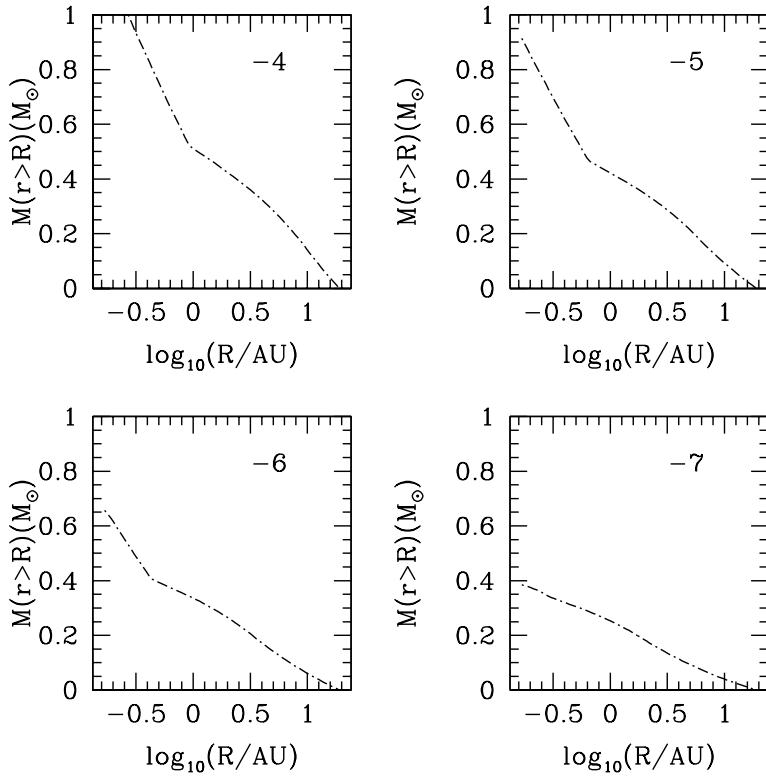


Figure 5.7 The mass of the disk integrated between radius R and the outer radius of 20 AU for steady-state $Q=2$ disks, at four accretion rates - 10^{-4} , 10^{-5} , 10^{-6} , and $10^{-7}M_{\odot} \text{ yr}^{-1}$. The central star mass is $1M_{\odot}$.

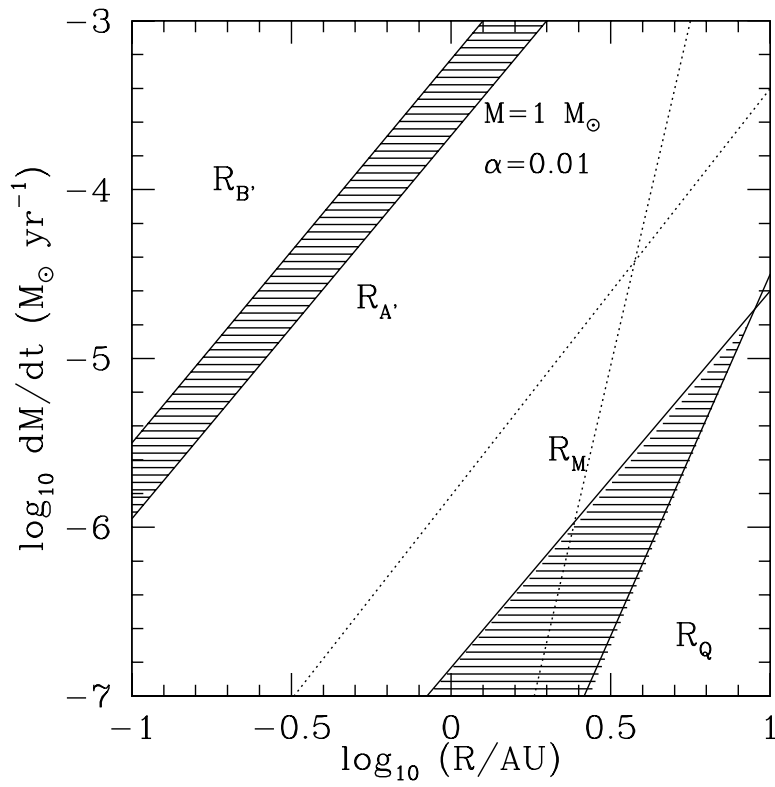


Figure 5.8 Same as Figure 5.2 for the parameters of Armitage et al. (2001) (see text)

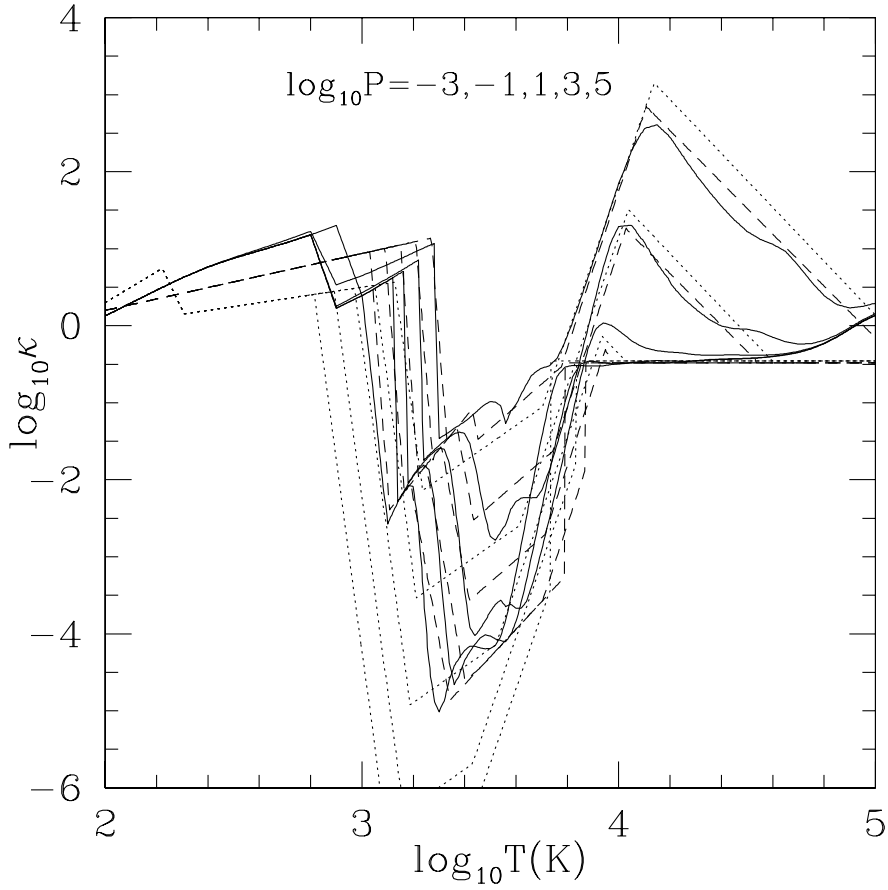


Figure 5.9 Rosseland mean opacities. The dotted lines show the Bell & Lin (1994) fit, the solid curves show the detailed opacity calculation of Zhu et al. (2007, 2008) (solid line), and the dashed lines show the simple fit to Zhu et al. opacities (Table 5.1).

CHAPTER 6

2-D simulations of FU Orionis disk outbursts

6.1 Abstract

We have developed time-dependent models of FU Ori accretion outbursts to explore the physical properties of protostellar disks. Our two-dimensional, axisymmetric models incorporate full vertical structure with a new treatment of the radiative boundary condition for the disk photosphere. We find that FU Ori-type outbursts can be explained by a slow accumulation of matter due to gravitational instability. Eventually this triggers the magnetorotational instability, which leads to rapid accretion. The thermal instability is triggered in the inner disk but this instability is not necessary for the outburst. An accurate disk vertical structure, including convection, is important for understanding the outburst behavior. Large convective eddies develop during the high state in the inner disk. The models are in agreement with Spitzer IRS spectra and also with peak accretion rates and decay timescales of observed outbursts, though some objects show faster rise timescale. We also propose that convection may account for the observed mild-supersonic turbulence and the short-timescale variations of FU Orionis objects. This chapter has been published in the paper: “Two-dimensional Simulations of FU Orionis Disk Outbursts”, 2009, ApJ, 701, 620 with Lee Hartmann, Charles Gammie, and Jonathan McKinney.

6.2 Introduction

The FU Orionis systems are a small but remarkable class of young stellar objects which undergo outbursts in optical light of 5 magnitudes or more (Herbig, 1977). While the rise times for outbursts are usually very short ($\sim 1 - 10$ yr), the decay

timescales range from decades to centuries. In outbursts, they exhibit F-G supergiant optical spectra and K-M supergiant near-infrared spectra dominated by deep CO overtone absorption. The FU Ori objects also show distinctive reflection nebulae, large infrared excesses of radiation, wavelength dependent spectral types, and “double-peaked” absorption line profiles (Hartmann & Kenyon, 1996). The accretion disk model for FU Ori objects proposed by Hartmann & Kenyon (1985, 1987a, 1987b) and Kenyon et al. (1988) can explain the peculiarities enumerated above in a straightforward manner.

Bell & Lin (1994) suggested that the thermal instability (TI) was responsible for FU Ori outbursts. To agree with the outburst mass accretion rates ($\sim 10^{-4}M_{\odot} \text{ yr}^{-1}$) and the outburst duration time ($\sim 100 \text{ yr}$), with the TI, Bell & Lin used very low viscosities both before and after the outbursts. However, this theory predicts that the outburst is confined to inner disk radii $\lesssim 0.1\text{AU}$, whereas Zhu et al. (2007, 2008) found that the high accretion rate region must extend to $\gtrsim 0.5\text{AU}$, based on modeling *Spitzer* IRS data.

Bonnell & Bastien (1992) suggested that a binary companion on an eccentric orbit could perturb the disk and cause repeated outbursts of accretion. However, in the case of FU Ori, no close companion is known, and no radial velocity variation has been detected (?). Vorobyov & Basu (2005, 2006) suggested that gravitational instabilities might produce the non-steady accretion, but could not carry out the calculation within the inner disk; thus the details of the accretion event are uncertain. ? suggested that planets might dam up disk material until a certain point, resulting in outbursts. This model also depends upon the TI and assumes a very low viscosity as in Bell & Lin (1994).

The rediscovery and application of the magnetorotational instability (MRI) to disk angular momentum transport have revolutionized our understanding of accretion in ionized disks (e.g. Balbus & Hawley 1998 and references therein). However, it was recognized that T Tauri disks are cold and thus likely to have such low ionization levels that the MRI cannot operate, at least in some regions of the disk (e.g., Reyes-Ruiz & Stepinski 1995). Gammie (1996) suggested that nonthermal ionization by

cosmic rays could lead to accretion in upper disk layers, with a "dead zone" in the midplane. This picture implies that accretion is not steady throughout the disk, and the mass should pile up at small radii.

Armitage et al. (2001) considered the time evolution of layered disks including angular momentum transport by the gravitational instability (GI). Within a certain range of mass addition by infall in the outer disk, they obtained episodic outbursts of accretion at $\sim 10^{-5}M_{\odot}\text{yr}^{-1}$ lasting $\sim 10^4$ yr. However, these outbursts are too weak and last too long compared with FU Ori outbursts. Gammie (1999) and Book & Hartmann (2004) were able to get outbursts more like FU Ori behavior with a different set of parameters. The Armitage, Gammie, Book & Hartmann models were vertically averaged and had schematic treatments of radial energy transport.

Earlier models of layered disk evolution have been based on phenomenological one-zone, or two-zone, models for the vertical structure of the disk. It is quite difficult to formulate these models in a consistent way, particularly near transition radii where the temperature or ionization structure of the disk changes sharply and radial energy transport may be important. To make progress it is necessary to consider more accurate vertical structure and more accurate energy transport models.

In this chapter, we construct two-dimensional (axisymmetric) layered disk models. We find that the MRI triggering by the GI can explain FU Ori-type outbursts if the MRI is thermally activated at $T_M \sim 1200$ K. In chapter 6.3, the equations and methods of the 2D models are introduced. In chapter 6.4, outburst behavior is described. In chapter 6.5, we focus on vertical structure and convection in the disk. We discuss implications of the 2D simulations compared with observations in chapter 6.6, and summarize our results in chapter 6.7.

6.3 Methods

In this work we are particularly interested in accurately modeling the flow of energy within the disk. A full treatment would numerically follow the development of MRI, GI, and radiative, convective, and chemical energy transport in 3D. As this is not yet possible, we use the phenomenological α -based viscosity to represent the angular

momentum transport by the MRI and GI and heating by dissipation of turbulence. An accurate treatment of energy balance (viscous heating and radiative cooling) is essential to understand the outburst, especially for the thermal instability. We implemented the realistic radiative cooling in the ZEUS-type code of McKinney& Gammie (2002).

To test our code, we set a hot region in an optically thick disk region and then let the radiative energy diffuse without evolving the hydrodynamics. The hot region expands nicely in a round shape in R-Z space with the correct flux. We have also tested the total energy conservation during our outburst simulations, finding that the energy deficit during outburst is only $< 1\%$ of the total energy radiated.

6.3.1 Viscous heating

The momentum equation and energy equations are

$$\rho \frac{Dv}{Dt} = -\nabla p - \rho \nabla \Psi - \nabla \cdot \Pi, \quad (6.1)$$

$$\rho \frac{D}{Dt} \left(\frac{e}{\rho} \right) = -p \nabla \cdot v + \Phi - \Lambda. \quad (6.2)$$

Here, as usual, $D/Dt \equiv \partial/\partial t + v \cdot \nabla$ is the Lagrangian time derivative, ρ is the mass density, v is the velocity, e is the internal energy density of the gas, p is the gas pressure, Ψ is the gravitational potential, and Λ is the radiative cooling rate. The dissipation function Φ is given by the product of the anomalous stress tensor Π with the rate-of-strain tensor ξ ,

$$\Phi = \Pi_{ij} \xi^{ij} \quad (6.3)$$

(sum over indices), where the anomalous stress tensor is the term-by-term product

$$\Pi_{ij} = 2\rho\nu_V \xi_{ij} S_{ij} \quad (6.4)$$

(no sum over indices), where S_{ij} is a symmetric matrix filled with 0 or 1 that serves as a switch for each component of the anomalous stress. In current simulations, we switched on all the component of the anomalous stress. It is not yet known whether

any prescription for Π_{ij} is a good approximation for modeling MHD turbulence. We set the viscosity coefficient to $\nu_V = \alpha(c_s^2/\Omega)\sin^3\theta$, which vanishes rapidly near the poles (McKinney& Gammie, 2002). α is the viscosity parameter and Ω is the angular velocity at radius R .

The equation of state is

$$p = (\gamma - 1) e. \quad (6.5)$$

and the sound speed is

$$c_s^2 = \gamma \frac{k_B T}{\mu} \quad (6.6)$$

where γ and μ are the adiabatic index and the mean molecular weight. We assume $\gamma = 5/3$ and $\mu = 2.4M_P$ where M_P is the mass of one proton. The adiabatic index and mean molecular weight will change at different temperatures and pressure (especially during outburst when the disk is fully ionized) and a fully self-consistent treatment would use a tabulated equation of state, which will be studied in future.

6.3.2 Radiative cooling

In an accretion disk, radiation is the main cooling mechanism, and radiation energy and pressure can affect the disk dynamics. Numerically, there are two different approaches to treat the radiative transport in an accretion disk. One is to solve the full radiative transfer equation

$$\rho \frac{D}{Dt} \left(\frac{E}{\rho} \right) = -\nabla \cdot F - \nabla v : P + 4\pi\kappa_P B - c\kappa_E E \quad (6.7)$$

with the material energy equation:

$$\rho \frac{D}{Dt} \left(\frac{e}{\rho} \right) = -p\nabla \cdot v - 4\pi\kappa_P B + c\kappa_E E \quad (6.8)$$

in both the optically thick and thin regions by an implicit method (Turner & Stone, 2001; Wünsch et al., 2005; Hirose et al., 2006). Here, as above, ρ, e, v , and p are the gas mass density, energy density, velocity and scalar isotropic pressure respectively, while E, F , and P are the total radiation energy density, momentum density and

pressure tensor, respectively. κ_P and κ_E are Planck mean and energy mean absorption coefficients. An implicit method is required because of the extremely short time step needed by the explicit method (grid size over the speed of light), but the implicit method is time consuming, requiring solution of an $N^2 \times N^2$ matrix equation at each timestep.

A second, less accurate but less costly, approach is to add a radiative source (heating/cooling) term in the energy equation, use the diffusion approximation in the optically thick region, and use an approximation to treat the optically thin region (Boss, 2002; Boley et al., 2006; ?). When the radiation pressure is negligible, as in the case for protostellar disks, and the radiation field is nearly in equilibrium ($D(E/\rho)/Dt = 0$), equations 6.7 and 6.8 become

$$\rho \frac{D}{Dt} \left(\frac{e}{\rho} \right) = -p \nabla \cdot v - \Lambda \quad (6.9)$$

where $\Lambda = \nabla \cdot F$ and F is the radiative flux.

We examine the justification for ignoring the advection term (within the term on the left side of Eq. 6.7) and the term describing work done by radiation on the gas (second term of the right side of Eq. 6.7) following the criterion given by Mihalas & Weibel Mihalas (1984). If in one system, L is the characteristic size, u is the characteristic velocity and τ is the optical depth of L , the terms describing the advection and the work done by the radiation can be ignored if $\tau \gg 1$ and $\tau \times u/c \ll 1$, which is called static diffusion limit. This criterion can be simply understood as follows:

The timescale for radiation to propagate across a region of length L and mean optical depth τ is of order

$$t_E \sim L\tau/c. \quad (6.10)$$

For comparison, the material crossing time of this region is

$$t_u \sim L/u, \quad (6.11)$$

so that the ratio of these two timescales is

$$\frac{t_E}{t_u} \sim \frac{u}{c} \tau. \quad (6.12)$$

If this ratio is far less than one, the region is in radiative quasi-equilibrium before the material carrying radiation energy away so that the energy emitted and absorbed equals to the diffusion term (Eq. 6.7). In a 3-D accretion disk, this typical velocity is the Keplerian velocity. However in our 2-D axisymmetric simulation, this velocity is just the mean radial velocity of the gas. Thus, t_u is close to the viscous time which is longer than the time for sound to cross a scale height H by a factor of order $\alpha^{-1}(R/H)^2$.

In our simulations, even at the maximum temperatures achieved in the innermost disk, $u/c \lesssim 10^{-5}$ (chapter 6.5) and so the approximation of radiative equilibrium should be valid except at very large optical depths. It turns out that, during the outburst, vertical Rosseland mean optical depths $\sim 10^4$ in the innermost disk. Thus our approximation is justified, though it may break down at smaller radii than we have considered here.

In detail, the radiative transfer in the optically thick disk, defined as the region where $\tau > \tau_{thick}$, is given in the diffusion approximation by

$$\Lambda = \nabla \cdot F, \quad (6.13)$$

where the flux F is

$$F = -\frac{16\sigma\beta T^3}{\chi_R\rho} \nabla T, \quad (6.14)$$

and β is the flux limiter,

$$\beta = \frac{2+y}{6+3y+y^2}, \quad (6.15)$$

with

$$y = \frac{4}{\chi_R\rho T} |\nabla T|. \quad (6.16)$$

where χ_R is the Rosseland mean of the absorption coefficient.

The optically thin region is more complicated. In this region we restrict our considerations to radiative transport in the vertical direction only. We have developed two methods to solve this problem in collaboration with members of the Indiana disk group (D. Durisen, K. Cai, & A. Boley, 2008, personal communication). The first method considers the cooling rate of every cell in the optically thin region can be written as:

$$\Lambda = \rho\kappa_P(T) \left(4\sigma T^4 - 4\pi J(Z) \right) - \rho\kappa_P(T_e)\sigma T_e^4 e^{-\tau_e(Z)} \quad (6.17)$$

where $\kappa_P(T)$ is the Planck mean opacity at the temperature T , T_e is the temperature of the envelope, and also $J(Z)$ and $\tau_e(Z)$ are the mean intensity and the optical depth of the envelop at height Z in the disk atmosphere. The first term is the energy emitted by the cell, while the second and third terms are the energy absorbed from the optically thick region and from the envelope. Using the two stream approximation,

$$J(Z) = \frac{1}{4\pi} \int I d\Omega = \frac{1}{4\pi} (2\pi I_+ + 2\pi I_-). \quad (6.18)$$

This treatment assumes flux conservation and thus ignores energy dissipation in the atmosphere. The net flux F_b from the disk photosphere is then

$$F_b = \int I \mu d\Omega = \pi (I_+ - I_-), \quad (6.19)$$

where μ is the cosine of the angle measured from the vertical. Thus

$$J(Z) = \frac{1}{2} (I_+ + I_-) = \frac{F_b}{2\pi} + I_-(Z). \quad (6.20)$$

F_b is approximately

$$F_b = \frac{4\sigma (T_b^4 - T_e^4)}{3(\tau_b + 2/3)} \quad (6.21)$$

where T_e is a term which accounts for the external irradiation (see equation (10) in Boley et al. (2006)). T_b and τ_b are the temperature and optical depth of the first optically thick cell right below the photosphere (again, see Boley et al. (2006)). Finally,

we must set $I_-(Z)$ to obtain a closed expression for Λ :

$$I_-(Z) = \int_Z^\infty \rho\kappa_P \frac{\sigma T(z)^4}{\pi} dz + \frac{\sigma T_{env}^4 e^{-\tau_{en}(Z)}}{\pi}. \quad (6.22)$$

which is the intensity from the optically thin region above height Z . Theoretically, the first term should also have $e^{-\tau}$. However, since we only consider the optically thin region here, we ignore it to simplify the calculation and save computational time.

The second method is much simpler but limited to this particular problem with no irradiation. As we do not consider irradiation, we can use the usual gray atmosphere result. Without the third term in equation (6.17), we have

$$\Lambda = \rho\kappa_P(T) \left(4\sigma T^4 - 4\pi J(Z) \right), \quad (6.23)$$

and in a gray case

$$J = \frac{\sigma}{\pi} T^4(Z) = \frac{\sigma}{\pi} \left(\frac{3}{4} T_{eff}^4 \left(\tau + \frac{2}{3} \right) \right), \quad (6.24)$$

where T_{eff} is given by the boundary flux $F_b = \sigma T_{eff}^4$ as equation 6.21. In detail, counting θ grid cell index i as increasing with increasing θ and τ , we set the first grid with $\tau(R, \theta_i) > 3$ as the boundary grid and $\tau_b = \tau(R, \theta_i)$. Then we derive the effective temperature (or equivalently, the boundary flux) using the gray approximation

$$F_b = \sigma T_{eff}^4 = \frac{4\sigma T_b^4}{3(\tau_b + 2/3)}. \quad (6.25)$$

With T_{eff} , we use equation 6.24 to set the temperatures of all cells at $R, \theta < \theta_i$, and use the diffusion equation (6.14) at all $r, \theta \geq \theta_i$. This way of matching the "optically thin" (gray) atmosphere to the "optically thick" (diffusion equation) interior removes the temperature jump seen at the boundary between the two treatments seen in the simulations of ?.

Both methods give similar results if there is no irradiation (see chapter 6.8 Appendix A) - basically, they are the same except for the assumed directionality of the radiation field. We use the second method in this chapter, although the first method

is of interest for cases in which external irradiation is important.

We have adopted the Bell & Lin (1994) opacity fits to facilitate comparison with previous calculations (Bell & Lin, 1994; Armitage et al., 2001); subsequent improvements in low-temperature molecular opacities will modify results at low temperatures (Zhu et al 2009), but should not substantially affect the outburst behavior driven at higher temperatures.

6.3.3 Angular Momentum Transport

To complete the model we need a prescription for the dimensionless viscosity α . The key physics we want to capture is the dependence of the MRI and GI transport on position in the disk (see, e.g., Miller & Stone 2000 for MRI activity as a function of height in the disk).

For the MRI, we set $\alpha_M = 0.1$ when $T > T_M$, where T_M is a critical temperature (typically 1200K) where thermal ionization makes the disk conductive enough to sustain the MRI. ¹ In addition we calculate $\Sigma_+ = \int_0^\theta R d\theta' \rho$ (and in models where the disk is not assumed to be symmetric about the midplane, $\Sigma_- = \int_\theta^\pi R d\theta' \rho$) and set $\alpha_M = 0.1$ if Σ_+ or $\Sigma_- < \Sigma_{crit}$, where Σ_{crit} is the maximum surface density of the MRI active layer on one side of the disk (In our current model we assume $\Sigma_{crit}=50$ g cm⁻²). Otherwise the disk is magnetically 'dead' and $\alpha_M = 0$. Also to avoid the strong MRI viscous heating at the disk's upper photosphere with very low density, we set $\alpha = 0$ for the region with $\tau < 10^{-3}$.

The value of α_M predicted by theory is uncertain, with widely-varying estimates depending upon mean magnetic fluxes, magnetic Prandtl numbers, and other assumptions (Guan et al. 2008, Johansen & Levin 2008, Fromang et al. 2007). Given these uncertainties, observational constraints take on special significance. A recent review of the observational evidence by King, Pringle, & Livio (2007) argues that α_M must be large, of the order 0.1-0.4, based in part on observations of dwarf novae and X-ray binaries where there is no question of gravitational instability. Our empirical study

¹3D MHD simulations suggest that the energy dissipation rate per unit mass is slightly higher at $\sim 2H$, which means α is not constant with height

of FU Ori, where we were able to constrain the radial extent of the high accretion state, implies values of $\alpha \sim 0.1$. (Zhu et al. 2007).

For the GI, we calculate the Toomre Q parameter

$$Q = \frac{c_s \Omega}{\pi G \Sigma}. \quad (6.26)$$

When $Q \sim 1$ the disk is gravitationally unstable. Full global models (Boley et al., 2006) and physical arguments (Gammie 2001) suggest that if the disk is sufficiently thin angular momentum transport by GI is localized and can be crudely described by an equivalent α . We set

$$\alpha_Q(R, \theta) = e^{-Q(R)^2}, \quad (6.27)$$

which is independent of θ . This has the sensible effect of turning on GI driven angular momentum transport when $Q < 2$ and turning off GI driven angular momentum transport when Q is large. In regions with both GI and MRI we set $\alpha = \alpha_M$ (in these regions $\alpha_M \gg \alpha_Q$).

The maximum α_Q is < 0.1 during the simulations, consistent with our assumption that fragmentation does not occur. Our prescription for α_Q on Q is heuristic and other forms are plausible. Gammie (2001) and Lodato & Rice (2004, 2005) found that the amplitude of GI depends on the cooling rate in addition to Q ; and Balbus & Papaloizou (1999) argued that the angular momentum flux carried by GI is a global effect and the local viscosity description can only be valid near the corotation radius. However, using self-consistent cooling, Boley et al. 2006 showed that the α_{GI} agrees with the Gammie description very well, which assumes that the GI viscous heating is locally balanced by the cooling. Recent smooth particle hydrodynamics SPH simulations by Cossins et al. (2009) also showed that GI disks with tightly wound spiral arms can be approximated by a local treatment.

6.4 2D results

We use spherical polar coordinates and assume axisymmetry in all our simulations. To sample both the inner disk and the outer disk, we use a logarithmic radial grid

(radial grids are uniform in $\log(R-R_{in})$) from 0.06-40 AU and a uniform θ grid in $(0.5 \pm 0.15)\pi$. This gives adequate radial resolution for both the inner and outer disk, and spans a large enough range in θ to include the optically thick region of the disk. Parameters for all the 2D simulations are listed in Table 6.1.

6.4.1 Initial and Boundary Conditions

All our disk models begin with the initial temperature distribution

$$T(R, \theta) = 300(R/AU)^{-1/2}K, \quad (6.28)$$

and $\rho = \Sigma(R)/(H2\pi^{1/2}) \exp(-R^2\theta^2/(2H^2))$, $H \equiv c_s/\Omega$ from 0.4-100 AU², so the disk is approximately in dynamical equilibrium. We set $\Sigma(R)$ using a $\dot{M}=10^{-5} M_\odot/\text{yr}$ constant α ($\alpha = 0.1$) one-zone accretion disk model (see Equation 3 in Whitney et al. (2003)). Although this is not an exact steady-state model, the disk relaxes rapidly at the beginning of the simulation.

We apply outflow boundary conditions (Stone & Norman, 1992) to all boundaries. In some simulations the disk is assumed to be symmetric about the midplane to reduce computational cost; for these half-disk simulations we use a reflecting boundary condition (Stone & Norman, 1992) at the midplane. The inner boundary is set to either 0.06 AU, 0.1 AU, or 0.3 AU to examine how different inner radii affect disk evolution. These parameters are listed in Table 6.1.

We follow the evolution of the disk for 10^5 years. Typically several outbursts occur during the simulation. After the first outburst, the subsequent outbursts are similar and do not depend on the initial condition. Thus, we use the disk density and temperature distribution after the first two outbursts as the new initial condition to study the third outburst for various 1D and 2D models. The disk mass for this initial condition is $\sim 0.5 M_\odot$.

²At this stage we use larger radii and lower grid resolution than Table 6.1 to make the disk quickly evolve to the state just before the outburst is triggered. When the outburst is about to be triggered, we interpolate the grid to get a higher resolution grid from 0.06-40 AU.

6.4.2 Outbursts

In the protostellar phase, the disk is unlikely to transport mass steadily from ~ 100 AU all the way to the star at an accretion rate matching the mass infall rate $10^{-6} - 10^{-4} M_{\odot} \text{ yr}^{-1}$ from the envelope to the outer disk. The outburst sequence we find here is qualitatively similar to that found by Armitage et al. (2001), Gammie (1999), and Book & Hartmann (2001). Mass added to the outer disk moves inwards due to GI, but piles up in the inner disk as GI becomes less effective at small R. Eventually, the large Σ and energy dissipation leads to enough thermal ionization to trigger the MRI. Then the inner disk accretes at a much higher mass accretion rate, which resembles FU Orionis-type outbursts. After the inner disk has drained out and becomes too cold to sustain the MRI, the disk returns to the low state. During the low state mass continuously accretes from large radius (or from an infalling envelope) causing matter to pile up at the radius where GI becomes ineffective yet again, leading to another outburst.

Figures 6.1- 6.5 show the disk temperature and density structure at four consecutive stages of the outburst for our fiducial model. Figure 6.1 is shown in R-Z coordinate while figures 6.2 and 6.3 are shown in $\log_{10}R-\theta$ coordinates (R from 0.06 to 40 AU, θ from 1.1 to $\pi/2$). Since the GI, MRI and TI are taking place at quite different radii, most of our plots are in $\log_{10}R-\theta$ coordinates so that all of them can be seen in one figure, although it is less intuitive than R-Z coordinates. The black solid curves plotted on top of the color contours delimit regions of differing α . Regions above the top solid curve limit the low- ρ photosphere with $\tau < 10^{-3}$ to $\alpha = 0$. Between the top and next lower solid curve lies the MRI-active layer with $\Sigma_{+} < 50 \text{ g cm}^{-1}$ and $\alpha = \alpha_M = 0.1$. Regions below the two solid curves constitute the "dead zone" with only α_Q if any. The vertical dashed lines at large radii represent $\alpha_Q = 0.025$.

Panel (a) of Figures 6.1-6.3 show the disk temperature structure before the outburst. The disk is too cool to sustain any MRI except in the active layer. The contours in Figures 6.1-6.3 show the outer disk ($R > 1 \text{ AU}$) is geometrically thick, with a ratio of vertical scale height H to radius $H/R \sim 0.2$, and massive, while the inner disk is thin with a low surface density. The inner disk is stable against GI and cannot

transport mass effectively. The mass coming from the GI driven outer disk piles up at several AU. The GI thus gradually becomes stronger at several AU and the disk heats up.

The disk midplane temperature at 2 AU eventually reaches the MRI trigger temperature ($T_M \sim 1200$ K) and MRI driven angular momentum transport turns on. Panel (b) of Figures 6.1-6.3 show the stage when the thermal-MRI is triggered at the midplane around 2AU. The thermal-MRI active region are outlined by the semicircular α contour around 2 AU in these figures. After the MRI is activated, α increases from $\alpha_Q(2AU) \sim 0.01$ to $\alpha_M = 0.1$, which leads to a higher mass accretion rate. Afterwards, the MRI active region expands both vertically and radially until the whole inner disk becomes fully MRI active.

As more and more mass is transferred to the inner disk, the temperature continues to rise. At $T \sim 4000$ K the disk becomes thermally unstable and T rises rapidly to $\sim 2 \times 10^4$ K. Panel (c) of Figures 6.1-6.3 show the moment the TI is initiated in the innermost disk. With the temperature leap, the pressure of the TI active region also increases significantly. Thus the TI active region expands and compresses the TI non-active region, leading to a lower density of the TI active region than nonactive region (lower density at midplane around 0.1 AU in panel (c) of Fig. 6.3).

Panel (d) of Figures 6.1-6.3 show that after the TI is triggered in the innermost disk, the TI front travels outwards to ~ 0.3 AU until the entire inner disk is in a "high state." The hot inner disk ($R < 0.2$ AU) is puffed up to $H/R \sim 0.15$. The mass accretion rate is $2 \times 10^{-4} M_\odot \text{ yr}^{-1}$ at this stage. The central temperature has a sharp drop at 0.3 AU, beyond which the disk is in a thermally stable state at $T \simeq 3000$ K. Details of the TI are discussed in chapter 6.9 Appendix B. At this transition from the high to low state around 0.2AU, some temperature and density fluctuations are present, which results from convection. We will discuss convection in detail in chapter 6.5.

The TI high state ($T_c \sim 10,000$ K, panel (d) of Fig. 6.1-6.3) lasts for $\sim 10^2$ years, draining the inner disk ($R < 0.5$ AU) until it is not massive and hot enough to sustain the TI high state; it then returns to the TI low state. The inner disk may temporarily

return to the high state due to MRI-driven mass inflow but eventually mass is drained from the MRI active region, it becomes MRI inactive, and the disk returns to the state shown in panel (a).

Figure 6.4 shows the vertically integrated surface density at the above stages. Before the outburst, the surface density peaks around 2 AU (long-dash curve); this radius divides the inner, GI stable disk from the outer GI unstable disk. Once the MRI is triggered at 2 AU, it transports mass into the inner disk effectively. At the moment the TI is triggered (dotted curve), the surface density of the inner disk is already one order of magnitude higher than that before the MRI is triggered. During the TI fully active stage (solid curve), the relatively low surface density region within 0.3 AU corresponds to the TI high stage with $T_{c,i} \sim 10^4$ K. The density fluctuations around 0.3 AU result from convection at the transition between the TI high and low states as seen in Figures 6.1 and 6.3. We discuss the details of convection in chapter 6.4.3

Figure 6.5 shows the effective temperature distributions at the same stages as above. When the MRI is triggered, the effective temperature increases dramatically with the increasing accretion rate. Eventually the whole inner disk almost accretes at a constant rate and the effective temperature is similar to that of a steady accretion solution at $M\dot{M} = 1.8 \times 10^{-4} M_{\odot}^2 yr^{-1}$ (smooth solid curve). The discrepancy at small radii may be caused by the outflow inner boundary condition of the 2D simulation, which means all the velocity gradients relative to the coordinates (R, θ) are 0.

6.4.3 Resolution Study

Figure 6.6 shows the mass accretion rates during an outburst for models with four different numerical resolutions. In general the vertical linear resolution must be higher than the radial linear resolution to resolve the vertical structure of the disk, particularly the exponential density drop in the disk photosphere. With $N_R = 320$ grid cells and $N_{\theta} = 112$ grid cells, every grid is 5 times longer radially than vertically.

The simulations have a similar maximum mass accretion rate and outburst timescale as long as $N_R \gtrsim 100$ grid cells. This suggests that the models are, crudely speaking,

converged.

Notice that models with $N_R \geq 324$ grid cells have complex substructure during outburst. This is caused by convection in the TI high state region. Lower resolution models barely resolve the convective eddies and thus damp away this substructure.

6.4.4 Boundary effects

We have also explored the effect of varying the inner boundary radius R_{in} on the models. Figure 6.7 shows $\dot{M}(t)$ for a set of models with $0.06\text{AU} \leq R_{in} \leq 0.3\text{AU}$, with one two-sided (not equatorially symmetric) model at $R_{in} = 0.06\text{AU}$. All models have $N_R = 320$ and $N_\theta = 112$, except the two-sided model, which has $N_\theta = 224$.

The outburst amplitude and duration are nearly independent of R_{in} as long as R_{in} is far enough in that the TI can be triggered; the TI is not triggered when $R_{in} = 0.3\text{AU}$, and so the outburst is slightly stronger and shorter. One implication of the lack of sensitivity of the outburst profile to R_{in} is that, while the TI can sharpen the outburst slightly, the outburst timescale and maximum mass are largely set in the outer disk: where the MRI becomes active, how much mass is accumulated during the quiescent stage, and so on.

When the TI is triggered, $\dot{M}(t)$ exhibits strong short-timescale variations (panel (b,c,d) of Fig. 6.7). This is caused by convection during the transition between the TI high and low states; the large temperature gradients at the transition make it highly convectively unstable by the Schwarzschild criterion (see chapter 6.4 for details).

Convection at the high state-low state transition radius changes the character of the $\dot{M}(t)$ variability in 2D models compared to 1D (vertically averaged) models. In 1D evolution models flickering at any radius will propagate through the entire inner disk, making the entire inner disk flicker between the low and high states. Thus the mass accretion rate varies violently during 1D evolutions. To avoid this, Bell & Lin (1994) used an α prescription designed to make α increase sharply from the low to the high states. In 2D models, on the other hand, flickering propagates both radially and vertically. For example, consider a region near the midplane that wants to jump to the high state will soon experience convective cooling and return to the low state.

This acts to localize and dampen low state-high state flickering.

For models with $R_{in} = 0.06\text{AU}$ (panel (c) in Fig. 6.7), $\dot{M}(t)$ varies less violently than in models with $R_{in} = 0.1\text{AU}$ because the inner edge is far from the convection associated with the low state high state transition. As the resolution increases, however, the $R_{in} = 0.06\text{AU}$ model becomes more and more variable. These models, and especially the convection zones, are not converged even at our highest resolution. This is not a major concern, as the fine structure of convection in our axisymmetric, phenomenological α viscosity model will not be the same as the fine structure of convection in a three dimensional, MHD turbulent disk; further resolving this structure would not improve the model.

One aspect of the details of convection is worth commenting on. Panel (d) in Figure 6.7 shows a full-disk model, which exhibit less variability than the half-disk models. Convection in the full-disk models can penetrate, rather than reflecting back from, the midplane. This feature of disk convection is consistent with linear theory (Ruden et al. 1988), which shows that the most unstable mode has no nodes in v_z . Because the maximum mass accretion rates and the outburst duration times are similar for half-disk and full-disk models, most of our simulations have been carried with one-sided models to save computation time. However, we need to use the full-disk models to study convection during the outburst.

6.5 Vertical Structure and Convection

Though our 2D simulations exhibit complex time-dependent behavior, the vertical structure of the simulated disk can be well fit by a simple analytical calculation plus some basic assumptions.

Assuming local energy dissipation and with a given effective temperature and viscosity parameter α , the disk structure can be defined by the following equations. Assuming all the viscosity-generated energy radiates vertically, we have

$$\frac{9}{4}\nu_V\rho\Omega^2 = \frac{d}{dz}(F), \quad (6.29)$$

where the vertical flux F is

$$F = \frac{4\sigma}{3} \frac{dT_\tau^4}{d\tau}, \quad (6.30)$$

the viscosity is

$$\nu_V = \alpha c_s^2 / \Omega, \quad (6.31)$$

and

$$d\tau = -\rho\kappa(T, p)dz. \quad (6.32)$$

With hydrostatic equilibrium,

$$\frac{dp}{dz} = -\frac{GM_*\rho z}{R^3}, \quad (6.33)$$

and the equation of state,

$$p = \frac{k_B}{\mu} \rho T. \quad (6.34)$$

ρ, T , and p are functions of Z . Equation 8.36 can be integrated towards the midplane given $T_{eff} = T(\tau = 2/3)$ as the boundary condition. The integration is halted at z_f , where the total viscous heating is equal to σT_{eff}^4 . In general $z_f \neq 0$ so we change the initial conditions and repeat the integration until $z_f = 0$, in which case we have the self-consistent vertical structure solution. This procedure is identical to that described in Zhu et al. (2009); we will call these local vertical multi-zone (LVMZ) models.

Figure 6.9 shows the vertical structure at 0.1 AU from the 2D simulation and that from the LVMZ with the same central temperature. Though the 2D model cannot resolve the region where $T \sim 10^4 K$, the 2D model otherwise agrees with the LVMZ very well, which means that at 0.1 AU the local treatment is a good approximation even during the TI high state, and that radial energy transport is not important. We find that in general the simulation follows the 'S' curve calculated by the LVMZ very well during the whole TI activation process (see chapter 6.9 Appendix B).

In the lower left panel of Figure 6.9, the pressure plateau around $\tau \sim 10$ is caused by the rapid increase in opacity with increasing temperature near $\sim 10^4 K$ as H ionizes

(see chapter 5.8). This means that the optical depth can change significantly while the pressure remains nearly the same.

The large vertical temperature gradient causes this region to become convectively unstable. As shown in the lower right panel, the dense gas is on top of the thin gas at $\tau < 100$ which is clearly unstable against convection or Rayleigh-Taylor instability. Though this convective region is only at the surface and barely resolved at 0.1 AU, it extends to the whole disk at 0.2 AU, where convective patterns even penetrate the mid-plane (Fig. 6.10).

Convection occurs wherever the Schwarzschild criterion is violated: $\nabla_S \equiv d \log T / d \log P > (\gamma - 1) / \gamma = 0.4$ in our case ($\gamma = 5/3$). For an optically thick disk, if the opacity can be described as $\kappa = \kappa_0 T^\beta P^\epsilon$ (Bell & Lin, 1994; ?), Rafikov (2007) derives $\nabla_S > (1 + \epsilon) / (4 - \beta)$. Thus, the disk is convectively unstable when its temperature is in the range with the opacity satisfying $(1 + \epsilon) / (4 - \beta) > (\gamma - 1) / \gamma = 0.4$.

Before the outburst, the disk is convectively stable. The active layer has a lower temperature than the dust sublimation temperature. Thus, $(1 + \epsilon) / (4 - \beta) \simeq 0.3$, using the Bell & Lin (1994) opacities. The numerical simulation also shows ∇_S is slightly smaller than $(\gamma - 1) / \gamma = 0.4$, which implies it is convectively stable.³ The dead zone is isothermal without any energy generation, which means it is also convectively stable with $\nabla_S \sim 0$.

During the TI high state, however, the disk exhibits a variety of convective features at $R < 0.6 \text{ AU}$, where $T > 2000 \text{ K}$. The inner disk consists of three distinct convective regions:

- 1) At $0.35 \text{ AU} < R < 0.6 \text{ AU}$, the disk is hot enough that the dust has sublimated and the gas is in molecular form ($2000 \text{ K} < T < 5000 \text{ K}$) with TiO and H₂O opacities dominating the opacity. Based on the opacity given by Bell & Lin (1994), $(1 + \epsilon) / (4 - \beta) \sim 1$ so that the disk is convectively unstable. Our numerical simulations have also shown that $\nabla_S > 0.4$ in these regions (changing from 0.4 at $R \sim 0.6 \text{ AU}$ to 1 at

³We assume $\gamma = 5/3$ in our simulations. But at temperatures somewhat lower than the H₂ dissociation temperature, $\gamma \sim 7/5$, which implies $(\gamma - 1) / \gamma \sim 0.3$. Thus, the dusty disk may be convectively unstable. A self-consistent thermodynamic treatment will be considered in future.

$R \sim 1\text{AU}$). However, convection turns out to be inefficient in these regions, with convective speeds far less than the sound speeds (lower right panel of Fig. 6.10).

2) At $0.15 \text{ AU} < R < 0.35 \text{ AU}$, the midplane is hot enough that hydrogen begins to be ionized. The midplane is thermally unstable, and $(1 + \epsilon)/(4 - \beta)$ even becomes negative. The disk heats up until the midplane temperature $> 2 \times 10^4 \text{K}$ and it becomes thermally stable. The surface, however, is still far cooler than $2 \times 10^4 \text{K}$, with the effective temperature $\sim 2000 \text{K}$. At some height in the disk there is a transition where the opacity depends steeply on the temperature and convection is strong. At these radii the transition is close to the midplane and strong convection stirs the entire disk. The largest scale eddies penetrate the midplane.

Figure 6.11 shows a velocity map of the convective eddies in region (2). We study them by inserting trace particles. These particles rise up with the hot 'red' fingers which are in the TI high state. When they approach the surface, they enter the region which is cool, dense and in the TI low state. Then they fall with the cool 'green' fingers to the midplane where they will be heated up again. The convective velocity can be estimated by assuming the particles in the red fingers are accelerated by the buoyancy force from the surrounding dense green fingers. Consider the red fingers are in TI high state with $T \sim 20,000 \text{ K}$ and ρ_r , while the green fingers are in TI low state with $T \sim 2,000 \text{ K}$ and $\rho_g \sim 10\rho_r$. Thus, in the rest frame of the green fingers

$$v_r \sim \left(\frac{H_e a}{2}\right)^{1/2} \sim \left(\frac{H_e g_h \rho_g - \rho_r}{2 \rho_r}\right)^{1/2} \sim (4.5 H_e g_h)^{1/2} \quad (6.35)$$

where H_e is height of the eddy. $g_h = GM_*/R^3 \times H/2$. While the velocity of the red fingers in the rest frame of the green fingers is

$$v_g \sim \left(\frac{H_e g_h \rho_g - \rho_r}{2 \rho_g}\right) \sim (0.5 H g_h) \quad (6.36)$$

The real eddy velocity should be between v_g and v_r . If $H/R \sim 0.1$, $H_e = 0.5 H$ and $R = 0.2 \text{ AU}$, we derive $v_g \sim 2.3 \text{ km s}^{-1}$ and $v_r \sim 7.1 \text{ km s}^{-1}$. Thus the average eddy velocity should be around 4 km s^{-1} . The maximum velocity should not be larger than twice

the average velocity. The lower left panel shows the velocity of these eddies, whose velocity is around 4 km s^{-1} . The maximum velocity takes place at the surface. Although convection is subsonic at the midplane, it is supersonic at the surface (lower right panel in Fig. 6.10).

3) At $R < 0.15\text{AU}$ most of the region is already in the TI high state with $T > 2 \times 10^4\text{K}$. Thus $(1 + \gamma)/(4 - \beta) \sim 0.3$, which is similar to the numerical simulation. The surface region where the high state joins to the low state is, however, still convectively unstable (refer to Fig. 6.9 which shows ∇_S is very large at the transition). Unfortunately our simulation barely resolves this region.

Generally, convection in our simulation is strongly correlated with TI (which is not surprising, since both are related to steep gradients in the opacity). In the outer region where the TI is inactive, convection is weak and inefficient. When the TI is active, the convection patterns depend on the vertical height of the point where hydrogen begins to ionize. If this transition is close to the midplane, convection is strong and penetrates the midplane. Otherwise, only the surface is affected by convection.

6.6 Discussion

Using our adopted parameters, our 2D simulations produce outbursts which are similar to FU Orionis outbursts, with comparable maximum mass accretion rates ($\sim 2 \times 10^{-4}M_{\odot} \text{ yr}^{-1}$) and decay timescales ($\sim 100\text{yrs}$). The outbursts begin with the GI transferring mass to the inner disk until it is hot enough to activate the MRI; at that point the disk accretes at a much higher mass accretion rate because of the much higher efficiency of the MRI in transferring angular momentum.

Our outburst scenario is similar to that of Armitage et al. (2001). However, their outbursts were at a much lower mass accretion rate, $\sim 10^{-5}M_{\odot} \text{ yr}^{-1}$, and lasted a longer time, $\sim 10^4 \text{ yr}$. As discovered by Book & Hartmann (2001) and explained in Zhu et al. (2009), their weaker and slower outbursts are due to their lower MRI trigger temperatures ($T_M \sim 800\text{K}$) and smaller $\alpha_M = 0.01$. Specifically, with a lower T_M , the MRI is triggered at a larger radius with a lower surface density, resulting in

less mass accumulation in the inner disk. Combined with a smaller α , this results in a lower mass loss rate and a longer viscous timescale.

Our choice of $T_M \sim 1200\text{K}$ is close to the temperature range at which dust is expected to sublimate. This suggests that the mechanism for turn-on of the MRI thermally may be controlled by the elimination of the small dust grains that effectively absorb electrons and thus quench the MRI.

Our radiative transfer modeling of FU Ori (Zhu et al. 2007) suggested that to fit the *Spitzer Space Telescope* IRS spectrum, the rapidly-accreting, hot inner disk must extend out to ~ 1 AU, inconsistent with a pure thermal instability model (Bell & Lin, 1994). In our 2D results we find MRI triggering at about 2 AU, much more consistent with the *Spitzer* data and our previous analysis in Zhu et al. 2009. As FU Ori has a smaller estimated central star mass ($0.3 M_\odot$) than the $1 M_\odot$ used in our simulations, its hot inner disk should be slightly smaller than derived here, but still in agreement with observations.

Non-Keplerian rotation has not been observed from optical to near-IR ($5\mu\text{m}$) lines (?) since these lines come from inner disk within 1 AU where the disk is not massive. However, due to the fact that the disk is massive and gravitationally unstable at large radii (>2 AU), the disk has slightly sub-Keplerian rotation there and this effect may be observable in the far-IR or submm (Lodato & Bertin, 2003).

We cannot calculate meaningful optical (B magnitude) light curves for comparison with the historical observations of FU Ori objects because our inner disk radius is too large; this results in our maximum effective temperatures being too low in comparison with observations. (This constraint was due to the very long computation times required during outburst; moving the inner radius inward greatly lengthens the computing time.) We therefore computed a $1\mu\text{m}$ light curve as a prediction to compare with future observations (Fig. 6.13), assuming that the disk radiates like a blackbody at each radius's effective temperature; the lower panel shows the disk's surface and central temperature at 0.06 AU. The outburst has rise time ~ 10 years, which is similar to V 1515 Cyg but longer than FU Ori. The thermal instability is triggered on a much shorter timescale: as the lower panel shows, the disk's central

temperature rises sharply within 1 year. However, since the mass at the inner disk is still low, the mass accretion rate and the effective temperature cannot increase significantly until the MRI transfers more mass from the outer disk to the inner disk on a viscous timescale. Overall, our simulation agrees with V 1515 Cyg reasonably well but has a longer rise time than FU Ori and V 1057 Cyg. This might be improved by using a smaller inner radius, a consistent central mass, and a self-consistent boundary condition (Kley & Lin, 1999).

Our simulation suggests that the short-timescale variations appearing in the light curves of FU Ori (Kenyon et al., 2000) might be caused by convection in the high state to low state transition region. The observations show $\Delta M \simeq 0.035$ and timescales of less than one day. The amplitude of the variability in the 2D models is $\Delta M \sim 0.2$ (see Fig. 6.13). In 3D the amplitude of the variability will be reduced because there will be several convective eddies at each radius and averaging over these will reduce the variability. If we assume that the azimuthal extent of a convective eddy is $\sim H$, then there will be $m = 2\pi R/H$ convective eddies and the variability will be reduced by a factor of $m^{1/2} \sim 5$ if $H/R \sim 0.2$, suggesting a variability of $\Delta M \sim 0.04$. This agreement the data is encouraging, but it is likely that the details of convection in a magnetized, three dimensional disk will be different from that found in our viscous, axisymmetric models. The modest success of our model, however, might motivate the development of energetically self-consistent 3D magnetohydrodynamical (MHD) models of the inner disk of FU Ori.

The timescale of variability in our 2D models (months) is much longer than the observed 1 day. The timescale of variability might be shortened by (1) increased resolution, since the timescale of variability in our models increases with resolution; (2) switching off all components of stress in Equation 6.4 except the r - Φ component, since the other components act to retard and smooth convection (3) replacing the viscosity model used here by MHD turbulence, since the viscosity tends to suppress small scale structure; (4) 3D effects, since one might expect to see variability on timescales of $2\pi/(m\Omega) \sim 1$ day, using $R = 0.2\text{AU}$ and our estimate for m from above. Overall, although convective behavior revealed by our current simulations are

very preliminary (they depend on the simulation resolution, opacity, details of the turbulence etc.), it seems reasonable that convection accounts for the short-timescale variability of FU Orionis objects.

Hartmann, Hinkle, & Calvet (2004) found that some mildly supersonic turbulence ($\sim 2 c_s$) was needed to explain the width of ^{12}CO first-overtone lines of FU Ori . High resolution spectral modeling suggests that CO lines broadened with ~ 4 km/s turbulent velocity fit the observations well (Zhu et al. 2007). Hartmann, Hinkle, & Calvet (2004) proposed that the MRI could be a mechanism to drive the supersonic turbulence, while here we suggest that convection could also drive the turbulence. Convection is subsonic at the midplane in the TI high state, but as the convective eddies travel to the surface the temperature drops and convection becomes supersonic (see the lower right panel of Fig. 6.10). Numerical simulations (lower left panel of Fig. 6.10) and the simple analytical estimate (Eq. 6.36) suggest the 5 km s^{-1} is a typical convective velocity.

We also studied the disk central temperature at the stage when the MRI is activated and then moves inwards. The transition between the TI active and inactive region is sharp and occurs over a radial interval comparable to the disk scale height. The fronts travel at 2.7 km s^{-1} , which is almost the sound speed at $T = 1000 \text{ K}$. This thermal front velocity is much higher than αc_s predicted by Lin et al. (1985) and we will discuss this phenomenon in detail in chapter 7. Notice that in our model the stress is assumed to respond instantaneously to a change in the temperature caused by the radial energy diffusion ; this may indeed be the case if magnetic field mixes into the newly heated gas from the hot side of the transition front. If the magnetic field takes longer than $\sim \Omega^{-1}$ to build up then the front will travel more slowly.

Radiation pressure starts to become significant during the TI high state, with $P_r/P_t \sim 0.3$ in the innermost regions. We have conducted some experiments including radiation pressure using the diffusion approximation and find generally similar behavior to what has been shown in this chapter, though the disk is slightly thicker with the inclusion of radiation pressure. Again, we note that our inner radius is considerably larger than those of T Tauri stars, so radiation pressure might be more

important as accreting material joins the central star.

6.7 Conclusions

We have studied the time evolution of FU Orionis outbursts in a layered disk scenario, using an axisymmetric two dimensional viscous hydrodynamics code with radiative transfer. Both the MRI and GI are considered as angular momentum transport mechanisms and are modeled by a phenomenological α prescription. Besides the surface of the disk ionized by cosmic rays and X-rays, the MRI is also considered to be active as long as the disk's temperature is above a critical temperature T_M , so that thermal ionization can provide enough ions to couple the plasma to the magnetic field.

Starting with a massive disk equivalent to a constant α disk with $\dot{M}=10^{-4} M_{\odot}/\text{yr}$ and $\alpha=0.1$, several outbursts appear during our simulation. These outbursts begin with the GI transferring mass to the inner disk until the inner disk gradually becomes gravitationally unstable. Eventually the disk at 2 AU is hot enough to trigger the MRI and then the MRI active region expands throughout the whole inner disk. With the increasing temperature since the MRI is transferring more mass to the inner disk, the TI is triggered and a “high state” expands outwards to 0.3 AU. The outburst state lasts for hundreds of years and drains the inner disk; the disk then returns to the low state.

Convection appears at the inner disk during the TI high state. In the outer region ($0.35 < R < 0.6\text{AU}$), where the TI is inactive, convection is weak and inefficient. At $0.15 < R < 0.35\text{AU}$ during outburst, there is a hydrogen ionization zone at $z \sim H$, and strong convection is present. The convection even penetrates the midplane to form antisymmetric convective rolls. In the innermost region most of the disk is hot, the hydrogen ionization zone is close to the photosphere, and weak convection is confined to the disk surface.

Our model shows maximum accretion rates and outburst duration timescales similar to those of the known FU Orionis objects. Unlike the pure TI theory, our model produces an AU scale inner disk with high mass accretion rate, in agreement with

the observational constraints.

With some simple assumptions our simulations have produced FU Orionis-like outbursts. They also pose some interesting questions for future study. In chapter 7 we will compare our 2-D results to 1-D simulations; the latter will allow us to consider longer disk evolutionary timescales.

A dynamical GI simulation at AU scale, with both self-gravity and radiation, will be important to understand angular momentum transport by GI and the thermal structure of the inner disk. However, considering the large Keplerian velocity of the inner disk, a self-consistent radiation hydrodynamic scheme will be needed. Our simulations have also shown that convection is important in FU Orionis objects due to the large vertical temperature gradient at the hydrogen ionization zone. A fully 3-D simulation with both MHD and radiation, together with a self-consistent treatment of the equation of state, will be essential to understanding the role of convection. Also the very inner disk where the MRI is thermally activated by the irradiation and the boundary layer may also play a role in the disk evolution.

6.8 Appendix A: Radiative cooling scheme tests

To test the radiative transfer scheme (and particularly the boundary condition at the disk photosphere), we have constructed a disk model in which the viscous heating is turned off when $\tau < 100$. This makes the vertical flux constant for $\tau < 100$ and allows us to test our scheme against a gray atmosphere model. The disk structure shown here is that calculated with Method 1 as discussed in chapter 6.3.2. The structure calculated with Method 2 is even in a better agreement than Method 1, since it directly uses the gray atmosphere structure as the boundary condition.

The left panel in Figure 6.14 shows the flux through the atmosphere at different heights for one radius, while the dotted line is $F = \sigma T_{eff}^4$ with T_{eff} derived from the simulation. The right panel shows the disk temperature structure at this radius from the 2D simulation (solid line) and the theoretical gray atmosphere temperature structure ($T^4 = 3/4 T_{eff}^4 (\tau + 2/3)$) (dotted line). The vertical structure in the 2D simulation agrees well with the gray atmosphere structure, and improves on the original

scheme of ? by eliminating a temperature jump at the photosphere.

6.9 Appendix B: Thermal instability

The thermal instability (TI) model was developed to account for outbursts in dwarf novae systems (Faulkner, Lin, & Papaloizou 1983). But it also has features that make it attractive for explaining FU Ori outbursts (Bell & Lin, 1994). Although in this chapter we find that MRI triggering is mainly responsible for initiating FU Orionis outbursts, the TI still exists and can be triggered during the outburst. With the increasing mass accretion rate by the MRI operating, the innermost disk is heated up to hydrogen ionization and the disk becomes thermally unstable. Finally, TI sets in and the innermost disk enter a high (fully ionized) state.

The basic idea behind the TI can be illustrated by the disk $\Sigma - T_c$ relationship ('S' curve, Fig.6.12). The disk is in thermal equilibrium on this curve. To the left of the curve cooling exceeds heating and to the right heating exceeds cooling. As the disk central temperature reaches 3000K the disk transitions from the low-state lower branch to the high-state ($T_c \sim 2 \times 10^4$ K) upper branch; it cannot sit on the unstable middle branch.

6.9.1 'S' curve of 2D models

As discussed in chapter 6.4.1, the LVMZ method (?) produces similar vertical structure to our 2D models. Here, we use the LVMZ to calculate the disk's $\Sigma - T_c$ relation at 0.1 AU in Figure 6.12. The solid line is the equilibrium curve, while the crosses show Σ and T_c at 0.1 AU during 2D simulations; the disk moves from the lower left to the upper right with time. The crosses trace the LVMZ curve remarkably well. Since the LVMZ assumes the local cooling through surface balances local viscous heating, it follows that 2D effects, such as radial transport of heat, are not important in this region.

6.9.2 'S' curve of 1D models

In one zone model, where the midplane opacity is used at all z and the total surface density replaces $\rho(z)$, the 'S' curve can be obtained via

$$F_{vis} = F_{rad}. \quad (6.37)$$

Thus,

$$\frac{9}{4}\alpha\Omega\Sigma c_s^2 = 2\sigma T_{eff}^4, \quad (6.38)$$

where Σ is the surface density and c_s is the sound speed at the local central disk. For an optically-thick disk, we have $T_c^4 = \frac{3}{8}\tau_R T_{eff}^4$, where $\tau_R = \kappa_R \Sigma$ and κ_R is the Rosseland mean opacity (?). Then,

$$T_c^3 = \frac{27}{64\mu\sigma}\alpha\Omega\Sigma^2\mathcal{R}_c\kappa_R, \quad (6.39)$$

where \mathcal{R}_c is the gas constant, and μ is the mean molecular weight. This T_c and Σ relationship is shown in Figure 6.12, which differs significantly from the LVMZ 'S' curve.

These 'S' curves again make the point that the observed large outer radius, 0.5 – 1 AU, of the high accretion rate portion of the FU Ori disk poses difficulties for the pure thermal instability model. Even in the situation explored by ?, in which the thermal instability is triggered by a massive planet in the inner disk, the outer radius of the high state is still the same as in Bell & Lin (1994), $\sim 20 R_\odot$. The relatively high temperatures ($2 - 4 \times 10^3$ K) required to trigger the thermal instability (due to the ionization of hydrogen) are difficult to achieve at large radii; they require large surface densities which in turn produce large optical depths, trapping the radiation internally and making the central temperature much higher than the surface (effective) temperature.

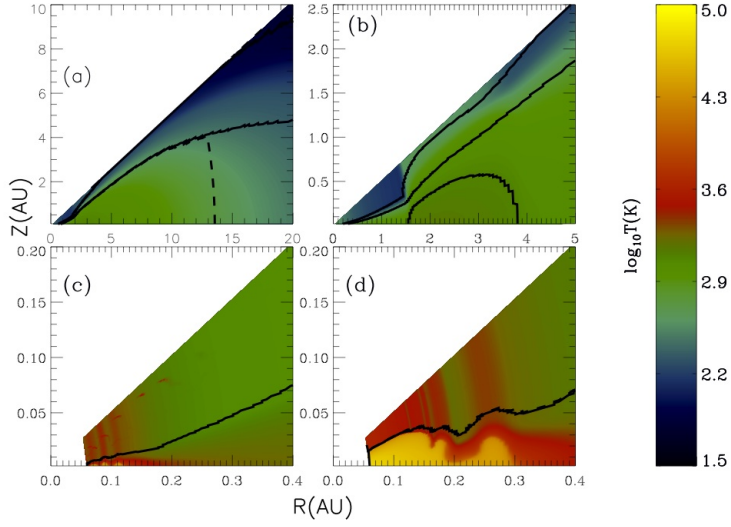


Figure 6.1 The disk's temperature color contours at four stages during the outburst in R-Z coordinate. The black curves are the α contours which also outlines different regions in the disk. The vertical dashed line in Panel (a) shows $\alpha_Q = 0.025$. (a) is the stage before the outburst. (b) represents the stage when the MRI is triggered at 2 AU. (c) represents the moment when the TI is triggered at the innermost region. (d) is the stage when the TI is fully active within 0.3 AU.

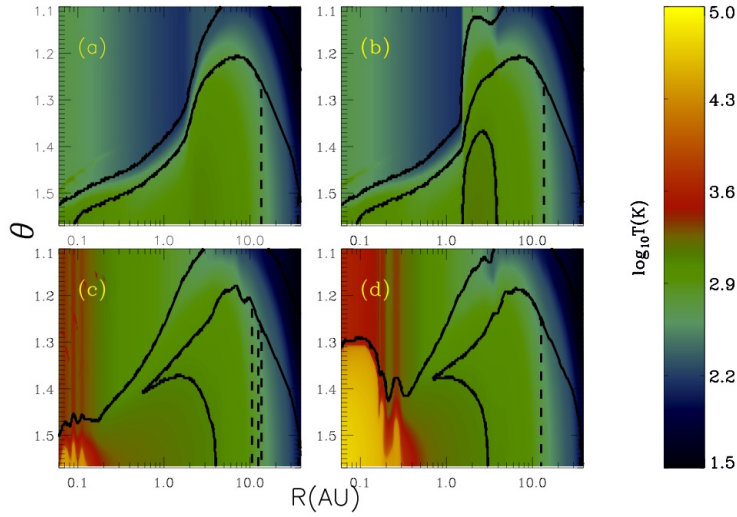


Figure 6.2 The disk's temperature color contours at four stages during the outburst, the same as Fig. 6.1. The black curves are the α contours which also outlines different regions in the disk: the uppermost atmosphere, active layer, and the dead zone close to the midplane. The dashed line shows $\alpha_Q = 0.025$. (a) is the stage before the outburst. (b) represents the stage when the MRI is triggered at 2 AU. (c) represents the moment when the TI is triggered at the innermost region. (d) is the stage when the TI is fully active within 0.3 AU.

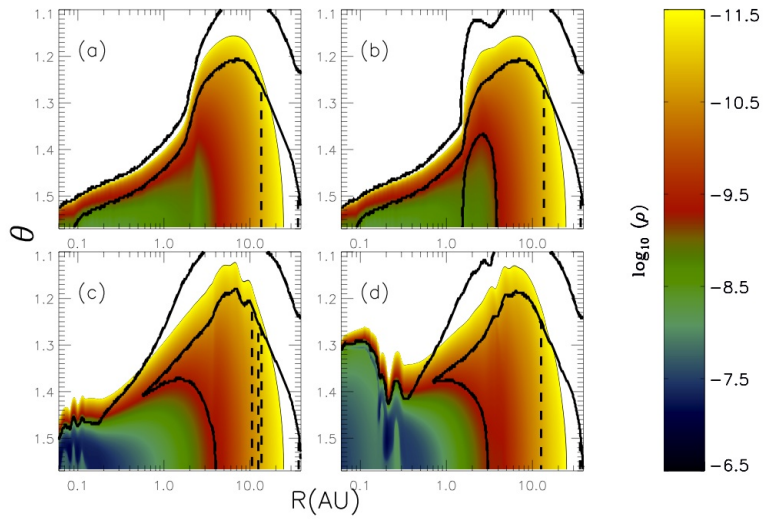


Figure 6.3 Similar to Figure 6.2 but shows the density contours. The high density white regions close to the midplane in (c) and (d) correspond to the region at the TI low state in Figure 6.2. Because it is much colder than the midplane which is at the TI high state, it needs a high density to balance the pressure.

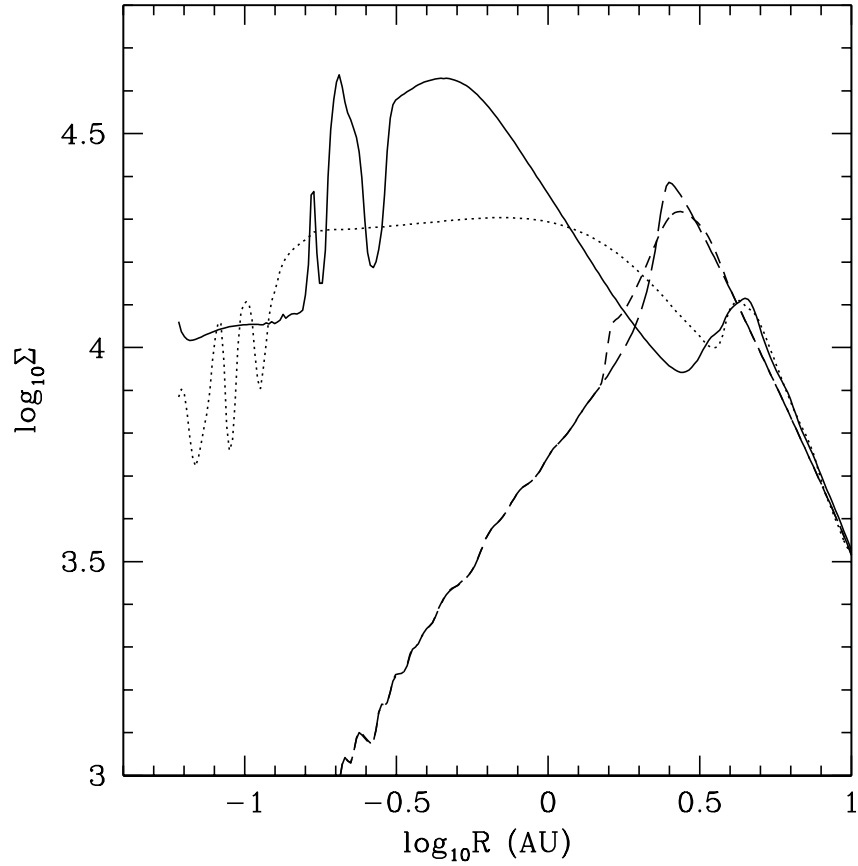


Figure 6.4 The distribution of the vertically integrated surface density at four corresponding stages as shown Figure 6.2. The long dashed line is the stage before the outburst, while the short dashed line represents the stage when the MRI is triggered at 2 AU. The dotted line shows the moment when the TI is triggered. Finally, the solid line shows the TI fully active stage.

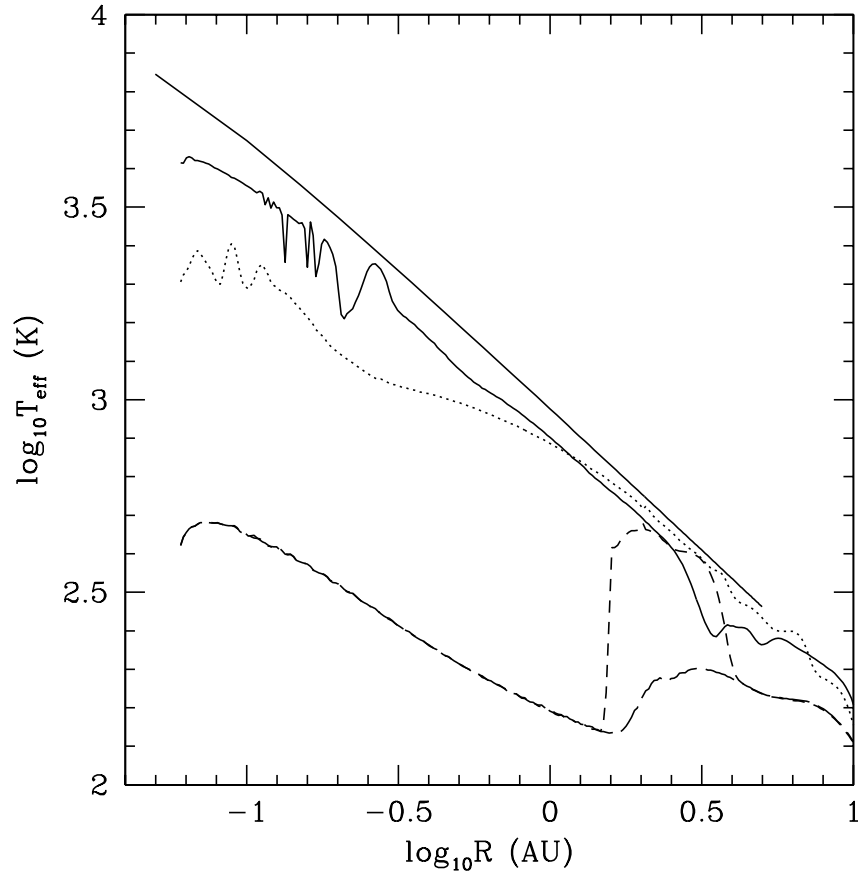


Figure 6.5 Similar to Figure 6.4 but shows the effective temperature distribution at the four stages. The long dashed line is the stage before the outburst, while the short dashed line represents the stage when the MRI is triggered at 2 AU. The dotted line shows the moment when the TI is triggered. The solid line shows the TI fully active stage, while the uppermost solid line shows the effective temperature of a steady accretion disk with $\dot{M} \sim 2 \times 10^{-4} M_{\odot} \text{ yr}^{-1}$ and $R_{\text{in}} \sim 5 R_{\odot}$

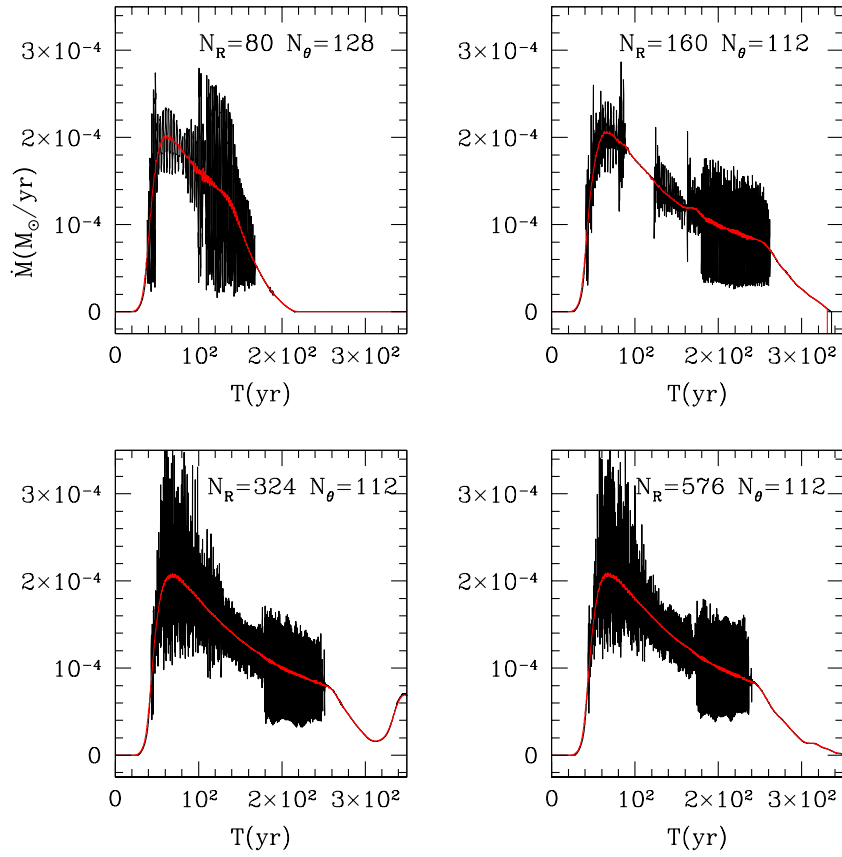


Figure 6.6 The disk's mass accretion rate through the innermost boundary with time for models with four different resolutions. The red lines are the mass accretion rates after being smoothed.

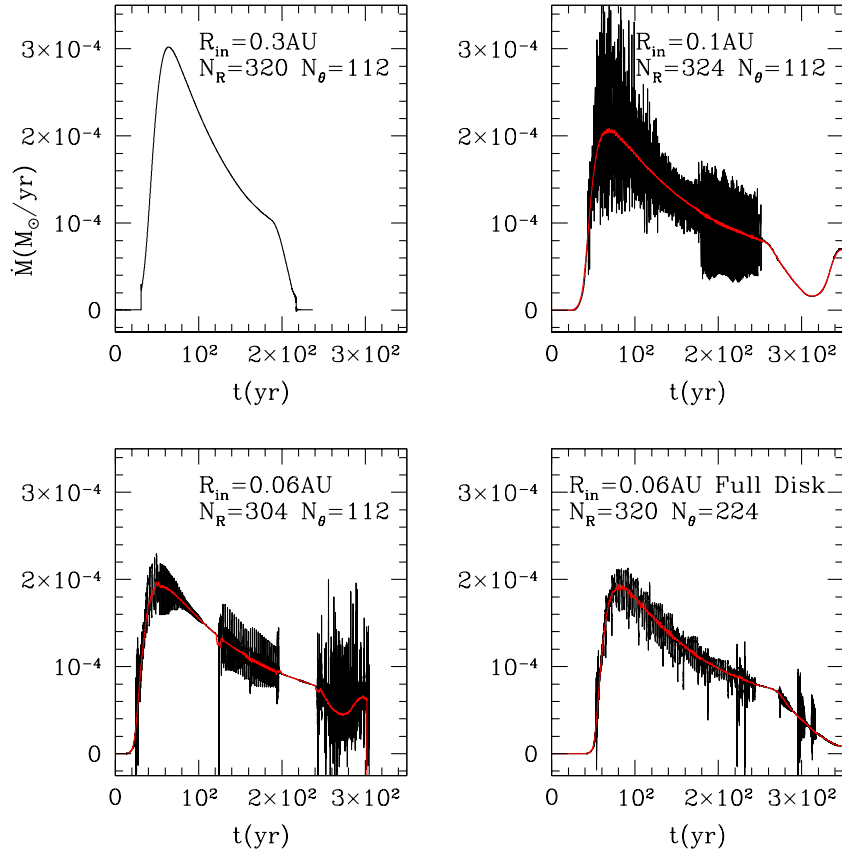


Figure 6.7 The disk's mass accretion rate for different disk configurations. The first three panels show the disk's mass accretion rate for half-disk models with different inner radius (0.3 AU to 0.06 AU). The lower right panel shows the disk's mass accretion rate for a full disk with the inner radius 0.06 AU. The red lines are the mass accretion rates after being smoothed.

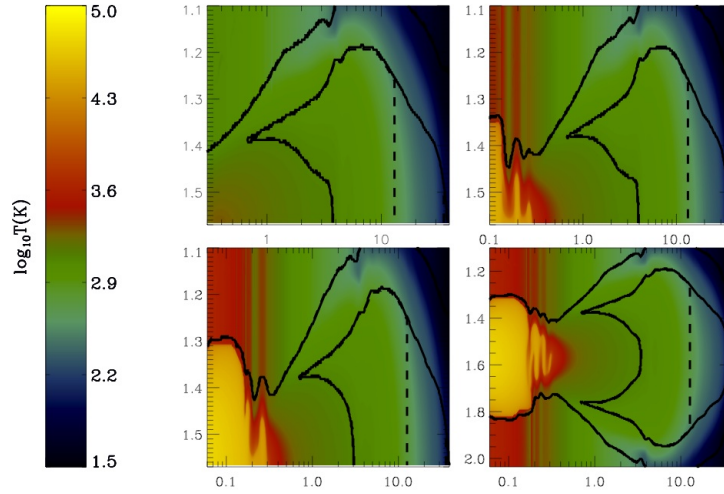


Figure 6.8 The temperature contours at the stage when their mass accretion rates reach maximum for the four models shown in Figure 6.7.

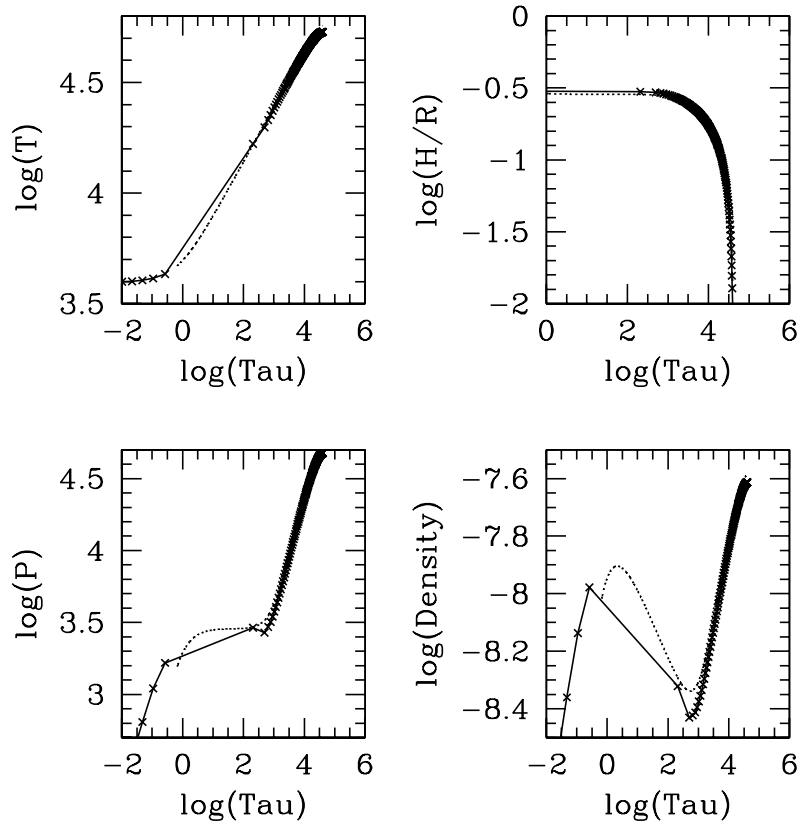


Figure 6.9 The disk's vertical structure at 0.1 AU in the TI active stage. The crosses are from the 2D simulation grids, while the dotted lines are the disk structure at the same central temperature calculated by the LVMZ method.

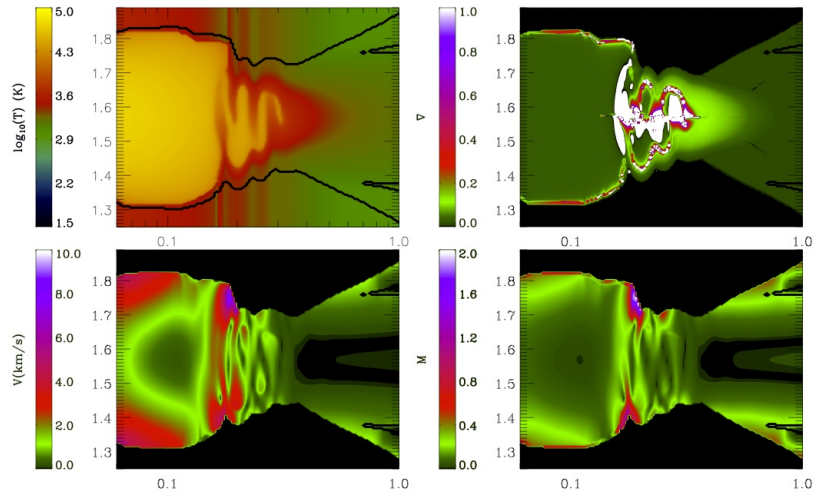


Figure 6.10 The contours for the temperature, temperature gradient, velocity and Mach number at the TI active stage. The white regions in the temperature gradient contour are due to the gradient larger than the shown range from 0 to 1. The optically thin region has been masked off in order to have the convective patterns in the optically thick region stand out.

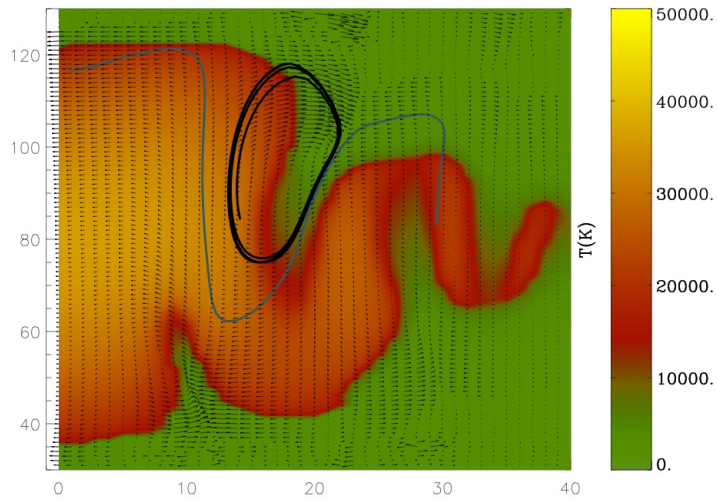


Figure 6.11 The velocity vectors of the computational grid are plotted on top of the temperature contours at the TI active region. The black and blue curves are the traces of two test particles which are originally placed at the midplane at 0.4 and 0.8 AU.

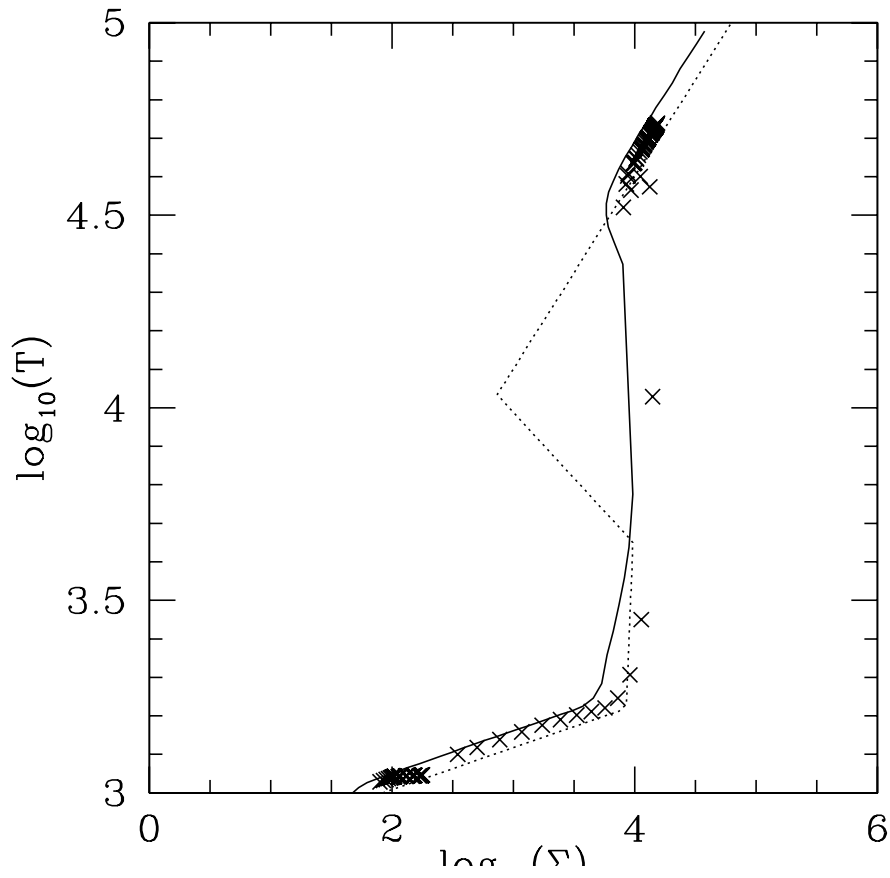


Figure 6.12 The 'S' curve calculated by the LVMZ (solid curve) and the midplane approximation (dotted curve) at 0.1 AU. The crosses trace the Σ and T_c from the 2D simulation.

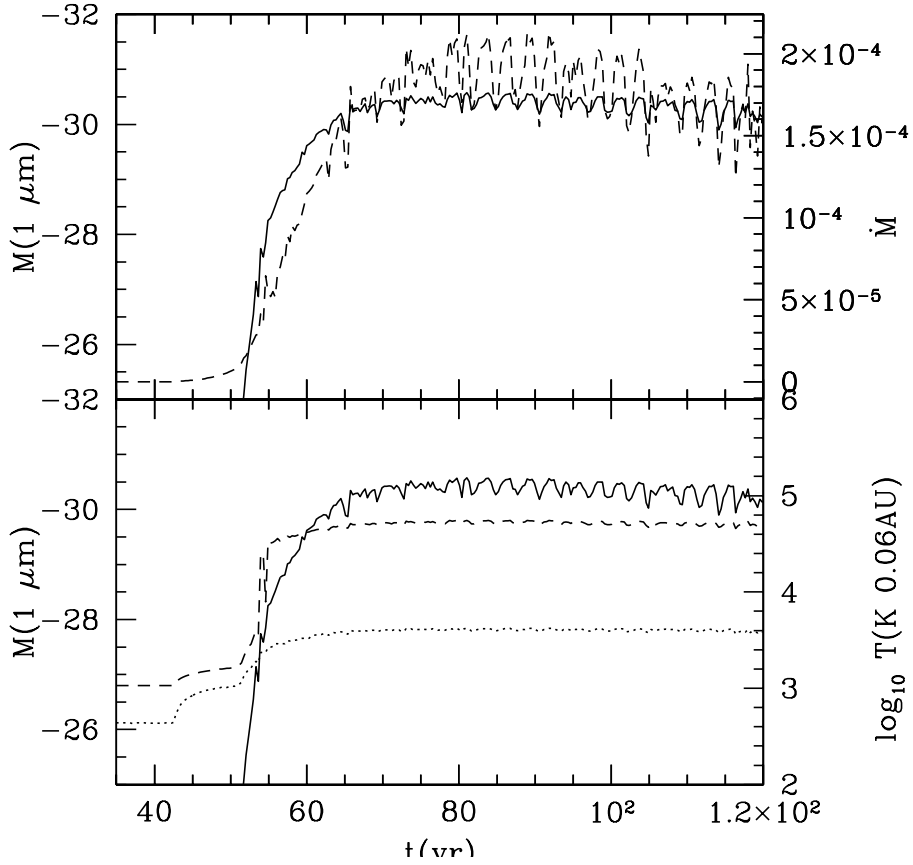


Figure 6.13 The solid curve shows the $1\mu\text{m}$ magnitude derived from the 2D disk at the beginning of the outburst. The dashed curve in the upper panel shows the mass accretion rate, while the dashed and dotted curves in the lower panel show the midplane and surface temperature at 0.06 AU respectively.

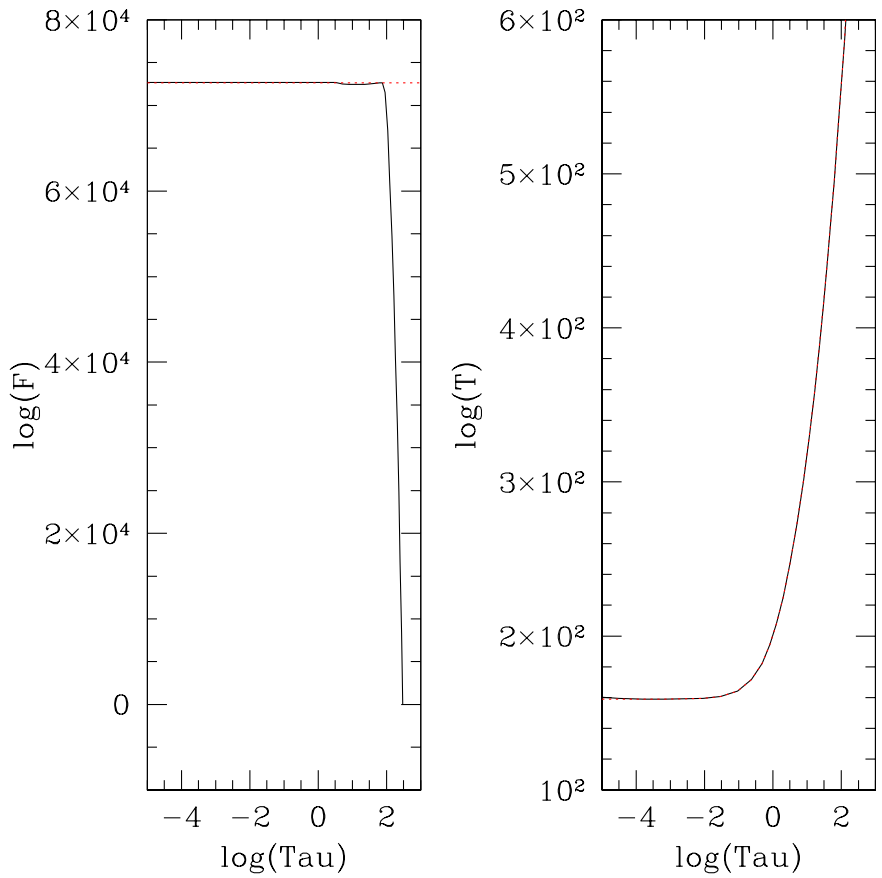


Figure 6.14 Grey atmosphere test. In this test, when $\tau < 100$, the viscous heating (2D) is turned off so that the flux is a constant there and can be compared with the gray atmosphere structure. The left panel shows the flux through the atmosphere at different heights, while the dotted line is $F = \sigma T_{eff}^4$. The right panel shows the disk temperature structure at one radius from the 2D simulation (solid line) and the theoretical gray atmosphere temperature structure ($T^4 = 3/4 T_{eff}^4 (\tau + 2/3)$) (dotted line).

Table 6.1 2D models

Labels	inner radius (AU)	half or full disk	resolution ^a
A	0.3	half	80 × 112
B	0.3	half	160 × 112
C	0.3	half	320 × 112
D	0.1	half	80 × 128
E	0.1	half	160 × 112
F	0.1	half	324 × 112
G	0.1	half	576 × 112
H	0.06	half	304 × 112
I	0.06	half	512 × 112
J	0.06	full	128 × 240
K	0.06	full	320 × 224

^aradial resolution × vertical resolution

CHAPTER 7

Long-term Evolution of Protostellar and Protoplanetary Disks. I. Outbursts

7.1 Abstract

As an initial investigation into the long-term evolution of protostellar disks, we explore the conditions required to explain the large outbursts of disk accretion seen in some young stellar objects. We use one-dimensional time-dependent disk models with a phenomenological treatment of the magnetorotational instability (MRI) and gravitational torques to follow disk evolution over long timescales. Comparison with our previous two-dimensional disk model calculations (Zhu et al. 2009b, Z2009b) indicates that the neglect of radial effects and two-dimensional disk structure in the one-dimensional case makes only modest differences in the results; this allows us to use the simpler models to explore parameter space efficiently. We find that the mass infall rates typically estimated for low-mass protostars generally result in AU-scale disk accretion outbursts, as predicted by our previous analysis (Zhu et al. 2009a, Z2009a). We also confirm quasi-steady accretion behavior for high mass infall rates if the values of α -parameter for the magnetorotational instability is small, while at this high accretion rate convection from the thermal instability may lead to some variations. We further constrain the combinations of the α -parameter and the MRI critical temperature, which can reproduce observed outburst behavior. Our results suggest that dust sublimation may be connected with full activation of the MRI. This is consistent with the idea that small dust captures ions and electrons to suppress the MRI. In chapter 8 we will explore both long-term outburst and diskevolution with this model, allowing for infall from protostellar envelopes with differing angular

momenta. This chapter has been published in the paper: “Long-term Evolution of Protostellar and Protoplanetary Disks. I. Outbursts”, 2010, *ApJ*, 713, 1134 with Lee Hartmann, Charles Gammie, Laura Book, Jacob Simon, and Eric Engelhard.

7.2 Introduction

In the standard model of low-mass star formation, a molecular cloud core collapses to a protostar over timescales of $\sim 10^5$ yr (e.g., Shu, Adams, & Lizano 1987), consistent with observations (Kenyon et al. 1990; Enoch et al. 2008). However, steady accretion of this mass onto central stars with a plausible mass-radius relation results in accretion luminosities that are larger than those observed in low-mass protostars (Kenyon et al. 1990, 1994; Enoch et al. 2009). One solution to this “luminosity problem” is that most infalling matter first falls to the circumstellar disk and then is accreted to the star during short-lived outbursts; in this model protostars are usually observed in quiescence. The FU Orionis objects provide direct evidence for this type of behavior, with maximum accretion rates of $10^{-4} M_{\odot} \text{ yr}^{-1}$ over periods of decades to centuries (Hartmann & Kenyon 1996), which also directly suggests $\sim 10^{-2} M_{\odot}$ in the disk at ~ 1 AU.

A number of theories have been proposed to explain FU Orionis outbursts, including thermal instability in the inner disk (Bell & Lin 1994), binary interactions (Bonnell & Bastien, 1992), and gravitational clumping at several AU (Vorobyov & Basu 2005, 2006). In chapter 5, we explored the possibility that outbursts might result because of a mismatch between the mass fluxes that can be transported by the magnetorotational instability (MRI) in the inner disk, and the gravitational instability (GI) in the outer disk. Using steady thin disk theory, we argued that outbursts are to be expected when disks are driven by mass addition lower than $10^{-4} M_{\odot} \text{ yr}^{-1}$, as initially found by Armitage, Livio, & Pringle (2001). We then developed a two-dimensional model of FU Orionis disks, which verified that outbursts of accretion similar to those observed could be produced using reasonable parameters for MRI transport when thermal ionization dominates (Z2009 b).

The computationally-intensive nature of two-dimensional (let alone three-dimensional)

simulations of outbursts makes it difficult to conduct studies of the effects of differing parameters on disk evolution over significant timescales. We have therefore developed one-dimensional disk models to follow disk evolution. While such models have limitations, they can serve as a starting point to investigate the landscape of possible disk evolutionary pathways. The diversity of disk properties among stars of nearly the same age and mass (e.g., Hartmann 2009) is plausibly the result of differing initial conditions, and models of the type we explore here can begin to address this possibility.

In chapter 7.3 we describe our 1-D, two-zone model, and compare its outburst properties with our 2-D models in chapter 7.4. In chapter 7.5 we present the results of a parameter study designed to show when outbursts occur and how the outburst strength and frequency depend on the adopted parameters. We present our discussion and conclusions in chapter 7.6 and chapter 7.7. The present work, in which we assume constant mass addition to the outer disk, serves as a starting point for our subsequent investigation of long-term disk evolution with mass addition due to infall from a rotating protostellar envelope in chapter 8.

7.3 One-dimensional two-zone models

In this chapter we adopt a version of the “layered accretion” disk model originally put forward by Gammie (1996). In this model, unless the disk is warm enough that thermal ionization is sufficient to couple the magnetic field effectively to the neutral disk material, only an upper layer of the disk can sustain the MRI due to non-thermal ionization by cosmic and/or X-rays. A significant amount of work has been done to study the properties of the active layer (e.g. Sano et al. 2000, Turner & Sano 2008, Bai & Goodman 2009), however due to the complex physics and chemistry involved, further theoretical or even observation study is needed. Here, we assume that the mass column density which can be ionized is roughly constant with radius (see, e.g., Glassgold, Najita & Igea 2004). If the total disk surface density Σ in the “cold” regions is less than the limiting active layer column density Σ_a , the disk is assumed to be completely viscous with a given α_M viscosity parameter due to MRI activity.

On the other hand, if the disk surface density is higher than this limit, then only the surface layers are assumed to exhibit the MRI.

Our one-dimensional, two-zone models (1D2Z) thus in general exhibit two layers: the surface layer and the central or “dead” zone ¹ with surface density Σ_d . The dead zone is assumed to have little or no MRI activity, though it may exhibit transport due to GI (see below). The temperatures T_a and T_d are averages which characterize the corresponding layers.

The surface density evolves according to the mass conservation and angular momentum conservation equations,

$$2\pi R \frac{\partial \Sigma_i}{\partial t} = \frac{\partial \dot{M}_i}{\partial R}, \quad (7.1)$$

$$2\pi R \frac{\partial}{\partial t} (\Sigma_i R^2 \Omega) = \frac{\partial}{\partial R} (\dot{M}_i R^2 \Omega) + \frac{\partial}{\partial R} (2\pi R^2 W_{R\phi,i}), \quad (7.2)$$

where $\dot{M}_i = -2\pi \Sigma_i R v_i$ is the radial mass flux in the disk, the stress $W_{R\phi,i} = R \Sigma_i \nu_i d\Omega/dR$, and subscript i denotes either ‘a’ (active layer) or ‘d’ (dead zone).

Assuming Keplerian rotation, equations (8.1) and (8.2) can be simplified to

$$\partial_t \Sigma_i = \frac{2}{R} \partial_R \left(\frac{1}{R\Omega} \partial_R (-R^2 W_{r\phi}) \right), \quad (7.3)$$

where $\partial_R \equiv \partial/\partial R$. The constant infall rate \dot{M}_{in} is set as an inflow outer boundary condition with $\dot{M}_{in} = 10^{-4}$, 10^{-5} , and $10^{-6} M_\odot \text{ yr}^{-1}$.

The parameter Σ_A is the maximum non-thermally ionized surface density, assumed constant during each calculation. If at a given timestep $\Sigma_a > \Sigma_A$, the excess mass of the active layer ($\Sigma_a - \Sigma_A$) is added to the dead zone ($\Sigma_d = \Sigma_d + \Sigma_a - \Sigma_A$). Conversely, if $\Sigma_a < \Sigma_A$ and $\Sigma_d \neq 0$, part of the dead zone is assumed to be non-thermally ionized, in which case Σ_a is set to be Σ_A and Σ_d decreases to $\Sigma_d - (\Sigma_A - \Sigma_a)$. Setting $\Sigma_A = \text{const.}$ is a crude approximation; it is likely that Σ_A varies with radius and depends on the local abundance of dust and flux of ionizing radiation.

¹Here “dead” refers to magnetically dead without MRI but it could transport angular momentum due to the gravitational instability.

The temperatures are determined by the balance between the heating and radiative cooling,

$$C_{\Sigma,i}\partial_t T_i = Q_{heat,i} - Q_{cool,i}, \quad (7.4)$$

where the heat capacity is $C_{\Sigma,i} = \Sigma_i c_{s,i}^2 / T_i$. For the active layer, the cooling rate is determined by

$$Q_{cool,a} = \frac{16}{3}\sigma(T_a^4 - T_{ext}^4)\frac{\tau_a}{1 + \tau_a^2}, \quad (7.5)$$

where σ is the Stefan-Boltzmann constant, T_{ext} represents the irradiation from the central star, and τ_a is the optical depth of the active layer. The final factor in equation (7.5) is an approximate form which accommodates both optically thin and thick cooling. We assume

$$T_{ext}^4 = fL/(4\pi R^2\sigma), \quad (7.6)$$

where L is the total luminosity of the star and $f(R)$ accounts for the non-normal irradiation of the disk by the central star; here we set $f(R) = const. = 0.1$. The active layer optical depth is given by

$$\tau_a = \frac{1}{2}\Sigma_a\kappa(\rho_a, T_a), \quad (7.7)$$

where κ is the Rosseland opacity derived from Z2009a at the active layer density and temperature, $\rho_a = \Sigma_a/2H_a$, $\rho_d = (\Sigma_a + \Sigma_d)/2H_d$, and H_a and H_d are the scale height of the active layer and the dead zone.

The dead zone has a cooling rate similar to that of the active layer. If the active layer is optically thick, the incident radiation flux into the dead zone from the active layer is σT_a^4 . Thus the cooling rate is

$$Q_{cool,d} = \frac{16}{3}\sigma(T_d^4 - T_a^4)\frac{\tau_d}{1 + \tau_d^2}, \quad (7.8)$$

with

$$\tau_d = \frac{1}{2}\Sigma_d\kappa(\rho_d, T_d). \quad (7.9)$$

However, if the active layer is optically thin, the incident flux becomes $\sigma(T_a^4\tau_a + T_{ext}^4)$,

and

$$Q_{cool,d} = \frac{16}{3}\sigma(T_d^4 - T_a^4\tau_a - T_{ext}^4)\frac{\tau_d}{1 + \tau_d^2}. \quad (7.10)$$

With increasing temperature the radiative cooling time, which constrains the numerical timestep, becomes small. For computational efficiency we then make the equilibrium approximation

$$T_a^4 = \frac{8(T_d^4 - T_{ext}^4)}{3\tau_d}, \quad (7.11)$$

when the disk midplane temperature is $> 5000\text{K}$.

The heating rate of the dead zone is just the viscous heating rate, while, in the active layer, the heating rate consists of its own viscous heating and the radiation from the underlying dead zone:

$$Q_{heat,a} = Q_{visc} + Q_{cool,d}, \quad (7.12)$$

In the case when the active layer is optically thin, this equation is modified to

$$Q_{heat,a} = Q_{visc} + \tau_a Q_{cool,d}. \quad (7.13)$$

The viscous heating term is

$$Q_{visc} = \frac{3}{2}W_{R\phi}\Omega, \quad (7.14)$$

where $W_{R\phi} = (3/2)\Sigma_i\nu_i\Omega$. To evaluate the viscosity ν_i , we have considered both MRI and GI transport. The net viscosity ν_i is the sum of both,

$$\nu_i = \alpha_i \frac{c_{s_i}^2}{\Omega} \quad (7.15)$$

where $\alpha_i = \alpha_Q + \alpha_M$ and

$$\alpha_Q = e^{-Q^4}. \quad (7.16)$$

The MRI viscosity is assumed to have a fixed value of α_M whether the region in question is thermally or non-thermally ionized. We assume that above some critical

temperature T_M the MRI is fully activated throughout the disk with viscosity parameter α_M . The Toomre instability parameter Q is evaluated using the disk central (midplane) temperature T_d , the total surface density ($\Sigma_a + \Sigma_d$), and assuming Keplerian rotation. The form of α_Q is motivated by a desire to make gravitational torques significant only when $Q \lesssim 1.4$, as indicated by global three-dimensional simulations (e.g., Boley et al 2006).

There are uncertainties in adopting the above approach to transport. GIs involve large scale density waves that cannot be captured with a local viscous treatment, although local treatments are adequate under some circumstances (??). As discussed in Z2009a, the essential properties of this treatment are the assumptions that disks with GI have Q -values of order unity, and that the GI produce local dissipation of the accretion energy. Under these assumptions, the precise form of α_Q will not affect the disk's evolution, as long as α is a steeply declining function of Q near ~ 1.5 . To make this point clear, we ran the same simulation for a test case but with the α_Q prescription of Lin & Pringle (1987,1990). As expected, the different forms of α_Q have no effect on the disk outbursts.

Similarly, whether the MRI can be fully activated in a non-thermally-ionized layer depends in part upon whether small dust grains have been sufficiently depleted (e.g., Sano et al. 2000). This is a complicated problem with substantial observational and theoretical uncertainties; we therefore adopt the simplest possible approach. It turns out that the value of Σ_a is unimportant for understanding large outbursts (Z2009a), as long as the GI in the dead zone transports more mass than the active layer; but Σ_a does have important effects on the long-term disk evolution at low accretion rates, as discussed in chapter 8.

It is now clear that the magnetic fields that give rise to α_M diffuse radially (Lesur & Longaretti 2008, Guan & Gammie 2009, Fromang & Stone 2009) and take time to build up and decay (e.g. Hirose et al. 2009). To account for these effects we introduce an evolution equation for α_M :

$$\frac{\partial \alpha_M}{\partial t} = -\Omega \frac{\alpha_M^2 - \alpha_{M,o}^2}{\alpha_M^2 + \alpha_{M,o}^2} + \frac{H^2 \Omega}{2} \frac{\partial^2 \alpha_M}{\partial R^2}, \quad (7.17)$$

where $\alpha_{M,o}$ is the equilibrium value for α_M . The first term permits α_M to relax up, or down, as T_M is crossed. The second term corresponds to radial diffusion of the magnetic field. For numerical reasons we set the dimensionless radial diffusion coefficient to 0.5 (the radial diffusion coefficient is actually a function of distance from the midplane).

7.4 Outburst behavior

In the protostellar phase, the disk is unlikely to transport mass steadily from ~ 100 AU all the way to the star at an accretion rate matching the mass infall rate $10^{-6} - 10^{-4} M_{\odot} \text{yr}^{-1}$ from the envelope to the outer disk. This mismatch leads to outbursts which are qualitatively similar to that found by Armitage et al. (2001), Book & Hartmann (2005), and in our 2-D hydrodynamic simulations (Z2009b). In summary, before the outburst, mass added to the outer disk moves inwards due to GI, but piles up in the inner disk as GI becomes less effective at smaller radii. Eventually, the large Σ and energy dissipation leads to enough thermal ionization to trigger the MRI at several AU. The MRI front quickly moves in across the inner disk and the inner disk accretes at a higher mass accretion rate, resembling FU Orionis-type outbursts. This high mass accretion rate during the outburst also makes the inner disk thermally unstable. After the inner disk has been drained by the outburst and becomes too cold to sustain the MRI, the disk returns to the low state. With the mass continuously accreted from the outer radii (or from an infalling envelope), the disk evolves to conditions leading to another outburst. This MRI triggered by GI outburst can also be understood as the classical thermal instability, but the S-curve is formed primarily by the variation of α near T_M , rather than variations in opacity and assumed variation in α near hydrogen ionization (e.g. Bell & Lin (1994)).

To test how 1D2Z models simulate the outbursts compared with 2-D simulations, we set up a test case with all the parameters adopted from our previous 2-D simulations (Z2009b). In both 1-D and 2-D simulations, we have used an updated opacity from Z2009a and $T_M=1500$ K. Because Z2009b do not consider irradiation, the irradiation factor f in equation (8.4) for the 1D2Z simulation is set to be 0. The inner

radius in both cases is set to 0.2 AU.

Figure 7.1 shows the mass accretion rate as a function of time for both 1-D and 2-D simulations. As shown, the 1-D simulations closely resemble 2-D simulations at the equilibrium states, such as the state before the outburst is triggered and the state during the outburst. For some rapid, or small scale, disk variations, such as the MRI front propagation and the convective eddies in the hot inner disks, the 2-D simulations exhibit more complex behavior than the 1-D simulations, so the outbursts differ in detail. In particular the 1-D simulations show an initial high \dot{M} peak at the beginning of the outburst that is not seen in 2-D. The 1-D simulations also show “drop outs” in accretion that do not occur in 2-D.

In detail, starting from the MRI activation at ~ 2 AU, the MRI active region moves inwards. During this process, mass piles up at the inner boundary of the active region, because the disk is MRI active beyond this boundary and has a higher mass accretion rate than the MRI inactive disk at smaller radius. In 1-D simulations, which do not capture the effects of radial pressure gradients, mass piles up at this boundary. When this mass eventually accretes on to the central star there is a sharp peak in \dot{M} .

The \dot{M} drop-outs during outbursts in the 1-D simulations are related to the thermal instability associated with hydrogen ionization. The drop-outs occur when the inner disk returns to the TI low state in 1-D; in 2-D radial and vertical convection smooths out variations in the accretion rate and allows the inner disk to remain in the high state.

Despite the initial \dot{M} peak and the drop-outs in the 1-D model, the outburst timescale, \dot{M} , and consequently the total mass accreted during one outburst are similar in 1-D and 2-D simulations (Fig. 7.1). This similarity is due to the fact that the outburst timescale and \dot{M} are just determined by the radius where the MRI is triggered and by α_M ; the total mass accreted during one outburst is the mass difference before and after the outbursts, which are both equilibrium states.

7.5 Parameter study

Having tested that the 1-D models reproduce the general properties of the outbursts (maximum \dot{M} , duration time, etc.), we next turn to a parameter study with 1-D models to test the predictions of Z2009a using steady state models.

The radial range considered is from ~ 0.2 AU to 30 AU. We adopt a constant inflow boundary condition at 30 AU. The inner boundary 0.2-0.3 AU is chosen to avoid instabilities which occur at the smallest radius where there is a transition between thermal and non-thermal activation of the MRI, here called R_i .

We find that, at least for our phenomenological model, R_i is unstable. Wünsch et al. (2006) has also found even with a 2-D radiative transfer hydrodynamic layered model, this instability still occurs. R_i oscillates around a mean radius, with thermal fronts washing inward and outward. This is similar to thermal instability but due to α variations between the dead zone and the inner MRI active region (Wünsch et al., 2006). However, we should be cautious in this instability, especially since dust may be sublimated before MRI activation. Then the inner disk may become optically thin due to the low opacity of the gas, and direct irradiation from the central star would ionize the dust wall. A proper treatment of R_i needs a 3-D MHD simulation with irradiation, dust physics, and ionization physics. Because this treatment is impractical, we set the inner boundary of our model just outside R_i . R_i depends on a variety of parameters (central star luminosity, the irradiation angle to the disk's surface, active layer surface density, the MRI trigger temperature and its viscosity parameter). Generally, R_i increases as the heating rate increases. In the end we set the inner boundary to 0.2AU if $\alpha_M=0.01$ and 0.3 AU if $\alpha_M=0.1$.

The infall is treated as a constant mass inflow at the disk outer edge at 30 AU. This assumption may not be applicable to study the disk's long-term evolution during the entire infall stage (10^5 years) since the infall centrifugal radius increases with time; this is explored extensively in chapter 8. Over the timescale of a single outburst, as studied in this chapter, this assumption is a good approximation as long as the infall centrifugal radius is larger than the MRI stable radius (R_M 1-10 AU in Figure 8.5).

Because protostars are thought to form over $\sim \text{few} \times 10^5$ yr, the average infall rate should be 10^{-6} - $10^{-5} M_{\odot} \text{yr}^{-1}$ (Stahler 1988; Hartmann et al. 1997); numerical simulations suggest the infall rate could be up to $10^{-4} M_{\odot} \text{yr}^{-1}$ at the earliest stages (Bate et al. 2003). Thus we study the disk evolution with infall rates varying from $10^{-4} M_{\odot} \text{yr}^{-1}$ to $10^{-6} M_{\odot} \text{yr}^{-1}$.

We neglect any change in the central star mass over the outburst timescale, which is a reasonable approximation. The effect of changing central mass over longer evolutionary timescales is included in chapter 8.

What is α_M ? Observations of dwarf novae, X-ray binaries, and FU Ori suggest $\alpha \sim 0.1$ (King et al. 2007; Zhu et al. 2007). T Tauri disk observations suggest $\alpha \sim 0.01$ (Hartmann et al. 1998). MHD simulations suggest $\alpha \gtrsim 0.01$, with the precise value depending on the resolution, treatment of small-scale dissipation, stratification, and treatment of radiation transport (e.g. Fromang & Papaloizou 2007, Guan et al. 2009, Davis et al. 2009, Shi et al. 2009; Hartmann et al. 1998). Because the situation is not yet resolved, we will consider cases with $\alpha_M = 0.01$ and $\alpha_M = 0.1$.

The MRI activation temperature T_M is not known precisely (it depends on the location of alkali metals, their ionization rate, the abundance of small grains, and the threshold ionization fraction for MRI turbulence), so we consider cases with $T_M=1400$ K and 1800 K. These values are chosen, consistent with our opacity prescription, to represent cases with and without dust.

7.5.1 Dependence on \dot{M}_in

Figures 7.2 – 7.4 show the outbursts with different infall rates varying from $10^{-4} M_{\odot} \text{yr}^{-1}$ to $10^{-6} M_{\odot} \text{yr}^{-1}$. For a given set of disk parameters (α_M, T_M), the disk accretes quasi-steadily if the infall rate is high enough (small variations could still appear due to the classical thermal instability, as discussed in chapter 7.6.1). If $\alpha_M = 0.01$, the disk accretes steadily if the infall rate is $10^{-4} M_{\odot} \text{yr}^{-1}$, while outbursts appear with smaller infall rates. With a bigger $\alpha_M = 0.1$, the disk accretes nonsteadily/in outburst for all the cases with infall rates $10^{-4} M_{\odot} \text{yr}^{-1}$ - $10^{-6} M_{\odot} \text{yr}^{-1}$. This is consistent with our predictions from the steady state models (Z2009a).

The outbursts become shorter with smaller infall rates \dot{M}_{in} . For example, with $\alpha_M=0.1$ and $T_M=1400$ K, the outbursts last 800, 500, and 400 years for $\dot{M}_{in} = 10^{-4}$, 10^{-5} , and $10^{-6}M_\odot \text{ yr}^{-1}$. This can be explained by the fact that the MRI is triggered at larger radii with larger \dot{M}_{in} and thus the outburst (viscous) timescale is longer (chapter 7.6.1). The simple analytical calculation in the Appendix shows that the outburst timescale is

$$t \sim \frac{R_Q^2}{\nu} \sim 960 \frac{0.1}{\alpha_M} \left(\frac{\dot{M}_{in}}{10^{-4}M_\odot \text{ yr}^{-1}} \right)^{1/9} \left(\frac{M}{M_\odot} \right)^{2/3} \text{ yr}. \quad (7.18)$$

for $T_M=1400$ K, where R_Q is the GI-induced MRI activation radius which will be discussed in chapter 7.6. This agrees with the numerical simulations reasonably well. The mass accretion rates during the outbursts are similar.

The infall rate also determines the outburst frequency. The time between two outbursts is significantly shorter with $\dot{M}_{in} = 10^{-4}M_\odot \text{ yr}^{-1}$ than with $\dot{M}_{in} = 10^{-5}M_\odot \text{ yr}^{-1}$, because the mass accreted to the star during all the outbursts should be equal to the mass from infall integrated over the same period of time. Since the outburst timescale is insensitive to the infall rate ($\sim \dot{M}_{in}^{1/9}$), we assume each outburst transports $\sim 0.03M_\odot$, which is suggested by the observation of FU Ori, and thus the timescale between two outbursts is $0.03 M_\odot/\dot{M}_{in}$. Therefore higher infall rates lead to more frequent outbursts.

7.5.2 Dependence on α_M and T_M

The effect of α_M on the outburst can be seen by comparing the upper and lower panels of Figures 7.2-7.4. For a given \dot{M}_{in} and T_M , with a higher α_M the outburst is shorter and stronger. This is because the outburst timescale is close to the viscous timescale, which is inversely proportional to α_M while the mass accretion rate is proportional to α_M . This can be understood using Equation (7.18) and

$$\dot{M} = 5 \times 10^{-4} \frac{\alpha_M}{0.1} M_\odot \text{ yr}^{-1}, \quad (7.19)$$

as shown in the Appendix for the $T_M=1400$ K case.

On the other hand, comparing the left and right panels of Figures 7.2 - 7.4, we find that the disks with higher T_M have shorter but stronger outbursts. The outburst is shorter because the MRI is triggered at a smaller radius if T_M is higher, resulting in a shorter viscous timescale. Figure 7.5 shows the disk's condition just before the MRI is triggered in the case $T_M=1400$ K (the solid curve) and $T_M=1800$ K (the dotted curve). The MRI is triggered at 3 AU with $T_M=1400$ K and 1.5 AU with $T_M=1800$ K. The outburst is stronger with higher T_M because the surface density at the MRI trigger radius with $T_M=1800$ K (1 AU) is much higher than the surface density at the MRI trigger radius with $T_M=1400$ K (3 AU) (upper left panel in Fig. 7.5). Thus, with higher T_M , the smaller but more massive inner disk leads to shorter but stronger outbursts.

Our simulations also indicate that the outbursts with higher T_M accrete less mass than those with lower T_M no matter what the infall rate is (Table 7.1), because the outbursting inner disk extends to smaller radii, and thus contains less mass, for a higher T_M .

7.5.3 Dependence on M_* and Σ_A

Protostars have a variety of masses, most of which are less than $1 M_\odot$. We also calculated results for central star masses (0.3, and $0.1 M_\odot$) with the same T_M (1400 K) and $\alpha_M=0.1$, and the infall rate $\dot{M}_{in} = 10^{-5} M_\odot \text{yr}^{-1}$. The mass accretion rates with time for these cases are shown in Figure 8.7. The outbursts have similar mass accretion rates, but the outburst is slightly shorter with a less massive central star, as suggested by equation (7.18). In addition the mass accreted during an outburst is not significantly affected by its central star mass (Table 7.1). The outbursts are broadly similar, even though the central star masses differ by a factor of 10.

Another uncertainty in a layered disk model is Σ_A , which depends on the flux of ionizing radiation and the abundance and size distribution of the dust. In protostars with mass infall rates from $10^{-6} M_\odot \text{yr}^{-1}$ to $10^{-4} M_\odot \text{yr}^{-1}$, most of the infall mass is transported to the inner disk by the GI in the dead zone, and mass transport through the active layer is negligible. Thus Σ_A has little effect on the unsteady accretion and

the outburst (Fig. 7.6), but it does affect the mass accretion rate in the low state. The mass accretion rate in a layered disk is determined by the active layer mass accretion rate at R_i . At $R < R_i$ the disk is MRI active due to thermal ionization. Thus the disk mass accretion rate should be proportional to $\Sigma_A \alpha_M$, which is shown in Figure 7.6.

7.6 Discussion

7.6.1 Unsteady accretion region

The above parameter study can be simply summarized in the $\dot{M} - R$ plane as shown in Figure 8.5, which builds upon the steady state vertical structure calculations (Z2009a; an analytical analysis is given in the Appendix). The shaded regions in Figure 8.5 are the radii at which disk accretion is expected to be unsteady if the mass infall rate is constant.

The solid curve farthest to the lower right in the Figure (labeled R_Q) is the radius where the central temperature of a pure GI-driven disk ($Q=1$ disk) would reach T_M (e.g. 1400 K). In other words, at a given infall rate \dot{M}_{in} , pure GI disks can accrete steadily beyond R_Q by the GI, but within R_Q the MRI will be activated. Up and to the left of R_Q in Figure 8.5 another solid curve, labeled R_M , denotes the radii at which a pure MRI disk of the given α_M would have a central temperature of T_M . If the disk is MRI active, it can accrete steadily purely by the MRI within R_M , but beyond R_M the MRI will be turned off. When R_M and R_Q cross a smooth transition between the GI and MRI exists and steady accretion is possible. From the left panel of Figure 8.5, we see that the disk can accrete steadily with $\alpha=0.01$ and $\dot{M}_{in} = 10^{-4} M_\odot \text{ yr}^{-1}$. This is observed in the time evolution discussed in chapter 7.5.1 and Figure 7.2 (see also Armitage et al. (2001)).

We predict that in the shaded regions matter will pile up through the action of GI, trigger the MRI, and produce an outburst. The dotted curve shows R_Q and R_M if $T_M=1800$ K (at which temperature all dust has sublimated). R_Q and R_M at 1800 K are smaller than they are at 1400 K because of the temperature plateau around

the dust sublimation temperature (Z2009a; also can be seen at $R \sim 2\text{--}10$ AU in Figs. 7.5). Thus if T_M is higher, outbursts are expected to be shorter because the outburst drains the small inner disk ($R < R_Q$) on a shorter viscous timescale (as demonstrated in Figures 7.2-7.4). The effect of α_M can also be seen by comparing the left and right panels of Figure 8.5.

The classical thermal instability will also be triggered at the infall phase as shown by the upper left shaded band in Figure 8.5. Even the ‘steady’ accretion case discussed above with $\alpha=0.01$ and $\dot{M}_{in} = 10^{-4}M_\odot \text{ yr}^{-1}$ is subject to thermal instability at $R < 1AU$. The two lines shown in Figure 8.5 correspond to the two limiting values of the “S curve” (e.g., Faulkner, Lin, & Papaloizou 1983) at which transition to the high (rapid accretion) state and the low (slow accretion) state occur. The instability depends on the disk’s vertical structure (different “S curves”) which behaves differently in 2-D than in 1-D, as discussed in chapter 7.4. We expect nature to behave somewhat more like the 2-D than the 1-D case, so for the steady accretion model discussed above convection will add small variations in \dot{M} and we refer to these steady accretion cases as quasi-steady. Generally, the thermally unstable region is distinctive at $\dot{M} > 10^{-5}M_\odot \text{ yr}^{-1}$, which suggests the TI may be common for protostellar disks.

The solid dots in Figure 8.5 are the MRI trigger radii from our 1-D simulations when $T_M = 1400\text{K}$. Although the trigger radii do not fall precisely on R_Q , most of them are in the shaded region, indicating that this $\dot{M} - R$ plane has predicted non-steady accretion, with potential outbursts, to occur for infall rates $\lesssim 10^{-5}M_\odot \text{ yr}^{-1}$ for $\alpha_M = 0.01$ and $\lesssim 10^{-4}M_\odot \text{ yr}^{-1}$ for $\alpha_M = 0.1$. For $\dot{M} = 10^{-4}M_\odot \text{ yr}^{-1}$ and $\alpha_M = 0.01$, the MRI-GI instability won’t occur based on this $\dot{M} - R$ plane, which agrees with the 1-D simulations. Generally, our $\dot{M} - R$ plane results provide a good guide to the parameters for which unsteady accretion occurs.

The outbursts and TI in quasi-steady accretion could provide a much hotter thermal history for the protostellar disks, which may have imprints on meteorites and the chemicals in the protostellar disks.

7.6.2 Steady vs Non-steady accretion

The non-steady disk accretion in our model is the result of the inability of the inner disk to transport mass inward at the same rate as mass is fed in from the outer disk by infall, $10^{-5}M_{\odot} \text{ yr}^{-1}$. This mass pileup eventually leads to MRI activation and outbursts. Even after infall ends, the dead zone evolves with time if the mass addition from the outer disk due to GI and viscous stresses exceeds what can be carried inward by the active layer.

Terquem (2008) was able to construct steady-state disk accretion solutions with active layers and "dead" zones. The difference is due to the assumptions of both finite, non-GI viscosity in the dead zone and to assuming a very much lower mass accretion rate, $10^{-8}M_{\odot} \text{ yr}^{-1}$. At such low accretion rates, even very low non-GI dead zone viscosities and comparable active layer properties suffice to transport mass at these rates through the inner disk, which is not possible in our disks driven on the outside at high mass infall rates (except for small centrifugal radii, in which case the disk becomes fully MRI-active).

7.6.3 Constraints from observations of FU Orionis objects

FU Orionis objects are outbursting systems with maximum disk accretion rates $\dot{M} \sim 10^{-4}M_{\odot} \text{ yr}^{-1}$ and a decay time of decades to hundreds of years (Hartmann & Kenyon 1996). These properties constrain our parameter space.

The outbursts produced by 1D2Z models are sensitive to α_M and T_M . Figures 2-4 show that $\alpha_M=0.1$, $T_M=1800$ K leads to outbursts that are too strong ($\dot{M}=10^{-3}M_{\odot} \text{ yr}^{-1}$), while $\alpha_M=0.01$, $T_M=1400$ K leads to outbursts that are too long (3000 yr)². If $T_M=1400$ K, the outburst start at ~ 3 AU (Figure 7.5), so α_M needs to be large to produce the correct decay timescale. If $T_M = 1800$ K the outburst is triggered at ~ 1 AU, so $\alpha_M \sim 0.01$ is required to maintain the correct outburst timescale.

²The observed decay time is $\sim \tau_d = (d \ln F / dt)^{-1}$ (F is the flux; thus τ_d is an e-folding time). In principle the outburst could have nonexponential time dependence and the duration of the outburst could differ from τ_d . In our models, however, the luminosity exceeds the preoutburst luminosity for a time only slightly longer than τ_d .

One uncertainty here is that α_M in a non-thermally ionized active layer may not be the same as α_M in a thermally ionized, dust free, fully conducting medium. Thus we mostly constrain α_M in the latter (outburst stage) from the decay timescale; α_M in the active layer is not well-constrained by outbursts.

Another uncertainty is related to our assumption of constant Σ_A . If Σ_A is instead a function of radius the disk's long term evolution will change. At early stages, however, if the GI in the outer disk dominates the disk's accretion, variation of Σ_A will have little effect on the outburst mechanism discussed here.

The central star mass and infall rate do not significantly change the outbursts. This agrees with the observation that FU Orionis outbursts occur for protostars with different infall rates (Quanz et al. 2007 and Zhu et al 2008 found that FU Orionis objects could be either Class 0 or Class I objects.).

Zhu et al. (2007) argued that the decay timescale for FU Ori implies $\alpha \sim 0.02-0.2$. This conclusion can be tested with our 1-D simulations. The last column in Table 7.1 shows the viscous timescale calculated using R_M and T_M :

$$t_v \sim \frac{R_M^2}{\nu}, \quad (7.20)$$

where

$$\nu = \alpha \frac{c_s^2}{\Omega}, \quad (7.21)$$

c_s and Ω are calculated with T_M and R_M .

Comparing with the outbursts' duration in column 6, we see the viscous time is close to the outburst time for $T_M=1400$ K. If $T_M=1800$ K, the viscous time is 2-3 times longer than the outburst time, which may be due to the disk's temperature during the outburst being higher than T_M if the MRI is triggered at smaller radius as $T_M=1800$ K case. However, since constraining α by using the viscous timescale is an order of magnitude estimate, our simulations are consistent with the Zhu et al (2007) estimate.

7.7 Conclusions

In this chapter, we have evolved a one-dimensional layered disk model including both MRI and GI to study the unsteady disk accretion of protostars. The 1-D models reproduce the general properties of 2-D (axisymmetric) outbursts reasonably well, such as the outbursting mass accretion rate, duration and the accreted mass during one outburst. Because the 1-D model is faster, it enables us to study outbursts in an extended parameter space.

Our results confirm that the disk can accrete steadily with high infall rates ($\dot{M}_{in} \sim 10^{-4} M_{\odot} \text{ yr}^{-1}$ if $\alpha_M = 0.01$; Armitage et al. (2001)). This steady accretion may still have short timescale variations, however, due to the thermal instability in the inner disk, as suggested by our earlier, 2-D simulations.

We also confirm the prediction by Z2009a that protostars are likely to accrete unsteadily/in outbursts for infall rates $\lesssim 10^{-5} M_{\odot} \text{ yr}^{-1}$ with $\alpha_M = 0.01$ and $\lesssim 10^{-4} M_{\odot} \text{ yr}^{-1}$ for $\alpha_M = 0.1$. Outbursts are triggered at $r \sim 1 - 10$ AU for protostellar infall rates $\sim 10^{-5} - 10^{-6} M_{\odot} \text{ yr}^{-1}$. The outbursts are stronger and shorter with larger α_M or T_M . The total mass accreted during one outburst mainly depends on T_M . While the outbursts are slightly shorter for more massive central stars, the outburst \dot{M} is nearly independent of central star mass. The active layer surface density only affects the mass accretion rate in the low state; it has little effect on the outburst.

By comparing with the mass accretion rate and duration of observed FU Orionis events, we can constrain a combination of α_M and T_M . If α_M is low (0.01), T_M needs to be high (1800 K, higher than the dust sublimation temperature); if α_M is high (0.1) then T_M needs to be low ($\lesssim 1400$ K).

Our results show that 1-D, two zone models can capture the basic features of disk evolution, given our assumptions about the action of the MRI and GI. In chapter 8 we will address disk evolution over a much longer timescale, explicitly taking into account mass infall from a rotating protostellar cloud.

7.8 appendix

By assuming a marginally gravitationally stable ($Q=1.5$) disk, the disk's structure is determined with a given \dot{M} , and thus the radius where the outburst is triggered (R_Q in Fig. 8.5 and Z2009a) can be derived. Unlike Z2009a where the detailed vertical structure is calculated numerically to give R_Q , here we give simple analytical results for R_Q by assuming the disk is vertically isothermal with constant opacity at a given radius.

First, if $\kappa=C\tau^\alpha P^\beta$, the relationship between Σ and the central (midplane) temperature T_c is given by

$$T_c^4 = \frac{3}{8} T_{eff}^4 \tau = \frac{3}{16} T_{eff}^4 \Sigma \kappa. \quad (7.22)$$

Using the form for κ and using $\rho_c = \Sigma/2H$, where H is the disk scale height,

$$T_c = 3^{1/(4-\alpha-\beta/2)} 2^{(-4-\beta)/(4-\alpha-\beta/2)} T_{eff}^{4/(4-\alpha-\beta/2)} \Sigma^{(1+\beta)/(4-\alpha-\beta/2)} C^{1/(4-\alpha-\beta/2)} \\ \times \Omega^{\beta/(4-\alpha-\beta/2)} \left(\frac{k}{\mu m_H} \right)^{\beta/(8-2\alpha-\beta)}, \quad (7.23)$$

or equivalently

$$\Sigma = 3^{-1/(1+\beta)} 2^{(4+\beta)/(1+\beta)} T_{eff}^{-4/(1+\beta)} T_c^{(4-\alpha-\beta/2)/(1+\beta)} C^{-1/(1+\beta)} \Omega^{-\beta/(1+\beta)} \left(\frac{k}{\mu m_H} \right)^{-\beta/(2+2\beta)}, \quad (7.24)$$

where Ω is the angular velocity at R , k is the Boltzmann constant and m_H is the unit molecular mass.

Then with $Q=c_s\Omega/\pi G\Sigma$, and inserting equation (7.24) into Q to derive the relationship between R and T_c at a given Q and \dot{M}

$$R = 3^{4/(9+6\beta)} 2^{(-14-2\beta)/(9+6\beta)} \pi^{(-4-2\beta)/(9+6\beta)} \left(\frac{\dot{M}_{in}}{\sigma} \right)^{2/(9+6\beta)} T_c^{(2\alpha+2\beta-7)/(9+6\beta)} C^{2/(9+6\beta)} \\ \times G^{1/(9+6\beta)} M^{(3+2\beta)/(9+6\beta)} \left(\frac{k}{\mu m_H} \right)^{(1+2\beta)/(9+6\beta)} Q^{(-2-2\beta)/(9+6\beta)}. \quad (7.25)$$

The dust opacity fitting from Z2009a suggests, at $T \lesssim 1400$ K, $\alpha=0.738$, $\beta=0$ and $C=0.053$. If we plot the relationship between R and \dot{M} by given $T_c=T_M=1400$ K

and $Q=1.5$, we find

$$R_Q = 11 \left(\frac{\dot{M}_{in}}{10^{-4} M_\odot \text{yr}^{-1}} \right)^{2/9} \left(\frac{M}{M_\odot} \right)^{1/3} \text{AU}, \quad (7.26)$$

which corresponds well with the R_Q calculated in Figure 8.5.

Since $R_Q \propto \dot{M}^{2/9}$ for $T_M=1400$ K case, the outburst timescale is roughly

$$t \sim \frac{R_Q^2}{\nu} \sim 960 \frac{0.1}{\alpha_M} \left(\frac{\dot{M}_{in}}{10^{-4} M_\odot \text{yr}^{-1}} \right)^{1/9} \left(\frac{M}{M_\odot} \right)^{2/3} \text{yr}, \quad (7.27)$$

where ν is calculated for $T_c=T_M=1400$ K. During outburst, however, T_c could be higher than the MRI trigger temperature T_M , especially in the inner part of the disk.

If we further assume the outburst $\dot{M} \sim \nu \Sigma(R_Q)$ (this is the steady accretion disk solution which may not be true in the time-dependent case), we find

$$\dot{M} \sim 3\pi\nu\Sigma \sim \frac{3\alpha_M c_{so}^2 c_{st}}{GQ}. \quad (7.28)$$

Here we explicitly distinguish between the sound speed c_{so} during the outburst and the sound speed c_{st} before MRI activation. For an order of magnitude estimate we assume $c_{so} \sim c_{st} \sim c_s(1400\text{K})$ and so

$$\dot{M} = 5 \times 10^{-4} \frac{\alpha_M}{0.1} M_\odot \text{yr}^{-1} \quad (7.29)$$

which agrees with the numerical simulations for $T_M=1400$ K reasonably well considering we are using a steady state assumption.

We have only applied the above equations for the $T_M=1400$ K case, since the detailed vertical structure is important if $T_M=1800$ K where the midplane is dust-free while the surface has dust. Also the outburst is triggered at a smaller radius for $T_M=1800$ K, and thus the disk temperature during the outburst can be much higher than the MRI trigger temperature.

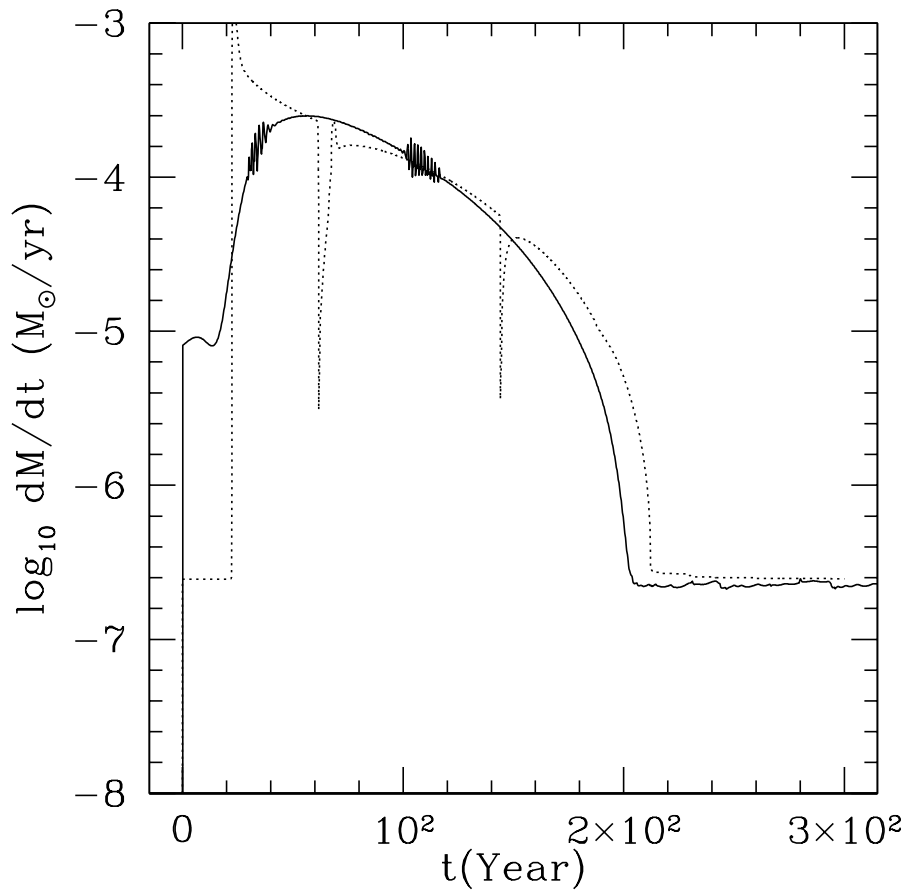


Figure 7.1 The mass accretion rate with time for both 1-D (dotted curve) and 2-D (solid curve) simulations.

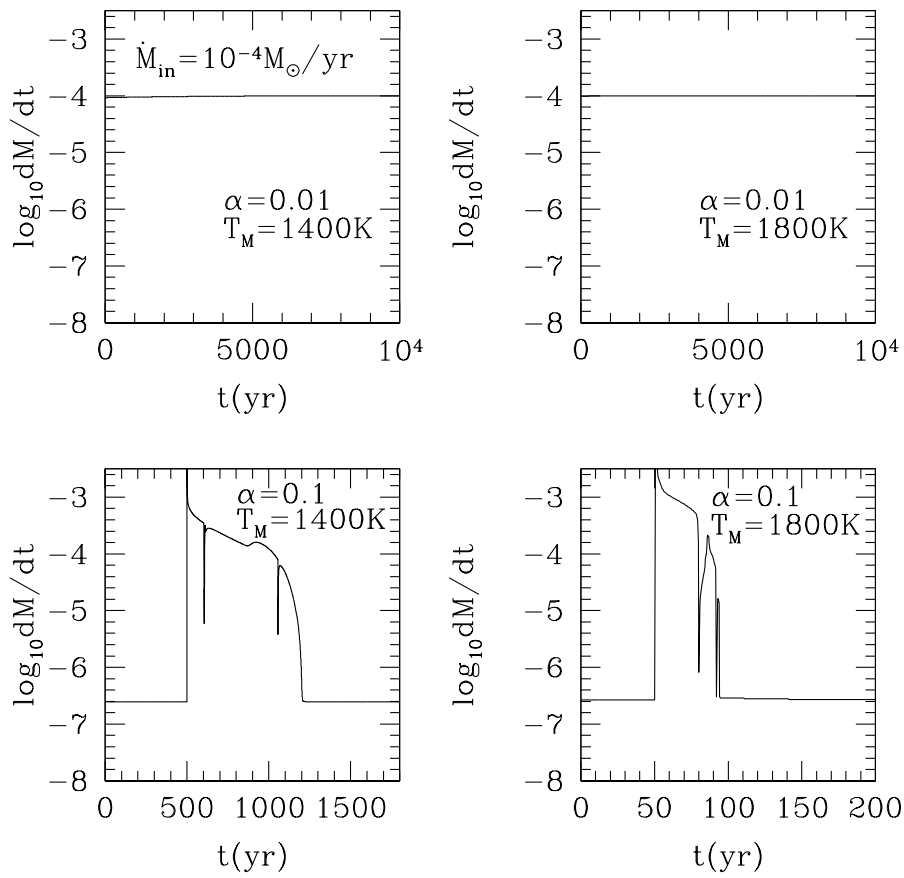


Figure 7.2 The mass accretion rate with time for different α_M and T_M for the mass infall rate of $10^{-4} M_{\odot} \text{yr}^{-1}$.

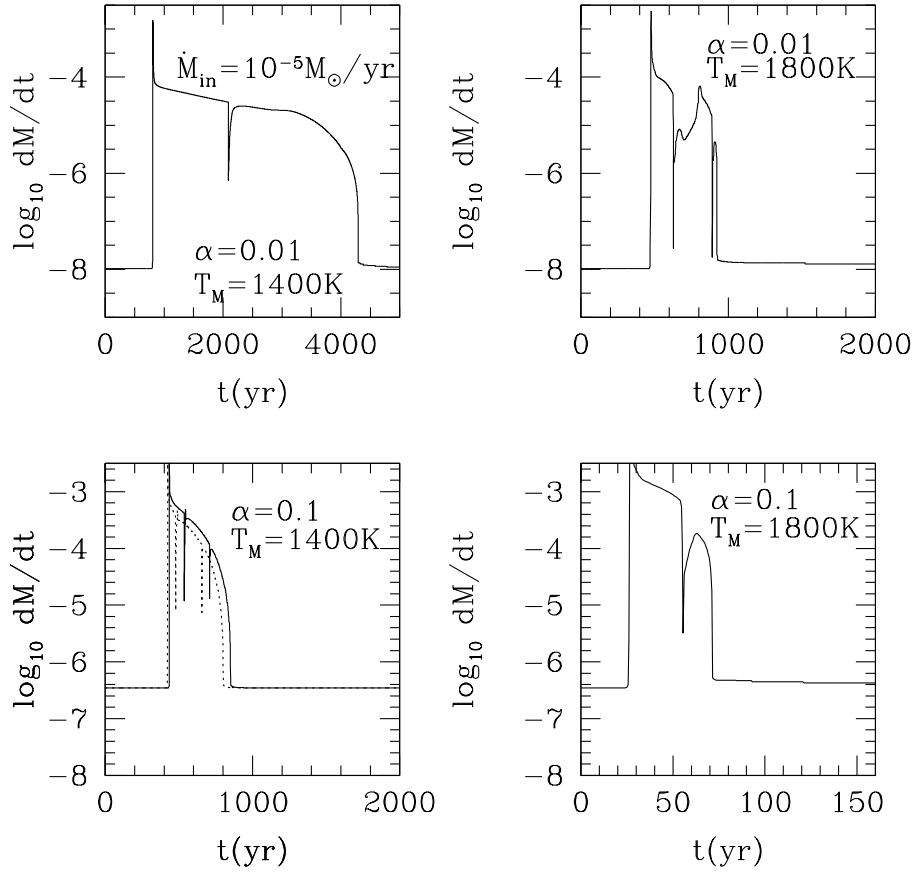


Figure 7.3 The mass accretion rate with time for different α_M and T_M for the mass infall rate of $10^{-5} M_{\odot} yr^{-1}$. Compared with the solid curves which are from the simulation with $\alpha_Q = \exp(-Q^4)$, the dotted curve in the lower left panel shows the outburst obtained using the α_Q prescription of Armitage et al. (2001).

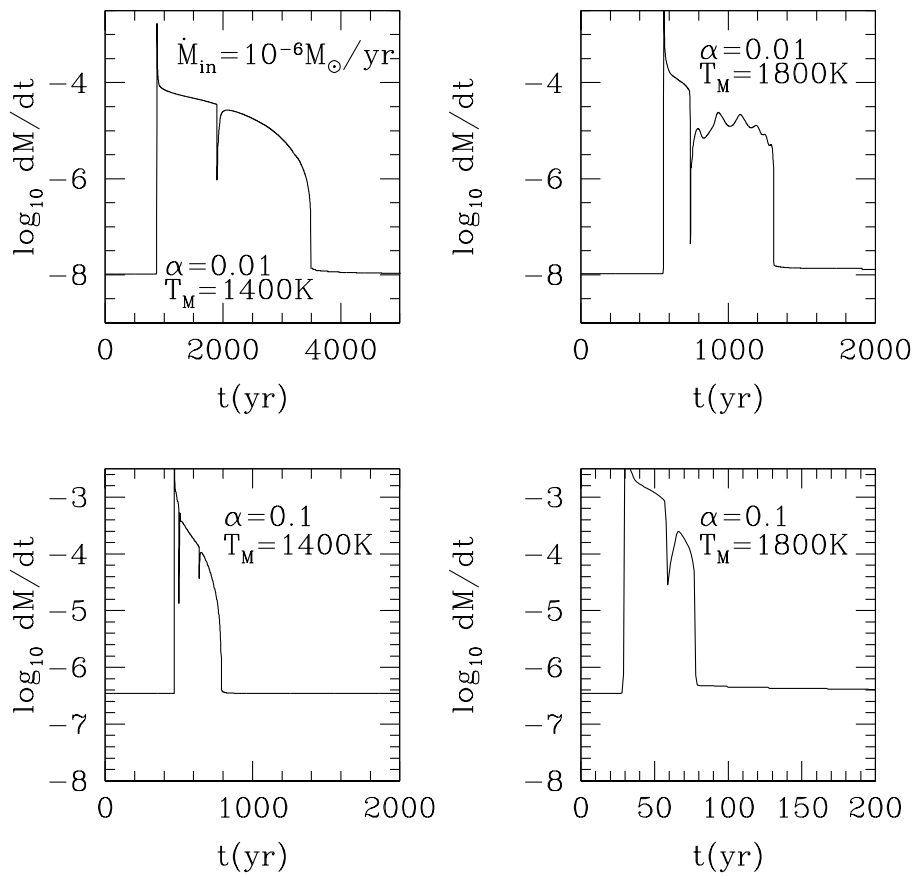


Figure 7.4 The mass accretion rate with time for different α_M and T_M for the mass infall rate of $10^{-6} M_{\odot} yr^{-1}$.

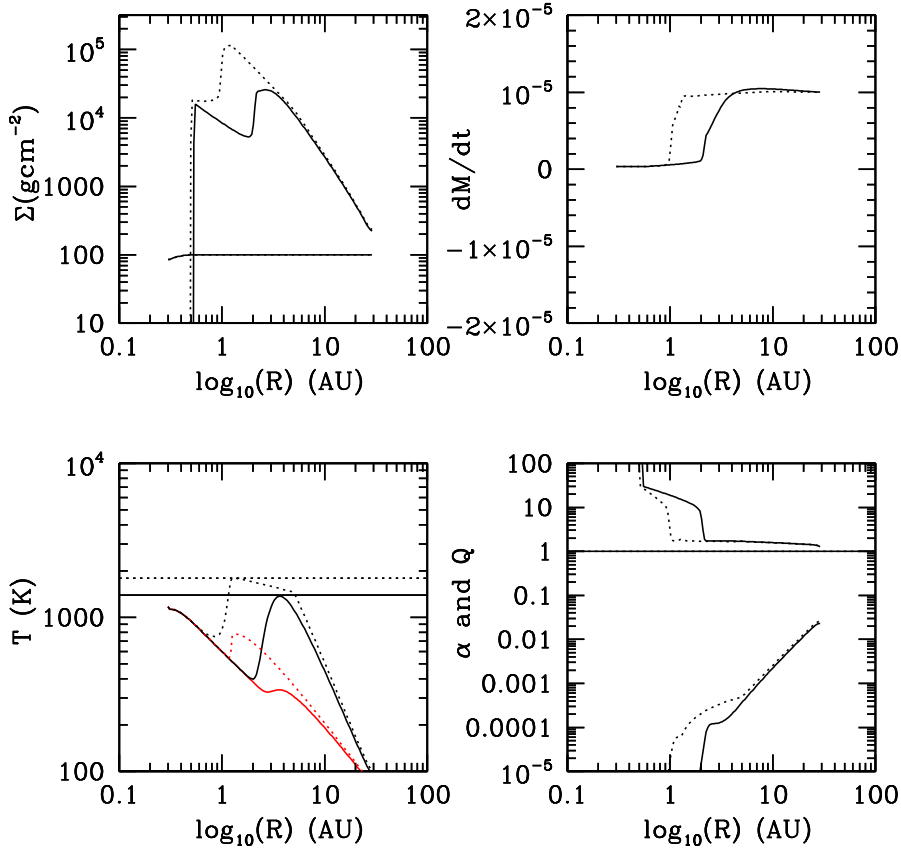


Figure 7.5 The disk's radial structure at the stage just before the MRI is triggered in cases where $T_M = 1800$ K (dotted curve) and $T_M = 1400$ K (solid curve). The horizontal dotted line in the lower left panel shows $T_M = 1400$ K. The MRI is triggered at ~ 3 AU for $T_M = 1800$ K case and at ~ 1.5 AU for $T_M = 1400$ K case.

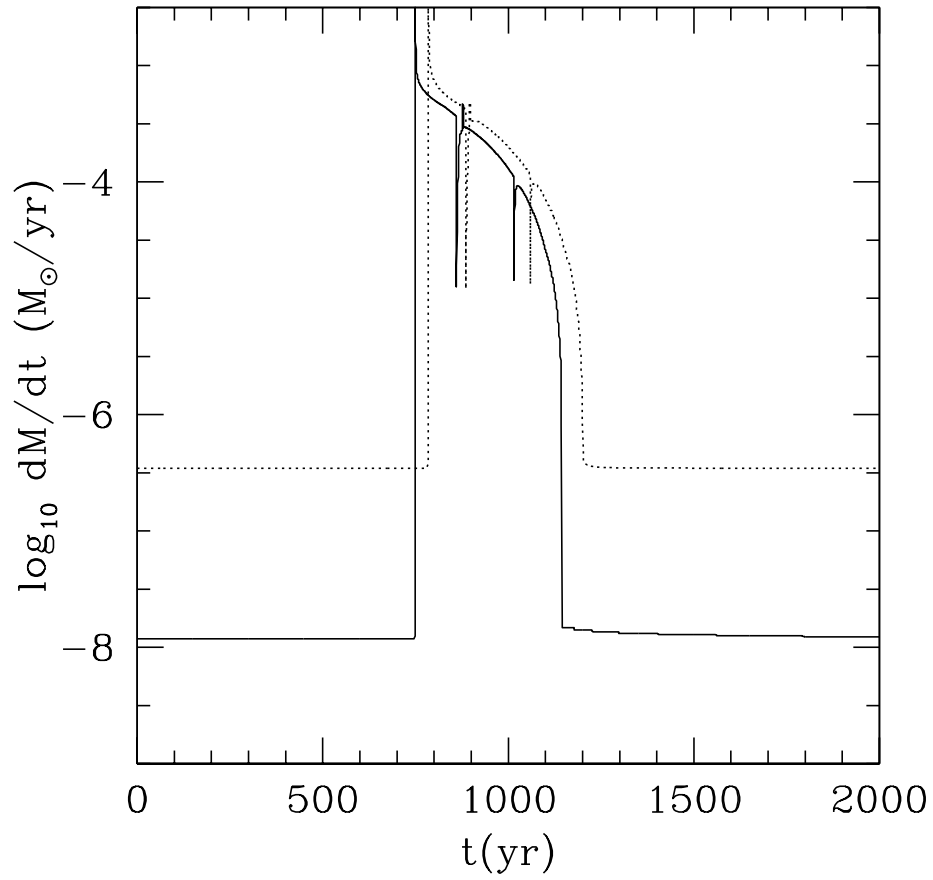


Figure 7.6 The disk mass accretion rate with time for different active layer surface density (50 g cm^{-2} for the dotted curve and 10 g cm^{-2} for the solid curve). $\alpha_M=0.1$ and $T_M=1400 \text{ K}$.

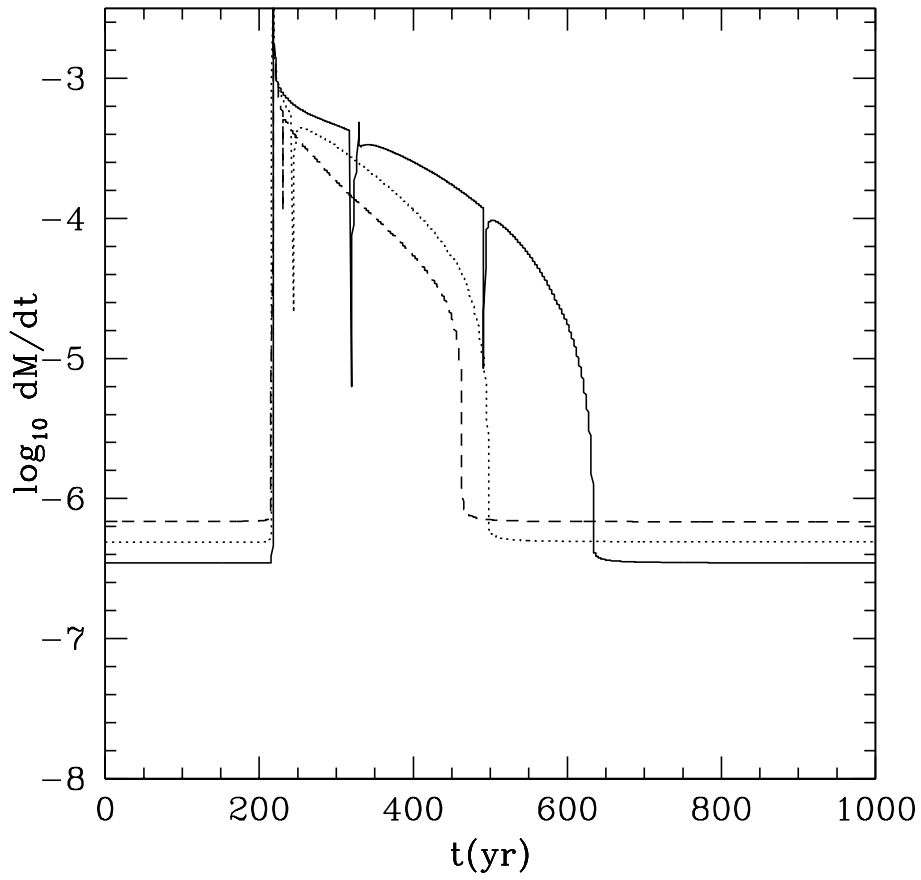


Figure 7.7 The mass accretion rate with time for different central star masses: $1 M_{\odot}$ (solid curve), $0.3 M_{\odot}$ (dotted curve), $0.1 M_{\odot}$ (dashed curve). The infall rate is $10^{-5} M_{\odot} \text{ yr}^{-1}$, $T_M=1400 \text{ K}$, and $\alpha=0.1$.

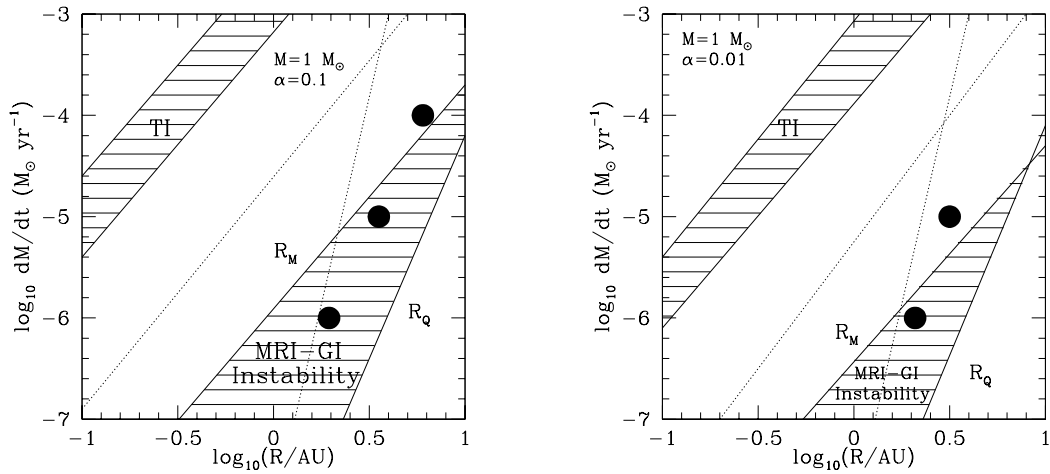


Figure 7.8 Unstable regions in the $R - \dot{M}$ plane for a $1M_{\odot}$ central star. The shaded region in the lower right shows the MRI-GI instability with the MRI trigger temperature of 1400 K. The dotted curves show R_M and R_Q (the boundaries of the MRI-GI instability shaded region; see text for definition) for an MRI trigger temperature of 1800 K. The shaded region in the upper left shows the region subject to classical thermal instability. The solid dots represent the radii where the MRI is triggered in 1-D simulations for $T_M=1400$ K.

Table 7.1 1D2Z models

M_* M_\odot	infall rate $M_\odot \text{ yr}^{-1}$	α	T_M K	outburst \dot{M}^a $M_\odot \text{ yr}^{-1}$	duration yr	accreted mass ^b M_\odot	R_M^c AU	viscous time ^d yr
1	10^{-4}	0.1	1400	2×10^{-4}	700	0.7	6	428
1	10^{-4}	0.1	1800	10^{-3}	50	0.02	1.8	182
1	10^{-5}	0.1	1400	2×10^{-4}	400	0.057	3.5	327
1	10^{-5}	0.1	1800	10^{-3}	40	0.024	1.2	150
1	10^{-5}	0.01	1400	5×10^{-5}	4000	0.045	3.2	3127
1	10^{-5}	0.01	1800	8×10^{-5}	400	0.01	1.2	1490
1	10^{-6}	0.1	1400	2×10^{-4}	350	0.08	1.9	240
1	10^{-6}	0.1	1800	10^{-3}	50	0.02	0.85	125
1	10^{-6}	0.01	1400	5×10^{-5}	3000	0.04	2.1	2533
1	10^{-6}	0.01	1800	8×10^{-5}	800	0.015	0.87	1268
0.3	10^{-5}	0.1	1400	2×10^{-4}	300	0.04	2.3	145
0.1	10^{-5}	0.1	1400	2×10^{-4}	250	0.025	1.43	66

^athe mass accretion rate at the half-time of the outburst

^bthe mass accreted during one outburst

^cthe MRI trigger radius

^dThe viscous timescale is calculated by using R_M and T_M .

CHAPTER 8

Long-term Evolution of Protostellar and Protoplanetary Disks. II. Layered Accretion with Infall

8.1 Abstract

We use one-dimensional two-zone time-dependent accretion disk models to study the long-term evolution of protostellar disks subject to mass addition from the collapse of a rotating cloud core. Our model consists of a constant surface density magnetically coupled active layer, with transport and dissipation in inactive regions only via gravitational instability. We start our simulations after a central protostar has formed, containing $\sim 10\%$ of the mass of the protostellar cloud. Subsequent evolution depends on the angular momentum of the accreting envelope. We find that disk accretion matches the infall rate early in the disk evolution because much of the inner disk is hot enough to couple to the magnetic field. Later infall reaches the disk beyond ~ 10 AU, and the disk undergoes outbursts of accretion in FU Ori-like events as described in Zhu et al. 2009c. If the initial cloud core is moderately rotating most of the central star’s mass is built up by these outburst events. Our results suggest that the protostellar “luminosity problem” is eased by accretion during these FU Ori-like outbursts. After infall stops the disk enters the T Tauri phase. An outer, viscously evolving disk has structure that is in reasonable agreement with recent submillimeter studies and its surface density evolves from $\Sigma \propto R^{-1}$ to $R^{-1.5}$. An inner, massive belt of material—the “dead zone”—would not have been observed yet but should be seen in future high angular resolution observations by EVLA and ALMA. This high surface density belt is a generic consequence of low angular momentum transport efficiency

at radii where the disk is magnetically decoupled, and would strongly affect planet formation and migration. This chapter has been published in the paper: “Long-term Evolution of Protostellar and Protoplanetary Disks. II. Layered Accretion with Infall”, 2010, *ApJ*, 713, 1143 with Lee Hartmann, and Charles Gammie.

8.2 Introduction

In the picture of low-mass star formation from large, cold protostellar clouds, any small initial rotation of the cloud will lead to the formation of an accretion disk to conserve angular momentum; thus much, if not most, of the mass of low-mass stars is probably accreted from disks. However, if disks transport the infalling mass steadily to the central star, accretion luminosities are considerably higher than typically observed protostellar luminosities (Kenyon et al. 1990, 1994; Enoch et al. 2008; Evans et al. 2009). This “luminosity problem” can be alleviated if disks spend most of their evolution accreting slowly, undergoing episodic accretion outbursts where most of the mass is added to the central stars. One implication of non-steady accretion is that mass may pile up in specific regions of disks, which could have significant consequences for understanding planet formation.

Over the past decade, disk angular momentum transport by the magnetorotational instability (MRI) (Balbus & Hawley 1998) and by the gravitational instability (GI) (Durisen et al. 2007) has become much better understood. It seems likely that both types of instability need to be considered to understand protostellar accretion. At early evolutionary stages the disk is likely to be quite massive with respect to the central protostar, suggesting that GI may be important; in addition, these disks are so cold that thermal ionization cannot sustain the MRI, which requires coupling of the magnetic field to the mostly-neutral gas through collisions (e.g., Reyes-Ruiz & Stepinski 1995). On the other hand, external ionizing sources (cosmic and/or X rays) can provide the necessary ionization for MRI activation up to a limiting surface density, ionizing the outer surfaces of the disk and leading to accretion in an “active layer”, leaving a “dead zone” in the midplane (Gammie 1996). In addition, at high accretion rates, the inner disk can become thermally-ionized, as in FU Ori outbursts

(Zhu et al. 2007, 2009b).

Mismatches in the transport rate between the GI and MRI can lead to outbursts of accretion (Armitage et al. 2001, Zhu et al. 2009 bc). In Zhu et al. 2010 (chapter 7), we constructed one-dimensional, time-dependent disk models to study the protostellar unsteady accretion. These models assume both thermally-activated and layered MRI-driven accretion along with a local treatment of the GI. We further adopted steady mass addition at a specified outer disk radius to drive the system. We found that accretion in protostellar disks is unsteady over a wide range of parameters because of a mismatch between GI transport in the outer disk and MRI transport in the inner disk. Our results for outburst behavior in these one-dimensional model were sufficiently comparable to our previous two-dimensional simulations of outbursts (Zhu et al. 2009c), confirming the utility of the faster 1D simulations to explore wider ranges of parameter space.

In this chapter we extend our results from chapter 7 to study long-term disk evolution from the protostellar phase to the T Tauri phase, using a more self-consistent treatment for infall from a collapsing, rotating cloud core. This allows us to study the effect of the initial core rotation and different disk accretion configurations (layered accretion, GI-only accretion, and constant- α accretion) on the disk formation and evolution. Rice, Mayo, & Armitage (2009) have also investigated somewhat similar one-dimensional models but do not assume layered accretion.

Our models treat the same phase of evolution as Vorobyov & Basu (2005, 2006, 2007) investigated with two-dimensional models. They also argue that protostellar accretion is generally non-steady, but for a different reason, specifically the accretion of clumps created by gravitational instabilities. Kratter et al. (2010) have also investigated the protostellar accretion phase with three-dimensional numerical simulations. Although our treatment of the core collapse and the GI is much more schematic than used in the above investigations, we are able to treat radiative cooling more realistically, and can follow disk evolution to much smaller radii, where the (thermally-activated) MRI can become important. Furthermore, our two-zone disk model allows us to study the effects of different disk accretion configurations

efficiently. The variety of disk structures predicted by our simulations with different initial cloud core rotations and disk accretion mechanisms can be tested by future EVLA and ALMA observations, which will help us to better understand disk accretion and planet formation.

We describe our one-dimensional, two-zone model with self-consistent infall in chapter 8.3. In chapter 8.4 we explore the behavior of the disk models with infall. In chapter 8.5 we discuss the implications of our results, and summarize our conclusions in chapter 8.6. We defer all derivations to the chapter 8.7 and 8.8.

8.3 1D2Z models with infall

The one-dimensional two zone (1D2Z) disk model has been introduced in chapter 7. It consists of two vertically averaged layers (the surface layer and the “dead zone”) evolving independently. The surface density evolves according to the mass and angular momentum conservation equations in cylindrical coordinates,

$$2\pi R \frac{\partial \Sigma_i}{\partial t} - \frac{\partial \dot{M}_i}{\partial R} = 2\pi g_i(R, t), \quad (8.1)$$

$$2\pi R \frac{\partial}{\partial t} (\Sigma_i R^2 \Omega) - \frac{\partial}{\partial R} (\dot{M}_i R^2 \Omega) = 2\pi \frac{\partial}{\partial R} (R^2 W_{R\phi, i}) + 2\pi \Lambda_i, \quad (8.2)$$

where Σ is the total surface density, Ω is the angular frequency, $\dot{M}_i = -2\pi \Sigma_i R v_i$ is the radial mass flux in the disk, $W_{R\phi, i} = R \Sigma_i \nu_i d\Omega/dR$, ν_i is the viscosity, and i denotes ‘a’ (active layer) or ‘d’ (dead zone). $2\pi g_i(R, t)$ and $2\pi \Lambda_i$ are the mass and angular momentum flux brought by the infalling matter into the disk (Cassen & Moosman 1981). Assuming instantaneous centrifugal balance,¹ equations 8.1 and 8.2 can be simplified to

$$\begin{aligned} \dot{M}_i &= 6\pi R^{1/2} \frac{\partial}{\partial R} (R^{1/2} \Sigma_i \nu_i) + \frac{2\pi R^2 \Sigma_i}{M_r} \frac{\partial M_r}{\partial t} \\ &\quad - 4\pi \left(\frac{R}{GM_r}\right)^{1/2} (\Lambda_i - g(R, t) R^2 \Omega(R)), \end{aligned} \quad (8.3)$$

¹The validity of this assumption with infall has been shown in Appendix B in Cassen & Moosman (1981). Instantaneous centrifugal balance is a good approximation in our simulations because the change of the central star mass on an orbital time is very small.

where M_r is the sum of the mass of the central star (M_c) and the disk mass within R , using the approximation of the gravitational potential adopted by Lin & Pringle (1990). The first term in equation 8.3 represents disk accretion due to viscosity; the second term is due to the central star mass changing with time; and the third term is due to the infalling matter (Cassen & Moosman 1981). Since the infalling matter only falls onto the surface of the disk, we assume g_d and Λ_d are 0, thus g_a and Λ_a can be written as g and Λ for short. The effect of the infalling matter onto the disk is limited to just two free functions: $g(R,t)$ and $\Lambda(R,t)$.

The surface densities Σ_a and Σ_d exchange mass as described in chapter 7 to maintain $\Sigma_a \leq \Sigma_A$, where Σ_A is the maximum MRI active layer surface density and is assumed to be a constant throughout the disk (Gammie 1996). We solve equation 8.3 and 8.1 sequentially: \dot{M}_i is calculated with the current disk temperature and Σ_i , and then it is inserted into equation 8.1 to update Σ_i at the next timestep.

The disk temperature is determined by the balance between the heating and radiative cooling. Here the external temperature T_{ext} , which represents the heating effect of the irradiation from the central star is assumed to be

$$T_{ext}^4 = \frac{fL}{4\pi R^2\sigma}, \quad (8.4)$$

where L is the total luminosity of the star and changes with the central star mass by

$$\frac{L_*}{L_\odot} = \frac{8M_*}{9M_\odot} + \frac{1}{9} \quad (8.5)$$

which is a fit to the T-Tauri star birthline from Kenyon & Hartmann(1995). The change of luminosity has little effect on the disk evolution in our simulations. σ is the Stefan-Boltzmann constant, and f is the coefficient, which accounts for the non-normal irradiation from the central star at the disk's surface. We assume $f=0.1$ in this chapter. The viscous heating rate of the disk is

$$Q_{visc} = \frac{3}{2}W_{R\phi}\Omega, \quad (8.6)$$

where the stress $W_{R\phi} = 3/2\Sigma_i\nu_i\Omega$ assuming Keplerian rotation. Both gravitational and magneto-rotational instabilities are considered. The anomalous viscosity ν_i is

$$\nu_i = \alpha_i \frac{c_{s_i}^2}{\Omega}, \quad (8.7)$$

where c_{s_i} are the sound speed of the active layer and the dead zone, $\alpha_i = \alpha_Q + \alpha_M$ and

$$\alpha_Q = e^{-Q^4}. \quad (8.8)$$

The Toomre parameter Q is calculated using the disk central temperature (T_d) and the total surface density ($\Sigma_a + \Sigma_d$). The form of α_Q is motivated by a desire to make gravitational torques become important only when $Q \lesssim 1.4$, as indicated by global three-dimensional simulations (e.g., Boley et al 2006). The parameter α_M is set to be 0.01 when the disk temperature is above the preset critical MRI temperature for thermal activation ($T_M=1500$ K is assumed in this chapter) or at the surface active layer. Since the rise time of MRI is about the orbital timescale (Stone et al. 1996), we assume that the MRI viscosity grows on the orbital timescale up to α_M whenever the temperature is above the critical temperature (T_M). The effects of different values of α_M , T_M , and Σ_a on outbursts are discussed in chapter 7. The treatment of radiative cooling is the same as in chapter 7.

Recent observations suggest that the density structure of protostellar molecular cores, when circularly-averaged, can be approximated by static Bonnor-Ebert spheres (Alves et al. 2001; di Francesco et al. 2007; Ward-Thompson et al. 2007). Though real clouds have more complex structure (e.g., Benson & Myers 1989), resulting in more complicated patterns of infall (Kratte et al. 2010), we adopt this simplified structure to limit the number of model parameters. This leads us to use an approximate model of infall corresponding to that expected from a critical Bonnor-Ebert sphere, which exhibits similarities to that of the collapse of the singular isothermal sphere (Terebey, Shu, & Cassen 1984).

Analytical and numerical studies (Foster & Chevalier 1992; Henriksen et al. 1997; Gong & Ostriker 2009) have shown that the collapse of the critical Bonnor-Ebert

sphere can be divided into two stages. In the first stage, the roughly constant-density inner region collapses to the central regions nearly simultaneously; then in the second stage, infall from the remaining cloud core ($\rho \propto r^{-2}$ region ²) is at a rate similar to c_{sc}^3/G (c_{sc} is the sound speed at the cloud core temperature) of the singular isothermal sphere (SIS) collapse model (Shu 1977). We assume that our simulation starts at the end of the first stage of very rapid collapse of low-angular momentum material, so the central star initially has the mass of the inner flat region of the Bonnor-Ebert sphere, and the collapse of the remaining cloud follows the singular isothermal sphere solution (Shu 1977).

We use a two-component density profile to represent the Bonnor-Ebert sphere as in Henriksen et al. (1997). The two density components are

$$\rho = \rho_c \text{ at } \xi < \sqrt{2}, \quad (8.9)$$

$$\rho = 2\rho_c \xi^{-2} \text{ at } \sqrt{2} < \xi < 6.5, \quad (8.10)$$

where ρ_c is the central density, r is in the normalized unit $\xi = r/(c_{sc}^2/4\pi G\rho_c)^{1/2}$, c_{sc} is the sound speed of the cloud and $\rho = 2\rho_c \xi^{-2}$ is the density profile of the SIS model. $\xi=6.5$ corresponds to the critical Bonnor-Ebert sphere radius and the radius of the flat density region $\xi = \sqrt{2}$ corresponds to $r_{ic}=(c_{sc}^2/2\pi G\rho_c)^{1/2}$. The total mass of each component is

$$M(r < r_{ic}) = \frac{0.27c_{sc}^3}{G^{3/2}\rho_c^{1/2}} \quad (8.11)$$

$$M(r_{ic} < r < r_{cr}) = \frac{2.88c_{sc}^3}{G^{3/2}\rho_c^{1/2}}. \quad (8.12)$$

The total mass with this simplified density profile is $3.1c_{sc}^3/G^{3/2}\rho_c^{1/2}$, which is close to the mass of a real critical Bonnor-Ebert sphere $4.2c_{sc}^3/G^{3/2}\rho_c^{1/2}$. Since the flat inner region has 10% mass of the r^{-2} region, we assume the flat region has $0.1 M_\odot$ and the rest of the Bonnor-Ebert sphere has $1 M_\odot$.

²In this chapter, R denotes the cylindrical radius in the disk while r denotes the radius in the cloud core.

The rest of the $1 M_{\odot}$ cloud core beyond r_{ic} collapses in a manner similar to that of the singular isothermal sphere, in which case the inner regions collapse first due to their shortest free-fall times and this free-fall zone extends outwards linearly with time ($m_0 c_{sc} t$, where $m_0=0.975$.) (Shu 1977; Terebey, Shu, & Cassen 1984). Thus, the mass infall rate is $\dot{M}_{in}=m_0 c_{sc}^3/G$, which is constant during the collapse. At time t , all the material collapsing to the center was originally at the cloud radius $r_0=(m_0/2)c_{sc}t+r_{ic}$, where the addition of r_{ic} (the radius of the flat density region in the Bonnor-Ebert sphere) is due to the fact that we define $t=0$ as the time when the flat region in the Bonnor-Ebert sphere has already collapsed to the central star. If the protostellar cloud core is initially in uniform rotation with angular velocity Ω_c , the material falling in from different directions will have different angular momenta and arrive at the midplane at differing radii within the so called ‘‘centrifugal radius’’ (Cassen & Moosman 1981)

$$R_c = r_0^4 \frac{\Omega^2}{GM_c}, \quad (8.13)$$

where M_c is the central star mass. Assuming M_c increases with t , $R_c \propto t^3$, similar to that found by Terebey, Shu, & Cassen (1984) for the singular isothermal sphere collapse.

We use the Cassen & Moosman (1981) solution for the infall to the disk at a given time from a spherical cloud initially in uniform rotation. We start the infall from the transition radius r_{ic} at $t = 0$. Then the mass flux $g(R, t)$ and the angular momentum Λ brought by the infalling matter for a uniformly-rotating singular isothermal sphere is,

$$g(R, t) = \frac{\dot{M}_{in}}{4\pi R_c} \left(1 - \frac{R}{R_c}\right)^{-1/2}, \quad (8.14)$$

$$\Lambda(R, t) = g(R, t)R \left(\frac{GM_c}{R_c}\right)^{1/2} \quad \text{if } R \leq R_c, \quad (8.15)$$

and

$$g(R, t) = 0, \quad (8.16)$$

$$\Lambda(R, t) = 0 \quad \text{if } R > R_c. \quad (8.17)$$

where $\dot{M}_{in} = (m_0 c_{sc}^3 / G)$ is the infall rate and R_c is the centrifugal radius defined in equation 8.13. Inserting equations 8.14-8.17 into equations 8.1-8.3, we can simulate the disk evolution under the infall.

8.4 Layered accretion with infall

In all cases we start with $M_c = 0.1 M_\odot$ and a cloud mass of $1 M_\odot$. We adopt a temperature of 20K for the envelope. This parameter enters in setting the infall rate $\dot{M}_{in} = c_s c^3 / G = 4.2 \times 10^{-6} M_\odot \text{ yr}^{-1}$; thus the infall lasts $2.4 \times 10^5 \text{ yr}$, roughly consistent with observations (Kenyon et al 1990, 1994; Evans 2009). This leaves only one parameter to vary, the initial angular velocity of the cloud Ω_c , which affects the maximum centrifugal radius onto the resulting disk. For a singular isothermal sphere (SIS) core,

$$R_{cmax} \approx \frac{G^3 M_{co}^3 \Omega^2}{16 c_{sc}^8}, \quad (8.18)$$

where we have assumed that the central star mass at the end of infall is approximately the cloud core mass (M_{co}); thus

$$R_{cmax} \approx 12 \text{ AU} \left(\frac{\Omega_c}{10^{-14} \text{ rad s}^{-1}} \right)^2. \quad (8.19)$$

Since R_{cmax} directly constrains the disk size after the infall, it is the most important parameter determining the initial disk properties.

8.4.1 Fiducial model

We take as our fiducial model one with $\Sigma_A = 100 \text{ g cm}^{-2}$, $\alpha_M = 0.01$, and $\Omega_c = 10^{-14} \text{ rad s}^{-1}$ so that $R_{cmax} = 12 \text{ AU}$.

Figure 8.1 shows the fiducial model's mass accretion rate and the central star and disk masses as a function of time. The overall evolution can be divided into three distinct stages. Initially there is a phase of quasi-steady disk accretion, with the accretion rate matching the infall rate ($\dot{M}_{in} = 4.2 \times 10^{-6} M_\odot \text{ yr}^{-1}$). This occurs because the infall is to small radii where the disk can become hot enough to sustain the MRI thermally. As infall proceeds, thermal activation of the MRI cannot be sustained, and

gravitational instability takes over as the main mechanism of mass transfer. However, the GI is inefficient at these radii and so matter piles up. Eventually, the disk becomes opaque enough that the radiative trapping of the energy dissipated by the GI raises the central disk temperature sufficiently to thermally-activate the MRI, and an outburst of accretion occurs. As shown in chapter 7, the result is cycles of outbursts transferring material inward; the GI moves material in slowly until enough mass is accumulated with enough viscous dissipation to trigger the thermal MRI outbursts. Finally, after infall stops, the disk is not massive enough to sustain GI, and it accretes only from the MRI active layer. Since the outer disk has a surface density smaller than the maximum surface density that can be ionized by cosmic and/or X rays, it becomes fully viscous due to the MRI; this leads to continued expansion of the outer disk, with a slow draining of material into the inner disk and central star. During the T Tauri phase, the layered accretion itself may also trigger outbursts, depending on the detailed layered structure (see below).

The disk structure during the outburst stage is illustrated in Figure 8.2, shown at the time when the centrifugal radius (R_c) is 10 AU (labeled by the triangle). Although the infall ends at R_c , the disk extends far beyond R_c due to the outward mass transfer by the active layer. With the continuous infall, the disk is marginally gravitationally stable within R_c , and the energy dissipation due to the GI has significantly heated the disk so that the outburst will be triggered at 2 AU (the upper right panel shows that T_c is approaching 1500 K). At the time when infall ends, the region between ~ 1 AU and ~ 20 AU is still marginally gravitationally unstable, although the disk within 1 AU has been depleted by the previous outburst (Figure 8.3).

The innermost disk ($R < 0.1$ AU) is purely MRI active due to the high temperature there produced by viscous heating and irradiation. Due to the efficient mass transport by the MRI, this inner region can be depleted rapidly, but is limited by the accretion from the outer active layer. Eventually, a balance is achieved, and the inner disk behaves like a constant- α disk with mass accretion rate equal to the mass accretion rate of the innermost active layer (e.g., Gammie 1996).

In the standard layered accretion model, the disk mass accretion rate is set as

the active layer accretion rate at the dead zone inner radius where the MRI becomes thermally activated (e.g., Gammie 1996). We use the modification of the accretion rate including irradiation derived by Hartmann et al. (2006; see also the Appendix)

$$\dot{M} = 6.9 \times 10^{-9} \left(\frac{R}{0.2 \text{ AU}} \right) \left(\frac{M_c}{1 M_\odot} \right)^{-1/2} \left(\frac{\alpha_M}{10^{-2}} \right) \times \left(\frac{\Sigma_A}{100 \text{ g cm}^{-2}} \right) \left(\frac{L_*}{L_\odot} \right)^{1/4} \left(\frac{f}{0.1} \right)^{1/4} M_\odot \text{ yr}^{-1}, \quad (8.20)$$

where f is defined in equation 8.4. At the sublimation radius, f may be significantly larger than 0.1. With our numerical inner boundary 0.2 AU, the simulation shows the disk has a mass accretion rate $10^{-8} M_\odot \text{ yr}^{-1}$ in the quiescent state, which agrees with the above estimate.

As discussed in chapter 7, we find unstable behavior at the dead zone inner radius because of the rapid change in α_M . This accounts for the modest but significant variability seen during the quasi-steady state³. This instability cannot be reliably treated in our model, due to the complexity of the processes involved including MRI activation and dust sublimation; thus the precise nature of the variations in accretion during this phase is uncertain.

A massive, marginally gravitationally unstable dead zone remains well after the end of infall (upper left and lower right panels in Figure 8.3). This dead zone is maintained because the active layer mass accretion rate increases with radius (Gammie 1996). From the mass conservation equation one can derive the time dependence of

³Although we avoided this instability at the T Tauri phase by choosing the inner numerical boundary at 0.2 AU, this instability is present in our simulation in the first 10^5 years (short variations in Figure 8.1) when the dead zone inner radius is larger than 0.2 AU.

the total surface density $\Sigma = \Sigma_A + \Sigma_d$,

$$\begin{aligned} \frac{\partial \Sigma}{\partial t} &= -\frac{\partial}{R \partial R} \left(\frac{\dot{M}}{2\pi} \right) \\ &= 0.05 \left(\frac{1 \text{AU}}{R} \right) \left(\frac{M}{1 M_\odot} \right)^{-1/2} \left(\frac{\alpha_M}{10^{-2}} \right) \left(\frac{\Sigma_A}{100 \text{g cm}^{-2}} \right) \times \\ &\quad \left(\frac{L_*}{L_\odot} \right)^{1/4} \left(\frac{f}{0.1} \right)^{1/4} \text{g cm}^{-2} \text{yr}^{-1}. \end{aligned} \quad (8.21)$$

Thus $\partial \Sigma / \partial t > 0$ and $\propto R^{-1}$. The disk surface density thus increases linearly with time, more rapidly at smaller radii. When the surface density increases to the extent that the disk becomes gravitationally unstable, self-gravity transfers the excess mass and self-regulates the disk to an approximate $Q \sim 1$ state. From equation 8.21 one can see that it only takes 10^5 yr for the disk at 10 AU to become gravitationally unstable by layered accretion. Thus, active-layer accretion can maintain a dead zone that is marginally gravitationally unstable well after infall stops.

A sharp density drop appears at the outer radius of the dead zone R_D (also shown in Reyes-Ruiz(2007) and Matsumura et al.(2009)) and R_D starts at the maximum centrifugal radius after the infall and gradually moves inward with time, so that the dead zone becomes increasingly narrow as the system evolves (see the chapter 8.7 Appendix). In the outer disk beyond R_D where only the active layer is present, the disk surface density evolves from a $\Sigma \propto R^{-1}$ distribution to an asymptotic $\Sigma \propto R^{-1.5}$ distribution at large times. This result can be understood by modeling it as a pure α disk but with a fixed Σ inner boundary, as discussed in the chapter 8.7 Appendix.

8.4.2 Varying core rotation

The initial disk size is constrained by the maximum infall radius R_{cmax} . We next consider the results for $\Omega_c = 3 \times 10^{-15} \text{rad s}^{-1}$ and $2 \times 10^{-14} \text{rad s}^{-1}$.

Figure 8.4 shows the accretion behavior of these models during the first 2 Myr. In the slowly-rotating case, all of the mass is accreted in a quasi-steady fashion, and the remaining disk mass is very small, whereas the collapse of the rapidly-rotating core results in very little quasi-steady accretion, an extended period of outbursts lasting

well beyond the end of infall, and a very massive disk.

The differing behavior of the three models can be understood with reference to Figure 8.5, which is a modification of the \dot{M} vs. R plane discussed by Zhu et al. (2009b). For the slowest-rotating core model, $R_{cmax} \sim 1$ AU (equation 8.19). Reference to Figure 8.5 shows that this radius is just within the maximum radius R_M for steady MRI-driven accretion at $\dot{M} = 4 \times 10^{-6} M_\odot \text{yr}^{-1}$. In this region, the disk can maintain a temperature greater than the critical value for MRI activation; the disk then accretes on to the star as a typical α -disk, with modest oscillations due to the instability at the inner disk edge described in the previous section (see also chapter 7). In the case of our fiducial model, $R_{cmax} \sim 12$ AU; this places the disk well beyond the region where the mismatch between GI and MRI occurs, resulting in outbursts. The fiducial model accretes quasi-steadily for the first 8×10^4 yr; at this point $R_c \sim 1$ AU. For the rapidly-rotating case, $R_{cmax} \sim 50$ AU; very little mass infalls to radii within the MRI-steady region, and most of the mass then gets accreted during outbursts. Because the mass transport is dominated by the GI at large radii, a relatively massive disk results. Note that the outer regions of the disk reside near the limit where gravitational fragmentation rather than simple transport might occur (chapter 8.8; chapter 8.5.4).

Thus the range of rotations chosen here (given our assumed model for the initial cloud core) approximately span the extremes of disk evolution; at smaller Ω_c , the accretion is almost spherical and occurs quasi-steadily, while for larger values of Ω_c gravitational fragmentation is likely to occur, considerably modifying disk evolution.

The disk mass and surface density distribution are also significantly affected by the initial core rotation. With $\Omega_c = 2 \times 10^{-14} \text{rad s}^{-1}$ (left panel in Figure 8.6), although the dead zone shrinks from 35 AU at the end of the infall phase (0.3 Myr) to 10 AU at the T Tauri phase (1 Myr), the disk is very massive ($0.3 M_\odot$) and still gravitationally unstable within 10 AU during the T Tauri phase. However, for smaller rotation $\Omega_c = 3 \times 10^{-15} \text{rad s}^{-1}$ (right panel), the dead zone is significantly smaller (2 AU) and has less mass ($0.05 M_\odot$).

When the initial core rotates slowly and R_{cmax} is small, the dead zone size is deter-

mined by R_{cmax} . However, if the initial core rotates fast and R_{cmax} is large, the dead zone size is constrained by the radius where the active layer becomes gravitationally unstable, as discussed further in the chapter 8.8 Appendix.

One important point is that even though the dead zone is small $< 50\text{AU}$, it can contain a significant fraction (or most) of the disk mass. Figure 8.7 shows that, no matter what the infall it is, most of the disk mass can be at small radii, rather than the large radii probed by current mm and sub-mm observations (in comparison with constant- α models).

8.4.3 Different disk configurations

The ionization structure of disk surface layers depends on the dust size spectrum and the flux of ionizing radiation and cosmic rays, and is therefore poorly constrained. Angular momentum transport in magnetically decoupled disks is also poorly understood, although recent work by Lesur & Papaloizou(2009), following Petersen et al.(2007), strongly suggests that a nonlinear instability driven by baroclinicity and radiative diffusion may give rise to hydrodynamic turbulence and angular momentum transport. Therefore we have investigated disks with a reduced active layer (chapter 8.4.1), and a residual dead zone viscosity (chapter 8.4.3).

Disks with less active layer and pure GI disks

Little is known about the disk active layer, which is dependent not only upon cosmic and/or X ray fluxes, but on the presence of dust which can absorb charges and reduce the MRI or even prevent it (Sano et al. 2000). Ambipolar diffusion at the low density active layer beyond 10 AU may further depress the effectiveness of the MRI (Chiang & Murray-Clay 2007). In addition, there may be no dynamo in the outer disk. Thus we consider disks with lower active-layer surface densities ($\Sigma_A < 100\text{g cm}^{-2}$).

The long-term disk evolution is determined by the product of $\alpha_M \Sigma_A$ (equations 8.20 and 8.21); thus, as long as the product $\Sigma_A \alpha_M$ stays the same, disk evolution is similar. Figures 8.2 and 8.3 show disks with $\Sigma_A = 100\text{g cm}^{-2}$ and $\alpha_M = 0.01$ and disks with $\Sigma_A = 10\text{g cm}^{-2}$ and $\alpha_M = 0.1$ have similar surface density, temperature, and mass accretion rate distributions at all times, only except that a lower Σ_A leads

to a less massive outer disk.

If $\alpha_M \Sigma_A$ is lower, the disk accretion rate is lower than our fiducial model; thus the infall mass takes longer to accrete onto the star. In addition, with a smaller Σ_A , the dead zone outer radius (R_D) is larger (equation 8.36).

In the extreme case when there is no active layer ⁴, the disk evolves towards $Q \sim 1$ during the simulation (Figure 8.8), since the GI is the only mechanism to transport mass from the outer disk inwards. The disk is very massive and has a sharp outer disk edge roughly at R_{cmax} (Vorobyov & Basu 2005, 2006, 2007). Without the active layer replenishing the innermost disk and the inner disk becoming gravitationally stable (due to the strong irradiation from the central star), the disk accretion rate drops to zero (upper left panel in Figure 8.8). During the T Tauri phase, the disk evolves to $Q \sim 2$ and stays at this gravitationally stable state (Figure 8.8). Thus the disk is massive ($0.2 M_\odot$) during the T Tauri phase. Even if the disk has some small residual viscosity at $Q \gg 1$, it has limited effect on disk evolution simply because, with $\alpha < 10^{-4}$, the viscous timescale is too long (more than 2 Myr to transport mass from 50 AU to the central star) (see also Vorobyov & Basu 2009).

Residual dead zone viscosity

In our fiducial model, we assume the dead zone has no viscosity at all. However, numerical MHD simulations have shown that the dead zone may not be totally “dead”, with a small residual viscosity. The viscosity could be due to the operation of the MRI with the ions turbulent mixing from the active layer (Ilgner & Nelson 2008) or from turbulence penetrating the dead zone from the active layer (Turner et al. 2007). Recent work by Lesur & Papaloizou (2009) also persuasively demonstrates the existence of a nonlinear instability driven by baroclinicity and radiative transport (the magnitude is not yet clear, and the existing evidence suggests that the instability weakens when radiative diffusion is small—when the Peclet number is large—as might be expected in a dead zone with large optical depth.

If the residual viscosity in the dead zone is $\alpha_{rd} \sim 10^{-5}$, it has a negligible effect on

⁴We allow thermal activation of the MRI when the disk temperature is higher than T_M .

disk evolution. Disk structure evolves simply on the viscous timescale; for $\alpha = 10^{-5}$, this is long compared to T Tauri lifetimes $\sim \text{few} \times 10^6$ yr.

However, if the residual $\alpha_{rd} \gtrsim 10^{-4}$, the dead zone can transport the mass at a rate comparable to the accretion rate of the active layer, with $\dot{M}_i \propto \Sigma_i \alpha_i$ and $\Sigma_d \gg \Sigma_a$. We assume the disk has a constant mass accretion rate after a long period of time, and at the stellar surface $d\Omega/dR=0$. Furthermore, if the disk is irradiation-dominated such that $T \propto R^{-1/2}$, $\nu_a = k_a R$ and $\nu_d = k_d R$ where k_a and k_d are constants and are proportional to α_a and α_d , we derive (in chapter 8.7 Appendix)

$$\Sigma_d = \frac{\dot{M}}{3\pi k_d R} \left[1 - \left(\frac{R_*}{R} \right)^{1/2} \right] - \frac{k_a}{k_d} \Sigma_a. \quad (8.22)$$

If the dead zone transports mass at a rate higher than the active layer, the last term can be neglected for an order of magnitude argument. Compared with a constant- α disk having the same mass accretion rate, the layered disk has a surface density higher than the constant- α disk by a factor of α/α_d . If we assume the outer pure MRI active disk and the inner layered disk has the same mass accretion rate, and the outer disk only has ν_a while the inner dead zone is dominated by ν_d , the disk's surface density will change by a factor of α_a/α_d within the dead zone outer radius R_D , which is shown in Figure 8.9. Also this density change at R_D is more gradual (equation 8.22 is a smooth function of R) than the zero dead zone viscosity case. This can have a significant impact on planet migration (chapter 8.5.6).

8.5 Discussion

8.5.1 Dead zones and star formation by disk accretion

The main result of our work is that star formation through disk accretion, assuming a sufficiently large initial disk that the MRI is not thermally activated throughout the disk, generally results in a dense belt of material - the “dead zone” -which has implications for disk structure and planet formation.

To demonstrate this more clearly, we show the results for a constant- α disk for the same infall model. By comparison with layered disks in Figure 8.7, constant-

α disks have similar outer disk but lack the massive dead zone. Constant- α disks respond to infall just as layered disks do: a faster rotating core leads to a more massive disk since the infall mass onto larger radii takes longer to accrete to the central star. Our models show that with the same α in constant- α models, cores with $\Omega_c = 2 \times 10^{-14} \text{rad s}^{-1}$ lead to disks 10 times more massive than the disks produced by cores with $\Omega_c = 3 \times 10^{-15} \text{rad s}^{-1}$ at 1 Myr. However, even if we allow constant-alpha disks to have different values of alpha (Figure 8.10), all these models produce surface densities far in excess of 100 g cm^{-2} over large areas of the disk at the end of infall (lower left panel of Figure 8.10). Thus, *a reduced angular momentum transport efficiency associated with the failure of the MRI at $\Sigma > 100 \text{ g cm}^{-2}$ implies the formation of a dense belt or dead zone in the disk.*

Another feature of the constant- α model is that, although the core rotation determines the disk mass, the disk surface density shape depends most strongly on α . This can be simply explained by the similarity solution of the constant- α disk where the shape of the disk is determined by the scaling radius (Hartmann et al. 1998), which is proportional to t and α . Thus as long as t and α are the same, the disk surface density has similar shape. We also notice that, even for a constant- α disk, the disk is gravitationally unstable at the infall phase with a reasonable set of parameters ($\alpha=0.01$ and $\Omega_c=2 \times 10^{-14} \text{rad s}^{-1}$) (Figure 10).

8.5.2 Relation to previous work

As mentioned in the introduction, previous investigations by Vorobyov & Basu (2006, 2007) and Kratter et al. (2008, 2010) have considered the evolution of disks formed by infall from rotating cloud cores with angular momentum transport by GI. Vorobyov & Basu find outbursting behavior, as we do, but for different reasons; specifically, in their models time-dependent accretion is driven by gravitational clumping, which we cannot treat in one dimension. However, with more realistic energy equations, it is harder to lead to strong gravitational clumping. Kratter et al. (2010) studied more generalized models of infall; they did not find clumping but found conditions for which fragmentation would occur, which agrees with our estimate in chapter 8.8

Appendix B.

Unlike these investigations, we study slowly rotating cloud cores forming single stars without disk fragmentation, focussing on disk evolution after the central core collapse. We treat the GI as a local phenomenon, which may be problematic if the disk is very massive (Lodato & Rice 2005). However, during later stages when the disk is less massive, a local treatment appears to be reasonable (Lodato & Rice 2004, Cossins et al. 2009a). In addition, we are able to treat radiative cooling more realistically; the treatment of thermal physics plays a crucial role in GI transport (e.g., Durisen et al. 2007) and MRI-GI outbursts (chapter 7).

Lodato & Rice (2005) found recurrent episodes of gravitational instability in a massive disk. Boley & Durisen (2008) considered three-dimensional simulations of gravitationally-unstable disks with accurate radiative transfer, and also suggested that high mass fluxes could result from the rapid onset of GI, producing something like an FU Ori outburst. The question is whether this behavior is a transient due to an initial condition, which may or may not be realizable as part of a natural evolutionary sequence. This GI outburst could be a boost in the MRI activation.

Rice et al. (2009) also considered the evolution of disks formed by infall with GI as the transport mechanism. They also find that massive disks result, which leads them to suggest that another mechanism of viscosity must be operating to drain disks. We address this possibility in chapter 8.5.5.

Our treatment differs from all of the above in including MRI transport with layered accretion. This results in our outer disks tending to evolve viscously rather than through GI, so that mass accretion can continue even after the disk is gravitationally stable. Perhaps most importantly, our one-dimensional model allows us to treat the very innermost disk at the same time considering the outer disk evolution, something that is extremely difficult to do with two- or three-dimensional codes. This allows us to demonstrate behavior not seen in the other simulations; specifically, the onset of MRI-driven accretion in the inner disk, which tends to dominate the outburst behavior - or, as we have shown, result in a phase of quasi-steady disk accretion while low angular momentum core material is infalling.

At high accretion rates, it appears almost certain that the MRI should operate, as temperatures become high enough to sublime dust, which might otherwise absorb charges. This notion is supported by observations of FU Ori (Zhu et al. 2007, 2008), which indicate that the disk can be hot enough to eliminate dust out to radial scales of order 1 AU. Thus we argue that inclusion of the MRI is important for any understanding of accretion onto central protostars.

The behavior of non-thermally activated MRI by X-ray or cosmic ray radiation is much more uncertain, but its inclusion can also have important effects not seen in pure GI treatments. In our layered simulations, during the T Tauri phase the GI has limited effects on the long term disk evolution and the disk mass accretion rate is controlled by the active layer, as discussed in chapter 8.4. To confirm this, we have run the same simulation as before but with the α_Q from Armitage et al. (2001), which is based on Lin & Pringle (1987, 1990). We found that the different forms of α_Q have little effect on the long term evolution of a layered disk; the T Tauri disk evolution is more determined by the active layer. In both treatment of α_Q , the layered accretion leads to a relatively massive “inner belt” within 30 AU and a viscous disk beyond 30 AU (Figure 8.3).

8.5.3 Outbursts and luminosity problem

Our model predicts that protostars will undergo FU Ori-like outbursts of rapid mass accretion to accumulate a significant amount of their mass, helping to solve the luminosity problem (chapter 8.2). Here we look at the question of luminosity evolution more closely.

The largest current survey of star-forming regions bearing upon this issue is that of the c2d Spitzer Legacy project (e.g, Enoch et al. 2009, Evans et al. 2009), which strongly suggests that protostellar accretion is time variable, with prolonged periods of low accretion rates. Evans et al. (2009) estimate that half of the mass of a typical low-mass star is accreted during only $\sim 7\%$ of the Class I lifetime, which they estimate as ~ 0.5 Myr. In our fiducial model, roughly half of the mass is accreted quasi-steadily during the first $\sim 10^5$ yr, with the other half being accreted during outbursts within

the next $\sim 1.5 \times 10^5$ yr. This agrees with the c2d observations that half of the mass is accreted during high mass accretion rate stage. However, the outburst behavior (episodic accretion) for the individual protostar does depend on the initial rotation of the cloud core. The $\Omega_c = 2 \times 10^{-14}$ case accretes almost entirely via outbursts, while the low-rotation case accretes essentially all of the stellar mass quasi-steadily.

Evans et al. (2009) found that 59% of Class 0/I stars have bolometric luminosities smaller than $1.6 L_\odot$. However, in our fiducial model, 30% of the Class 0/I phase is in the quasi-steady accretion phase with luminosity $\sim 13 L_\odot$ ($GM_*\dot{M}/R_*$ by assuming $\dot{M}=4 \times 10^{-6} M_\odot \text{ yr}^{-1}$ and $M_*/R_*=M_\odot/10R_\odot$), much larger than $1.6 L_\odot$. One possible solution of this problem is that the extinction toward the protostar during this quasi-steady phase is high, with $A_V \gtrsim 400$ using our model parameters; it might thus be difficult to identify these objects in such early stages of evolution.

Another possible solution is the oscillation of the thermal MRI region (Wünsch et al. 2006) can lead to additional variations in the mass accretion rate and accretion luminosity (which is the reason we call the first steady accretion phase “quasi-steady”; variations are clearly seen in Figure 8.1 during the first 10^5 years)(see chapter 8.4.1). We have avoided concentrating on this feature because it depends on the complex physics at the inner edge of the dead zone, which is unclear to us now. Nevertheless, this potentially unstable behavior may be important in understanding protostellar accretion in general and may even provide a mechanism for explaining EXor outbursts (Herbig 1977). Further investigation of this problem with a realistic calculation of the onset of the MRI is needed.

Some other limitations of our models are that the infall is axisymmetric with a constant infall rate, and that the GI is treated as a local effect. If the infall has a complex pattern and the GI has a strongly global character, the angular momentum transport during the infall phase could be very efficient (Larson 1984) and disk accretion may be more variable (Vorobyov 2009) or even form warped disk (Bate et al. 2009).

There is also a distinction between the model predictions for outbursts during the infall phase and those which occur after infall ends, during the T Tauri phase.

Though they are both triggered by mass accumulation, this is caused by GI during the infall phase, which is independent of the layered structure (chapter 7), while the outbursts during the T Tauri phase are triggered by the mass accumulation from active layer accretion, which is sensitive to the assumed value of Σ_a .

8.5.4 Rotation and Fragmentation

Our most rapidly-rotating model formally predicts FU Ori-like outbursts during the T Tauri phase, driven by active layer accretion. However, this T Tauri phase outburst behavior is uncertain because it sensitively depends on active layer properties and the massive disks which would produce such behavior fragment instead into multiple stellar systems with individually smaller disks (Rapidly-rotating cores tend to produce large disks that are subject to gravitational fragmentation at $R \gtrsim 50$ AU in a realistic disk, see Rafikov 2009; Cossins et al. 2009b; see chapter 8.8 Appendix B).

Finally, we consider possible values of envelope angular momentum. Typical observational estimates of the ratio of rotational kinetic to gravitational energy span a range of three orders of magnitude (e.g., Caselli et al. 2002), and thus are difficult to apply to our simulations. Moreover, the total angular momentum is extremely sensitive to assumptions about the distribution of mass with radius as well as the (not necessarily uniform) angular velocity; as cores are generally not Bonnor-Ebert spheres, or even axisymmetric about the rotation axis (Tobin et al. 2009), making it difficult to compare with observations. As mentioned above, cores with more angular momentum than our fastest-rotating model are likely to fragment into multiple systems. Whether significant numbers of slowly-rotating cores exist which can produce diskless T Tauri stars, or T Tauri systems with very low-mass disks, will require more detailed observational analyses of the complex geometries of starless cores.

8.5.5 Dead zones: do they exist?

We have shown that a natural consequence of our layered model is the formation of dead zones that may remain relatively massive for more than 10^6 yr (also Vorobyov & Basu 2006, 2007; Rice et al. 2009). This stands in contrast with purely viscous

models of disk evolution, as shown in Figure 8.7. An advantage of highly-viscous models is that they provide an explanation for disk accretion rates during the T Tauri phase (Hartmann et al. 1998; Dullemond, Natta, & Testi 2006), whereas the layered accretion model has some difficulties in explaining T Tauri accretion rates (Hartmann et al. 2006). On the other hand, the pure viscous models are unable to explain FU Ori outbursts, which require large mass reservoirs at distance scales on the order of an AU (Armitage, Livio, & Pringle 2001; Zhu et al. 2007, 2008, 2009).

At present the best that can be said is that the MRI is likely to operate at $r \lesssim 0.1\text{AU}$, and it is unlikely to operate at larger radii where the temperature is lower. Even the standard form of the minimum-mass solar nebula (Weidenschilling 1977), let alone the recent amplification suggested by Desch (2007; Figure 8.12), indicates surface densities well in excess of those thought to be penetrated by cosmic rays, or even stellar X-rays. At any rate, the associated change (presumably decrement) in angular momentum transport efficiency where the MRI shuts off is likely to give rise to a feature in the surface density.

At first sight, the surface densities of the dead zones in our evolutionary models seem unreasonably large in comparison with previous models. However, Terquem (2008) has shown that, even for a constant mass accretion rate layered model, the dead zone is very massive. Reyes-Ruiz (2007) has also shown that a massive disk still exists even if the dead zone has some residual viscosity. Some of our models do not predict values of Σ much higher than that of the Desch (2007) model (Fig. 8.12). If the dead zone has some residual viscosity with $\alpha > 10^{-4}$, the dead zone mass can be significantly reduced but still relatively massive compared with a constant- α disk (Figure 8.13). Furthermore, some exoplanetary systems have masses substantially larger than that of Jupiter, suggesting that more than minimum mass solar nebulae are required, especially if migratory loss of solid bodies is significant.

Have high surface density regions been ruled out by recent interferometric observations of submm dust emission in disks, such as those of Andrews et al. (2009)? To examine this possibility, in Figure 8.13 we compare various models (our fiducial model, fiducial model with a residual dead zone viscosity, and a constant- α accre-

tion model) with the suite of disk structures inferred by Andrews et al. (2009). The agreement between the Andrews et al. results and our models in the outer disk is not surprising, because they adopted viscous disk solutions like ours to model the observed interferometric visibilities⁵. If we adopt the same opacity as Andrews et al. , we find that there is no strong signal in the disk surface brightness distribution at the edge of the dead zone because it is optically thick and the temperature distribution is dominated by irradiation from the central star (the brightness temperatures for the layered model and the constant- α model are the same at 1 mm in Figure 8.14). The model does predict a possible feature at $\lambda \sim 1$ cm where the outer disk becomes optically thin (Figure 8.14); this might be testable with the EVLA. The high surface densities in the dead zone may lead to rapid coagulation of the solid particles, however, reducing the optical depth contrast between the dead zone and the MRI-active outer disk region.

Our results suggest the potential importance of dead zones for simply providing a large mass reservoir for solid body formation. Higher density regions may be problematic in that timescales for radial drift of small bodies and Type I migration become much shorter; on the other hand, this may be offset by having more material to start with, and other features of the dead zone may help provide “traps” where planetesimal can form efficiently (Rice et al. 2004) and migration can be halted or even reversed (see the following section).

In this connection it is worth noting the existence of the so-called “transition” disks, where outer, optically-thick disks surrounding T Tauri stars have very large inner disk holes - either partially or fully evacuated (e.g, Espaillat et al. 2007). In some cases these large inner disk holes may be the result of tidal torques from companion (binary) stars, but in others giant planets may be the cause of the inner disk clearing. In the latter case, it may be necessary to have multiple giant planets form nearly simultaneously over a range of radii in order to explain the sizes of these disk holes.

⁵We want to point out that the viscous model for disk turbulence is least reliable at the edge of the disk. No global MHD simulations have been done to show the outer edge of the disk can be approximated by α disk.

The dead zones of our models, with relatively large surface densities over a significant range of radii, may be able to promote the necessary runaway growth.

8.5.6 R_D and planet migration

The sharp density jump at the dead zone outer radius (R_D) can significantly affect the planet migration outside the dead zone (Matsumura & Pudritz 2007); the associated torque on the planet depends on R_D , the density jump factor F , and the width of the density jump.

In the framework of this chapter, we derive the first two parameters analytically and test it numerically. For R_D , chapter 8.4.1 and chapter 8.7 have shown that it starts at the outer disk at the end of the infall, and then travels inwards with time at a speed given in equation 8.39 in chapter 8.7. With the initial $R_D \sim R_{cmax}$ (if we only consider the slow rotating core: no GI fragmentation and active layer GI as discussed in chapter 8.7 the Appendix) and the speed of R_D , the position of R_D can be derived at any time later (Figure 8.11). Based on equation 8.39, the speed of R_D gets slower when moving inwards, which is seen in Figure 8.11.

We can derive F if the dead zone residual α is small enough ($\alpha < 10^{-5}$). With such a small dead zone residual viscosity, the disk is gravitationally unstable within R_D . Thus the surface density jump can be simply derived by dividing the surface density of the $Q=1$ disk to Σ_A ,

$$F = \frac{\Sigma_{Q=1}}{\Sigma_A} = \frac{c_s \Omega}{\pi G \Sigma_A} = \left(\frac{45 AU}{R_D} \right)^{7/4} \left(\frac{100 g cm^{-2}}{\Sigma_A} \right) \quad (8.23)$$

Here we have assumed the temperature profile as $T=200 \text{ K}(R/1 \text{ AU})^{-1/2}$. Thus, as the dead zone moves inwards (R_D becomes smaller), F increases. However, the density jump width, which is the last parameter required to calculate the torque on the planet, cannot be constrained by our 1D simulation.

8.5.7 MMSN and planet formation in the layered disk

Although at the early stage the inner disk is massive, at later stage ($\sim \text{Myr}$) the outer disk (beyond 10 AU) is comparable to the minimum mass solar nebulae (MMSN)

from Weidenschilling (1977) (Figure 8.12). Due to the boundary effect at the dead zone outer radius R_D (chapter 8.4.1 and chapter 8.7), the outer disk evolves towards $\Sigma \propto R^{-1.5}$ as in the standard MMSN. Furthermore, if the dead zone is massive, R_D moves inwards very slowly (chapter 8.5.5); then $\Sigma \propto R^{-1.5}$ lasts for a long time.

If planets form in a massive dead zone, they may be lost by inward migration; however, some may be trapped at the inner boundary (Kretke et al. 2009) or outer boundary (Matsumura et al. 2007,2009) of the dead zone.

8.6 Conclusions

In this chapter, we have constructed a one-dimensional two-zone accretion disk model to study disk formation and long-term evolution under the collapse of a BE rotating core. The model evolution can be divided into three stages. At the early stage, when the mass falls to the inner disk within AU scale, the MRI can be sustained in the inner disk and efficiently and steadily transfers the infalling mass to the central star. Later, when the mass falls beyond AU scale, the disk goes to the outburst stage due to the accretion rates' mismatch by the MRI and GI as described in chapter 7. After the infall completes, the disk enters the T Tauri phase and evolves on its own. Cores with higher initial rotation end up with a more massive disk and more disk episodic accretion events (outbursts). As long as the initial cloud core does not rotate extremely slowly to form a tiny disk ($R_{max} \sim 1$ AU), more than half of the star mass is built up by outbursts, which eases the “luminosity” problem.

Disks exhibit a variety of behavior during the T Tauri phase. For a disk with accretion sustained only by gravitational instability, the disk evolves towards a $Q=1$ disk and the disk truncates at a radius slightly larger than the maximum centrifugal radius of the infall. If the disk has an active layer at the surface, however, the active layer can extend to a much larger radius and a sharp density drop develops at a characteristic radius R_D that separates the marginally gravitationally stable dead zone and the MRI active but gravitationally stable outer disk. The density jump at R_D may be observable by the EVLA and ALMA. The formation of a dense belt of material is associated with the failure of magnetically driven transport due to low

ionization at intermediate radius in the disk; the only ways to avoid this are (1) if there is a separate, equally efficient hydrodynamic transport mechanism, or (2) if for some reason the MRI fails in the outer disk as well, perhaps due to dynamo failure.

8.7 Appendix A. Layered accretion

For a layered disk dominated by viscous heating, Gammie (1996) showed that the central temperature and the mass accretion rate at the radius R are

$$T_c = 290 \left(\frac{R}{1\text{AU}} \right)^{-3/5} \left(\frac{M_c}{1M_\odot} \right)^{1/5} \left(\frac{\alpha_M}{10^{-2}} \right)^{2/5} \times \left(\frac{\Sigma_A}{200\text{g cm}^{-2}} \right)^{4/5} \text{ K}, \quad (8.24)$$

$$\dot{M} = 1.17 \times 10^{-7} \left(\frac{R}{1\text{AU}} \right)^{9/10} \left(\frac{M_c}{1M_\odot} \right)^{-3/10} \left(\frac{\alpha_M}{10^{-2}} \right)^{7/5} \times \left(\frac{\Sigma_A}{200\text{g cm}^{-2}} \right)^{9/5} M_\odot \text{yr}^{-1}, \quad (8.25)$$

where the Bell & Lin (1994) opacity has been used.

In the irradiation dominated limit, the disk temperature is the external temperature (equation 8.4), $\sigma T^4 = fL_*/4\pi R^2$. In this case the disk temperature and mass accretion rate with radii are

$$T_c = 221 \left(\frac{L_*}{L_\odot} \right)^{1/4} \left(\frac{R}{1\text{AU}} \right)^{-1/2} \left(\frac{f}{0.1} \right)^{1/4} \text{ K}, \quad (8.26)$$

$$\dot{M} = 6.9 \times 10^{-8} \left(\frac{R}{1\text{AU}} \right) \left(\frac{M_c}{1M_\odot} \right)^{-1/2} \left(\frac{\alpha_M}{10^{-2}} \right) \times \left(\frac{\Sigma_A}{200\text{g cm}^{-2}} \right) \left(\frac{L_*}{L_\odot} \right)^{1/4} \left(\frac{f}{0.1} \right)^{1/4} M_\odot \text{yr}^{-1}. \quad (8.27)$$

Comparing equations 8.27 and 8.25, we see that the disk is irradiation dominated if the active layer has surface density ($\Sigma_A < 10^2 \text{ g cm}^{-2}$), or α_M is smaller than 10^{-2} ,

or the luminosity is significantly larger than the stellar radiation ($L > 10L_\odot$).

8.7.1 A.1 Dead zone

In either of the above cases the layered disk accretion rates increase nearly linearly with radius, which results in piling up mass in the dead zone at small radii. Using the mass conservation equation

$$R \frac{\partial \Sigma}{\partial t} = - \frac{\partial}{\partial R} \left(\frac{\dot{M}}{2\pi} \right), \quad (8.28)$$

$\partial \Sigma / \partial t \propto R^{-1}$. Thus the layered disk surface density increases linearly with time and it increases more rapidly at smaller radii. If we assume the dead zone has zero residual viscosity (non-zero residual viscosity has been discussed in chapter 8.4.3) and active layer viscosity $\nu_a = kR^n$, disk evolution becomes:

$$\frac{\partial \Sigma}{\partial t} = 3n \left(n + \frac{1}{2} \right) k \Sigma_A R^{n-2}. \quad (8.29)$$

Thus

$$\Sigma(R, t) = 3n \left(n + \frac{1}{2} \right) k \Sigma_A R^{n-2} t + C, \quad (8.30)$$

which increases linearly with time due to the layered accretion, as shown by Matsumura & Pudritz (2007).

The dead zone starts at 0.1 AU and ends at the radius where the disk surface density is smaller than Σ_A (the dead zone outer radius R_D), leaving only the MRI active layer ionized by cosmic and/or X rays at larger radii. This pure MRI active outer disk beyond R_D evolves like a constant- α viscous disk. However since the active layer of the inner disk accretes mass inwards, the dead zone is gradually depleted so that R_D moves inwards with time.

To determine the dead zone size (R_D) during the layered disk evolution, we need to know its initial position just after the infall. Initially R_D should be close to R_{cmax} inside of which the infall mass lands. However this is only true if the initial core rotates slowly and R_{cmax} is small. If the initial core rotates rapidly and R_{cmax} is large, the dead

zone size is constrained by the radius where the active layer becomes gravitationally unstable. Generally, the dead zone cannot extend to $R > 50 \text{ AU}$ if $\Sigma_A = 100 \text{ g cm}^{-2}$ due to the active layer GI. This is because the GI can be very efficient in transporting mass and angular momentum when $Q < 1$, and the surface density with $Q=1$ can be considered as an upper limit that the disk surface density cannot exceed during the evolution. For a layered disk dominated by viscous heating, Gammie (1996) has shown that the Toomre Q parameter at R is

$$Q = 1800 \left(\frac{R}{1 \text{ AU}} \right)^{-9/4} \left(\frac{M_c}{1 M_\odot} \right)^{3/4} \left(\frac{\alpha_M}{10^{-2}} \right)^{1/2} \left(\frac{\Sigma_A}{\Sigma} \right). \quad (8.31)$$

At the outer dead zone radius (R_D), $\Sigma = \Sigma_A$; with the condition that $Q > 1$,

$$R_D < 28 \left(\frac{M_c}{1 M_\odot} \right)^{1/3} \left(\frac{\alpha_M}{10^{-2}} \right)^{2/9} \text{ AU}. \quad (8.32)$$

For an irradiation dominated disk, we derive a similar condition:

$$Q = \frac{c_s \Omega}{\pi G (\Sigma_a + \Sigma_d)}, \quad (8.33)$$

assuming

$$T(R) = 200 \text{ K} \left(\frac{R}{\text{AU}} \right)^{-1/2}. \quad (8.34)$$

Then,

$$Q(R_D) = \left(\frac{45 \text{ AU}}{R_D} \right)^{7/4} \left(\frac{100 \text{ g cm}^{-2}}{\Sigma_A} \right). \quad (8.35)$$

Since $Q(R_D) > 1$,

$$R_D < 45 \left(\frac{100 \text{ g cm}^{-2}}{\Sigma_A} \right)^{4/7} \text{ AU}. \quad (8.36)$$

In either case, $R_D \lesssim 50 \text{ AU}$. To test this, we computed a case with a $\Omega_c = 2 \times 10^{-13} \text{ rad s}^{-1}$ core. The core mass falls into R_{cmax} as large as 400 AU, but the dead zone beyond 30 AU is quickly cleared by the GI so that R_D is smaller than 30 AU during the T Tauri phase.

After we know the initial R_D position, the motion of R_D can be derived by con-

sidering the mass conservation at R_D . For the region extending from $R_D - \Delta R$ to R_D ,

$$R \frac{\partial \Sigma}{\partial t} + \frac{\Delta(R \Sigma_a v_R)}{\Delta R} = 0. \quad (8.37)$$

Assuming the mass flux (or v_R) at R_D is zero, which will be justified in some cases later, and considering the time for the dead zone within ΔR to be depleted is Δt , we got

$$R \frac{\Sigma_{tot}}{\Delta t} - \frac{(R \Sigma_a v_R)}{\Delta R} = 0, \quad (8.38)$$

thus

$$v_D = \frac{\Delta R}{\Delta t} = v_R \frac{\Sigma_a}{\Sigma_{tot}} = \frac{\dot{M}(R_D)}{2\pi R(\Sigma_a + \Sigma_d)}. \quad (8.39)$$

where \dot{M} is as equation 8.27. If we insert \dot{M} we can derive $v_D \propto 1/(\Sigma_a + \Sigma_d)$. Considering $\Sigma_a + \Sigma_d$ is larger at smaller radii, the speed of R_D decrease with time when it is moving inwards. Finally, when R_D moves to the very inner radii where $\Sigma_d \gg \Sigma_a$, R_D is almost halted.

8.7.2 A.2 Outer pure MRI active disk beyond R_D

Beyond R_D the disk is purely MRI active with a constant α_M . Its surface density evolution can be solved by

$$\frac{\partial \Sigma}{\partial t} = \frac{1}{R} \frac{\partial}{\partial R} \left[3R^{1/2} \frac{\partial}{\partial R} (\nu \Sigma R^{1/2}) \right]. \quad (8.40)$$

with the boundary condition $\Sigma_{R_D} = \Sigma_A$. If $\nu = kR^n$, this solution can be simplified by dividing it into two parts

$$\Sigma(R, t) = \Sigma'(R, t) + \Sigma_A \left(\frac{R}{R_D(t)} \right)^{-n-1/2}, \quad (8.41)$$

where the first term on the right comes from the disk evolution with a zero surface density boundary condition at R_D ($\Sigma_{R_D} = 0$), and the second term is the effect of the non-zero boundary surface density at R_D . The first term behaves like the similarity solution with a R^{-1} part and a power law decrease part at larger radius, and it

eventually decreases to zero with time. The surface density evolution is determined by the competition between the first and the second term. During the infall phase, the disk is massive, and the first term is larger than the second term, thus the disk behaves like a similarity solution. Then after infall stops, as the disk accretes and R_D moves inwards, both of these two terms decrease, and as shown above, R_D moves inwards more slowly. Eventually R_D can be considered independent of t ; the first term goes to zero and the second term dominates so that we have $\Sigma \propto R^{-1.5}$ (if $n=1$), which distinguishes it from the self-similarity solution.

Next, we consider the late stage when R_D is independent of time analytically by the Green's function method. If the viscosity ν is a function of radius, equation 8.40 is a linear equation for Σ and can be solved by a Green's function (Lust 1952; Lynden-Bell & Pringle 1974). If $\nu = kR^n$, the above equation becomes

$$\frac{\partial \Sigma}{\partial t} = \frac{1}{R} \frac{\partial}{\partial R} \left[3R^{1/2} \frac{\partial}{\partial R} \left(k \Sigma R^{n+1/2} \right) \right], \quad (8.42)$$

and the radial dependence of Σ is a linear combination of the Bessel functions $J_{+\mu}$ and $J_{-\mu}$, where $\mu^2 = 1/4(2-n)^2$ (Lynden-Bell & Pringle 1974). However for a fixed Σ inner boundary condition at R_D ,

$$\Sigma(R = R_D, t) = \Sigma_A, \quad (8.43)$$

we can substitute Σ with Σ'

$$\Sigma(R, t) = \Sigma'(R, t) + \Sigma_A \left(\frac{R}{R_D} \right)^{-n-1/2}, \quad (8.44)$$

so that equation 8.42 and the boundary condition 8.43 changes to

$$\frac{\partial \Sigma'}{\partial t} = \frac{1}{R} \frac{\partial}{\partial R} \left[3R^{1/2} \frac{\partial}{\partial R} \left(k \Sigma' R^{n+1/2} \right) \right], \quad (8.45)$$

and

$$\Sigma'(R = R_D, t) = 0, \quad (8.46)$$

which becomes a normal disk evolution equation of Σ' with a zero surface density boundary condition. The solution of Σ' is well studied and this disk expands with limit $t \rightarrow \infty$, $\Sigma' \rightarrow 0$, thus from equation 8.44, we derive $t \rightarrow \infty$, $\Sigma \rightarrow \Sigma_A(R/R_D)^{-n-1/2}$. Thus as long as the disk evolves long enough the impact of any initial condition will be washed out, and the boundary term dominates the surface density distribution with $\Sigma \propto R^{-n-1/2}$.

In the irradiation dominated case, $n=1$, we transform equation 8.45 by writing $x = R^{1/2}$ and $\sigma = \Sigma' R^{3/2}$ (Pringle 1991) to get

$$\frac{\partial \sigma}{\partial t} = \frac{3k}{4} \frac{\partial^2 \sigma}{\partial x^2}. \quad (8.47)$$

with the boundary condition $\sigma = 0$ at $x = x_D = R_D^{1/2}$. The general solution is then

$$\sigma(x, t) = \int_{-\infty}^{\infty} A_\lambda e^{-\lambda^2 t} \sin[\lambda(x - x_D)/c] d\lambda. \quad (8.48)$$

where $c^2 = 3k/4$. A_λ is determined by the initial conditions. Following Pringle (1991), in order to obtain the Green's function, we set the initial condition with

$$\sigma(x, t = 0) = \sigma_0 \delta(x - x_1). \quad (8.49)$$

With the delta function Fourier transform $\int \exp(2\pi x \lambda i) d\lambda = \delta(x)$ and $x > x_D$, we derive

$$A_\lambda = -\frac{\sigma_0}{\pi c} \sin[\lambda(x_D - x_1)/c]. \quad (8.50)$$

Thus the solution for the initial condition 8.49 is

$$\begin{aligned} \sigma(x, x_1, t) = & \frac{\sigma_0 t^{-1/2}}{2\pi^{1/2} c} \{ \exp[-(x - x_1)^2/3kt] \\ & - \exp[-(x + x_1 - 2x_D)^2/3kt] \}, \end{aligned} \quad (8.51)$$

Finally, the solution $\sigma(x, t)$ for any initial condition $\sigma(x, t = 0) = \sigma'(x)$ is

$$\sigma(x, t) = \int \frac{\sigma'(x_1)t^{-1/2}}{2\pi^{1/2}c} \{ \exp[-(x - x_1)^2/3kt] - \exp[-(x + x_1 - 2x_D)^2/3kt] \} dx_1. \quad (8.52)$$

and

$$\Sigma(R, t) = \sigma(R, t)R^{-3/2} + \Sigma_A \left(\frac{R}{R_D} \right)^{-3/2}, \quad (8.53)$$

where the first term is the disk evolution with a zero boundary condition and the second term is the fixed Σ boundary effect. As $t \rightarrow \infty$, $\Sigma \rightarrow \Sigma_A(R/R_D)^{-3/2}$.

Figure 8.15 shows the evolution of the constant $\alpha = 0.01$ disks with two different boundary conditions: $\Sigma(10 \text{ AU})=50 \text{ g cm}^{-2}$ (black curves) and $\Sigma(10 \text{ AU})=0 \text{ g cm}^{-2}$ (red curves). The initial conditions are set as

$$\Sigma(R \leq 50\text{AU}, t = 0) = 50 \text{ g cm}^{-2}, \quad (8.54)$$

$$\Sigma(R > 50\text{AU}, t = 0) = 0 \text{ g cm}^{-2}. \quad (8.55)$$

As shown in figure 8.15, the disk with zero boundary condition behaves quite similar to the similarity solution. However, for the $\Sigma(10 \text{ AU})=50 \text{ g cm}^{-2}$ disk, the influence of the boundary becomes significant with a part $\Sigma \propto R^{-1.5}$ and a outer part decreasing exponentially.

The mass accretion rate at R_D decreases to zero eventually ($\Sigma \propto R^{-n-1/2}$). This can be shown by assuming $\Sigma = gR^m$ and $\nu = kR^n$. Inserting these into

$$\dot{M} = 6\pi R^{1/2} \frac{\partial}{\partial R} (\nu \Sigma R^{1/2}), \quad (8.56)$$

we find

$$\dot{M} = 6\pi k g (m + n + \frac{1}{2}) R^{m+n}. \quad (8.57)$$

In the asymptotic case as discussed above with $\Sigma \propto R^{-n-1/2}$, $\dot{M} = 0$, which means at $t \rightarrow \infty$, $\dot{M} \rightarrow 0$ at the inner boundary R_D , so no mass flow in the disk. This can

be simply understood because the disk has zero torque with $\Sigma \propto R^{-n-1/2}$ if $\nu = kR^n$.

However, notice that this $\Sigma \propto R^{-3/2}$ behavior is only observed for layered disks with small or negligible dead zone viscosity, so that at very late stage R_D is very small and almost fixed.

8.7.3 A.3 Residual dead zone viscosity

If the residual dead zone viscosity $\alpha_{rd} \gtrsim 10^{-4}$, the dead zone can transport the mass at a rate comparable to the accretion rate of the active layer, considering $\dot{M}_i \propto \Sigma_i \alpha_i$ and $\Sigma_d \gg \Sigma_a$. If we assume the disk has a constant mass accretion rate after a long period of time, then $\dot{M} = -2\pi R \Sigma_a \nu_{Ra} - 2\pi R \Sigma_d \nu_{Rd}$ is a constant and we can integrate the angular momentum equation to derive

$$(\Sigma_a \nu_{Ra} + \Sigma_d \nu_{Rd}) R^3 \Omega = (\nu_a \Sigma_a + \nu_d \Sigma_d) R^3 \frac{d\Omega}{dR} + C. \quad (8.58)$$

If we assume at the stellar surface R_* $d\Omega/dR$ is 0, we find $C = -\dot{M} \Omega R_*^2 / 2\pi$. Thus

$$\nu_a \Sigma_a + \nu_d \Sigma_d = \frac{\dot{M}}{3\pi} \left[1 - \left(\frac{R_*}{R} \right)^{1/2} \right]. \quad (8.59)$$

Furthermore, if the disk is irradiation-dominated so that the temperature is $\propto R^{-1/2}$, we have $\nu_a = k_a R$ and $\nu_d = k_d R$ where k_a and k_d are constants and proportional to α_a and α_d . So

$$\Sigma_d = \frac{\dot{M}}{3\pi k_d R} \left[1 - \left(\frac{R_*}{R} \right)^{1/2} \right] - \frac{k_a}{k_d} \Sigma_a. \quad (8.60)$$

If the dead zone transports mass at a rate higher than the active layer, the last term can be neglected for order of magnitude argument. And compared with a constant- α disk having the same mass accretion rate, the layered disk has a surface density higher than the constant- α disk by a factor of α/α_d . If we assume the outer pure MRI active disk and the inner layered disk has the same mass accretion rate, and the outer disk only has ν_a while the inner dead zone is dominated by ν_d , the disk's surface density will increase by a factor of α_a/α_d within the dead zone outer radius R_D , which is shown in Figure 8.9. Also this density change at R_D is more gradual

(equation 8.22 is a smooth function of R) than the zero dead zone viscosity case.

8.8 Appendix B. GI disk fragmentation radius

Gammie (2001) has pointed out that when the disk cooling timescale $t_{cool} \leq 3\Omega^{-1}$ the disk will fragment. By assuming local dissipation, Gammie (2001) has shown that

$$t_{cool} = \frac{4}{9\gamma(\gamma - 1)\alpha\Omega}. \quad (8.61)$$

Thus, the disk will fragment if $\alpha > 0.06$ (Rice et al. 2005). However, the above fragmentation condition has only been tested for disks without any irradiation. With irradiation dominated disk, t_{cool} is hard to be defined and $\alpha > 1$ condition are used by Rafikov (2009) instead (Here we use $\alpha > 0.06$ to be consistent with the non-irradiated case.).

For a constant accretion rate we have

$$\alpha \frac{c_s^2}{\Omega} \Sigma = \frac{\dot{M}}{3\pi}. \quad (8.62)$$

Combined with $Q=1.5$, we derive

$$\alpha = \frac{\dot{M}G}{2c_s^3}. \quad (8.63)$$

Thus the disk will fragment if $\dot{M}G/2c_s^3 > 0.06$.

For a viscous heating dominated $Q=1$ disk, at a given mass accretion rate (\dot{M}), the relationship between T_c and R is given in Equation (23) in chapter 7. If we reorganize the equation and assume $\beta=0$ ($\kappa=CT^\alpha P^\beta$) with $Q=3/2$, we got

$$T_c = 3^{2/(7-2\alpha)} 2^{-12/(7-2\alpha)} R^{-9/(7-2\alpha)} \left(\frac{\dot{M}}{\sigma} \right)^{2/(7-2\alpha)} C^{2/(7-2\alpha)} \left(\frac{\mathfrak{R}}{\mu} \right)^{1/(7-2\alpha)} G^{1/(7-2\alpha)} M^{3/(7-2\alpha)} \pi^{-4/(7-2\alpha)}, \quad (8.64)$$

Inserting this into $\dot{M}G/2c_s^3 > 0.06$,

$$R > 0.5 \times 0.12^{(14-4\alpha)/27} \pi^{-4/9} G^{(-11+4\alpha)/27} C^{2/9} \sigma^{-2/9} \left(\frac{k}{\mu m_h} \right)^{(8-2\alpha)/9} M^{1/3} \dot{M}^{(-8+4\alpha)/27}. \quad (8.65)$$

With our dust opacity $\alpha=0.738$ (Zhu et al. 2009 b), the critical fragmentation radius $R \propto \dot{M}^{-0.19}$. Thus the fragmentation radius is insensitive to \dot{M} in the viscous heating dominated case and ~ 100 AU (Figure 8.5).

For an irradiation dominated case (low mass accretion rate), c_s in equation 8.63 is determined by the irradiation (equation 8.4), thus

$$R > 0.06 (\dot{M}G)^{-4/3} \left(\frac{k}{\mu m_h} \right)^2 \left(\frac{fL}{4\pi\sigma} \right)^{1/2}. \quad (8.66)$$

In this case the critical fragmentation R has a sharper dependence on $\dot{M}^{-4/3}$ (Figure 8.5). The GI fragmentation region is outlined in Figure 8.5, which agrees with Figure 10 of Cossins et al. (2009)b.

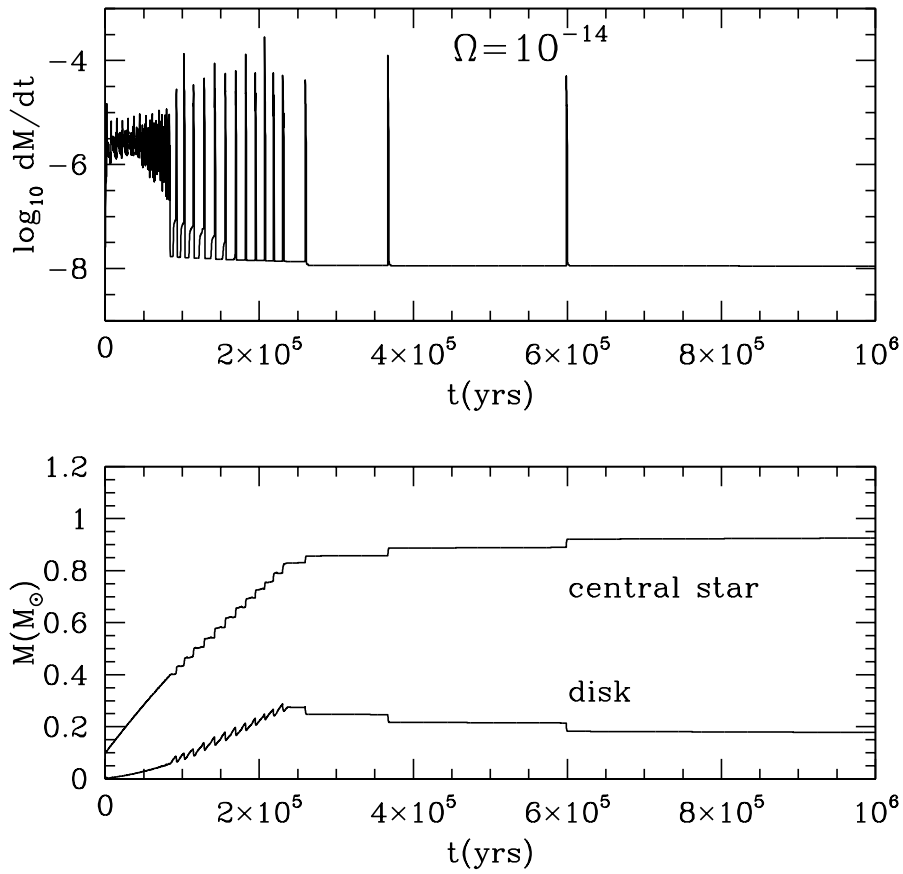


Figure 8.1 The disk mass accretion rate (upper panel) and the mass of the central star and disk (lower panel) with time for our fiducial model ($\Omega_c = 10^{-14} \text{rad s}^{-1}$). The upper curve in the lower panel represents the central star mass while the lower one represents the disk mass.

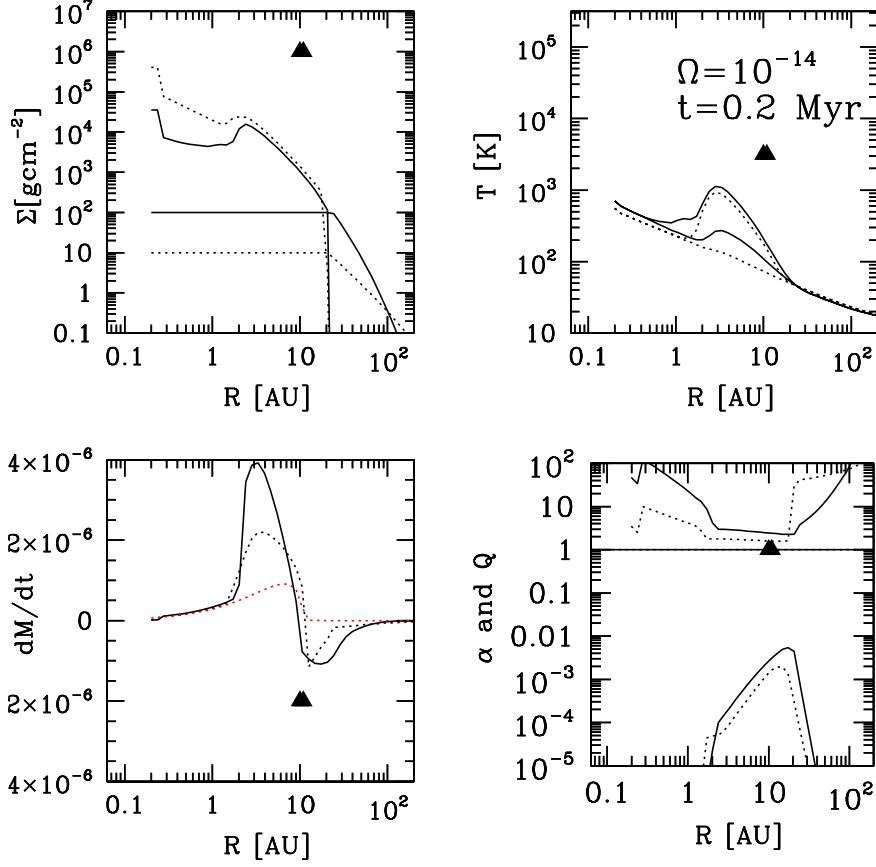


Figure 8.2 The disk surface density, temperature structure, mass accretion rate and α and Q -parameter at the end of the infall phase (0.2 Myr) for various models. Our fiducial model (solid curves, $\Sigma_A = 100$ g cm $^{-2}$ and $\alpha_M = 0.01$) and the model with a less massive active layer but a stronger MRI viscosity (dotted curves, $\Sigma_A = 10$ g cm $^{-2}$ and $\alpha_M = 0.1$) are shown. The triangle labels the centrifugal radius at this time. In the upper left panel, the curves with higher surface densities within 20 AU represent the dead zone surface density, while the ones with $\Sigma < 100$ g cm $^{-2}$ and extend much further represent the active layer surface density. The upper curves in the upper right panel show the midplane temperature while the lower curves show the active layer temperature. The black curve in the lower left panel shows the disk mass accretion rate, while the red curve shows the portion of the mass accretion rate lead by the infall (the third term in equation 8.3). The upper curve in the lower right panel shows the Q parameter while the lower curve shows the midplane α (caused by GI).

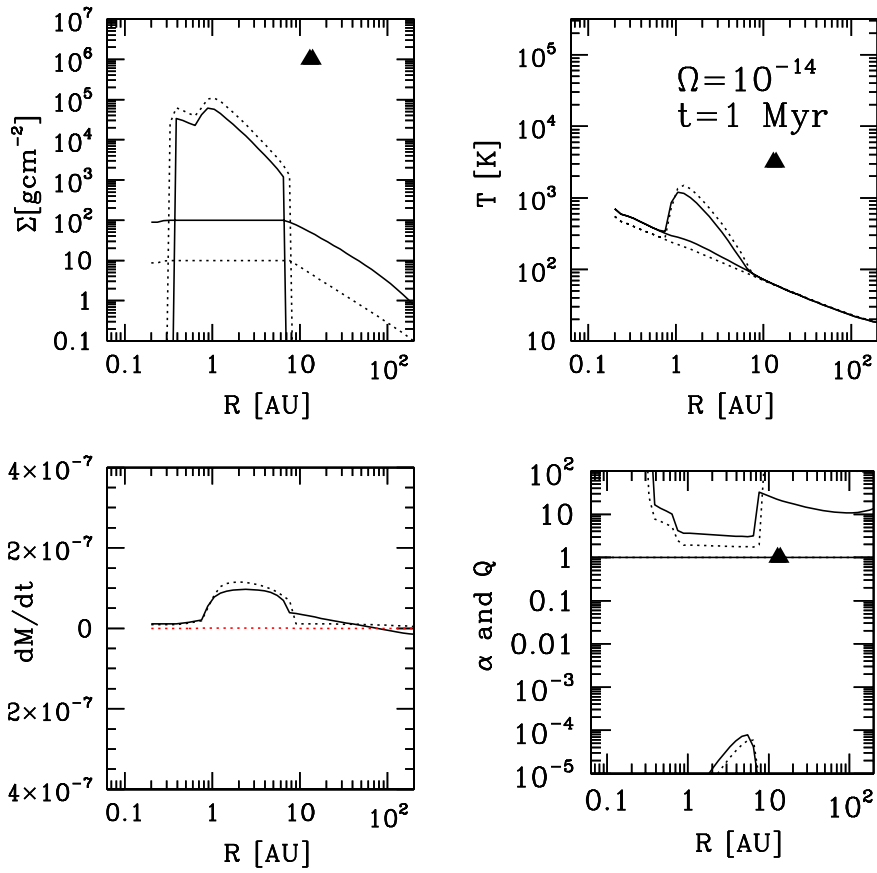


Figure 8.3 The same as figure 8.2 but at $t=1$ Myr. The triangle labels the maximum centrifugal radius.

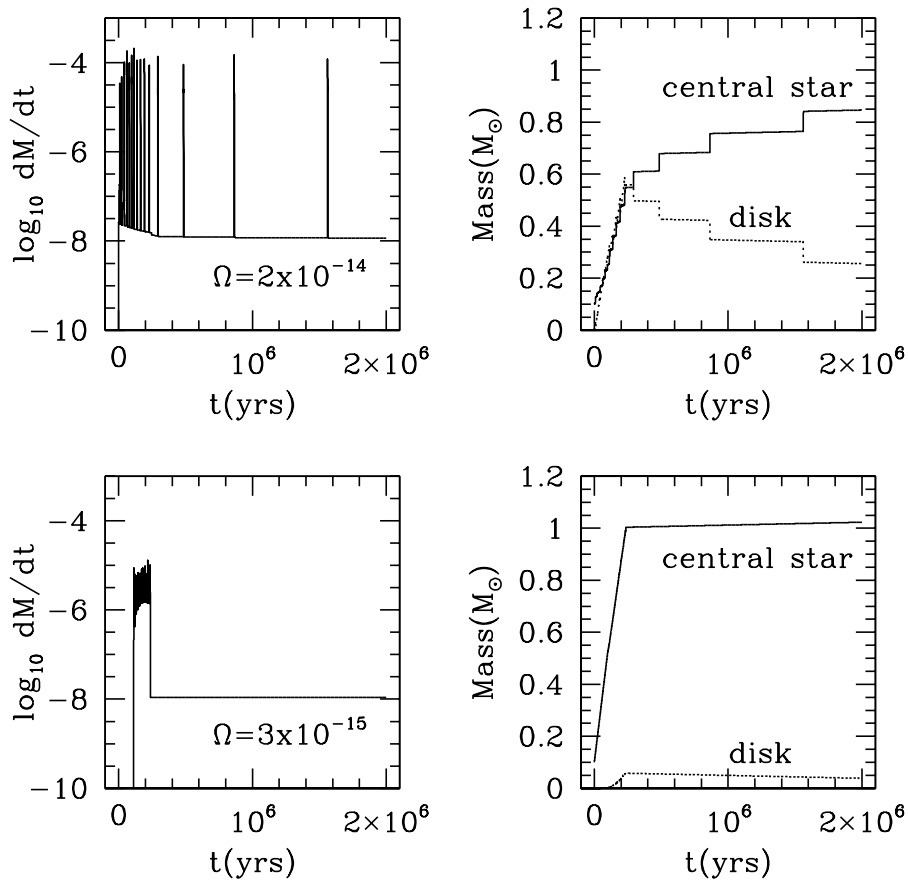


Figure 8.4 The disk mass accretion rates and the mass of the central star and disk with time for different core rotations. The upper two panels show the simulation with $\Omega_c = 2 \times 10^{-14} \text{ rad s}^{-1}$, while the lower ones with $\Omega_c = 3 \times 10^{-15} \text{ rad s}^{-1}$. The solid curves in the right panels show the mass of the central star with time while the dotted curves show the mass of the disk (dotted curve in the lower right panel is too close to 0 and hard to be seen).

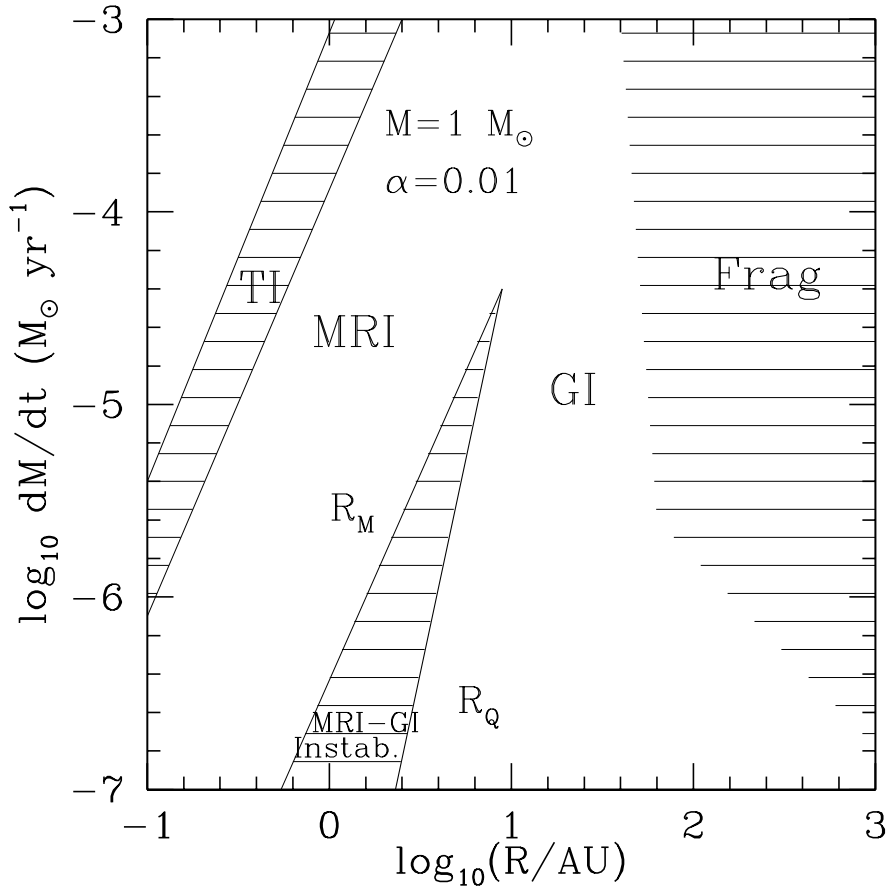


Figure 8.5 Unstable regions in the $R - \dot{M}$ plane for an accretion disk around $1M_{\odot}$ central star. The shaded region in the upper left shows the region subject to classical thermal instability. The shaded region in the middle shows where the central temperature of steady GI models exceeds an assumed MRI trigger temperature of 1400 K, thus subject to MRI-GI instability. The lines labeled R_M and R_Q are the maximum MRI and minimum GI steady accretion radius (the boundaries of the shaded region, detail in Zhu et al. 2009b). The shaded region on the right shows where the GI disk will fragment (See chapter 8.8 Appendix B for details). The fragmentation limit agrees with Cossins et al. (2009)b.

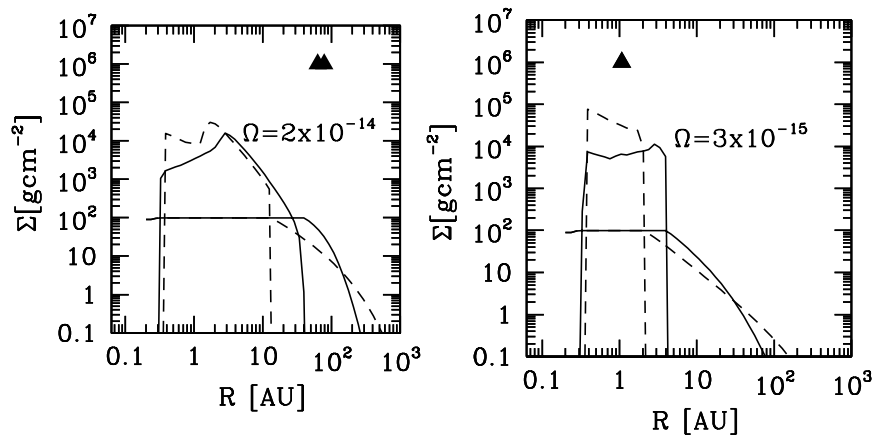


Figure 8.6 The disk surface density with radii for different rotation cores as shown in figure 8.4 at 0.3 million years (solid curves) and 1 million years (dashed curves).

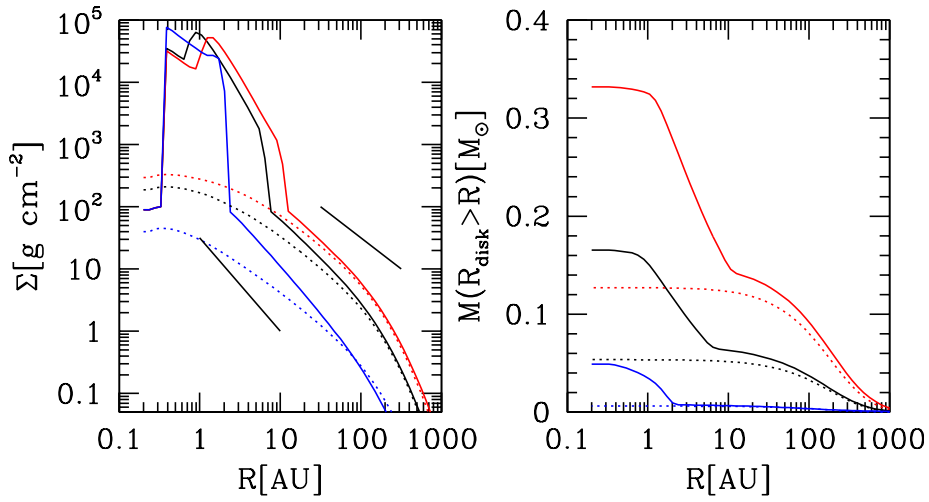


Figure 8.7 The disk surface density distributions at 1 million years for various models. Layered models (solid curves) and constant- α models ($\alpha=0.01$, dotted curves) for $\Omega = 2 \times 10^{-14} \text{ rad s}^{-1}$ (red curves), $\Omega = 10^{-14} \text{ rad s}^{-1}$ (black curves), and $\Omega = 3 \times 10^{-15} \text{ rad s}^{-1}$ (blue curves). The two black lines indicate $\Sigma \propto R^{-1}$ and $\Sigma \propto R^{-1.5}$ respectively. The right panels show the disks' mass beyond R ($M(R) = \int_R^\infty 2\pi R \Sigma dR$).

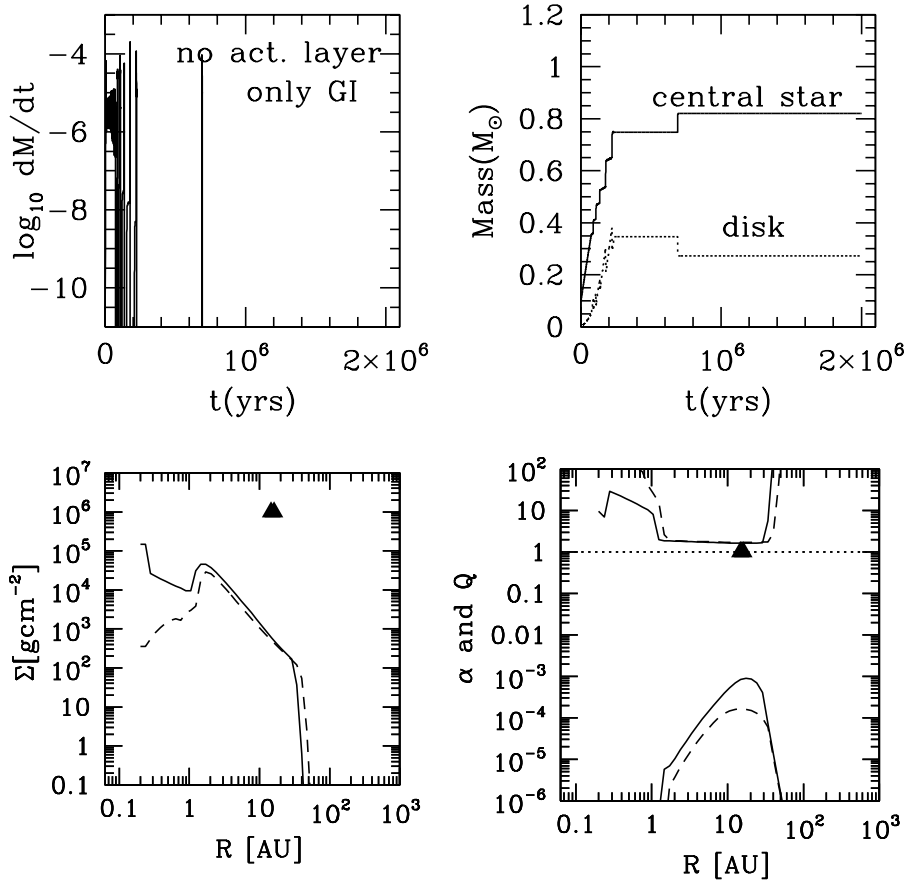


Figure 8.8 Disk evolution of the model without the active layer, in which case only GI has been considered to transport mass from the outer disk to the inner disk. Other parameters are the same as the fiducial model. The upper left panel shows the disk mass accretion rates and the upper right panel shows the masses of the central star and disk with time. The lower left panel shows the disk surface density distribution at 0.3 million years (solid curve) and 1 million years (dashed curve). The lower right panel shows the disk α and Q parameter at 0.3 and 1 Myr.

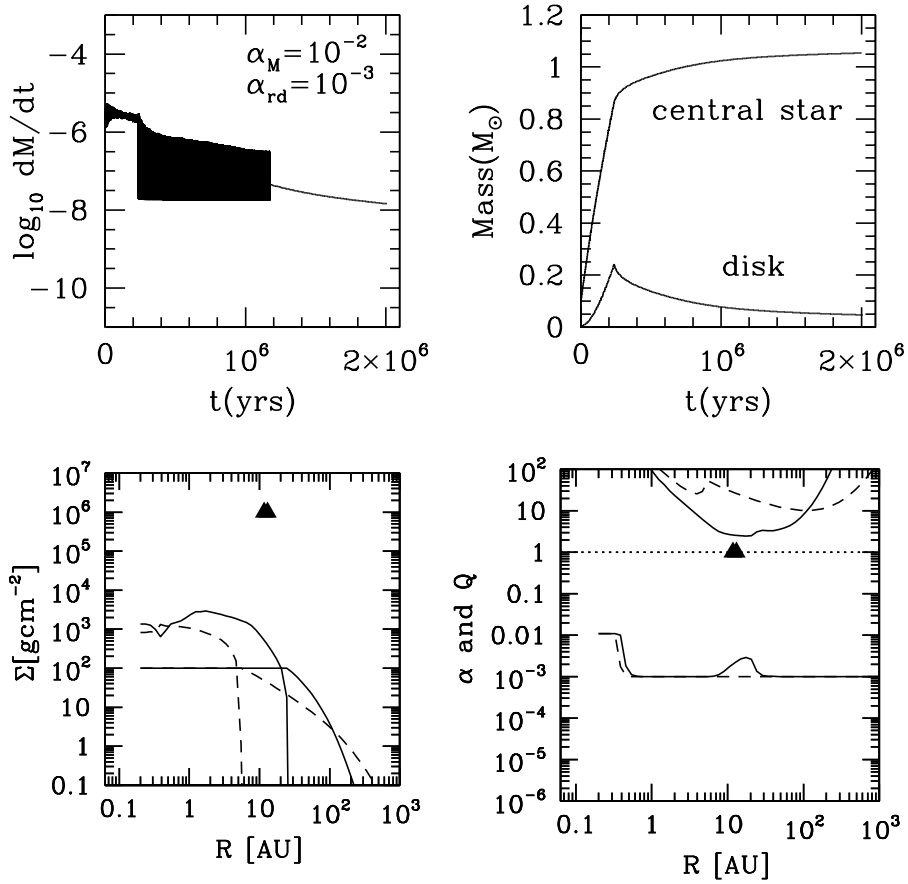


Figure 8.9 Disk evolution of the model similar to our fiducial layered model but with a residual dead zone viscosity ($\alpha_{rd} = 10^{-3}$). The upper left panel shows the disk mass accretion rates and the upper right panel shows the masses of the central star and disk with time. The lower left panel shows the disk surface density at 0.3 million years (solid curve) and 1 million years (dashed curve). The lower right panel shows the disk α and Q parameter at 0.3 and 1 million years.

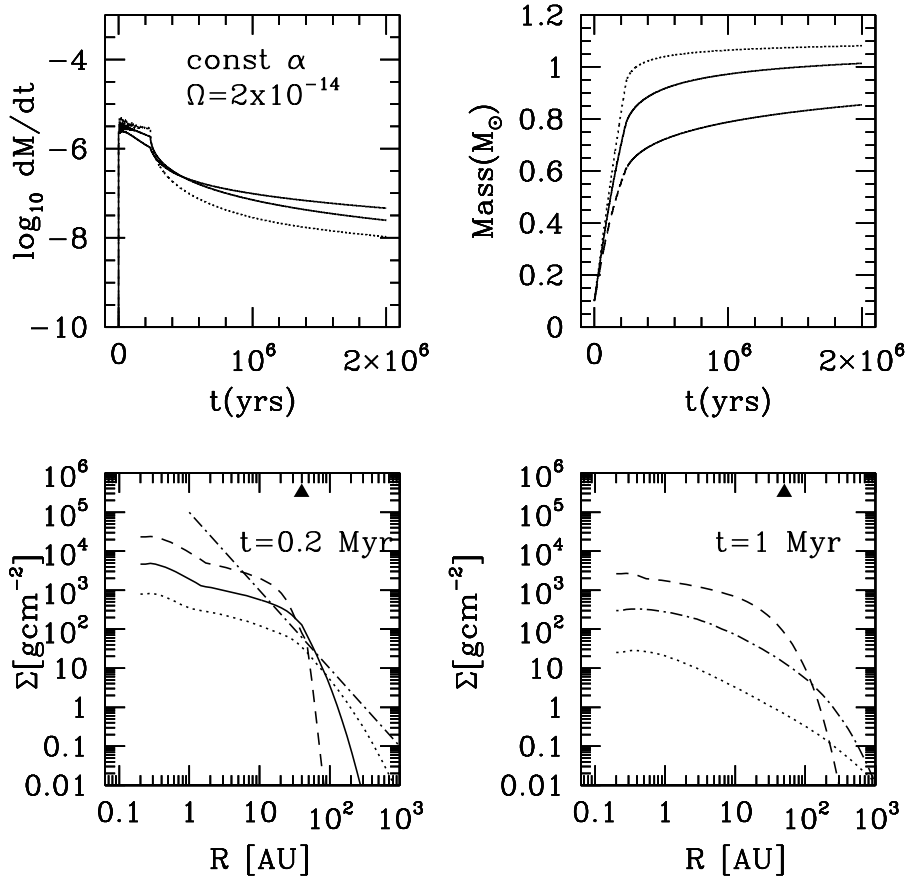


Figure 8.10 Constant- α disks. Long dashed curve is with $\alpha=10^{-3}$; solid curve is $\alpha=0.01$; dotted curve is $\alpha=0.1$ with $\Omega_c=2\times 10^{-14}$ rotating core. Upper panels show the disk mass accretion rate (upper left panel) and central star mass (upper right panel) with time, while lower panels show the disk surface densities at 0.2 million years (lower left panel) and 1 million years (lower right panel). The dash-dotted line in the lower left panel shows the surface density corresponding to $Q=1$ disk.

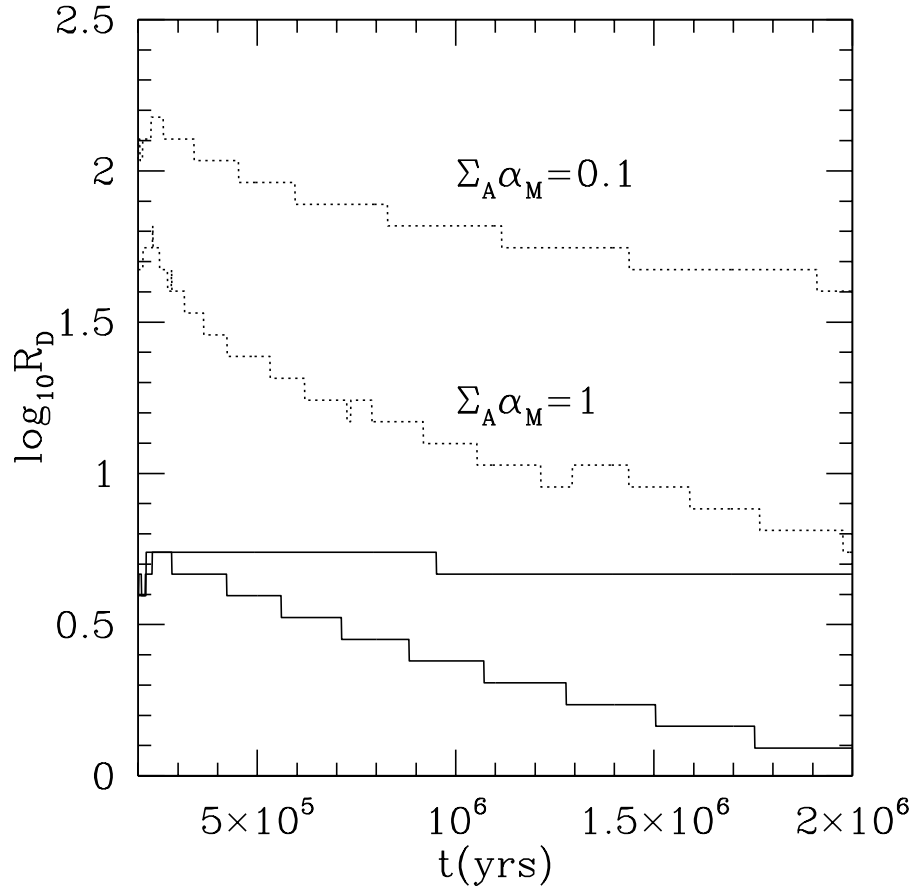


Figure 8.11 In the layered disk model, the dead zone outer radius R_D with time for $\Omega_c = 2 \times 10^{-14} \text{rad s}^{-1}$ (upper two curves) and $\Omega_c = 3 \times 10^{-15} \text{rad s}^{-1}$ (lower two curves). Two different configurations of the layered disk have been considered ($\Sigma_A \alpha_M = 1$ and $\Sigma_A \alpha_M = 0.1$).

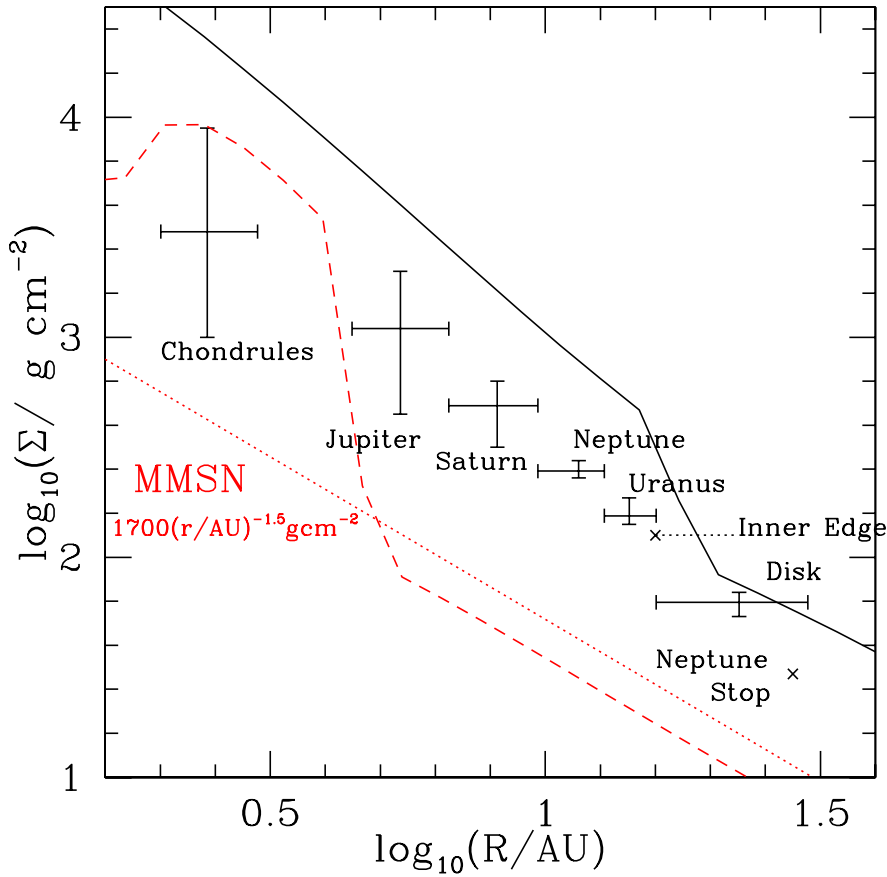


Figure 8.12 Our simulated disk surface density compared with different MMSN models. The black solid curve is the surface density from one of our layered models ($\Omega = 2 \times 10^{-14} \text{ rad s}^{-1}$ at 0.6 Myr) compared with the surface density of the primordial disk constrained by Desch (2007). The red dashed curve is the surface density from our $\Omega = 10^{-14} \text{ rad s}^{-1}$ model at 2 Myr compared with the Minimum mass solar nebulae from Weidenschilling (1977) (dotted red curve).

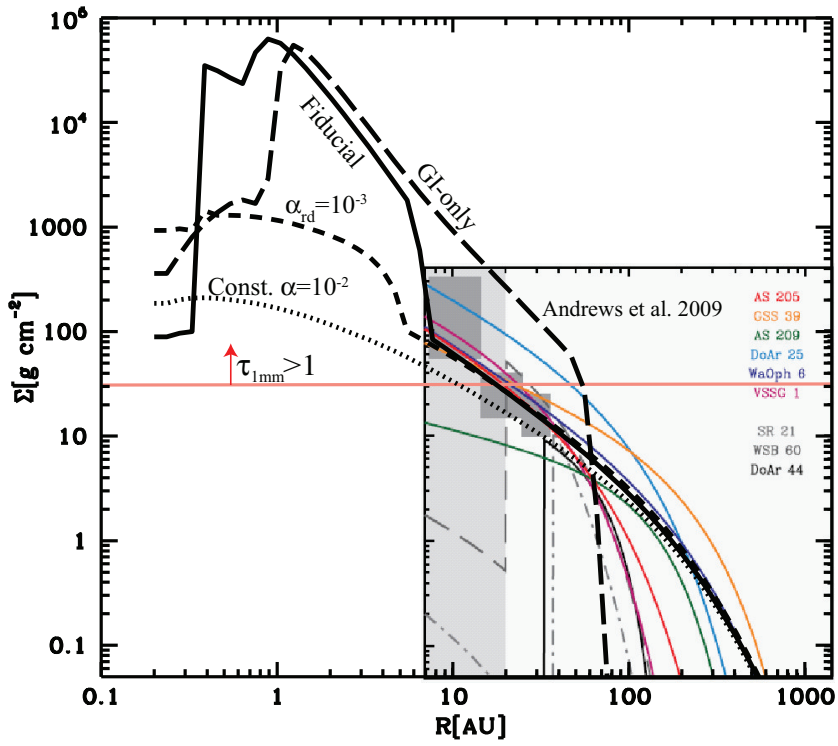


Figure 8.13 The disk surface density distribution of various models. Our fiducial model (solid curve), fiducial model with a residual dead zone viscosity ($\alpha_{rd} = 10^{-3}$, dashed curve), a constant- α ($\alpha=0.01$) model (dotted curve) and a pure-GI model(long dashed curve) at 1 Myr compared with the disk surface densities constrained by millimeter observations of Ophiuchus (colored curves, Andrews et al. 2009).

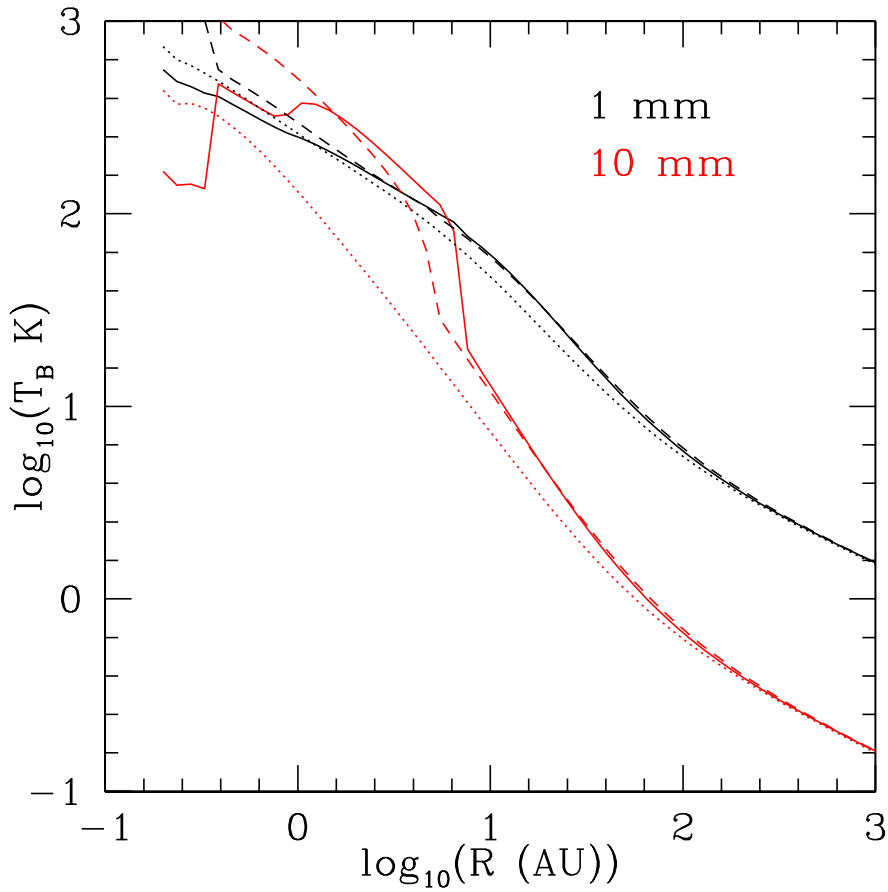


Figure 8.14 The disk surface brightness temperature for the models in Figure 8.13. The fiducial model (solid curve), the fiducial model with a dead zone residual viscosity ($\alpha_{rd} = 10^{-3}$) (dashed curve), and a constant- α model with $\alpha=0.01$ (dotted curve) at 1 millimeter (black curves) and 10 millimeters (red curves). EVLA will be able to distinguish these different disk structures at 10 millimeters.

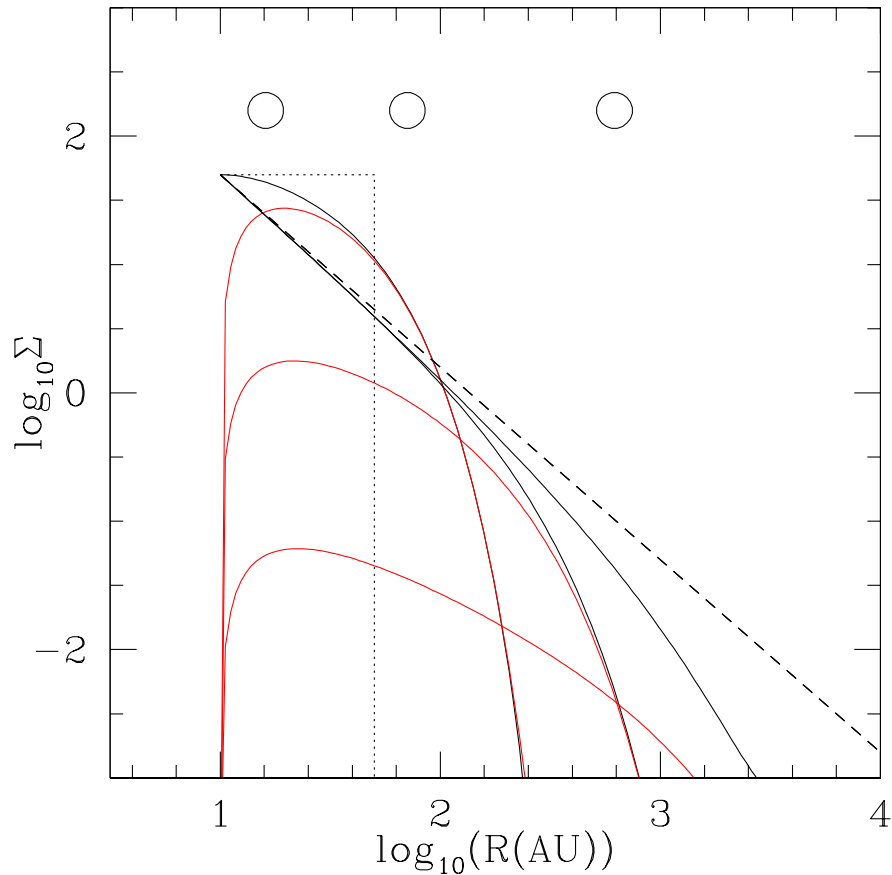


Figure 8.15 The viscous disk surface density with radii. At $t=50, 500, 5000$ kyr (curves from up to bottom) with the fixed Σ inner boundary condition (Black curves for the inner boundary $\Sigma=50 \text{ g cm}^{-2}$ while the red curves for $\Sigma=0 \text{ g cm}^{-2}$). The dotted curve extending to 50 AU shows the disk initial condition, while the dashed line shows the asymptotic limit $\rho \propto R^{-1.5}$. The open dots at the top shows the scaling radius (see the definition in Lynden-Bell & Pringle 1974) $R_{t+10} \text{ AU}$ at $t=50, 500, 5000$ kyr.

Table 8.1 1D2Z models at 0.3 and 1 Myr

cloud Ω	Σ_A g cm ⁻²	α_M	R_D 0.3/1 Myr AU	M_{in}^a M_\odot	M_o^b M_\odot	M_t^c M_\odot
2×10^{-14}	100	0.01	40/13	0.29/0.19	0.18/0.14	0.47/0.33
2×10^{-14}	10	0.01	127/66	0.42/0.33	0.05/0.09	0.48/0.42
2×10^{-14}	0	0.01	-/-	0.47/0.41	-/-	0.47/0.41
1×10^{-14}	100	0.01	24/7.6	0.17/0.1	0.07/0.06	0.24/0.16
1×10^{-14}	10	0.01	47/34	0.32/0.23	0.008/0.022	0.32/0.26
3×10^{-15}	100	0.01	4.6/2.4	0.05/0.04	0.006/0.007	0.057/0.049
3×10^{-15}	10	0.01	5.5/4.6	0.06/0.06	0.0004/0.001	0.063/0.063
3×10^{-15}	0	0.01	-/-	0.064/0.064	-/-	0.064/0.064

^aThe disk mass within R_D

^bThe disk mass beyond R_D

^cThe total disk mass

CHAPTER 9

Transitional and Pre-Transitional disks: Gap Opening by Multiple Planets ?

9.1 Abstract

We use two-dimensional hydrodynamic simulations of viscous disks to examine whether dynamically-interacting multiple giant planets can explain the large gaps (spanning over one order of magnitude in radius) inferred for the transitional and pre-transitional disks around T Tauri stars. In the absence of inner disk dust depletion, we find that it requires three to four giant planets to open up large enough gaps to be consistent with inferences from spectral energy distributions, because the gap width is limited by the tendency of the planets to be driven together into 2:1 resonances. With very strong tidal torques and/or rapid planetary accretion, fewer planets can also generate a large cavity interior to the locally formed gap(s) by preventing outer disk material from moving in. In these cases, however, the reduction of surface density produces a corresponding reduction in the inner disk accretion rate onto the star; this makes it difficult to explain the observed accretion rates of the pre/transitional disks. We find that even with four planets in disks, additional substantial dust depletion is required to explain observed disk gaps/holes. Substantial dust settling and growth, with consequent significant reductions in optical depths, is inferred for typical T Tauri disks in any case, and an earlier history of dust growth is consistent with the hypothesis that pre/transitional disks are explained by the presence of giant planets. We conclude that the depths and widths of gaps, and disk accretion rates in pre/transitional disks cannot be reproduced by a planet-induced gap opening scenario alone. Significant dust depletion is also required within the gaps/holes. Order of magnitude estimates

suggest the mass of small dust particles ($\lesssim 1\mu\text{m}$) relative to the gas must be depleted to $10^{-5} - 10^{-2}$ of the interstellar medium value, implying a very efficient mechanism of small dust removal or dust growth. This chapter has been published in the paper: “Transitional and Pre-transitional Disks: Gap Opening by Multiple Planets?”, 2011, *ApJ*, 729, 47 with Richard Nelson, Lee Hartmann, Catherine Espaillat, and Nuria Calvet.

9.2 Introduction

The transitional and pre-transitional disks around young stars exhibit strong dust emission at wavelengths $\gtrsim 10\mu\text{m}$, while showing significantly reduced fluxes relative to typical T Tauri disks at shorter wavelengths (e.g., Calvet et al. 2002, 2005; D’Alessio et al. 2005; Espaillat et al. 2007, 2008). In the pre-transitional disks, there is evidence for emission from warm, optically-thick dust near the star (Espaillat et al. 2007, 2008, 2010), while in the transitional disks the emission at $\lesssim 10\mu\text{m}$ appears to be due entirely to optically-thin dust (Calvet et al. 2002, 2005; Espaillat et al. 2010). The depletion of near- to mid-infrared emission is generally interpreted as being due to evacuation of the disk interior to scales ~ 5 to ~ 50 AU (Marsh & Mahoney 1992; Calvet et al. 2002, 2005; Rice et al. 2003; Schneider et al. 2003; Espaillat et al. 2007, 2008, 2010; Hughes et al. 2009), an interpretation confirmed in some cases via direct sub-mm imaging (e.g., Pietu et al. 2006; Brown et al. 2007, 2009; Hughes et al. 2009; Andrews et al. 2009).

One proposed mechanism for clearing inner disks while leaving the outer disk relatively undisturbed is the formation of giant planets, which can open gaps in disks (e.g., Lin & Papaloizou 1986; Marsh & Mahoney 1992; Nelson et al. 2000; Calvet et al. 2002; Rice et al. 2003), and which are expected to form initially at relatively small disk radii due to the shorter evolutionary timescales compared with the outermost disk. However, there are three observational challenges, as discussed further in chapter 9.3, which theoretical explanations of these systems must confront.

First, the transitional and pre-transitional disk systems exhibit average gas accretion rates close to T Tauri disk accretion rates ($\sim 10^{-8}M_{\odot}\text{yr}^{-1}$; Hartmann et al.

1998) onto their central stars (e.g. Calvet et al. 2002, 2005; Espaillat et al. 2007, 2008; Najita et al. 2007). Maintaining this accretion requires either a significant mass reservoir interior to the disk-clearing planets, or some way of allowing mass from the outer disk to move past the gap-clearing planets.

Second, the cleared regions in these disks are *large* (e.g. Espaillat et al. 2010). In the case of the transitional disks, the optically-thin region must extend from radii as large as tens of AU all the way in to the central star. Even the pre-transitional disks, which have evidence for optically-thick dust emission in the innermost regions, must have large disk gaps. Furthermore, the spectral energy distribution (SED) modeling suggests that the detected optically thick region may only extend to radii ~ 1 AU, with an extremely dust free region beyond, until reaching the outer optically-thick disk (Espaillat et al. 2010; chapter 9.3).

Third, the requirement that the gap/hole be optically thin implies that the mass of dust in sizes of order a micron or less must be extremely small. Thus, either the planet-induced gap is very deep and is effectively cleared of gas *and* dust, or the dust abundance is reduced by many orders of magnitude from abundances in the diffuse interstellar medium.

These three conditions must be fulfilled simultaneously. Photoevaporation has been proposed as one gap/hole clearing mechanism (Alexander & Armitage 2007, 2009), but requires the mass loss rate by the photoevaporation to be comparable to the disk accretion rate. Initial estimates of photoevaporative mass loss suggested values of $\sim 4 \times 10^{-10} M_{\odot} \text{ yr}^{-1}$ (Clarke et al. 2001), which would not be rapid enough to counteract accretion. More recent estimates suggest higher values, perhaps as much as $\sim 10^{-8} M_{\odot} \text{ yr}^{-1}$ due to the inclusion of X-rays (Gorti & Hollenbach 2009; Owen et al. 2010); however, the highest values are problematic, because then it becomes difficult to understand why so many T Tauri disks last for several Myr with accretion rates smaller than $10^{-8} M_{\odot} \text{ yr}^{-1}$ (Hartmann et al. 1998).

Najita, Strom, & Muzerolle (2007) suggested that giant planets might explain the transitional disks by creating a gap while still maintaining accretion onto the central star. Najita et al. argued that there is some evidence of reduction in the accretion

rates in transitional disks relative to the so-called “primordial” disks, perhaps by an order of magnitude, and that this was consistent with simulations of a single giant planet in the studies by Lubow & D’Angelo (2006) and Varniere et al. (2006). However, as discussed in chapter 9.3, the accretion rates of the pre/transitional disks are not very low in absolute magnitude. Moreover, while Varniere et al. (2006) were able to produce a large cleared inner region with a single planet, the study of Crida & Morbidelli (2007) calls this result into question (see also chapter 9.4).

In this chapter we consider whether disk gap formation by a multiple planet system can satisfy the following requirements: 1) creation of a gap extending over a large range in radius; 2) maintenance of the inner disk accretion rate by flow through the planet-created gap; and 3) sufficient reduction in the disk surface density within the gap such that extreme depletion of disk dust is not essential. We examine the problem in the context of viscous disks, with improvements over some previous simulations, including a more realistic temperature distribution and an improved inner boundary condition. We find that while multiple giant planets can indeed open large gaps, it is difficult to explain the inferred properties of the pre/transitional disks without invoking substantial depletion of small dust. We offer a speculative scenario in which combined dust depletion and planet formation explains the observations.

9.3 Inferred properties of pre/transitional disks

We first present a summary of properties of some of the known pre/transitional systems in Table 9.1 as derived from analysis of optical, infrared, and millimeter SEDs, including the pre-transitional disk systems LkCa 15, UX Tau A, Rox 44, and of the transitional disk GM Aur. The parameters are mostly taken from Espaillat et al. (2010), where the methods used to derive these estimates are discussed.

As indicated in Table 9.1, the estimated maximum extent of the inner optically-thick region in the pre-transitional disks is $\sim 0.2 - 0.4$ AU, while the inner edges of the optically-thick outer disks lie at $\sim 40 - 70$ AU. The location of the inner edge of the outer disk inferred from SED modeling is consistent with that derived using millimeter interferometry (Pietu et al. 2006; Andrews et al. 2009; S. Andrews, 2010,

private communication). The maximum extent of the inner disk is less certain and is based on SED modeling of the near-infrared emission. In this wavelength region, the flux in pre-transitional disks is dominated by the emission of the inner wall. To limit the size of the optically thick disk behind the inner wall, Espaillat et al. (2010) varied the maximum extent of this inner disk and fitted it to the SED of the object. The value listed in Table 9.1 represents the largest $R_{innerdisk}$ that does not produce too much excess emission, assuming a typical disk flaring structure. A caveat is that if the inner wall is “puffed up” relative to the disk behind it (e.g. Natta et al. 2001), or if the dust behind the inner wall is more settled than the wall, the inner disk would be in shadow and not emit strongly. However, we note that the near-infrared interferometric observations by Pott et al. (2010) are consistent with the dust emission being confined to a small radius as inferred from the SED modeling. The amount of *emitting* optically thin sub-micron-sized dust is small, $\sim 10^{-11} M_{\odot}$.

Transitional disks do not have the inner optically thick disk observed in the pre-transitional disks. The transitional disk of GM Aur has a 20 AU hole, based on modeling both the SED and submillimeter interferometric visibilities (Hughes et al. 2009). About $10^{-12} M_{\odot}$ of sub-micron-sized optically thin dust is necessary within the inner AU of the hole to reproduce the observed silicate emission in the near-infrared. Calvet et al. (2005) inferred that the inner emitting, optically thin dust in GM Aur is confined to within 5 AU by modeling its SED. While SED modeling is nonunique, the interferometric observations of Pott et al. (2010) indicated that this dust is confined within even smaller radii, $\lesssim 0.15$ AU (see also Akeson et al. 2005). Thus, as stated by Pott et al. (2010), the pre/transitional disks are often characterized by distinct dust zones “which are not smoothly connected by a continuous distribution of optically thick material”, which may be interpreted as the result of a highly cleared gap with an inner region of optically thin or thick dust.

The final important point to be made is that, as shown in Table 9.1, the gas accretion rates onto the central stars are substantial, $\sim 0.3 - 1 \times 10^{-8} M_{\odot} \text{ yr}^{-1}$, not much lower than rates typical of T Tauri stars (e.g., Hartmann et al. 1998). These high gas accretion rates agree with significant gas emission detected at the inner disk

by *Spitzer* (Najita et al. 2010). Thus, the depletion of dust optical depth appears to be orders of magnitude larger than any reduction in the gas accretion rate. This poses strong constraints on theories of the origin of pre/transitional disk structure, as we now show.

9.4 Methods: Disk–planet simulations

To simulate multiple giant planet systems, we use FARGO (Masset 2000). This is a two-dimensional hydrodynamic code which utilizes a fixed grid in cylindrical polar coordinates (R, ϕ) . FARGO uses finite differences to approximate derivatives, and the evolution equations are divided into source and transport steps, similar to those of ZEUS (Stone et al. 1992). However, an orbital advection scheme has been incorporated which reduces the numerical diffusivity and significantly increases the allowable timestep as limited by the Courant-Friedrichs-Lewy (CFL) condition. Thus FARGO enables us to study the interaction between the disk and embedded planets over a full viscous timescale for disks whose inner radii are considerably smaller than the radial locations of the embedded planets, which is an essential requirement for studying large gaps created by multiple planet systems.

We assume a central star mass of $1M_{\odot}$ and a fully viscous disk. We further assume a radial temperature distribution $T = 221(R/AU)^{-1/2}$ K, which is roughly consistent with typical T Tauri disks in which irradiation from the central star dominates the disk temperature distribution (e.g., D’Alessio et al. 2001). The disk is locally isothermal. The adopted radial temperature distribution corresponds to an implicit ratio of disk scale height to cylindrical radius $H/R = 0.029(R/AU)^{0.25}$. This differs from the $H/R = \text{constant}$ assumption used in many previous simulations, which implies a temperature distribution $T \propto R^{-1}$, which is inconsistent with observations. Consequently, our assumed temperature distribution with a constant viscosity parameter α ($\nu = \alpha c_s^2/\Omega$, where ν is the kinematic viscosity, c_s is the sound speed, Ω is the angular velocity) leads to a steady-disk surface density distribution $\Sigma \propto R^{-1}$ instead of the $\Sigma \propto R^{-1/2}$ which would result from either assuming both H/R and \dot{M} are constant, or both ν and viscous torque $(-2\pi R\Sigma\nu R^2 d\Omega/dR)$ are constant. This makes

a significant difference in the innermost disk surface densities, and thus the implied inner disk optical depths in our models will be larger.

We set $\alpha = 0.01$ for the standard cases. Given our assumed disk temperature distribution, we set the initial disk surface density to be $\Sigma=178 (R/\text{AU})^{-1} (0.01/\alpha)$ g cm^{-2} from $R \sim 1 - 200$ AU, which yields a steady disk solution with an accretion rate $\dot{M} \sim 10^{-8} M_{\odot} \text{yr}^{-1}$, typical of T Tauri disks (Gullbring et al. 1998; Hartmann et al. 1998). The mass within the radius R_{out} is then

$$\begin{aligned} M(R < R_{out}) &= \int_{R_{in}}^{R_{out}} 2\pi R \Sigma(R) dR \\ &= 1.26 \times 10^{-4} \frac{0.01}{\alpha} \left(\frac{R_{out}}{\text{AU}} - \frac{R_{in}}{\text{AU}} \right) M_{\odot}. \end{aligned} \quad (9.1)$$

With $R_{in}=1$ AU, $R_{out}=200$ AU, and $\alpha=0.01$, the total disk mass is thus $0.025 M_{\odot}$, reasonably consistent with observational estimates (e.g., Andrews & Williams 2005).

We use logarithmic spacing for the radial grid to span the large dynamic range needed. The azimuthal resolution is 256 cells covering 2π radians, and the radial resolution is adjusted so that each grid cell is square ($R\Delta\theta = \Delta R$).

Each planet in the disk can interact gravitationally with the other planets and with the disk. The interactions among multiple planets and the star are solved using a 5th order Runge-Kutta integrator. Each planet feels the acceleration from the disk given by

$$\mathbf{a} = -G \int_S \frac{\Sigma(\mathbf{r}')(\mathbf{r}_p - \mathbf{r}') dS}{(|\mathbf{r}' - \mathbf{r}_p|^2 + \epsilon^2)^{3/2}}, \quad (9.2)$$

where the integral is performed over the whole disk area S . Here \mathbf{r}_p denotes the planet's position, and ϵ is the smoothing length set to be $0.6H$, where H is the disk scale height at the planet's orbit.

To accurately simulate close encounters between planets, an additional timestep constraint is applied. For each pair of planets (i, j) we calculate the minimum timestep

$$dt = \frac{1}{400} \min \left(\frac{2\pi}{\Omega_{ij}} \right), \quad (9.3)$$

where $\Omega_{ij} = [G(m_i + m_j)/|\mathbf{r}_i - \mathbf{r}_j|^3]^{1/2}$ is an estimate of the orbital frequency that

each pair of planets (with masses m_i and m_j) would have if they were in orbit around each other, with $|\mathbf{r}_i - \mathbf{r}_j|$ being the absolute value of the distance between them. Throughout most of the simulations the time step size is determined by the normal CFL condition, but when a close encounter occurs the interaction is resolved by allowing Eq. (9.3) to determine the time step size.

Accretion onto the planet is simulated by depleting the disk surface density within the planet’s Hill radius, $R_H = (M_P/3M_*)^{1/3}r_p$, where M_P and M_* are the planet and stellar masses, respectively. This approach is required because of the necessity to evolve the disk-planet system for longer than the viscous time scale measured at the disk outer edge, which forces us to adopt a relatively low numerical resolution that prevents us from modeling accurately the gas flow onto the planet within the planet Hill sphere. Defining a dimensionless scaling parameter, f , we deplete the disk within $0.45R_H$ at a rate

$$\frac{d\Sigma}{dt} = -\frac{2\pi}{fT_P}\Sigma, \quad (9.4)$$

and between 0.45 and $0.75 R_H$ at a reduced rate

$$\frac{d\Sigma}{dt} = -\frac{2\pi}{3fT_P}\Sigma, \quad (9.5)$$

where T_P is the orbital period of the planet¹. We term f the planet accretion timescale parameter. During the intermediate stages of giant planet formation, after the formation of the solid core, but prior to the onset of rapid gas accretion, gas slowly settles onto the planet at a rate determined by the Kelvin-Helmholtz time scale. Depending on the opacity of the planet envelope, this phase lasts for up to a few Myr (Pollack et al. 1996; Papaloizou & Nelson 2005; Movshovitz et al. 2010). Once the planet reaches a value of $\sim 35 - 50 M_\oplus$, rapid gas accretion onto the planet is able to ensue, relatively unimpeded by the thermodynamic evolution of the atmosphere, and the planet can grow quickly to become a giant. during this final phase of growth, however, the planet contracts rapidly, becoming much smaller than its Hill sphere, and further gas

¹Note that our parametrization is different from the publicly available version of FARGO.

accretion must occur via flow through a circumplanetary disk (Papaloizou & Nelson 2005). Simulations presented by Ayliffe & Bate (2009) suggest that the circumplanetary disk has a radius $R_{cp} \simeq R_H/3$ and aspect ratio $(H/R)_{cp} \simeq 0.5$. Adopting these values, the viscous time scale for the circumplanetary disk

$$\tau_{acc} \simeq 1/(5\pi\alpha)T_P \equiv f/(2\pi), \quad (9.6)$$

from which we see that $f = 2/(5\alpha)$. Varying the value of α between representative values of 10^{-2} and 10^{-3} , leads to variations of the accretion time of between ~ 6 and 60 planet orbits. Since f is poorly constrained, we vary it by two orders of magnitude in this work: $1 \leq f \leq 100$.

Observations of exoplanets allow us to place some constraints on the value of f . Once gap formation ensues, mass accretion into the planet Hill sphere is controlled by the rate at which material is supplied to the planet by viscous evolution of the protplanetary disc. A mass accretion rate of $10^{-8} M_\odot/\text{yr}$ implies growth of the planet to masses $\geq 10 M_J$ over disc lifetimes of \sim few Myr if $f = 1$. Given that exoplanets with masses $> 10 M_J$ are relatively rare, this suggests that $f = 1$ is a reasonable lower limit. A value of $f = 100$ implies mass accretion onto the planet at the rate $\sim 10^{-9}$ - $10^{-10} M_\odot/\text{yr}$ (10^{-6} - $10^{-7} M_J/\text{yr}$). Such low values of f can barely explain the numerous exoplanets with masses in the range 1 - 5 M_J , suggesting that $f = 100$ is a reasonable upper limit.

We initiate most of our simulations with relatively low planet masses (details are given later in this section), and the fact that planets grow slowly if $f = 100$ means that during our simulations rapid type I and type III migration are likely to dominate the evolution of the planet orbits (Masset and Papaloizou 2003). To avoid this, we initiate simulations with $f = 100$ with the smaller value $f = 10$ until a gap opens and the planet reaches 1 M_J , at which point f is switched back to 100. The mass and momentum of the depleted portion of the disk are added to the planet's mass and momentum, such that the planet's migration will be (modestly) affected by its accretion from the disk.

As discussed by Crida, Morbidelli, & Masset (2007), a standard open inner boundary condition (Stone et al. 1992) in a fixed 2D grid can produce an unphysically rapid depletion of material through the inner boundary in the presence of the planets. There are two reasons for this. First, due to waves excited by the planet, the gas in the disk can have periodic inward and outward radial velocities larger than the net viscous velocity of accreting material. Thus, with the normal open boundary, material can flow inward while there is no compensating outflow allowed. Second, the orbit of the gas at the inner boundary is not circular due to the gravitational potential of the planets; again, as material cannot pass back out through the inner boundary, rapid depletion of the inner disk material is enhanced. As we are interested in the amount of gas depletion in the disk inward of the planet-induced gap(s) over substantial evolutionary timescales, it is important to avoid or minimize this unphysical mass depletion.

Crida et al. (2007) were able to ameliorate this problem by surrounding the 2D grid by extended 1D grids (see their Figure 5). We follow Pierens & Nelson (2008), who found reasonable agreement with the Crida et al. results while using a 2D grid only by limiting the inflow velocities at the inner boundary to be no more than a factor β larger than the viscous radial velocity in a steady state,

$$v_{rs} = -\frac{3\nu_{in}}{2R_{in}}, \quad (9.7)$$

where ν_{in} and R_{in} are the viscosity and radius at the inner boundary. Pierens & Nelson (2008) found satisfactory behavior for $\beta = 5$ in their simulations, based on a comparison with 1D-2D calculations. As our parameters differ somewhat from those of Pierens & Nelson, we also made a comparison with the 1D-2D setup in FARGO described by Crida et al. (2007), and found that $\beta = 3$ provided reasonable results. We adopted the normal open boundary condition as our outer boundary condition ². The open outer boundary allows mass to leave the computational domain, and in strongly perturbed disks containing massive planets this can cause a noticeable reduction in the disk mass over long time scales which in principle can reduce the

²This is different from the publicly available version of FARGO.

gas accretion rate through the disk. But because this effect requires a long time to develop, its effect on our results is very modest.

We do not use the 1D-2D grid method in this chapter because in some cases our planet masses grow considerably larger than one Jupiter mass, and the non-circular motion of the gas close to the 2D boundary is significant enough so that an artificial gap is opened at the interface between the 1D and 2D grids, which causes the code to crash.

Since our numerical inner boundary is far away from the real disk inner boundary, we assign the ghost zone density to be

$$\Sigma_g = \Sigma_1 \frac{R_1}{R_g} \quad (9.8)$$

to simulate the power law section of the constant α disk similarity solution, where subscript g denotes the ghost zone and 1 the first active zone.

In order to reduce problems related to relaxation from initial conditions, and to mimic the effect of accreting gas onto a protoplanet at the beginning of the rapid gas accretion phased discussed earlier in this section, we performed the following steps. First, we allowed for the planet mass to grow linearly from zero to its initial mass during the first 5000 years. For simulations where the planet accretes gas from the disc the initial mass is $0.1 M_J$, and is $1 M_J$ otherwise. During this period the planet does not feel the gravitational force from the disk and does not accrete gas. This step is necessary; otherwise the sudden presence of a one Jupiter mass planet in a Keplerian disk disturbs the disk so much that the excited acoustic waves can be present in the disk for a long time ³, and these waves gradually deplete the disk mass by creating flows through the outer boundary. Then we allow the planet to start accreting at 10^4 yr. Finally, we allow the planet to feel the disk's gravitational force gradually, starting at 10^4 yr and with full force at $t = 2 \times 10^4$ yr. This gradual ramping up of the gravitational effects is also important, since a sudden turn-on of gravity can kick the planet outside the gap it just opened. As well as being convenient

³Waves can reflect back from the boundary even with the open boundary condition.

from a computational point of view, this approach also ensures that gap formation arises both because of tidal torques and accretion onto the planet.

Problems with boundary conditions also led us to perform simulations without the indirect terms in the gravitational potential experienced by the disk and planets. These terms arise when working in the non-inertial reference frame based on the central star, as they account for the acceleration of the central star by the disk and planets. The resulting non-circular motions can cause problems at both inner and outer boundaries of our circular grid similar to those discussed above. Given the importance of these issues to our investigation of the disk surface density distribution exterior to gaps, we therefore did not include the indirect terms initially. We subsequently recomputed the models P4AN and P4A10 (see following section) to include the indirect terms to ensure that the planetary stability properties and the gap structures that we report in this chapter remain effectively unchanged; we do indeed find that this is the case. (The result for the P4A10 case with indirect terms is shown in Fig. 9.8) In performing these tests with the indirect terms we found it necessary to adopt the wave-damping boundary condition described in De Val-Borro et al. (2006) in order for the disk to remain well behaved at the outside edge. Adopting this boundary condition has very little influence, however, on the structure of the gap or the stability properties of the planetary systems, so we believe that the results presented in this chapter provide an accurate description of the features most important for comparing with observed pre/transitional disk structures.

9.5 Results

We performed simulations with 1, 2, 3 and 4 planets in the disk to study planet gap opening and gas flowing through gaps. The disk simulations evolve over 1 million years (Myr), which is the characteristic viscous timescale at $R \sim 100$ AU, and is also shorter than the time scale over which most T Tauri disks are observed to clear. The properties of the simulations are summarized in Table 9.2.

9.5.1 Viscous disks with one planet

For comparison and test purposes, we first calculated a case without planets (case PN). The disk evolves as expected for a viscous disk with constant α , maintaining a surface density $\Sigma \propto R^{-1}$ and a nearly constant mass accretion rate of $10^{-8}M_{\odot} \text{ yr}^{-1}$.

We then placed a single $1M_J$ (ramping up to $1M_J$ during the first 5000 yrs as discussed in chapter 9.4), non-accreting planet in the disk at 20 AU initially (case P1AN). After 0.5 Myr the planet has migrated in to ~ 8 AU (Fig. 9.1). The azimuthally-averaged surface density within the gap is reduced by about an order of magnitude (solid curve in the left panel of Fig. 9.1). The resulting gap is relatively shallow, as expected due to the high disk viscosity (Lin & Papaloizou 1993; Crida & Morbidelli 2007) and relatively large disk thickness at 20 AU where $H/R \simeq 0.061$. The viscous criterion for gap formation is $q > 40/R_e$, where q is the planet-star mass ratio and R_e is the Reynolds number. At 20 AU in a disk with $\alpha = 0.01$ clear gap formation is only expected for a planet with mass $M_P > 1.5M_J$. The thermal condition for gap formation, which determines if the disk response to the planet is non linear, requires $R_H > H$ at the planet location, which is only just satisfied for a $1M_J$ planet at 20 AU.

Because the planet is not allowed to accrete from the disk, and the tidal torques that it exerts are not strong enough to truncate the mass flow through the disk, accretion flow is channeled through the gap and arrives in the inner disk. Due to the continuous replenishment from the outer disk beyond the planet, the inner disk can maintain the $10^{-8}M_{\odot} \text{ yr}^{-1}$ accretion rate onto the central star (right panel of Fig. 9.1). As expected, the inner disk surface density is not strongly affected by the presence of the planet and is close to that obtained in the unperturbed viscous disk model PN described above.

We next allowed the planet to accrete, at a rate controlled by the parameter f as described in chapter 9.3. The planet starts out with a mass of $0.1M_J$ and is again placed at 20 AU. If $f = 1$ (case P1A1), after the initial phase when the planet accretes material around it and opens a gap, the inner disk surface density decreases by one order of magnitude, and consequently the accretion rate onto the central star also

decreases by one order of magnitude ($10^{-9}M_{\odot}\text{yr}^{-1}$) relative to the non-accreting case. This case is nearly equivalent to that studied by Lubow & D’Angelo (2006)⁴, who similarly found that $\sim 90\%$ of the disk accretion flows onto the planet, leaving only $\sim 10\%$ to pass through into the inner disk. On the other hand we have much higher disk surface densities inside the gap than do Varniere et al. (2006). As discussed in chapter 9.3, this difference is almost certainly due to the difference in the inner boundary condition. In test calculations performed which did not use the β -limiter on the radial velocity (chapter 9.3), we observed a similar rapid depletion of the inner disk (see also Crida & Morbidelli 2007).

As the planet mass grows with time, the gap becomes wider and deeper due to the removal of gas from the disk and the increasing effectiveness of the tidal torques. As 90% of the accreting disk mass is added to the planet at a rate $\sim 10^{-8}M_{\odot}\text{yr}^{-1}$, the planet grows to $10M_J$ after 1 Myr (left panel in Fig. 9.2), so that the gap is much deeper than the case where the planet does not accrete (left panel in Fig. 9.1).

If $f = 10$ (case P1A10), the inner disk surface density and mass accretion rate onto the central star is reduced to 30% of the non-accreting planet case. Because the planet accretes more slowly than in the $f = 1$ case, the planet is less massive (right panel in Fig. 9.2) and so the gap is shallower. The eccentricity for this case is lower than for P1A1 case (this is also true for multiple planet cases, as discussed below).

If $f = 100$ (case P1A100), the inner disk surface density and accretion rate onto the central star is barely affected by the planet (dotted curve in Fig. 9.1). Only 10% of the mass flowing through the gap accretes onto the planet. Thus, it takes 1 Myr for the planet to grow to $1M_J$. The accretion rates show an initial rapid decay due to the inner disk adjusting to the reduced flow from the outer disk; thereafter, the accretion rates show a slow decay or nearly-constant behavior, depending upon how fast the planet mass grows (which affects the mass transfer through the gap). With α as large as 0.01, the gap is shallow and the planet is not fully locked to the viscous evolution of outer edge of the gap, as there remains significant mass flow through the gap. The resulting planet migration timescale is $\sim 10^6$ yr (Fig. 9.2) while the

⁴Although their $f = 0.1$, the radius within which mass is added to the planet is 0.2 Hill radii.

viscous timescale at that radius is 1.8×10^5 yr; thus the planet does not migrate very far during the viscous timescale, allowing the inner disk mass accretion rate to approach a steady state. The reason for the migration being so much slower than the viscous evolution rate is that the flow of gas through the gap causes a positive corotation torque to be exerted on the planet (Masset 2002), reducing the rate of inward migration. This timescale estimate also suggests that if α is as large as 0.01, the supply of gas to accrete onto the star in transitional and pre-transitional disks must come from the outer disk to be sustained for ~ 1 Myr.

9.5.2 Viscous disks with two planets

Figure 9.3 shows the cases (P2A) with two accreting planets originally placed at 12.5 and 20 AU. The gap opened by the joint action of the two planets is considerably wider than in the single planet case (by roughly a factor of three between the outer and inner edge of the gap).

If neither of the planets are accreting (P2AN), the inner disk surface density (solid curve in Fig. 9.3) and the mass accretion rate onto the star are close to the no planet case as expected after a period of initial relaxation. However, if both of the planets are accreting rapidly ($f = 1$, P2A1) the accretion rate onto the central star and the surface density in the disk interior to the gap are both reduced by almost two orders of magnitude (long-dashed curve in Fig. 9.3), as expected since each planet accretes roughly 90% of the viscous flow, leaving only 1% to make it through the gap.

The planets' orbital properties for the P2A1 case are shown in the left panel of Figure 9.4. The two planets migrate inwards at a significantly slower rate than in the one planet case (Kley 2000; compare Fig. 9.2). Due to the common gap formed by two planets, the torque from the outer disk on the inner planet is almost zero. Although the outer planet tries to migrate toward the inner planet, the latter pushes the outer planet outwards by locking it into 2:1 resonance. The eccentricity of the planets is also driven up as they move into 2:1 resonance (Fig. 9.4), as seen in other simulations (e.g., Snellgrove et al. 2001; Kley et al. 2005; Pierens & Nelson 2008). The outer planet's mass grows faster than the inner planet because the outer planet

is continuously being fed by material from the outer disk.

With median and slow planet accretion rates ($f=10$ and 100 , cases P2A10, P2A100), the disk accretion rates onto the central star and the inner disk surface densities are reduced by factors similar to that of the equivalent single planet cases. Unlike the P2A1 case, both of these planets almost grow at the same rate (right panel of Fig. 9.4) because there is enough mass flow passing the outer planet to feed the inner planet.

9.5.3 Viscous disks with three and four planets

Including more giant planets in the disk produces wider gaps, as expected (see Figs. 9.5 and 9.7 for the case with three and four planets, respectively). However, the greater the number of planets that are present, the more the accretion flow reaching the inner disk is reduced. Fast planetary accretion ($f=1$) quickly results in decreasing both the inner disk surface density and the mass accretion rate by more than two orders of magnitude, while median and slow planet accretion ($f=10$ and 100) lead to less than one order of magnitude reduction initially. There is a longer-term decay of the mass accretion rate, which is due to the fact that the inclusion of more planets disturbs the disk more, and over long time scales this causes mass to be depleted from the disk as it escapes through the open outer boundary.

The planets' orbital properties are shown in Figs. 9.6 and 9.8. In most cases, the planets are trapped into 2:1 resonances between each pair of adjacent planets. The middle panel of Fig. 9.8 displays the time evolution of the resonant angle $\phi=2\lambda_O-\lambda_I-\varpi_I$ associated with the 2:1 resonance, where $\lambda_I(\lambda_O)$ and $\varpi_I(\varpi_O)$ are respectively the mean longitude and longitude of pericenter of the inner (outer) planet of the pair. Whenever the resonant angle librates between the interval $[-\pi,\pi]$ the planets are trapped in a 2:1 resonance. The smaller the amplitude of libration, the deeper resonance locking. As in the two planet case (Figure 9.4), the planets' migration slows down due to resonance locking, possibly as a result of the growth of planetary eccentricity which can reduce the migration torques, and also due to the larger inertia associated with a resonant multi-planet system.

There are two cases, however, where planets experience a close encounter and are gravitationally scattered. The first case is P3A1 (left panel in Fig. 9.6), where the eccentricity of the middle planet is driven so high that its orbit overlaps with the inner planet's orbit, leading the inner planet to be scattered out from this system (in a hyperbolic orbit). The second case is P4AN (left panel in Fig. 9.8), where the innermost two planets slip out of 2:1 resonance leading to scattering. In this case the planets remain bound but switch their positions. It is clear that the disk model with $\alpha = 0.01$ leads to circumstances where three or four planet resonances can be maintained stably over Myr time scales, but can also lead to the break up of the resonances. This diversity of behavior appears to have a strong stochastic component, such that the stability of the planet system depends on the detailed history of disc-planet and planet-planet interactions.

We also performed some limited calculations of three or four planets in disks with a lower viscosity ($\alpha=0.002$) and a higher disk mass to give the same disk accretion rate. In contrast to the lower mass $\alpha = 0.01$ disks, these models all produced unstable planet systems which resulted in scattering and ejection of at least one planet from the system. This apparently occurs for two reasons. The first is that the low α disks result in deeper gaps, leading to a reduction in the eccentricity damping provided by the disk, thus favoring planetary instability. Secondly, the significantly larger disk mass probably has a more important dynamical influence on the resonant planetary systems, possibly helping to render the resonant configuration unstable. We will consider the effect of varying the viscosity in more detail in future.

9.6 Discussion

Returning to the questions posed at the end of the Introduction, our findings are as follows:

- 1) As seen in previous simulations, a single planet opens up a small gap. Multiple planets can open wider common gaps. However, in order to explain the pre-transitional disk gaps spanning almost an order of magnitude in radius without dust depletion (chapter 9.3), we need as many as three to four giant planets, given the

tendency of the viscously evolving disk to drive the planets into 2:1 resonances. This is a large number of such planets, given current exoplanet statistics which do not include examples of systems containing more than two planets in resonance. One possibility is that resonant planet systems which contain more than two planets are able to remain stable over significant time periods (~ 1 Myr) in the presence of the gas disk, whose contribution to eccentricity damping helps maintain dynamical stability. Once the gas disk dissipates, however, these resonant planetary systems may become unstable, leading eventually to ejection of some members and the formation of more sparsely populated systems of planets on eccentric orbits, similar to those observed. According to this hypothesis, large systems of planets help explain the presence of the large disk gaps in pre-transitional disks, and also explain the population of eccentric giant exoplanets.

In principle, the gaps could be widened for fewer planets if the orbits were eccentric; however, with large $\alpha=0.01$, we do not see high eccentricities in stable systems.

2) A high accretion rate past the planetary gap can be maintained if accretion onto the planets is sufficiently slow. Planetary accretion rates of $f = 10$ still permit substantial accretion ($>10\%$ accretion rate outside the gap) past the planets to the inner disk. However, the reduction in surface density interior to the gap is in proportion to the reduction in mass accretion rate. This differs from the results of Varniere et al. (2006) but is consistent with the results of Crida et al. (2007), and is almost certainly the result of the improved treatment of the inner boundary condition.

3) Carefully comparing our simulations with observations indicates that the pre/transitional disk systems require substantial reduction in dust opacities within the gaps (and inner disk if present) since the reductions in surface density there are not sufficient to explain the very small amount of dust required to fit the observations. For example, if we adopt the ISM opacity at $10 \mu\text{m}$ (the assumption used by Espaillat et al. (2010) to estimate optically-thin dust masses) of $\kappa \sim 10 \text{ cm}^2 \text{ g}^{-1}$, even the gaps with surface densities $\Sigma \gtrsim 0.1 \text{ g cm}^{-2}$ are still optically thick, which is the case for all but the $f = 1$ simulations. $f = 1$ simulations still have optical depth ~ 0.1 and they are the cases with an extreme upper limit on the expected planetary accretion rate, which leads to

low accretion rate onto the star (esp. with multiple planets). Furthermore, the dust depletion must be larger in the inner disk than in outer regions. This follows from our adoption of a realistic temperature distribution and improved inner boundary condition, which results in a significantly higher surface density at small radii than at large radii; thus the inner disk will not be optically thin unless the outer disk is also optically thin, which disagrees strongly with transitional disk observations.

One alternative is to place planets sufficiently close to the central star that the gap essentially extends either up to the dust destruction radius, or near to it; however, in that case it is difficult to extend the gap all the way out to 20 - 70 AU as observed (Table 1) when using only four planets. In principle it may be possible to accommodate additional planets at smaller orbital radii which truncate the inner disk to a smaller radius. The other alternative is to allow the planets to accrete more mass, depleting the inner disk; but then the mass accretion rate onto the central star is reduced by unacceptably large values.

Protoplanetary disks are probably not fully viscous (e.g., Gammie 1996), but the existence of “dead zones” and/or reduced viscosity regions is unlikely to improve the situation, as they will lead to higher surface densities for a given mass accretion rate, and may reduce the stability of systems of more than two planets in resonance.

9.6.1 Gap structure and dust depletion

A multi-giant planet model coupled with substantial dust depletion in the gap and inner disk does have an attractive feature. As pointed out in chapter 9.3, there is some evidence - both from SED modeling and from near-infrared interferometry - that the pre-transitional and transitional disks exhibit structure within the optically-thin disk gap or hole, such that the innermost gap region is much less cleared of small dust than the outer gap region. Schematically, we might identify the highly-cleared region with the true planet-driven gap, and the inner, optically-thin dust region with accreting gas that has been strongly depleted in dust but not so depleted in gas surface density. The idea is illustrated in Fig.9.9, which compares the inferred structure of one of the pre-transitional disk systems with the azimuthally-averaged dust surface density for

the P4A10 case.

In Fig. 9, the disk optical depth at 10 μm can be estimated by multiplying the dust surface density (dust refers to small dust particles which contribute to 10 μm opacity) by 1000 cm^2/g (which is estimated using the ISM opacity: a factor of 100 comes from the gas-to-dust mass ratio and 10 cm^2/g is the ISM opacity at 10 μm). Thus, disk regions with dust surface density $>10^{-3}$ g/cm^2 are optically thick. The dotted curve represents the dust surface density resulting from the model P4A10 assuming there is no dust depletion, which is obtained by dividing the gas surface density from the P4A10 simulation by the nominal gas-to-dust mass ratio ~ 100 . In this case even the gap is optically thick. The solid curve represents the case where we notionally deplete the dust content inside the gap by a factor of 100. This can explain the pre-transitional disks whose inner region within ~ 1 AU changes from being optically thick to optically thin, with the region beyond being almost dust free. This comparison with pre-transitional disks set a lower limit on the dust depletion factor, while the transitional disks can set a higher limit. If we assume all the dust inside the transitional disk gap has been detected (which is reasonable since transitional disks are optically thin), we can estimate the dust surface density by solving

$$\int_0^{R_{out,thin}} \Sigma_d(R) 2\pi R dR = M_d, \quad (9.9)$$

where $R_{out,thin}$ and M_d are given in Table 9.1, and is assumed to be $\Sigma_d(\text{AU})(R/\text{AU})^{-1}$. The derived Σ_d for GM Aur (<1 AU) using Table 9.1 is shown as the dashed curve in Fig. 9. By comparing with the dotted curve, we find the dust needs to deplete by a factor of $\sim 10^5$. Thus we estimate the dust-to-gas mass ratio in the inner disk is between 10^{-5} and 10^{-2} of the ISM value (0.01) for our model to be consistent with pre/transitional disks.

More broadly, a gap-opening perturbing body or bodies still remains a plausible explanation of the pre/transitional disks. This type of model naturally predicts a sharp transition in surface density at the outer gap edge, which is needed to explain the strong mid- and far-infrared emission of these systems. While radially-dependent

dust depletion might also mimic this effect, most T Tauri disks do not show this behavior. There are a significant number of T Tauri systems in which the disk is optically-thick at a wide range of radii, but which are much more geometrically flat based on their SEDs (e.g., the “group E” systems shown in Figure 7 of Furlan et al. 2006). These objects suggest that dust growth and settling can occur roughly simultaneously over a wide range of radii, without resulting in the abrupt change between optically-thin and optically-thick regions that occurs in the pre/transitional disks. In addition, the large outer disk gap radii (as much as 20-70 AU) pose a challenge for pure coagulation models at an age of $\sim 1 - 2$ Myr (Tanaka et al. 2005; Dullemond & Dominik 2005).

The requirement of significant dust depletion is not completely surprising, given the evidence for small dust depletion in many T Tauri disks without obvious gaps or holes (e.g., D’Alessio et al. 2001; Furlan et al. 2006). In addition, formation of giant planets via core accretion clearly requires dust growth. Indeed, an outstanding theoretical problem has been to avoid clearing inner disks by ages of 1 Myr or less (e.g., Dullemond & Dominik 2005; Tanaka et al. 2005), resulting in suggestions that small dust must be replenished to some extent by fragmentation as a result of collisions of larger particles.

A hypothesis which explains many features of pre/transitional disks using both giant planets and dust depletion can be outlined as follows. Dust coagulation and growth in the disk interior to ~ 20 AU ensues, leading to the formation of planetesimals, and eventually to the formation of a system of numerous giant planets. This system of giant planets forms a large common gap which covers radii from < 1 AU out to ~ 50 AU. Remnant planetesimals within the gap region, whose collisions can act as a secondary source of dust, are dynamically cleared out - preventing in situ secondary dust formation. After a viscous time scale corresponding to the size scale of the planetary system, the gas present in the planet-induced gap and the inner disk within 1 AU has originated largely from that part of the disk which lies out beyond the planetary system. This gas may be substantially depleted of small dust because of significant grain growth at large radii, combined with filtration of dust at the outer

edge of the gap (Paardekooper & Mellema 2006; Rice et al. 2006). Furthermore, small dust particles may manage to pass through the gap, but they can quickly coagulate to big dust particles (Dullemond & Dominik 2005). In this scenario, gas which accretes through the system at late times is strongly depleted of dust, can sustain a significant accretion rate onto the central star, and can provide a dust-rich wall at the outer edge of the gap required by SED modeling. We will explore this hypothesis in future.

9.6.2 Limitations

Our simulations are highly simplified, and this needs to be borne in mind when interpreting our results. The resolution we adopt is insufficient to resolve the gas flow within the planet Hill sphere, and so we are forced to adopt a simplified approach to simulating gas accretion onto the planet, instead of simulating the accretion process directly. As such the detailed evolution of the gas flow in and around the planet Hill sphere may not be modeled with a high degree of fidelity in our simulations. The simulations are two dimensional, which may not be a good approximation early on when the planet masses are low, but improves as the planet masses become large and gap formation occurs. We have neglected a detailed treatment of the gas thermodynamics, adopting instead a locally isothermal equation of state. A proper treatment would allow the local disk temperature to be determined by a balance between viscous and stellar heating, and radiative cooling, and this might affect details of the gap structure due to the changing optical depth of the gas and its thermal evolution there (although viscous heating is generally much smaller than stellar heating). Ayliffe & Bate (2010) suggest radiation due to circumplanetary disk accretion tends to suppress the spiral shocks and leads to a shallower gap (their Figure 18), which only increases the need for dust depletion within the gaps. Finally, we do not explicitly simulate the MHD turbulence that is believed to provide the effective viscous stresses in protoplanetary disks (Balbus & Hawley 1991). But it appears from previous simulations that adopting the usual α prescription gives results in broad agreement with MHD simulations when considering gap formation and giant planet migration (Nelson & Papaloizou 2003; Winters, Balbus & Hawley 2003; Papaloizou, Nelson & Snellgrove

2004). As such, we do not expect that the qualitative nature of our results have been compromised by the neglect of the above physical processes.

9.7 Summary

In this chapter we present 2-D hydrodynamic simulations to explore the possibility that the properties of pre/transitional disks are due to gap opening by planets in viscous disks. With an improved inner boundary condition, we found that the surface density of the disk interior to the planet-formed gap is depleted by the same factor as the mass accretion rate through the gap and into the inner disk is reduced. Thus, the substantial accretion rates of pre/transitional disks require substantial gas surface densities inside of planet-driven gaps. We also found that even multiple planets have difficulty in making large disk gaps and holes which are deep enough to explain the observations. Thus small grain depletion seems to be an essential part of the explanation of the structure of pre/transitional disks, and this may be explained by the dust growth or the accretion of grain-depleted gas from large disk radii at late times and dust filtration. In addition, multiple planets might account for the inferred structure within the gaps of pre/transitional disks, in which the inner gaps are much less cleared of small dust than outer gap regions.

Table 9.1. Stellar and Model Properties
of LkCa 15, UX Tau A, Rox 44, & GM Aur from Espaillat et al. 2010

	LkCa 15	UX Tau A	Rox 44	GM Aur
Stellar Properties				
M_* (M_\odot)	1.3	1.5	1.3	1.1
T_* (K)	4730	5520	4730	4350
\dot{M} ($M_\odot \text{ yr}^{-1}$)	3.3×10^{-9}	1.1×10^{-8}	9.3×10^{-9}	7.2×10^{-9}
Optically Thick Inner Wall				
R_{wall}^i (AU)	0.15	0.15	0.25	...
Optically Thick Inner Disk				
$R_{inner \text{ disk}}$ (AU)	<0.19	<0.21	<0.4	...
$M_{inner \text{ disk}}$ (M_\odot)	< 2×10^{-4}	< 6×10^{-5}	< 8×10^{-5}	...
Optically Thick Outer Wall				
R_{wall}^o (AU)	58	71	36	20
Optically Thick Outer Disk				
ϵ	0.001	0.001	0.01	0.5
α	0.0005	0.004	0.006	0.002
M_{disk} (M_\odot)	0.1	0.04	0.03	0.16
Optically Thin Dust in Gap/Hole				
M (M_\odot)	2×10^{-11}	...	2×10^{-11}	2×10^{-12}
a_{min} (μm)	0.005	...	0.005	0.005
a_{max} (μm)	0.25	...	0.25	0.25
$R_{out,thin}$ (AU)	4	...	2	1

Table 9.2 Models

case name	R_{in} AU	R_{out} AU	Σ_{1AU} g cm^{-2}	R_P^a AU	M_P^b M_J	Acc ^c f
PN	1.5	200	178	-	-	-
P1AN	1.5	200	178	20	1	No
P1A100	1.5	200	178	20	0.1	100
P1A10	1.5	200	178	20	0.1	10
P1A1	1.5	200	178	20	0.1	1
P2AN	0.75	200	178	12.5/20	1	No
P2A100	0.75	200	178	12.5/20	0.1	100
P2A10	0.75	200	178	12.5/20	0.1	10
P2A1	0.75	200	178	12.5/20	0.1	1
P3AN	0.5	200	178	7.5/12.5/20	1	No
P3A100	0.5	200	178	7.5/12.5/20	0.1	100
P3A10	0.5	200	178	7.5/12.5/20	0.1	10
P3A1	0.5	200	178	7.5/12.5/20	0.1	1
P4AN	0.5	200	178	5/7.5/12.5/20	1	No
P4A100	0.5	200	178	5/7.5/12.5/20	0.1	100
P4A10	0.5	200	178	5/7.5/12.5/20	0.1	10
P4A1	0.5	200	178	5/7.5/12.5/20	0.1	1

^aThe initial planet radii. The radii can change with time due to migration and planet-planet interaction.

^bThe initial planet mass. If Acc is not 'No', the mass can increase with time due to accretion from the disk.

^cThe accretion coefficient f is defined in Eqs 9.4 & 9.5.

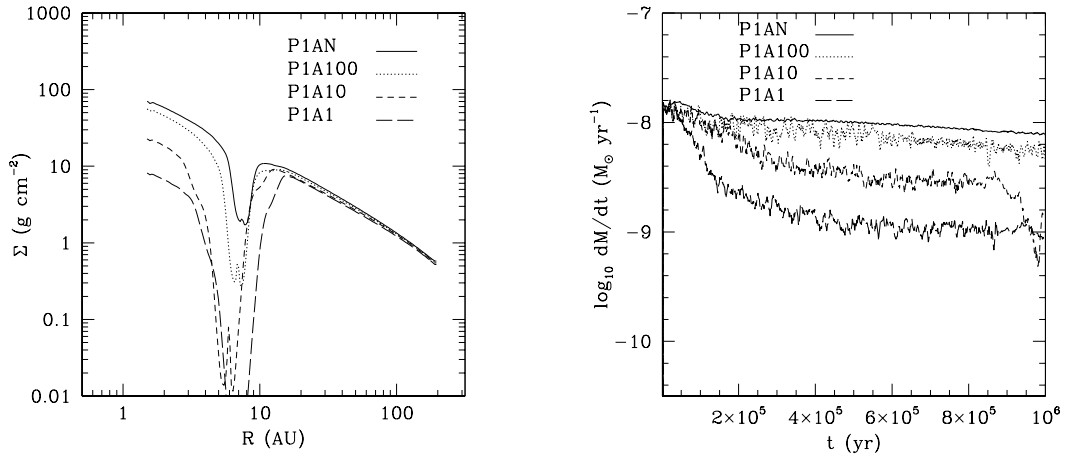


Figure 9.1 Left: disk surface densities at 0.5 Myr for viscous disks ($\alpha=0.01$) with one planet accreting at different rates. No planet accretion (solid curve), accretion on 100 ($f=100$) (dotted curve), 10 ($f=10$) (short-dashed curve), and 1 orbital timescales ($f=1$) (long-dashed curve; see text for further explanation). Right: the disk accretion rates onto the central star for these four cases. A comparison between the left and right panels demonstrates that the depletion of the inner disk surface density results in a proportional decrease in accretion rate onto the central star.

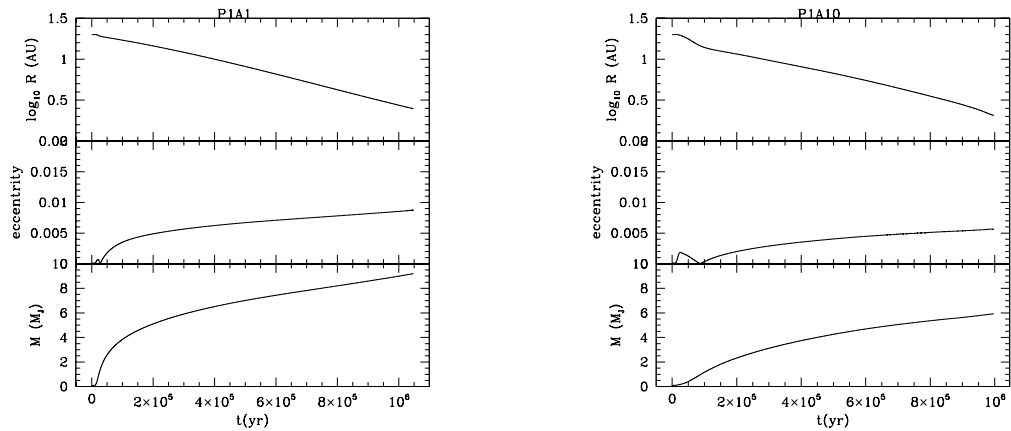


Figure 9.2 The planet's semi-major axis, eccentricity, and mass as a function of time for the P1A1 case (left) and P1A10 case (right).

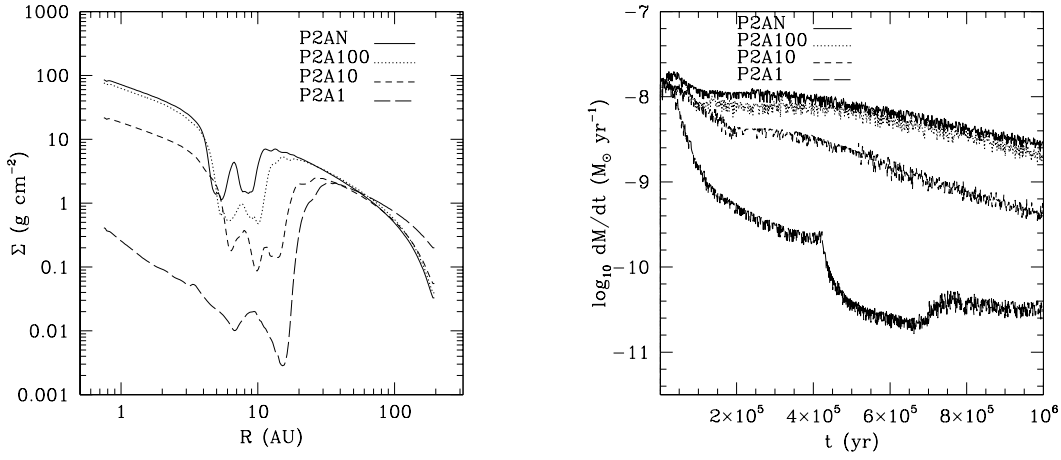


Figure 9.3 Left: disk surface densities at 0.5 Myr for two planets with no planet accretion (solid curve), $f=100$ (dotted curve), $f=10$ (short-dashed curve), and $f=1$ (long-dashed curve). Right: the disk accretion rates onto the central star for these four cases.

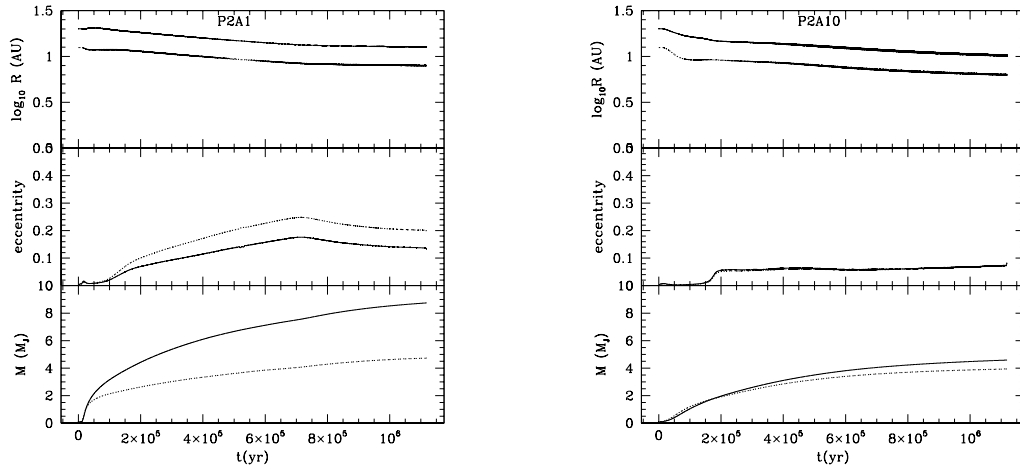


Figure 9.4 The planets' semi-major axis, eccentricities, and masses as a function of time for the two accreting planets in the P2A1 case (left) and P2A10 case (right). The solid curves represent the outer planet while the dotted curves represent the inner planet.

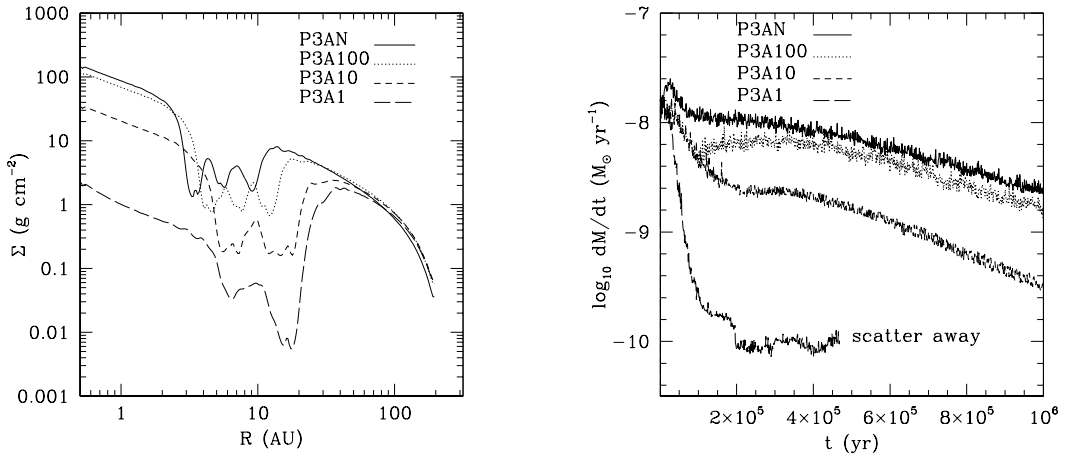


Figure 9.5 Left: disk surface densities at 0.4 Myrs for three planets with no planet accretion (solid curve), $f=100$ (dotted curve), $f = 10$ (short-dashed curve), and $f = 1$ (long-dashed curve). Right: the corresponding disk accretion rates.

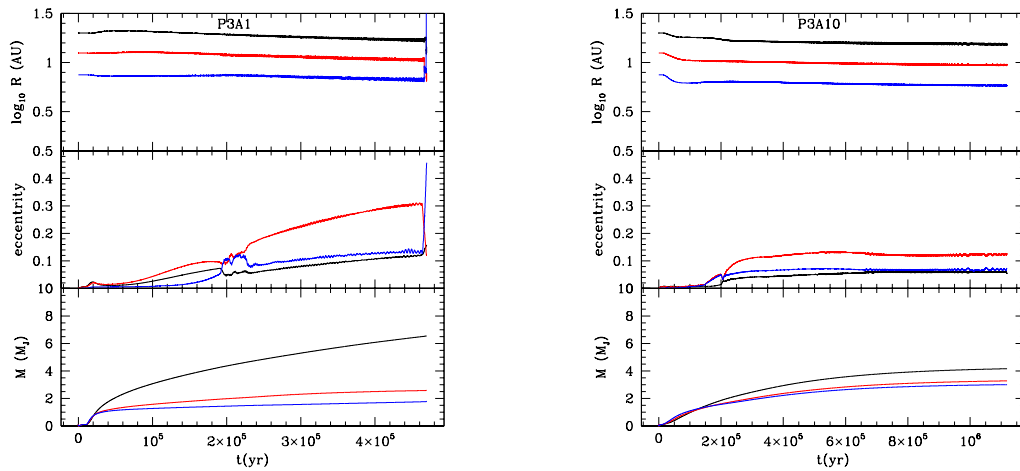


Figure 9.6 The planets' semi-major axis, eccentricities, and masses as a function of time for three accreting planets in P3A1 case (left) and P3A10 case (right).

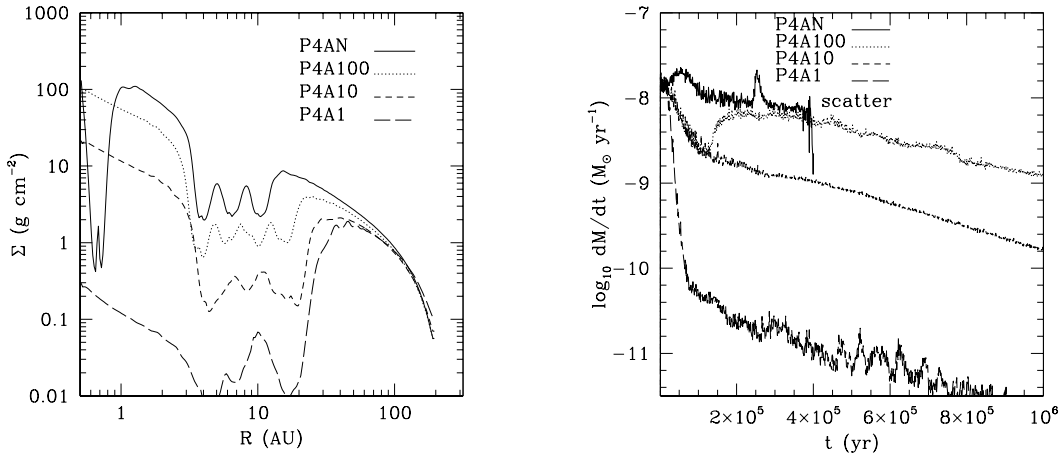


Figure 9.7 Left: disk surface densities at 0.4 Myrs for four planets with no planet accretion (solid curve), $f=100$ (dotted curve), $f = 10$ (short-dashed curve), and $f = 1$ (long-dashed curve). Right: the corresponding disk accretion rates.

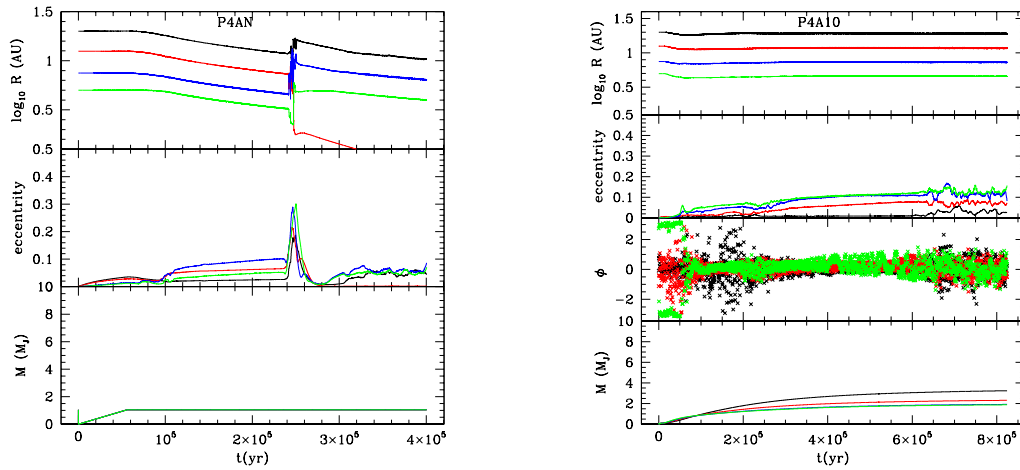


Figure 9.8 The planets' semi-major axis, eccentricities, resonant angles (2:1), masses with time for four planets in P4AN case (left) and P4A10 case (right). In the ϕ panel of the right figure, black, red, and green curves represent the resonant angle between the pairs of 4/3, 3/2, 2/1 planets (4 is the outermost one.).

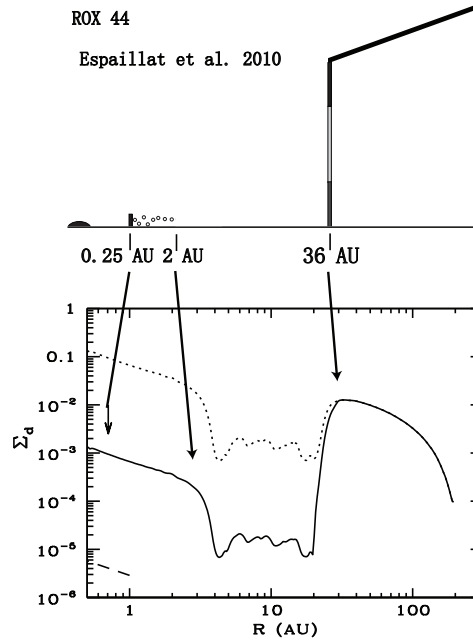


Figure 9.9 The pre-transitional disk structure taken from Espaillat et al. (2010) compared with the azimuthal-averaged dust surface density of the P4A10 case. The dotted curve represents the case with no dust depletion and the solid curve represents the case with the dust at the inner disk depleted by a factor of 100. The solid curve can explain the pretransitional disk structure as indicated by the arrows. The dashed curve is the dust surface density from the transitional disk GM Aur estimated by Eq. 9, which requires the dust to deplete by a factor of 10^5 by comparison with the dotted curve.

CHAPTER 10

Conclusions

10.1 Thesis Work

Since the typical observed protostellar luminosities are significantly lower than the luminosity expected from the steady protostellar disk accretion (Kenyon et al. 1990; Evans et al. 2009), protostars may accrete most of their mass by outbursts of rapid accretion. FU Orionis objects are candidates for these outbursting protostellar disks.

For the first part of my thesis, I estimated the size of FU Ori's hot, rapidly accreting inner disk is ~ 0.5 -1 AU using mid-IR spectra from Spitzer. Considering the outburst timescale ~ 100 yrs, the inferred disk viscosity parameter α is 0.2-0.02, consistent with simulations of the magnetorotational instability in accretion disks.

Then, I constrained the rotation curve of FU Ori disk by measuring line widths at different wavelengths (optical, 2.2 μm , 5 μm). I found the disk follows Keplerian rotation, which not only confirms the disk origin for outbursts but also confirms the high accretion disk extends to AU scale (where 5 μm absorption lines are produced) in agreement with our previous study.

Motivated by my constraints on FU Ori's accretion disk, I studied the disk's accretion regions by either MRI or GI. I found that neither models with accretion due solely to MRI nor GI are likely to transport disk mass at protostellar infall rates from the outer disk to the central protostar. Instead, the thermal activation of the MRI by the heating generated from GI will lead to outbursts. This outburst has been confirmed by two dimensional axisymmetric (R-Z) radiation-hydrodynamic simulations. The simulation agrees with FU Ori's decay timescale, peak accretion rates, and accretion disk size.

Following the 2-D studies, I constructed a simplified one-dimensional protoplanetary disk evolutionary model with mass addition from the rotating cloud core. The disk model consists of a MRI active layer and a dead zone. I found that 1) the disk undergoes FU Ori-like outbursts of accretion, when the infall lands to the disk beyond ~ 10 AU. If the initial cloud core is moderately rotating, most of the central star's mass is built up by these outbursting events, which alleviates the protostellar "luminosity problem" . 2) After the infall phase, an outer, viscously evolving disk has structure that is in reasonable agreement with recent submillimeter studies. But an inner, massive region the "dead zone" that has not been observed yet, should be detected in future high angular resolution observations by EVLA and ALMA. This high surface density region is a generic consequence of the layered accretion, and would strongly affect planet formation and migration.

The massive inner disk may suggest multiple planets form in a compact region, which may explain newly discovered "pretransitional and transitional disks" -protoplanetary disks having gaps and holes. For the second part of my thesis, I carried out hydrodynamic simulations to study gap opening by multiple giant planets. However, if the ISM dust-to-gas mass ratio is assumed, even four giant planets cannot open a gap as wide as that observed (planets are moved close to each other into 2:1 resonances by the viscous disk); furthermore the gap is not deep enough to be optically thin. Both findings suggest the dust-to-gas mass ratio within gaps/holes is significantly reduced, estimated between 10^{-5} and 10^{-2} of the ISM value, putting constraints on early planet formation. This may shed light on the condition at early planet formation stage.

10.2 Future work

With the recent Spitzer survey reviving the "luminosity problem", FU Orionis objects become the "missing link" between highly embedded young stellar objects and star formed T-Tauri systems. The unsteady accretion process may even alter the central star's structure and affect the young star's position on the H-R diagram (Baraffe, Chabrier, & Gallardo 2009). Besides these new questions, recent and near future

observations will put stringent constraints on the properties of the outbursting phenomenon and reveal its importance on the star formation process. For example, considering the high brightness of these outbursting events, they can be easily picked up by sky surveys from the transiting planet search program. Two YSO outbursting events have already been detected within one year's survey of the Palomar Transient Factory (PTF; Law et al. 2009; Rau et al. 2009; Miller et al. 2011; Covey et al. 2011). With \sim two thousand YSOs in the North America Nebula where the two outbursts were found within one year, it suggests each YSO may experience \sim 100-1000 outbursts considering the timescale of YSO is 10^5 - 10^6 years. This seems to agree with the hypothesis that most of the protostar's mass is accumulated by these outbursts and each outburst accrete $0.01 M_{\odot}$ onto the protostar.

With more samples on the time variable phenomena of YSOs will become available in the next decade, it is necessary to make observational prediction from our theoretical model, which will not only be tested by these new observations but can also serve as a guide for observation planning.

On the other hand, the outburst model will be improved in future. After the analytic estimate, 1 dimensional simulations and 2 dimensional R-Z simulations, I will carry out 2 dimensional R- ϕ simulations, which will be able to treat the gravitational instability self-consistently. One step further will be carrying 3-D MHD simulations to study MRI activation when the disk temperature is above the thermal ionization temperature. Ultimately, fully 3-D global MHD simulations with self-gravity, and radiative transfer will be needed to study this problem.

Regarding the transitional disks, 3-D simulations are also necessary to fully understand the gap structure. However considering many orders of magnitude difference in size between the circumstellar disk and the planet, adaptive/nested mesh grid algorithm is necessary to fully understand the gap opening.

Since the discovery of FU Ori 40 years ago, it gradually drew more and more attention due to its special role in the star formation process. On the other hand the discoveries of Transitional/Pretransitional disks are relatively recent, but due to their connection with planet formation, they are and will be in the spotlight in the

next decade. Both of these systems will advance our knowledge on star and planet formation with continuing combined theoretical and observational studies.

BIBLIOGRAPHY

- Adams, F. C., Lada, C. J., & Shu, F. H. 1987, *ApJ*, 312, 788
- Akeson, R. L., et al. 2005, *ApJ*, 635, 1173
- Alexander, D. R., & Ferguson, J. W. 1994, *ApJ*, 437, 879
- Alexander, R. D., & Armitage, P. J. 2007, *MNRAS*, 375, 500
- Alexander, R. D., & Armitage, P. J. 2009, *ApJ*, 704, 989
- Alves, J. F., Lada, C. J., & Lada, E. A. 2001, *Nature*, 409, 159
- Andre, P., Ward-Thompson, D., & Barsony, M. 2000, *Protostars and Planets IV*, 59
- Andrews, S. M., & Williams, J. P. 2005, *ApJ*, 631, 1134
- Andrews, S. M., Wilner, D. J., Hughes, A. M., Qi, C., & Dullemond, C. P. 2009, *ApJ*, 700, 1502
- Armitage, P. J., Livio, M., & Pringle, J. E. 2001, *MNRAS*, 324, 705
- Aspin, C., & Reipurth, B. 2003, *AJ*, 126, 2936
- Ayliffe, B. A., & Bate, M. R. 2009, *MNRAS*, 397, 657
- Bai, X.-N., & Goodman, J. 2009, *ApJ*, 701, 737
- Balbus, S. A., & Hawley, J. F. 1991, *ApJ*, 376, 214
- Balbus, S. A., & Hawley, J. F. 1998, *Reviews of Modern Physics*, 70, 1
- Balbus, S. A., & Papaloizou, J. C. B. 1999, *ApJ*, 521, 650

- Bally, J., Reipurth, B., & Davis, C. J. 2007, *Protostars and Planets V*, 215
- Baraffe, I., Chabrier, G., & Gallardo, J. 2009, *ApJ*, 702, L27
- Bate, M. R., Bonnell, I. A., & Bromm, V. 2003, *MNRAS*, 339, 577
- Beckwith, K., Hawley, J. F., & Krolik, J. H. 2008, *ApJ*, 678, 1180
- Bell, K. R., & Lin, D. N. C. 1994, *ApJ*, 427, 987
- Bell, K. R., Lin, D. N. C., Hartmann, L. W., & Kenyon, S. J. 1995, *ApJ*, 444, 376
- Benson, P. J., & Myers, P. C. 1989, *ApJS*, 71, 89
- Bernstein, R., Shectman, S. A., Gunnels, S. M., Mochnecki, S., & Athey, A. E. 2003, *Proc. SPIE*, 4841, 1694
- Boley, A. C., & Durisen, R. H. 2008, *ApJ*, 685, 1193
- Boley, A. C., Mejía, A. C., Durisen, R. H., Cai, K., Pickett, M. K., & D'Alessio, P. 2006, *ApJ*, 651, 517
- Bonnell, I., & Bastien, P. 1992, *ApJ*, 401, 654
- Book, L. G., & Hartmann, L. 2005, *BAAS*, 37, 1287
- Boss, A. P. 2002, *ApJ*, 576, 462
- Brandenburg, A., Nordlund, A., Stein, R., & Torkelsson, U. 1995, *ApJ*, 446, 741
- Brown, J. M., et al. 2007, *ApJ*, 664, L107
- Brown, J. M., Blake, G. A., Qi, C., Dullemond, C. P., Wilner, D. J., & Williams, J. P. 2009, *ApJ*, 704, 496
- Cai, K., Durisen, R. H., Boley, A. C., Pickett, M. K., & Mejía, A. C. 2008, *ApJ*, 673, 1138
- Calvet, N., et al. 2005, *ApJ*, 630, L185

- Calvet, N., D'Alessio, P., Hartmann, L., Wilner, D., Walsh, A., & Sitko, M. 2002, ApJ, 568, 1008
- Calvet, N., Hartmann, L., & Kenyon, S. J. 1991, ApJ, 383, 752
- Calvet, N., Patino, A., Magris, G. C., & D'Alessio, P. 1991, ApJ, 380, 617
- Caselli, P., Benson, P. J., Myers, P. C., & Tafalla, M. 2002, ApJ, 572, 238
- Cassen, P. 1993, Lunar and Planetary Institute Conference Abstracts, 24, 261
- Cassen, P., & Moosman, A. 1981, ICARUS, 48, 353
- Castelli, F. 2005, Memorie della Societa Astronomica Italiana Supplement, 8, 34
- Castelli, F., & Kurucz, R. L. 2004, ArXiv Astrophysics e-prints, arXiv:astro-ph/0405087
- Chandrasekhar, S. 1961, International Series of Monographs on Physics, Oxford: Clarendon, 1961,
- Chiang, E., & Murray-Clay, R. 2007, Nature Physics, 3, 604
- Clarke, C. J., Gendrin, A., & Sotomayor, M. 2001, MNRAS, 328, 485
- Clarke, C., Lodato, G., Melnikov, S. Y., & Ibrahimov, M. A. 2005, MNRAS, 361, 942
- Clarke, C. J., & Syer, D. 1996, MNRAS, 278, L23
- Cohen, M., Wheaton, W. A., & Megeath, S. T. 2003, AJ, 126, 1090
- Cohen, M., & Woolf, N. J. 1971, ApJ, 169, 543
- Cossins, P., Lodato, G., & Clarke, C. J. 2009, MNRAS, 393, 1157
- Cossins, P., Lodato, G., & Clarke, C. 2009b, arXiv:0910.0850
- Covey, K. R., et al. 2011, AJ, 141, 40
- Crida, A. 2009, ApJ, 698, 606

- Crida, A., Morbidelli, A., & Masset, F. 2007, *A&A*, 461, 1173
- Crida, A., & Morbidelli, A. 2007, *MNRAS*, 377, 1324
- D'Alessio, P., et al. 2005, *ApJ*, 621, 461
- D'Alessio, P., Calvet, N., & Hartmann, L. 2001, *ApJ*, 553, 321
- D'Alessio, P., Canto, J., Calvet, N., & Lizano, S. 1998, *ApJ*, 500, 411
- Desch, S. J. 1998, Ph.D. Thesis, U. Illinois.
- Desch, S. J. 2007, *ApJ*, 671, 878
- de Val-Borro, M., et al. 2006, *MNRAS*, 370, 529
- di Francesco, J., Evans, N. J., II, Caselli, P., Myers, P. C., Shirley, Y., Aikawa, Y., & Tafalla, M. 2007, *Protostars and Planets V*, 17
- Dominik, C., & Dullemond, C. P. 2008, *A&A*, 491, 663
- Dullemond, C. P., & Dominik, C. 2005, *A&A*, 434, 971
- Dougados, C., Cabrit, S., Lavalley, C., & Ménard, F. 2000, *A&A*, 357, L61
- Draine, B. T., & Lee, H. M. 1984, *ApJ*, 285, 89
- Draine, B. T., & Lee, H. M. 1987, *ApJ*, 318, 485
- Dullemond, C. P., Natta, A., & Testi, L. 2006, *ApJ*, 645, L69
- Durisen, R. H., Boss, A. P., Mayer, L., Nelson, A. F., Quinn, T., & Rice, W. K. M. 2007, *Protostars and Planets V*, 607
- Enoch, M. L., Evans, N. J., II, Sargent, A. I., Glenn, J., Rosolowsky, E., & Myers, P. 2008, *ApJ*, 684, 1240
- Enoch, M. L., Evans, N. J., Sargent, A. I., & Glenn, J. 2009, *ApJ*, 692, 973

- Espaillet, C., Calvet, N., D'Alessio, P., Hernández, J., Qi, C., Hartmann, L., Furlan, E., & Watson, D. M. 2007, *ApJ*, 670, L135
- Espaillet, C., Calvet, N., Luhman, K. L., Muzerolle, J., & D'Alessio, P. 2008, *ApJ*, 682, L125
- Espaillet, C., et al. 2010, *ApJ*, 717, 441
- Evans, N. J., et al. 2009, *ApJS*, 181, 321
- Fabricant, D., Cheimets, P., Caldwell, N., & Geary, J. 1998, *PASP*, 110, 79
- Faulkner, J., Lin, D. N. C., & Papaloizou, J. 1983, *MNRAS*, 205, 359
- Ferguson, J. W., Alexander, D. R., Allard, F., Barman, T., Bodnarik, J. G., Hauschildt, P. H., Heffner-Wong, A., & Tamanai, A. 2005, *ApJ*, 623, 585
- Fleming, T., & Stone, J. M. 2003, *ApJ*, 585, 908
- Foster, P. N., & Chevalier, R. A. 1992, *Bulletin of the AAS*, 24, 1215
- Foster, P. N., & Chevalier, R. A. 1993, *ApJ*, 416, 303
- Fromang, S., & Papaloizou, J. 2007 *å*, 476, 1113 (FP07)
- Fromang, S., Papaloizou, J., Lesur, G., & Heinemann, T. 2007, *A&A*, 476
- Fromang, S., & Stone, J. M. 2009, *arXiv:0906.4422*
- Furlan, E., et al. 2006, *ApJS*, 165, 568
- Furlan, E., et al. 2008, *ApJS*, 176, 184
- Gammie, C. F. 1996, *ApJ*, 457, 355
- Gammie, C. F. 1999, *ASP Conf. Ser. 160: Astrophysical Discs - an EC Summer School*, 160, 122
- Gammie, C. F. 2001, *ApJ*, 553, 174

- Glassgold, A. E., Najita, J., & Igea, J. 1997, ApJ, 480, 344
- Glassgold, A. E., Najita, J., & Igea, J. 2004, ApJ, 615, 972
- Goldreich, P., & Ward, W. R. 1973, ApJ, 183, 1051
- Gong, H., & Ostriker, E. C. 2009, ApJ, 699, 230
- Gorti, U., & Hollenbach, D. 2009, ApJ, 690, 1539
- Green, J. D., Hartmann, L., Calvet, N., Watson, D. M., Ibrahimov, M., Furlan, E., Sargent, B., & Forrest, W. J. 2006, ApJ, 648, 1099
- Greene, T. P., Aspin, C., & Reipurth, B. 2008, AJ, 135, 1421
- Greene, T. P., & Lada, C. J. 1996, AJ, 112, 2184
- Guan, X., & Gammie, C. F. 2008, ApJS, 174, 145
- Guan, X., & Gammie, C. F. 2009, ApJ, 697, 1901
- Guan, X., Gammie, C. F., Simon, J., and Johnson, B. M. 2008, ApJ, in prep.
- Guan, X., Gammie, C. F., Simon, J. B., & Johnson, B. M. 2009, ApJ, 694, 1010
- Gullbring, E., Hartmann, L., Briceno, C., & Calvet, N. 1998, ApJ, 492, 323
- Goodman, J., & Pindor, B. 2000, ICARUS, 148, 537
- Goodrich, R. W. 1987, PASP, 99, 116
- Hartmann, L. 1998, *Accretion processes in star formation* / Lee Hartmann. Cambridge, UK ; New York : Cambridge University Press, 1998. (Cambridge astrophysics series ; 32) ISBN 0521435072.,
- Hartmann, L., Boss, A., Calvet, N., & Whitney, B. 1994, ApJ, 430, L49
- Hartmann, L., Calvet, N., Gullbring, E., & D'Alessio, P. 1998, ApJ, 495, 385
- Hartmann, L., Cassen, P., & Kenyon, S. J. 1997, ApJ, 475, 770

- Hartmann, L., D'Alessio, P., Calvet, N., & Muzerolle, J. 2006, *ApJ*, 648, 484
- Hartmann, L., Heitsch, F., & Ballesteros-Paredes, J. 2009, *Revista Mexicana de Astronomia y Astrofisica Conference Series*, 35, 66
- Hartmann, L., Hinkle, K., & Calvet, N. 2004, *ApJ*, 609, 906
- Hartmann, L., & Kenyon, S. J. 1985, *ApJ*, 299, 462
- Hartmann, L., & Kenyon, S. J. 1987a, *ApJ*, 312, 243
- Hartmann, L., & Kenyon, S. J. 1987b, *ApJ*, 322, 393
- Hartmann, L., & Kenyon, S. J. 1991, *IAU Colloq. 129: The 6th Institute d'Astrophysique de Paris (IAP) Meeting: Structure and Emission Properties of Accretion Disks*, 203
- Hartmann, L., & Kenyon, S. J. 1996, *ARA&A*, 34, 207
- Hawley, J. F., Gammie, C. F., & Balbus, S. A. 1995, *ApJ*, 440, 742
- Hawley, J. F., Gammie, C. F., & Balbus, S. A. 1996, *ApJ*, 464, 690
- Henriksen, R., Andre, P., & Bontemps, S. 1997, *A&A*, 323, 549
- Herbig, G. H. 1977, *ApJ*, 217, 693
- Hernández, J. 2005, Ph.D. Thesis, Postgrado de Física Fundamental, Universidad de Los Andes, Venezuela.
- Hernández, J., Calvet, N., Briceño, C., Hartmann, L., & Berlind, P. 2004, *AJ*, 127, 1682
- Hinkle, K., Wallace, L., & Livingston, W. 1995, *PASP*, 107, 1042
- Hinkle, K. H., Cuberly, R. W., Gaughan, N. A., Heynssens, J. B., Joyce, R. R., Ridgway, S. T., Schmitt, P., & Simmons, J. E. 1998, *Proc. SPIE*, 3354, 810
- Hinkle, K. H., Joyce, R. R., Sharp, N., & Valenti, J. A. 2000, *Proc. SPIE*, 4008, 720

- Hinkle, K. H., et al. 2003, Proc. SPIE, 4834, 353
- Hirose, S., Krolik, J. H., & Blaes, O. 2009, ApJ, 691, 16
- Hirose, S., Krolik, J., De Villiers, J.-P., & Hawley, J. 2005, ApJ, 606, 1083
- Hirose, S., Krolik, J. H., & Stone, J. M. 2006, ApJ, 640, 901
- Hubeny, I. 1990, ApJ, 351, 632
- Hubickyj, O., Bodenheimer, P., & Lissauer, J. J. 2005, ICARUS, 179, 415
- Hughes, A. M., et al. 2009, ApJ, 698, 131
- Ibrahimov, M. A. 1999, Informational Bulletin on Variable Stars, 4691, 1
- Ilgner, M., & Nelson, R. P. 2006a, A&A, 445, 205
- Ilgner, M., & Nelson, R. P. 2006b, A&A, 445, 223
- Ilgner, M., & Nelson, R. P. 2006c, A&A, 455, 731
- Ilgner, M., & Nelson, R. P. 2008, A&A, 483, 815
- Jacoby, G. H., Hunter, D. A., & Christian, C. A. 1984, ApJS, 56, 257
- Johnson, B. M., & Gammie, C. F. 2003, ApJ, 597, 131
- Johansen, A., & Levin, Y. 2008, A&A, 490, 501
- Kalas, P., et al. 2008, Science, 322, 1345
- Kenyon, S. J., Gomez, M., Marzke, R. O., & Hartmann, L. 1994, AJ, 108, 251
- Kenyon, S. J., Calvet, N., & Hartmann, L. 1993, ApJ, 414, 676
- Kenyon, S. J., & Hartmann, L. 1987, ApJ, 323, 714
- Kenyon, S. J., & Hartmann, L. W. 1991, ApJ, 383, 664
- Kenyon, S. J., Hartmann, L. W., Strom, K. M., & Strom, S. E. 1990, AJ, 99, 869

- Kenyon, S. J., Hartmann, L., Gomez, M., Carr, J. S., & Tokunaga, A. 1993, *AJ*, 105, 1505
- Kenyon, S. J., & Hartmann, L. 1995, *ApJS*, 101, 117
- Kenyon, S. J., Hartmann, L., Imhoff, C. L., & Cassatella, A. 1989, *ApJ*, 344, 925
- Kenyon, S. J., Hartmann, L., & Hewett, R. 1988, *ApJ*, 325, 231 (KHH88)
- Kenyon, S. J., Hartmann, L., Imhoff, C. L., & Cassatella, A. 1989, *ApJ*, 344, 925
- Kenyon, S. J., Kolotilov, E. A., Ibragimov, M. A., & Mattei, J. A. 2000, *ApJ*, 531, 1028
- King, A. R., Pringle, J. E., & Livio, M. 2007, *MNRAS*, 376, 1740
- Kley, W. 2000, *MNRAS*, 313, L47
- Kley, W., Lee, M. H., Murray, N., & Peale, S. J. 2005, *A&A*, 437, 727
- Kley, W., & Lin, D. N. C. 1999, *ApJ*, 518, 833
- Kratter, K. M., Matzner, C. D., & Krumholz, M. R. 2008, *ApJ*, 681, 375
- Kratter, K. M., Matzner, C. D., Krumholz, M. R., & Klein, R. I. 2010, *ApJ*, 708, 1585
- Kretke, K. A., Lin, D. N. C., Garaud, P., & Turner, N. J. 2009, *ApJ*, 690, 407
- Kuiper, G. P. 1951, *Proceedings of the National Academy of Science*, 37, 1
- Kurucz, R. L., Peytreman, E., & Avrett, E. H. 1974, *Washington : Smithsonian Institution : for sale by the Supt. of Docs., U.S. Govt. Print. Off., 1974.*, 37
- Kurucz, R. L. 1993, *Kurucz CD-ROM*, Cambridge, MA: Smithsonian Astrophysical Observatory, —c1993, December 4, 1993,
- Kurucz, R. L. 2005, *Memorie della Societa Astronomica Italiana Supplement*, 8, 86

- Kurucz, R. L., & Avrett, E. H. 1981, SAO Special Report, 391,
- Kurucz, R. L., Peytremann, E., & Avrett, E. H. 1974, Washington : Smithsonian Institution : for sale by the Supt. of Docs., U.S. Govt. Print. Off., 1974., 37
- Larson, R. B. 1984, MNRAS, 206, 197
- Larson, R. B. 1983, Revista Mexicana de Astronomia y Astrofisica, vol. 7, 7, 219
- Law, N. M., et al. 2009, PASP, 121, 1395
- Lesur, G., & Longaretti, P.-Y. 2007, MNRAS, 378, 1471
- Lesur, G., & Papaloizou, J. C. B. 2009, arXiv:0911.0663
- Lesur, G., & Longaretti, P.-Y. 2009, A&A, 504, 309
- Lin, D. N. C., Faulkner, J., & Papaloizou, J. 1985, MNRAS, 212, 105
- Lin, D. N. C., & Papaloizou, J. 1980, MNRAS, 191, 37
- Lin, D. N. C., & Papaloizou, J. 1985, Protostars and Planets II, 981
- Lin, D. N. C., & Papaloizou, J. 1986, ApJ, 307, 395
- Lin, D. N. C., & Papaloizou, J. C. B. 1993, Protostars and Planets III, 749
- Lin, D. N. C., & Pringle, J. E. 1987, MNRAS, 225, 607
- Lin, D. N. C., & Pringle, J. E. 1990, ApJ, 358, 515
- Lodato, G., & Bertin, G. 2003, A&A, 408, 1015
- Lodato, G., & Clarke, C. J. 2004, MNRAS, 353, 841
- Lodato, G., & Rice, W. K. M. 2004, MNRAS, 351, 630
- Lodato, G., & Rice, W. K. M. 2005, MNRAS, 358, 1489
- Lubow, S. H., & D'Angelo, G. 2006, ApJ, 641, 526

- Lynden-Bell, D., & Pringle, J. E. 1974, MNRAS, 168, 603
- Malbet, F., et al. 2005, A&A, 437, 627
- Marois, C., Macintosh, B., Barman, T., Zuckerman, B., Song, I., Patience, J., Lafrenière, D., & Doyon, R. 2008, Science, 322, 1348
- Marsh, K. A., & Mahoney, M. J. 1992, ApJ, 395, L115
- Masset, F. 2000, A&AS, 141, 165
- Masset, F. S. 2002, A&A, 387, 605
- Masset, F. S., & Papaloizou, J. C. B. 2003, ApJ, 588, 494
- Matsumoto, T., & Hanawa, T. 2003, ApJ, 595, 913
- Matsumura, S., Pudritz, R. E., & Thommes, E. W. 2007, ApJ, 660, 1609
- Matsumura, S., Pudritz, R. E., & Thommes, E. W. 2009, ApJ, 691, 1764
- McKinney, J. C., & Gammie, C. F. 2002, ApJ, 573, 728
- McKinney, J. C., & Narayan, R. 2007, MNRAS, 375, 513
- Mihalas, D., & Weibel Mihalas, B. 1984, New York: Oxford University Press, 1984,
- Millan-Gabet, R., et al. 2006, ApJ, 641, 547
- Miller, K. A., & Stone, J. M. 2000, ApJ, 534, 398
- Miller, A. A., et al. 2011, ApJ, 730, 80
- Mould, J. R., Hall, D. N. B., Ridgway, S. T., Hintzen, P., & Aaronson, M. 1978, ApJ, 222, L123
- Movshovitz, N., Bodenheimer, P., Podolak, M., & Lissauer, J. J. 2010, ICARUS, 209, 616
- Muzerolle, J., Hartmann, L., & Calvet, N. 1998, AJ, 116, 2965

- Muzerolle, J., Calvet, N., Hartmann, L., & D'Alessio, P. 2003, *ApJ*, 597, L149
- Myers, P. C., Adams, F. C., Chen, H., & Schaff, E. 1998, *ApJ*, 492, 703
- Najita, J. R., Strom, S. E., & Muzerolle, J. 2007, *MNRAS*, 378, 369
- Najita, J. R., Carr, J. S., Strom, S. E., Watson, D. M., Pascucci, I., Hollenbach, D., Gorti, U., & Keller, L. 2010, *ApJ*, 712, 274
- Natta, A., Prusti, T., Neri, R., Wooden, D., Grinin, V. P., & Mannings, V. 2001, *A&A*, 371, 186
- Nelson, R. P., Papaloizou, J. C. B., Masset, F., & Kley, W. 2000, *MNRAS*, 318, 18
- Nelson, R. P., & Papaloizou, J. C. B. 2003, *MNRAS*, 339, 993
- O'dell, C. R., & Wen, Z. 1994, *ApJ*, 436, 194
- Owen, J. E., Ercolano, B., Clarke, C. J., & Alexander, R. D. 2010, *MNRAS*, 401, 1415
- Paardekooper, S.-J., & Mellema, G. 2006, *A&A*, 453, 1129
- Papaloizou, J., Faulkner, J., & Lin, D. N. C. 1983, *MNRAS*, 205, 487
- Papaloizou, J. C. B., & Nelson, R. P. 2005, *A&A*, 433, 247
- Papaloizou, J. C. B., Nelson, R. P., & Snellgrove, M. D. 2004, *MNRAS*, 350, 829
- Partridge, H., & Schwenke, D. W. 1997, *J. Chem. Phys*, 106, 4618
- Petersen, M. R., Julien, K., & Stewart, G. R. 2007, *ApJ*, 658, 1236
- Petrov, P. P., & Herbig, G. H. 2008, *AJ*, 136, 676
- Pierens, A., & Nelson, R. P. 2008, *A&A*, 482, 333
- Piétu, V., Dutrey, A., Guilloteau, S., Chapillon, E., & Pety, J. 2006, *A&A*, 460, L43

- Pollack, J. B., Hubickyj, O., Bodenheimer, P., Lissauer, J. J., Podolak, M., & Greenzweig, Y. 1996, ICARUS, 124, 62
- Popham, R., Narayan, R., Hartmann, L., & Kenyon, S. 1993, ApJ, 415,
- Popham, R., Kenyon, S., Hartmann, L., & Narayan, R. 1996, ApJ, 473, 422
- Pott, J.-U., Perrin, M. D., Furlan, E., Ghez, A. M., Herbst, T. M., & Metchev, S. 2010, ApJ, 710, 265
- Pringle, J. E. 1991, MNRAS, 248, 754
- Quanz, S. P., Henning, T., Bouwman, J., Ratzka, T., & Leinert, C. 2006, ApJ, 648, 472L127
- Quanz, S. P., Henning, T., Bouwman, J., van Boekel, R., Juhász, A., Linz, H., Pontoppidan, K. M., & Lahuis, F. 2007, ApJ, 668, 359
- Rafikov, R. R. 2005, ApJ, 621, L69
- Rafikov, R. R. 2007, ApJ, 662, 642
- Rafikov, R. R. 2009, ApJ, 704, 281
- Rau, A., et al. 2009, PASP, 121, 1334
- Rayner, J. T., Toomey, D. W., Onaka, P. M., Denault, A. J., Stahlberger, W. E., Watanabe, D. Y., & Wang, S.-I. 1998, Proc. SPIE, 3354, 468
- Reipurth, B., & Aspin, C. 1997, AJ, 114, 2700
- Reipurth, B., Hartmann, L., Kenyon, S. J., Smette, A., & Bouchet, P. 2002, AJ, 124, 2194
- Reipurth, B., & Aspin, C. 2004, ApJ, 608, L65
- Reipurth, B., Aspin, C., Beck, T., Brogan, C., Connelley, M. S., & Herbig, G. H. 2007, AJ, 133, 1000

- Reyes-Ruiz, M. 2007, MNRAS, 380, 311
- Reyes-Ruiz, M., & Stepinski, T. F. 1995, ApJ, 438, 750
- Rice, W. K. M., Armitage, P. J., Wood, K., & Lodato, G. 2006, MNRAS, 373, 1619
- Rice, W. K. M., Lodato, G., Pringle, J. E., Armitage, P. J., & Bonnell, I. A. 2004, MNRAS, 355, 543
- Rice, W. K. M., Mayo, J. H., & Armitage, P. J. 2009, arXiv:0911.1202
- Rice, W. K. M., Wood, K., Armitage, P. J., Whitney, B. A., & Bjorkman, J. E. 2003, MNRAS, 342, 79
- Ruden, S. P., Papaloizou, J. C. B., & Lin, D. N. C. 1988, ApJ, 329, 739
- Safronov, V. S. 1969, 1969.,
- Sandell, G., & Aspin, C. 1998, A&A, 333, 1016
- Sandell, G., & Weintraub, D. A. 2001, ApJS, 134, 115
- Sano, T., Miyama, S. M., Umebayashi, T., & Nakano, T. 2000, ApJ, 543, 486
- Sbordone, L., Bonifacio, P., Castelli, F., & Kurucz, R. L. 2004, Memorie della Societa Astronomica Italiana Supplement, 5, 93
- Schneider, G., Wood, K., Silverstone, M. D., Hines, D. C., Koerner, D. W., Whitney, B. A., Bjorkman, J. E., & Lowrance, P. J. 2003, AJ, 125, 1467
- Schwenke, D. W. 1998, Chemistry and Physics of Molecules and Grains in Space. Faraday Discussions No. 109, 321
- Shakura, N. I., & Sunyaev, R. A. 1973, A&A, 24, 337
- Shlosman, I., & Begelman, M. C. 1987, Nature, 329, 810
- Shu, F. H. 1977, ApJ, 214, 488

- Shu, F. H., Adams, F. C., & Lizano, S. 1987, *ARA&A*, 25, 23
- Simon, M., Dutrey, A., & Guilloteau, S. 2000, *ApJ*, 545, 1034
- Snellgrove, M. D., Papaloizou, J. C. B., & Nelson, R. P. 2001, *A&A*, 374, 1092
- Stahler, S. W. 1988, *ApJ*, 332, 804
- Stone, J. M., Hawley, J. F., Gammie, C. F., & Balbus, S. A. 1996, *ApJ*, 463, 656
- Stone, J. M., & Norman, M. L. 1992, *ApJS*, 80, 753
- Strom, K. M., Strom, S. E., Edwards, S., Cabrit, S., & Skrutskie, M. F. 1989, *AJ*, 97, 1451
- Syer, D., & Clarke, C. J. 1995, *MNRAS*, 277, 758
- Tanaka, H., Himeno, Y., & Ida, S. 2005, *ApJ*, 625, 414
- Tannirkulam, A., et al. 2008, *ArXiv e-prints*, 808, arXiv:0808.1728
- Terebey, S., Shu, F. H., & Cassen, P. 1984, *ApJ*, 286, 529
- Terquem, C. E. J. M. L. J. 2008, *ApJ*, 689, 532
- Tobin, J. J., Hartmann, L., Chiang, H.-F., & Looney, L. W. 2010, arXiv:1002.2362
- Toomre, A. 1964, *ApJ*, 139, 1217
- Turner, N. J. J., Bodenheimer, P., & Bell, K. R. 1997, *ApJ*, 480, 754
- Turner, N. J., & Sano, T. 2008, *ApJ*, 679, L131
- Turner, N. J., Sano, T., & Dziourkevitch, N. 2007, *ApJ*, 659, 729
- Turner, N. J., & Stone, J. M. 2001, *ApJS*, 135, 95
- Vallee, J. P. 2004, *NewA Rev.*, 48, 763
- van Ballegooijen, A. A. 1989, *Accretion Disks and Magnetic Fields in Astrophysics*, 156, 99

- Varnière, P., Blackman, E. G., Frank, A., & Quillen, A. C. 2006, *ApJ*, 640, 1110
- Vorobyov, E. I. 2009, *ApJ*, 704, 715
- Vorobyov, E. I., & Basu, S. 2005, *ApJ*, 633, L137
- Vorobyov, E. I., & Basu, S. 2006, *ApJ*, 650, 956
- Vorobyov, E. I., & Basu, S. 2007, *MNRAS*, 381, 1009
- Vorobyov, E. I., & Basu, S. arXiv:0802.2242v1
- Vorobyov, E. I., & Basu, S. 2009, *MNRAS*, 393, 822
- Ward-Thompson, D., André, P., Crutcher, R., Johnstone, D., Onishi, T., & Wilson, C. 2007, *Protostars and Planets V*, 33
- Weidenschilling, S. J. 1977, *Ap&SS*, 51, 153
- Weidenschilling, S. J. 1980, *ICARUS*, 44, 172
- Weidenschilling, S. J., Spaute, D., Davis, D. R., Marzari, F., & Ohtsuki, K. 1997, *ICARUS*, 128, 429
- Weintraub, D. A., Sandell, G., & Duncan, W. D. 1989, *ApJ*, 340, L69
- Weizsäcker, C. F. V. 1943, *Zeitschrift für Astrophysik*, 22, 319
- Welty, A. D., Strom, S. E., Edwards, S., Kenyon, S. J., & Hartmann, L. W. 1992, *ApJ*, 397, 260
- White, R. J., Greene, T. P., Doppmann, G. W., Covey, K. R., & Hillenbrand, L. A. 2007, *Protostars and Planets V*, 117
- White, R. J., & Hillenbrand, L. A. 2004, *ApJ*, 616, 998
- Whitney, B. A., Wood, K., Bjorkman, J. E., & Wolff, M. J. 2003, *ApJ*, 591, 1049
- Winters, W. F., Balbus, S. A., & Hawley, J. F. 2003, *ApJ*, 589, 543

- Wünsch, R., Klahr, H., & Różyczka, M. 2005, MNRAS, 362, 361
- Wünsch, R., Gawryszczak, A., Klahr, H., & Różyczka, M. 2006, MNRAS, 367, 773
- Zhu, Z., Hartmann, L., Calvet, N., Hernandez, J., Muzerolle, J., & Tannirkulam, A.-K. 2007, ApJ, 669, 483 (Paper I)
- Zhu, Z., Hartmann, L., Calvet, N., Hernandez, J., Tannirkulam, A.-K., & D'Alessio, P. 2008, ApJ, 684, 1281
- Zhu, Z., Espaillat, C., Hinkle, K., Hernandez, J., Hartmann, L., & Calvet, N. 2009a, ApJ, 694, L64
- Zhu, Z., Hartmann, L., & Gammie, C. 2009b, ApJ, 694, 1045
- Zhu, Z., Hartmann, L., Gammie, C., & McKinney, J. C. 2009c, ApJ, 701, 620
- Zhu, Z., Hartmann, L., Gammie, C. F., Book, L. G., Simon, J. B., & Engelhard, E. 2010a, ApJ, 713, 1134
- Zhu, Z., Hartmann, L., & Gammie, C. 2010b, ApJ, 713, 1143